Electron Diffraction Study Of The Structure Of Grain Boundaries In Germanium

By

Mohamed Hassen Ibrahim EL-Eraki

A Thesis Submitted For The Degree Of
Doctor In Philosophy
In The
University Of Liverpool

April 1989

Department of
Materials Science
and Engineering

ABSTRACT

The work described in this thesis is concerned with theoretical and experimental aspects of the study of interfacial sturcture in germanium bicrystals using selected-area diffraction (SAD), convergent-beam diffraction (CBED), and large-angle-convergent-beam diffraction (LACBED). The theoretical work comprises a crystallographic treatment which enables the diffraction groups for bicrystal specimens to be determined, taking into account the relative orientation and position of the adjacent crystals, and whether the interface is parallel (plan-view specimens) or perpendicular (edge-on specimens) to the specimen surfaces. Bicrystal specimens were prepared for electron microscopy from germanium polycrystals comprising large grains. The interfaces studied were $\Sigma=3(1\bar{1}\bar{1})$ and $\Sigma=3(\bar{1}1\bar{2})$, and $\Sigma=27(5\bar{5}\bar{2})$, and, in each case, both "edge-on" and "plan-view" specimens were prepared. It was found that the $\Sigma=3(1\bar{1}\bar{1})$ interface was planar, but the $\Sigma=3(\bar{1}1\bar{2})$ exhibited a facetted structure to some extent. The $\Sigma=27(5\bar{5}\bar{2})$ interface exhibited extensive facetting and decomposition, which complicated its investigation by electron diffraction.

Using relatively large spot sizes, it was found that the CBED patterns obtained with the incident probe straddling "edge-on" interfaces, corresponded to the superimposition of the CBED patterns obtained separately from the adjacent single crystals. This was explained in terms of the summation of scattering events occurring in an incoherently related manner in the adjacent crystals. On the other hand, CBED patterns from

"plan-view" specimens were interpreted in terms of the summation of coherently related scattering events in the adjacent crystals. However, the latter type of patterns did not reveal certain symmetries thought to be potentially present in the specimens, and this was consistent with the suppression of these symmetries in specimen preparation, e.g. the interface was not precisely parallel to the surfaces and did not occupy the central plane.

Selected-area diffraction was found to be particularly useful in the study of $\Sigma=3(\bar{1}1\bar{2})$ "plan-view" specimens. Evidence was obtained supporting an interfacial structure with centred 2x2 reconstruction. The intensities of additional reflections arising due to this reconstruction were found to be in good agreement with values calculated on the basis of kinematic theory and using the atomic positions determined by computer simulation *(Paxton et al. 1987).*

TABLE OF CONTENTS

Page No.

ACKNOWLEDGEMENTS. v

Chapter One. Introduction.

1.1. The importance of grain boundary structure 1.2
1.2. The objective of this thesis 1.4
1.3. The scope of the thesis 1.5

Chapter Two. Symmetry of Crystals and Bicrystals.

2.1. Introduction 2.2
2.2. Crystal symmetry 2.3
2.3. Dichromatic patterns 2.4
    2.3.1. Coincident symmetry elements 2.6
    2.3.2. Antisymmetry elements 2.7
2.4. Mathematical analysis; general principles 2.8
    2.4.1. Equivalent displacement and Wigner-Seitz cells 2.11
    2.4.2. The variation of the dichromatic pattern symmetry with relative displacement 2.12
2.5. Dichromatic complexes 2.13
    2.5.1. The variation of the dichromatic complex symmetry with relative displacement 2.15
2.6. Bicrystal symmetry 2.16
2.7. Relaxed bicrystals 2.17

Chapter Three. Experimental Techniques.

3.1. Specimen Preparation 3.2
    3.1.1. "Edge-on" Specimens 3.3

3.1.2. "Plan-View" Specimens 3.4

3.2. Transmission Electron Microscopy Techniques 3.5

3.2.1. Selected Area Diffraction 3.5

3.2.2. Convergent Beam Electron Diffraction 3.13

3.2.3. Large Angle Convergent Beam Electron Diffraction 3.17

Chapter Four. Diffraction Groups for Single Crystals and Bicrystals

4.1. Introduction 4.2

4.2. Types of symmetry 4.2

4.2.1. The ordinary symmetry elements 4.3

4.2.2. The anti-symmetry elements 4.3

4.3. Diffraction groups for single crystals 4.3

4.4. The bright field, projection diffraction, and whole pattern groups 4.7

4.4.1. The bright field groups 4.8

4.4.2. The projection diffraction groups 4.10

4.4.3. The whole pattern groups 4.11

4.5. Bicrystal diffraction groups 4.11

4.5.1. Diffraction groups for "plan-view" bicrystals 4.12

4.5.2. Diffraction groups for "edge-on" bicrystals 4.14

4.6. Experimental determinations of relative displacement 4.16

Chapter Five. The Experimental Results.

5.1. Macroscopic Investigations 5.2

5.1.1. Optical Microscopy 5.2

5.1.2. Scanning electron Microscopy 5.3

5.1.3. Laue Back-Reflection X-Ray Diffraction 5.3

5.2. Microscopic Investigations 5.5

5.2.1. $\Sigma=3$ "edge-on" specimens, "ia", "iia" and "iiia" 5.6
5.2.2. The "plan-view" $\Sigma=3$ specimens, "ib", "iib" and "iiib" 5.7
5.2.3. The "edge-on" $\Sigma=3$ specimen, "iva" 5.7
5.3. $\Sigma=3(\bar{1}1\bar{2})_\lambda$ grain boundary 5.8
5.3.1. The $[\bar{1}1\bar{2}]_\lambda$ SAD and CBED patterns 5.9
5.3.2. The $[110]_\lambda$ SAD and CBED patterns 5.10
5.3.3. The $[1\bar{1}\bar{1}]_\lambda$ SAD and CBED patterns 5.11
5.4. $\Sigma=27$ grain boundary 5.11
5.4.1. The $\Sigma=27$ "edge-on" specimen, "va" 5.11
5.4.2. The $\Sigma=27$ "plan-view" specimen, "vb" 5.13

Chapter Six. Discussion.

6.1. General remarks 6.3
6.2. Interfacial facetting and dissociation 6.4
6.3. Interpretation of CBED and LACBED patterns from "plan-view" and "edge-on" specimens 6.7
6.4. Interpretation of SAD patterns 6.10
6.5. Observation of $\Sigma = 3(1\bar{1}\bar{1})_\lambda$ boundary 6.13
6.5.1 Previous experimental observations and theoretical models of $\Sigma = 3(1\bar{1}\bar{1})_\lambda$ boundary 6.13
6.5.2. SAD patterns from "edge-on" and "plan-view" specimens 6.14
6.5.3. CBED patterns from "edge-on" specimen 6.15
6.5.4. CBED patterns from "plan-view" specimen 6.16
6.5.5. LACBED patterns from "edge-on" and "plan-view" specimen 6.16
6.5.6. Summary of observations 6.18
6.6. Previous experimental observations and theoretical models of $\Sigma = 3(\bar{1}1\bar{2})_\lambda$ boundary 6.19
6.6.1. SAD patterns from "edge-on" and "plan-view" specimens 6.20

6.6.2. CBED patterns from "edge-on" and "plan-view" specimens 6.24

6.6.3. Summary of observations 6.26

6.6.4. Observation of dissociation in $\Sigma = 3(\bar{1}1\bar{2})_\lambda$ "edge-on" specimen 6.27

6.7. Previous experimental observations and theoretical models of $\Sigma = 27(5\bar{5}\bar{2})_\lambda$ boundary 6.28

6.7.1. Dissociation of $\Sigma = 27(5\bar{5}\bar{2})_\lambda$ boundary 6.29

6.7.2. SAD patterns from "edge-on" and "plan-view" specimens 6.30

6.7.3. CBED patterns from "edge-on" and "plan-view" specimens 6.32

6.7.4. Summary of observations 6.33

Chapter Seven. Conclusions and suggestions for further work.

7.1. Conclusions regarding theoretical crystallography 7.1

7.2. Conclusions regarding experimental techniques 7.2

7.3. Conclusions regarding specific interfacial structures 7.2

7.4. Suggestions for further work 7.3

References ref.1

ACKNOWLEDGEMENTS

I would like to thank Dr. R.C. Pond for his thoughtful, valuable comments and stimulating supervision and his encouragement throughout the course of this work.

The author is most grateful to Dr. J.J. Bacmann for providing the germanium materials used in this study.

It is pleasure to thank Prof. C.J. Humphreys for allowing me to use the facilities in the micro-electronic laboratory.

I am grateful to many friends and colleagues for advice and assistance in using x-ray unit, ion beam miller, mechanical dimpling machine, ultrasonic drill, diamond saw, electron microscope and cold stage double-tilt specimen holder especially A. Green, Crispin Hetherington, E. Kevm, I. Salisbury, N. Huxford, R. Devenish, D.Eaglesham M. Aindow and J. Gillies.

The author would like to thank all those who supported him in this work, specially the financial support by the Egyptian government and the director and the staff of the Egyptian education bureau in London.

Finally, to my parents and my wife, Amina, without their loyalties this thesis would not have been possible.

CHAPTER ONE

INTRODUCTION

1.1. The importance of grain boundary structure........1.2
1.2. The objective of this thesis...................................1.4
1.3. The scope of the thesis..1.5

1.1. THE IMPORTANCE OF GRAIN BOUNDARY STRUCTURE.

Grain boundaries have significant influence on the properties of materials, for example, mechanical properties may be modified dramatically *(Smallman 1985)*, but in the present work we are particularly interested in semiconductor materials, where grain boundaries can have a profound influence on electrical properties such as resistivity, recombination efficiency and I-V characteristics. Grain boundaries in semiconductors are normally regarded as introducing deleterious electrical effects, but they can also play a role in determining the operating characteristics of several types of electronic devices. They severely limit the performance of some, such as thin film solar cells *(Chu et al. 1976)* and transistors *(Anderson 1980)*. On the other hand, in commercial varistors, the peculiar I-V characteristics of grain boundaries are actually used advantageously *(Mahan et al. 1979)*.

The long term objective of research into polycrystalline semiconductors is to understand the origin of properties in terms of interfacial structure. However, at present, only limited progress has been achieved toward this goal, see for example *Werner et al. 1982)*.

In the present study we are concerned with the structure of grain boundaries in germanium, and the relationship between grain boundary structure and electrical properties is outside of the scope of this thesis. The present understanding of the structure of semiconductor grain boundaries is firmly based on models developed for metallic boundaries. The most cogent of these currently under discussion is the Structural Unit Model, "SUM", *(Sutton 1984, Sutton and Vitek 1983)*. From computer generated relaxed grain boundary structures a small number of

3-dimensional atomic units that form the cores of boundaries have been identified. These units can also be considered as the cores of dislocations at the boundary, and so it is possible to describe the high angle grain boundaries formally as arrays of very closely spaced dislocations. Certain boundaries with very specific misorientation angles (Θ), usually about low index axes, contain only one structure unit. The core of the boundary is then simply a 2-dimensional array of these units. Between these favoured orientations, which are often calculated to have lower energy than boundaries with more complex core structures, the calculated structures show that many boundary cores can be described as linear combinations of units characteristic of the closest favoured boundaries. A small angular deviation from a favoured boundary misorientation can be accommodated by the introduction of a widely spaced array of new structural units into the boundary core, this unit being characteristic of the next favoured interface. These new structural units can also be thought of as a secondary dislocation array accommodating the misorientation away from the favoured boundary. Thus effective use of the "SUM" depends on the identification of a small number of structural units with which the core structure of boundaries within a particular misorientation range can be modelled. This model has a rather elegant correspondence with the earlier geometric models of grain boundaries, where the coincidence of lattice sites of the two crystals at the boundary plane is made the criterion for describing the boundary structure *(Pumphrey 1976 and Grimmer et al. 1974).*

Before the development of the experimental techniques that could be used to investigate the structure of grain boundaries by direct observation, some attention was paid to the modelling of interfaces in covalent materials, e.g. silicon and germanium. The boundaries were described as arrays of dislocations, and the atomic structures of the dislocation cores were modelled so as to minimise both the density of dangling bonds, and bond bending and stretching *(Hornstra 1959).*

Direct observation of grain boundary structures in semiconductors has only recently become common, and this can be related to the development of the current generation of High Resolution Electron Microscopes. With these instruments it is sometimes possible to resolve the atomic structure of crystals or bicrystals projected along certain low index directions *(Bourret et al. 1985a,b).* However, more conventional electron microscopic techniques, such as Selected Area Diffraction *(Hirsch et al. 1977),* Convergent Beam Electron Diffraction *(Steeds 1979),* and Large Angle Convergent Beam Electron Diffraction *(Tanaka et al. 1980),* can also be used to give useful information on boundary structure.

1.2. THE OBJECTIVE OF THIS THESIS.

The objective of this thesis is to study the structure of interfaces in germanium bicrystals supplied by *J. J. Bacmann.* The scheme of work to accomplish this study is divided into two programmes. The first programme is the preparation of germanium bicrystal specimens for transmission electron microscopy. The second one is determination of the structure and spacegroup of the germanium bicrystal specimens using electron microscopy. The first programme includes preparation of two different types of germanium bicrystal specimen depending on the orientation and position of the boundary plane with respect to the surface of the bicrystal specimen. One type is called "edge-on" specimen where the boundary plane is perpendicular to the specimen surfaces, and the other is called "plan-view", where the boundary plane is parallel to the specimen surfaces. The procedure for the preparation of germanium bicrystal specimens for electron microscopy comprises five steps. These steps are slicing germanium bulk materials, drilling the slice into 3mm discs, dimpling the discs, chemical etching of the discs and finally ion beam thinning of the discs. The techniques used for structure and spacegroup determinations in the second part of the programme are principally transmission electron microscopy, but optical microscopy, x-ray diffraction, and scanning electron microscopy were also used. Optical and scanning microscopy were used to detect the presence of the grain boundaries in germanium slices, and to photograph these. The Laue back-reflection X-ray method was used to determine the approximate orientation between the different grains present in a germanium slice. Transmission electron microscopy was used, first, to observe the microscopic structure of germanium bicrystals by employing bright-field and dark-field imaging techniques. Second, the precise orientation relationship between the bicrystal grains, the indices of the boundary planes and the periodicity of the interfacial boundary planes in germanium bicrystal specimens was determined using the Selected Area Diffraction (SAD) technique. Finally,it was intended to determine the spacegroup of germanium bicrystal specimens by making use of Convergent Beam Electron Diffraction (CBED) and Large Angle Convergent Beam Electron Diffraction (LACBED) techniques.

1.3. THE SCOPE OF THE THESIS.

In chapter two of this thesis we summarise, initially, the theoretical method for treating the symmetry of single crystals. Then we develop and formulate the theory which deals with the symmetry of bicrystals. Finally, this theory is applied to three germanium bicrystals with different relative orientations of the component crystals, which, in particular, the variation of bicrystal symmetry as the relative position of the crystals is changed is considered. In chapter three the experimental electron microscopical techniques used in the present study of interfaces are introduced in more detail. The theoretical aspects of the CBED technique are developed in chapter four, and, in particular presents a theoretical study of single crystal and bicrystal diffraction groups. First, the correspondences between single crystal point symmetries and the diffraction groups have been determined by a new procedure, and compared with those derived by *Buxton et al. (1974).* Secondly, the relations between single crystal point symmetries and bright-field, projection diffraction and whole pattern point groups of CBED patterns have been found using group theoretical methods, and tabulated. The equivalences between the "plan-view" bicrystal specimen point symmetries and the 31 diffraction groups are established, and found to be identical to those between single crystal point symmetries and the 31 diffraction groups *(Buxton et al. 1974).*

The experimental results obtained using the different techniques which have been used to study the structure of germanium interfaces are presented in chapter five. Chapter six presents the discussion of the experimental results, making use of the theoretical considerations included in chapters two and three. The principal conclusions reached in the present work and suggestions for further work are set out in chapter seven

CHAPTER TWO

Symmetry of Crystals and Bicrystals

2.1. Introduction....................................2.2

2.2. Crystal symmetry....................................2.3

2.3. Dichromatic patterns....................................2.4

  2.3.1. Coincident symmetry elements..............2.6

  2.3.2. Antisymmetry elements......................2.7

2.4. Mathematical analysis; general principles...........2.8

  2.4.1. Equivalent displacement and Wigner-Seitz cells........................2.11

  2.4.2. The variation of the dichromatic pattern symmetry with relative displacement.......2.12

2.5. Dichromatic complexes.................................2.13

  2.5.1. The variation of the dichromatic complex symmetry with relative displacement......2.15

2.6. Bicrystal symmetry..................................2.16

2.7. Relaxed bicrystals..................................2.17

2.1. INTRODUCTION.

The purpose of this chapter is to introduce the method devised by *Pond& Vlachavas (1983)* for treating the symmetry of bicrystals and to apply this procedure to the case of germanium bicrystals.

By way of introduction, we consider initially the symmetry of single crystals, and germanium in particular. We use the notation set out in the International Tables for Crystallography *(Hahn 1984)* for the matrix representation of symmetry operations.

The symmetry of dichromatic patterns, complexes and bicrystals depends on the relative orientation and position of the adjacent germanium crystals and in the latter case, the orientation of the interface. In the present work we are concerned with three distinct orientation relationships, which can be defined by the axis/angle pairs $<111>60^0$, $<110>38.94^0$ and $<110>31.59^0$, respectively; we refer to these as $\Sigma = 3$, $\Sigma = 9$ and $\Sigma = 27$ orientations and will define the parameter Σ later. The symmetry of the dichromatic pattern and complex for a given orientation relationship may vary as the relative position of the adjacent crystals changes and the determination of such variations will be discussed in some detail since experimental methods for measuring the relative position with considerable accuracy are available.

In the $\Sigma = 3$ case, the symmetry of the pattern and complex can belong to the hexagonal class and we have found it helpful to use the indexing method for such cases introduced by *F.C.Frank (1965)*.

2.2. CRYSTAL SYMMETRY.

The symmetry possessed by a crystal may be expressed concisely by one of the 230 crystallographic spacegroups *(Hahn 1984)*. Each group represents the combination of the crystal point symmetry operations (e.g. the identity, inversion, rotation by $2\pi/n$, $n = 1, 2, 3, 4$ or 6, reflection and roto-inversion) and the infinite set of translation vectors constituting the crystal's lattice. Each combination must transform the crystal into itself. Symmetry operations are represented in matrix notation *(Hahn 1984)* by the symbol (W, w), where W is (3x3) matrix and w is (3x1) column matrix. The former represents the rotation part and the latter represents the translation part of a symmetry operation.

We now consider the symmetry of germanium. Its lattice is F.C.C. and is represented schematically by the large&small circles in Fig.2.1(a). Fig.2.1(b), reproduced from the international tables for crystallography *(Hahn 1984)*, shows the symmetry elements present at the upper left quadrant of the lattice in Fig.2.1(a). Examination of this figure shows that, besides the 3-fold axes along <111> there are mirror planes perpendicular to <100> and <110>. Thus, the spacegroup of the F.C.C. lattice (Fig.2.1(a)) is $Fm\bar{3}m$ No. 225 *(Hahn 1984)*, which contains forty eight point symmetry operations as tabulated in Table 2.1. The number and the coordinate triplets of the symmetry operations (with respect to the chosen origin at position with site symmetry $m\bar{3}m$) are given in the first two columns; the point symmetry operations, W, are given in last column. Fig.2.1(b) and Table 2.1 show that the lattice does not exhibit mirror-glide planes or screw-rotation axes, and therefore its spacegroup is called symmorphic.

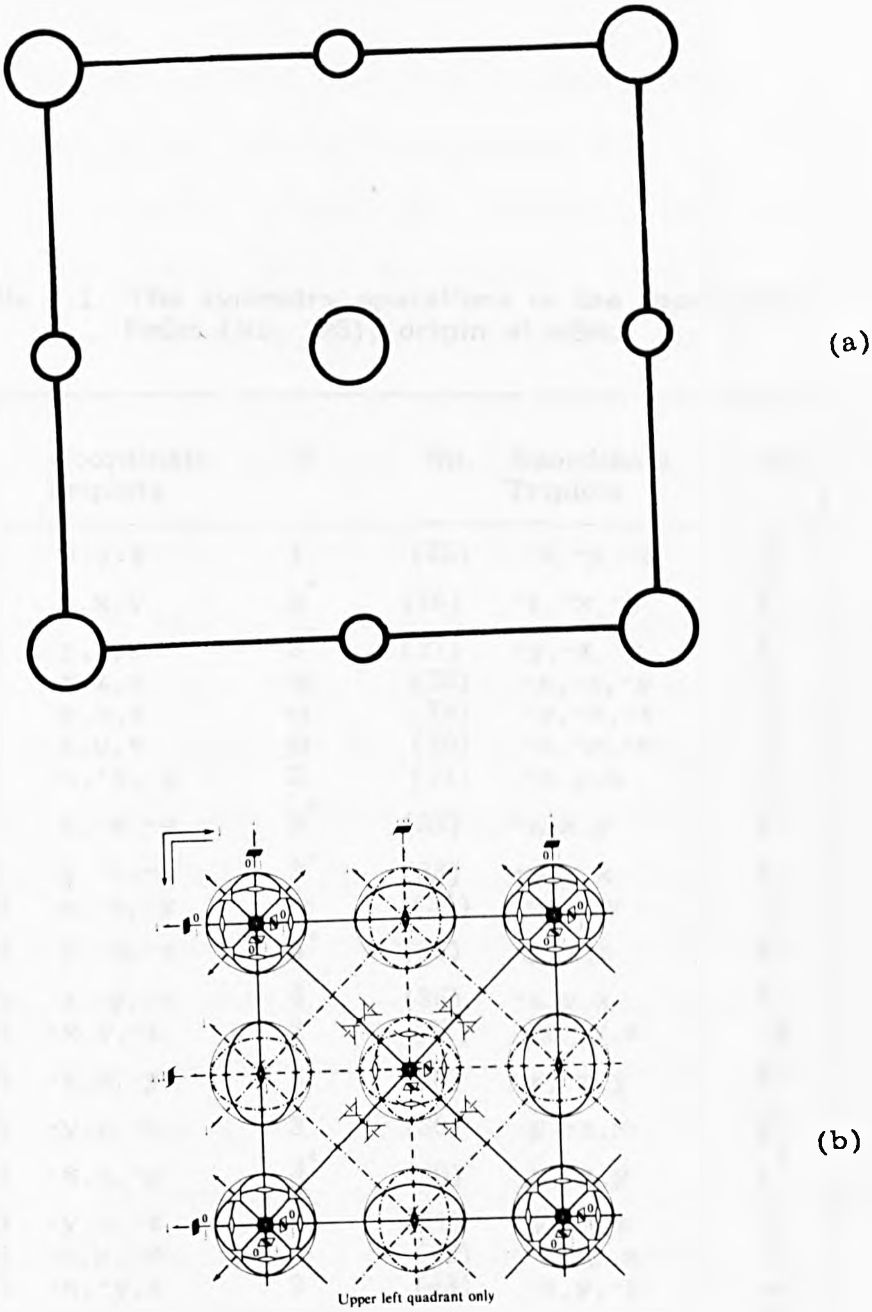

Fig. 2.1. (a) The projection along [001] of a face centre cubic (F.C.C.) lattice. Large and small circles are at heights 0 and $\frac{1}{2}$, respectively.

(b) The symmetry elements present at the upper left quadrant of the F.C.C. lattice in (a) (reproduced from Hahn 1984).

Table 2.1. The symmetry operations in the spacegroup $Fm\bar{3}m$ (No. 225); origin at $m\bar{3}m$.

No.	Coordinate Triplets	W	No.	Coordinate Triplets	W
(1)	x,y,z	1	(25)	-x,-y,-z	$\bar{1}$
(2)	z,x,y	3^+	(26)	-z,-x,-y	$\bar{3}^+$
(3)	y,z,x	3^-	(27)	-y,-z,-x	$\bar{3}^-$
(4)	x,z,y	m	(28)	-x,-z,-y	2
(5)	y,x,z	m	(29)	-y,-x,-z	2
(6)	z,y,x	m	(30)	-z,-y,-x	2
(7)	x,-y,-z	2	(31)	-x,y,z	m
(8)	z,-x,-y	3^+	(32)	-z,x,y	$\bar{3}^+$
(9)	y,-z,-x	3^-	(33)	-y,z,x	$\bar{3}^-$
(10)	x,-z,-y	m	(34)	-x,z,y	2
(11)	y,-x,-z	$\bar{4}^+$	(35)	-y,x,z	4^+
(12)	z,-y,-x	$\bar{4}^-$	(36)	-z,y,x	4^-
(13)	-x,y,-z	2	(37)	x,-y,z	m
(14)	-z,x,-y	3^+	(38)	z,-x,y	$\bar{3}^+$
(15)	-y,z,-x	3^-	(39)	y,-z,x	$\bar{3}^-$
(16)	-x,z,-y	$\bar{4}^+$	(40)	x,-z,y	4^+
(17)	-y,x,-z	$\bar{4}^-$	(41)	y,-x,z	4^-
(18)	-z,y,-x	m	(42)	z,-y,x	2
(19)	-x,-y,z	2	(43)	x,y,-z	m
(20)	-z,-x,y	3^+	(44)	z,x,-y	$\bar{3}^+$
(21)	-y,-z,x	3^-	(45)	y,z,-x	$\bar{3}^-$
(22)	-x,-z,y	$\bar{4}^-$	(46)	x,z,-y	4^-
(23)	-y,-x,z	m	(47)	y,x,-z	2
(24)	-z,-y,x	$\bar{4}^+$	(48)	z,y,-x	4^+

Fig. 2.2(a) shows a [001] projection of a germanium crystal; the basis atoms occupy the positions with coordinates 000; $\frac{1}{4}\frac{1}{4}\frac{1}{4}$ and those related by the face-centring translations. Germanium has the spacegroup $Fd\bar{3}m$ No. 227 *(Hahn 1984)*. Its symmetry operations are shown in Fig.2.2(b) and (c), and given in Tables 2.2(a) and (b), respectively. Column one gives the number of the symmetry operations, column two gives their coordinate triplets and the last three columns give the point symmetry operations, W, their glide or screw parts, w_g, and their location parts, w_l (due to the location of the symmetry operation), respectively. The origin of the spacegroup $Fd\bar{3}m$ may be taken at the position with site symmetry $\bar{4}3m$, as shown in Table 2.2(a), or at a centre of inversion at a position with site symmetry $\bar{3}m$, as shown in Table 2.2(b). Fig.2.2(a), (b), Tables 2.2(a) and (b) show that the spacegroup $Fd\bar{3}m$ contains screw-rotation and mirror-glide symmetry operations, i.e., germanium crystals are non-symmorphic and, by comparing these operations with those in Table 2.1 of the germanium lattice, one can see that there is a one to one correspondence between them, i.e., the germanium crystal's symmetry is isomorphous to its lattice, and is hence referred to as being holosymmetric.

2.3. DICHROMATIC PATTERNS.

A dichromatic pattern is created by misorienting two crystal lattices, one designated arbitrarily white and one black (distinguished here using the Greek letters λ, and μ, respectively), by a given angle about some axis passing through a lattice site considered as an origin. For example, the misorientation of two F.C.C. lattices by the following axis-angle pairs, $[1\bar{1}\bar{1}]_\lambda 60^\circ$, $[110]_\lambda 38.94^\circ$ and $[110]_\lambda 31.59^\circ$, create the dichromatic

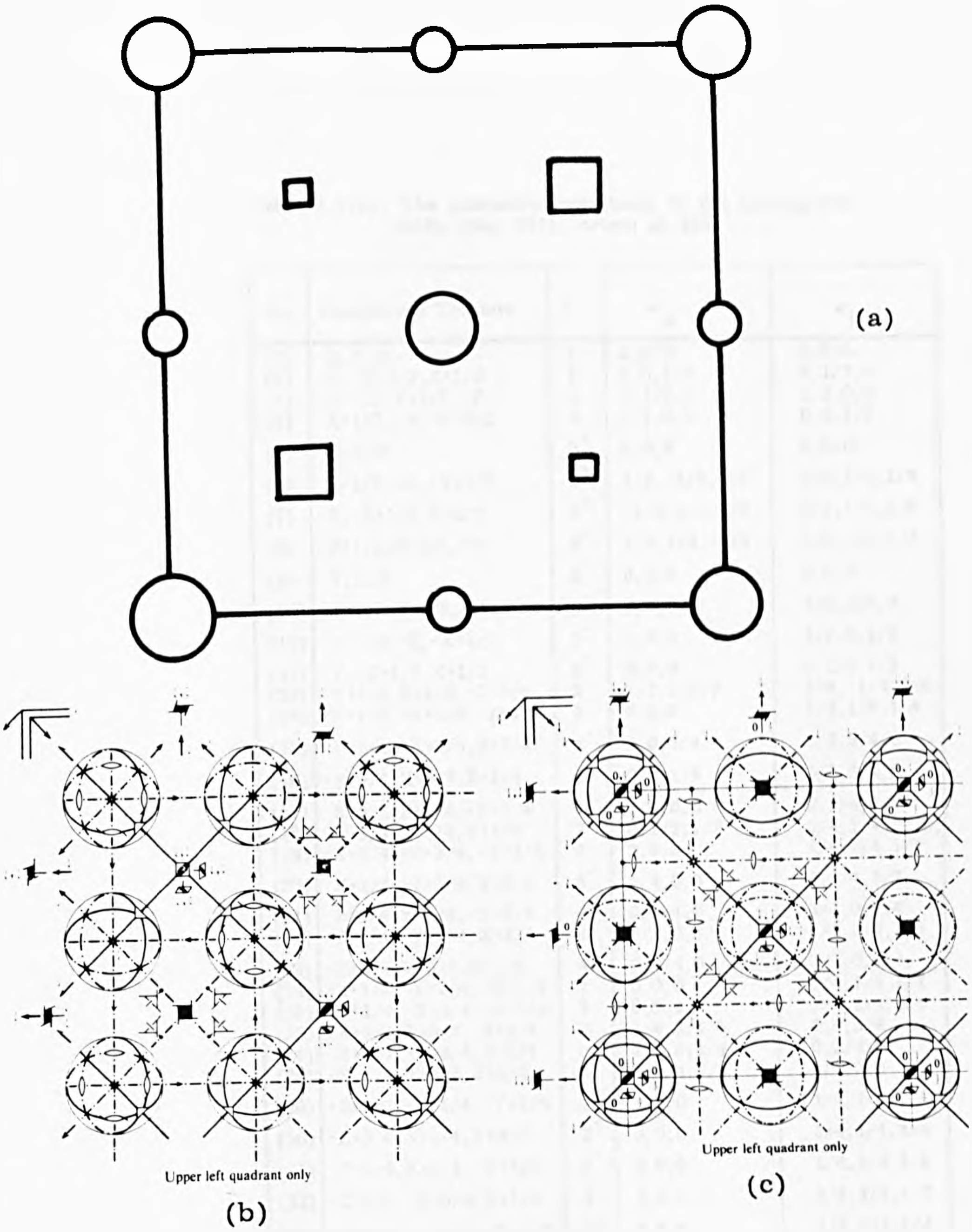

Fig. 2.2. (a) The projection along [001] of a diamond crystal. Large and small circles are at heights 0 and $\frac{1}{2}$, respectively. Small and large squares are at heights 1/4 and 3/4, respectively.

(b) The representation of some of the symmetry elements present at the upper left quadrant of (a), where the origin is chosen at centre ($\bar{3}m$), at 1/8 1/8 1/8 from the site which has symmetry $\bar{4}3m$ (reproduced from Hahn 1984).

(c) The same as (b), but the origin is chosen at $\bar{4}3m$, at -1/8 -1/8 -1/8 from centre ($\bar{3}m$).

Table 2.2(a). The symmetry operations in the spacegroup Fd$\bar{3}$m (No. 227); origin at $\bar{4}$3m.

No.	Coordinate Triplets	W	w_g	w_l
(1)	X,Y,Z	1	0,0,0	0,0,0
(2)	-X,-Y+1/2,Z+1/2	2	0,0,1/2	0,1/2,0
(3)	-X+1/2,Y+1/2,-Z	2	0,1/2,0	1/2,0,0
(4)	X+1/2,-Y,-Z+1/2	2	1/2,0,0	0,0,1/2
(5)	Z,X,Y	3^+	0,0,0	0,0,0
(6)	Z+1/2,-X,-Y+1/2	3^+	1/3,-1/3,1/3	1/6,1/3,1/6
(7)	-Z,-X+1/2,Y+1/2	3^+	-1/3,1/3,1/3	1/3,1/6,1/6
(8)	-Z+1/2,X+1/2,-Y	3^+	1/3,1/3,-1/3	1/6,1/6,1/3
(9)	Y,Z,X	3^-	0,0,0	0,0,0
(10)	-Y+1/2,Z+1/2,-X	3^-	0,0,0	1/2,1/2,0
(11)	Y+1/2,-Z,-X+1/2	3^-	0,0,0	1/2,0,1/2
(12)	-Y,-Z+1/2,X+1/2	3^-	0,0,0	0,1/2,1/2
(13)	Y+3/4,X+1/4,-Z+3/4	2	1/2,1/2,0	1/4,-1/4,3/4
(14)	-Y+1/4,-X+1/4,-Z+1/4	2	0,0,0	1/4,1/4,1/4
(15)	Y+1/4,-X+3/4,Z+3/4	4^-	0,0,3/4	1/4,3/4,0
(16)	-Y+3/4,X+3/4,Z+1/4	4^+	0,0,1/4	3/4,3/4,0
(17)	X+3/4,Z+1/4,-Y+3/4	4^-	3/4,0,0	0,1/4,3/4
(18)	-X+3/4,Z+3/4,Y+1/4	2	0,1/2,1/2	3/4,1/4,-1/4
(19)	-X+1/4,-Z+1/4,-Y+1/4	2	0,0,0	1/4,1/4,1/4
(20)	X+1/4,-Z+3/4,Y+3/4	4^+	1/4,0,0	0,3/4,3/4
(21)	Z+3/4,Y+1/4,-X+3/4	4^+	0,1/4,0	3/4,0,3/4
(22)	Z+1/4,-Y+3/4,X+3/4	2	1/2,0,1/2	-1/4,3/4,1/4
(23)	-Z+3/4,Y+3/4,X+1/4	4^-	0,3/4,0	3/4,0,1/4
(24)	-Z+1/4,-Y+1/4,-X+1/4	2	0,0,0	1/4,1/4,1/4
(25)	-X+1/4,-Y+1/4,-Z+1/4	$\bar{1}$	0,0,0	1/4,1/4,1/4
(26)	X+1/4,Y+3/4,-Z+3/4	d	1/4,3/4,0	0,0,3/4
(27)	X+3/4,-Y+3/4,Z+1/4	d	3/4,0,1/4	0,3/4,0
(28)	-X+3/4,Y+1/4,Z+3/4	d	0,1/4,3/4	3/4,0,0
(29)	-Z+1/4,-X+1/4,-Y+1/4	$\bar{3}^+$	0,0,0	1/4,1/4,1/4
(30)	-Z+3/4,X+1/4,Y+3/4	$\bar{3}^+$	0,0,0	3/4,1/4,3/4
(31)	Z+1/4,X+3/4,-Y+3/4	$\bar{3}^+$	0,0,0	1/4,3/4,3/4
(32)	Z+3/4,-X+3/4,Y+1/4	$\bar{3}^+$	0,0,0	3/4,3/4,1/4
(33)	-Y+1/4,-Z+1/4,-X+1/4	$\bar{3}^-$	0,0,0	1/4,1/4,1/4
(34)	Y+3/4,-Z+3/4,X+1/4	$\bar{3}^-$	0,0,0	3/4,3/4,1/4
(35)	-Y+3/4,Z+1/4,X+3/4	$\bar{3}^-$	0,0,0	3/4,1/4,3/4
(36)	Y+1/4,Z+3/4,-X+3/4	$\bar{3}^-$	0,0,0	1/4,3/4,3/4
(37)	-Y+1/2,-X,Z+1/2	g	1/4,-1/4,1/2	1/4,1/4,0
(38)	Y,X,Z	m	0,0,0	0,0,0
(39)	-Y,X+1/2,-Z+1/2	$\bar{4}^-$	0,0,0	0,1/2,1/2
(40)	Y+1/2,-X+1/2,-Z	$\bar{4}^+$	0,0,0	1/2,1/2,0
(41)	-X+1/2,-Z,Y+1/2	4^-	0,0,0	1/2,0,1/2
(42)	X+1/2,-Z+1/2,-Y	g	1/2,1/4,-1/4	0,1/4,1/4
(43)	X,Z,Y	m	0,0,0	0,0,0
(44)	-X,Z+1/2,-Y+1/2	$\bar{4}^+$	0,0,0	0,1/2,1/2
(45)	-Z+1/2,-Y,X+1/2	$\bar{4}^+$	0,0,0	1/2,0,1/2
(46)	-Z,Y+1/2,-X+1/2	g	-1/4,1/2,1/4	1/4,0,1/4
(47)	Z+1/2,-Y+1/2,-X	$\bar{4}^-$	0,0,0	1/2,1/2,0
(48)	Z,Y,X	m	0,0,0	0,0,0

Table 2.2(b). The symmetry operations in the spacegroup $Fd\bar{3}m$ (No. 227); origin at $\bar{3}m$.

No.	Coordinate Triplets	W	w_g	w_l
(1)	X,Y,Z	1	0,0,0	0,0,0
(2)	-X+3/4,-Y+1/4,Z+1/2	2	0,0,1/2	3/4,1/4,0
(3)	-X+1/4,Y+1/2,-Z+3/4	2	0,1/2,0	1/4,0,3/4
(4)	X+1/2,-Y+3/4,-Z+1/4	2	1/2,0,0	0,3/4,1/4
(5)	Z,X,Y	3^+	0,0,0	0,0,0
(6)	Z+1/2,-X+3/4,-Y+1/4	3^+	0,0,0	1/2,3/4,1/4
(7)	-Z+3/4,-X+1/4,Y+1/2	3^+	0,0,0	3/4,1/4,1/2
(8)	-Z+1/4,X+1/2,-Y+3/4	3^+	0,0,0	1/4,1/2,3/4
(9)	Y,Z,X	3^-	0,0,0	0,0,0
(10)	-Y+1/4,Z+1/2,-X+3/4	3^-	-1/3,1/3,1/3	7/12,2/12,5/12
(11)	Y+1/2,-Z+3/4,-X+1/4	3^-	1/3,1/3,-1/3	2/12,5/12,7/12
(12)	-Y+3/4,-Z+1/4,X+1/2	3^-	1/3,-1/3,1/3	5/12,7/12,2/12
(13)	Y+3/4,X+1/4,-Z+1/2	2	1/2,1/2,0	1/4,-1/4,1/2
(14)	-Y,-X,-Z	2	0,0,0	0,0,0
(15)	Y+1/4,-X+1/2,Z+3/4	4^-	0,0,3/4	1/4,1/2,0
(16)	-Y+1/2,X+3/4,Z+1/4	4^+	0,0,1/4	1/2,3/4,0
(17)	X+3/4,Z+1/4,-Y+1/2	4^-	3/4,0,0	0,1/4,1/2
(18)	-X+1/2,Z+3/4,Y+1/4	2	0,1/2,1/2	1/2,1/4,-1/4
(19)	-X,-Z,-Y	2	0,0,0	0,0,0
(20)	X+1/4,-Z+1/2,Y+3/4	4^+	1/4,0,0	0,1/2,3/4
(21)	Z+3/4,Y+1/4,-X+1/2	4^+	0,1/4,0	3/4,0,1/2
(22)	Z+1/4,-Y+1/2,X+3/4	2	1/2,0,1/2	-1/4,1/2,1/4
(23)	-Z+1/2,Y+3/4,X+1/4	4^-	0,3/4,0	1/2,0,1/4
(24)	-Z,-Y,-X	2	0,0,0	0,0,0
(25)	-X,-Y,-Z	$\bar{1}$	0,0,0	0,0,0
(26)	X+1/4,Y+3/4,-Z+1/2	d	1/4,3/4,0	0,0,1/2
(27)	X+3/4,-Y+1/2,Z+1/4	d	3/4,0,1/4	0,1/2,0
(28)	-X+1/2,Y+1/4,Z+3/4	d	0,1/4,3/4	1/2,0,0
(29)	-Z,-X,-Y	$\bar{3}^+$	0,0,0	0,0,0
(30)	-Z+1/2,X+1/4,Y+3/4	$\bar{3}^+$	0,0,0	1/2,1/4,3/4
(31)	Z+1/4,X+3/4,-Y+1/2	$\bar{3}^+$	0,0,0	1/4,3/4,1/2
(32)	Z+3/4,-X+1/2,Y+1/4	$\bar{3}^+$	0,0,0	3/4,1/2,1/4
(33)	-Y,-Z,-X	$\bar{3}^-$	0,0,0	0,0,0
(34)	Y+3/4,-Z+1/2,X+1/4	$\bar{3}^-$	0,0,0	3/4,1/2,1/4
(35)	-Y+1/2,Z+1/4,X+3/4	$\bar{3}^-$	0,0,0	1/2,1/4,3/4
(36)	Y+1/4,Z+3/4,-X+1/2	$\bar{3}^-$	0,0,0	1/4,3/4,1/2
(37)	-Y+1/4,-X+3/4,Z+1/2	g	-1/4,1/4,1/2	1/2,1/2,0
(38)	Y,X,Z	m	0,0,0	0,0,0
(39)	-Y+3/4,X+1/2,-Z+1/4	$\bar{4}^-$	0,0,0	3/4,1/2,1/4
(40)	Y+1/2,-X+1/4,-Z+3/4	$\bar{4}^+$	0,0,0	1/2,1/4,3/4
(41)	-X+1/4,-Z+3/4,Y+1/2	4^-	0,0,0	1/4,3/4,1/2
(42)	X+1/2,-Z+1/4,-Y+3/4	g	1/2,-1/4,1/4	0,1/2,1/2
(43)	X,Z,Y	m	0,0,0	0,0,0
(44)	-X+3/4,Z+1/2,-Y+1/4	$\bar{4}^+$	0,0,0	3/4,1/2,1/4
(45)	-Z+1/4,-Y+3/4,X+1/2	$\bar{4}^+$	0,0,0	1/4,3/4,1/2
(46)	-Z+3/4,Y+1/2,-X+1/4	g	1/4,1/2,-1/4	1/2,0,1/2
(47)	Z+1/2,-Y+1/4,-X+3/4	$\bar{4}^-$	0,0,0	1/2,1/4,3/4
(48)	Z,Y,X	m	0,0,0	0,0,0

patterns characterised by $\Sigma = 3$, $\Sigma = 9$ and $\Sigma = 27$, and these are shown in Fig.2.3(a), (b), and (c), respectively. In Fig.2.3(a) it can be seen that one in three lattice sites is coincident (half shaded), while in Fig.2.3(b) one in nine lattice sites is coincident, and in Fig.2.3(c) one in twenty seven lattice sites is coincident. This corresponds to our earlier assignment of $\Sigma = 3, 9, 27$ for these dichromatic patterns and it can be seen that Σ represents the reciprocal density of coincident lattice sites in a dichromatic pattern.

The symmetry operations of the white lattice's spacegroup are designated,

$$\mathcal{W}(\lambda) = (W(\lambda), w(\lambda)) \tag{2.1a}$$

where $W(\lambda)$ represents the rotation, reflection or inversion part, and $w(\lambda)$ the translation part. For example, the translation operation $\mathcal{W}(\lambda) = (I, t(\lambda))$, where, I, represents the identity operation and, $t(\lambda)$, is a lattice translation vector. For ordinary or proper rotation and reflection operations, $W(\lambda)$ represents ordinary n-fold rotation operations, mirror operations, inversion operation, roto-inversion operations, and $w(\lambda)$ equals zero or any lattice translation. Similarly, the symmetry operations of the black lattice's spacegroup are designated

$$\mathcal{W}(\mu) = (W(\mu), w(\mu)) \tag{2.1b}$$

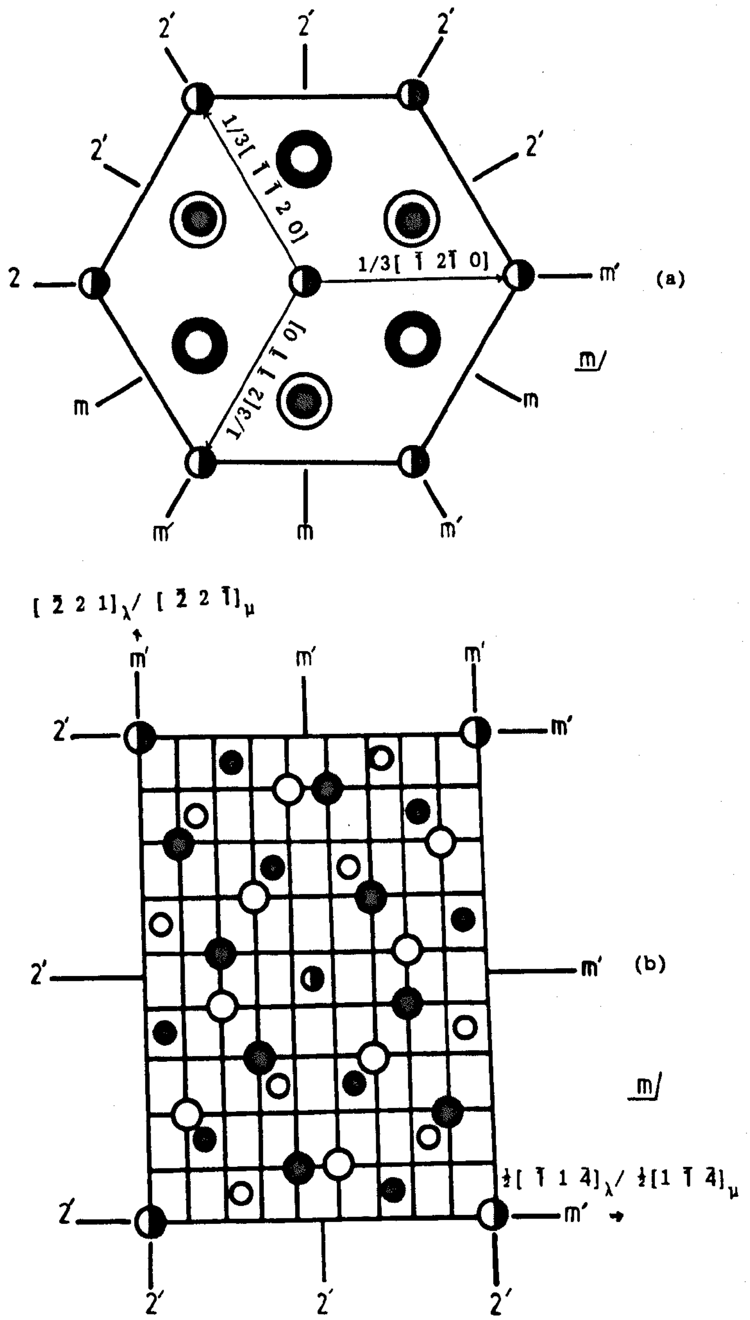

Fig. 2.3(a). The projection along $[1\bar{1}\bar{1}]$ of the $\Sigma=3$ dichromatic pattern formed by 2 F.C.C. lattices rotated about $[1\bar{1}\bar{1}]$ by an angle $\theta=60°$. The size of the symbols represents the...ABCABC... stacking along $[1\bar{1}\bar{1}]$.

(b). The projection along [110] of the $\Sigma=9$ dichromatic pattern formed by 2 F.C.C. lattices rotated about [110] by an angle $\theta=38.94°$. The size of the symbols represents the...ABAB... stacking along [110].

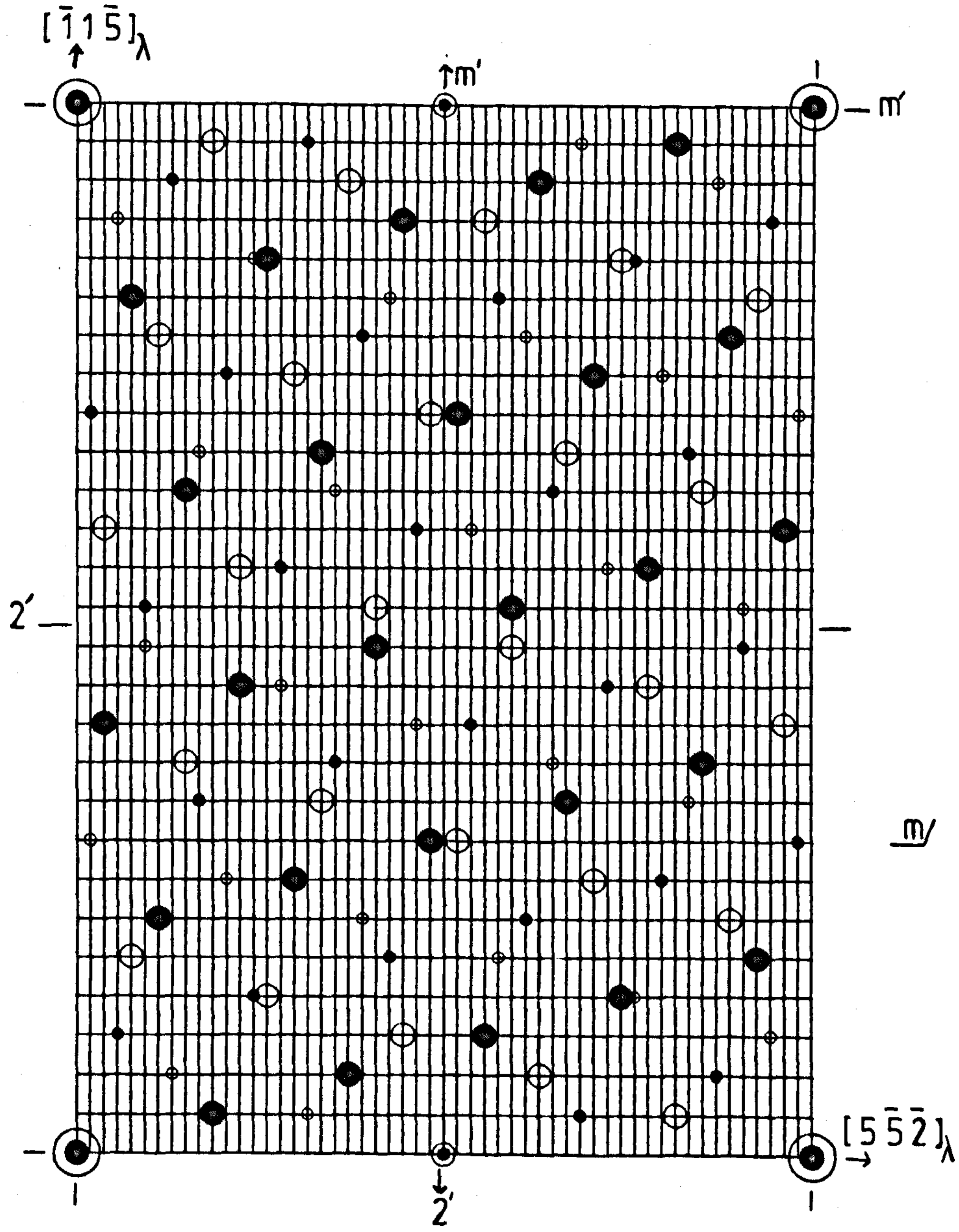

Fig. 2.3(c). The projection along [110] of the Σ=27 dichromatic pattern formed by 2 F.C.C. lattices rotated about [110] by an angle Θ=31.59°. The size of the symbols represents the...ABAB... stacking along [110].

where $W(\mu)$ and $w(\mu)$ have definition similar to those for the white lattice.

The transformation relating a white and black lattice is represented by

$$\mathcal{P} = (P, p) \tag{2.1c}$$

where, P is the matrix representing the transformation of vectors in the white to their counterparts in the black frame and, p, represents a rigid body shift of the black lattice with respect to the white (expressed in the white coordinate frame). The matrix representation of the transformation, P, (and its inverse P^{-1}) for the case of the $\Sigma = 3$, 9, and 27 dichromatic patterns are given in Table2.3. When $p = 0$, the i^{th} black symmetry operation expressed in the white coordinate frame then has the form $PW(\mu)_i P^{-1}$.

By inspection of the dichromatic patterns shown in Fig.2.3(a), (b), and (c), one can recognise that each pattern exhibits two types of symmetry operation called coincident and antisymmetry operations and these are described in the next two sections.

2.3.1. COINCIDENT SYMMETRY ELEMENTS.

This type of symmetry, designated $\mathcal{W}(c)$, arises when black and white lattice symmetry operations coincide.

Table 2.3. The pure linear transformation P and its inverse P^{-1} for Σ=3, 9, and 27.

No.	Σ	P Matrix	P^{-1} Matrix
(1)	3	$1/3 \begin{bmatrix} 2 & 1 & -2 \\ -2 & 2 & -1 \\ 1 & 2 & 2 \end{bmatrix}$	$1/3 \begin{bmatrix} 2 & -2 & 1 \\ 1 & 2 & 2 \\ -2 & -1 & 2 \end{bmatrix}$
(2)	9	$1/9 \begin{bmatrix} 8 & 1 & 4 \\ 1 & 8 & -4 \\ -4 & 4 & 7 \end{bmatrix}$	$1/9 \begin{bmatrix} 8 & 1 & -4 \\ 1 & 8 & 4 \\ 4 & -4 & 7 \end{bmatrix}$
(3)	27	$1/27 \begin{bmatrix} 25 & 2 & 10 \\ 2 & 25 & -10 \\ -10 & 10 & 23 \end{bmatrix}$	$1/27 \begin{bmatrix} 25 & 2 & -10 \\ 2 & 25 & 10 \\ 10 & -10 & 23 \end{bmatrix}$

Thus, for the given transformations, P, (Table 2.3) coincident symmetry operations must satisfy the following equivalence expression:

$$W(c) = W(\lambda) = P\, W(\mu)\, P^{-1} \qquad (2.2)$$

This expression shows that coincident translations arise when translation vectors with equal magnitudes are parallel in the black and white lattices, and coincident point symmetry operations arise when identical symmetry operations in the two lattices are both orientationally and translationally aligned. For example, in Fig.2.3(a), there are twelve coincident point symmetry elements, i.e, three diads along $[110]_\lambda$, $[101]_\lambda$, $[01\bar{1}]_\lambda$, three mirrors perpendicular to $[110]_\lambda$, $[101]_\lambda$, $[01\bar{1}]_\lambda$, two triads along $[1\bar{1}\bar{1}]_\lambda$, two roto-inversion triads along $[1\bar{1}\bar{1}]_\lambda$, centre of inversion at [000], and the identity. These twelve symmetry elements are tabulated in Table 2.4(a). In Fig.2.3(b), there are four coincident symmetry elements, i.e., the identity, a mirror perpendicular to $[110]_\lambda$, a centre of inversion at [000], and a diad along $[110]_\lambda$. These four coincident elements of symmetry are tabulated in Table 2.4(b). Similarly, Fig.2.3(c) shows four coincident symmetry elements similar to those in Fig.2.3(b), and tabulated in Table 2.4(c).

2.3.2. ANTISYMMETRY ELEMENTS.

This type of operation, designated W', relates black features to white and vice versa. The vector transformation from white to black and from black to white are given by $PW(\lambda)$ and $W(\mu)P^{-1}$, respectively, using the white coordinate frame, so antisymmetry operations arise in a dichromatic pattern when solutions to the following expression exist:

Table 2.4(a). The coincident symmetry elements of the dichromatic pattern of $\Sigma=3(1\ -1\ -1)$.

No.	W(c)[hkl]	W(c) Matrix
(1)	1	$\begin{bmatrix} 1 & 0 & 0 \\ 0 & 1 & 0 \\ 0 & 0 & 1 \end{bmatrix}$
(2)	3^{-}[1 -1 -1]	$\begin{bmatrix} 0 & -1 & 0 \\ 0 & 0 & 1 \\ -1 & 0 & 0 \end{bmatrix}$
(3)	3^{+}[1 -1 -1]	$\begin{bmatrix} 0 & 0 & -1 \\ -1 & 0 & 0 \\ 0 & 1 & 0 \end{bmatrix}$
(4)	$\bar{1}$[0 0 0]	$\begin{bmatrix} -1 & 0 & 0 \\ 0 & -1 & 0 \\ 0 & 0 & -1 \end{bmatrix}$
(5)	$\bar{3}^{-}$[1 -1 -1]	$\begin{bmatrix} 0 & 1 & 0 \\ 0 & 0 & -1 \\ 1 & 0 & 0 \end{bmatrix}$
(6)	$\bar{3}^{+}$[1 -1 -1]	$\begin{bmatrix} 0 & 0 & 1 \\ 1 & 0 & 0 \\ 0 & -1 & 0 \end{bmatrix}$
(7)	m[1 0 1]	$\begin{bmatrix} 0 & 0 & -1 \\ 0 & 1 & 0 \\ -1 & 0 & 0 \end{bmatrix}$
(8)	m[0 1 -1]	$\begin{bmatrix} 1 & 0 & 0 \\ 0 & 0 & 1 \\ 0 & 1 & 0 \end{bmatrix}$
(9)	m[1 1 0]	$\begin{bmatrix} 0 & -1 & 0 \\ -1 & 0 & 0 \\ 0 & 0 & 1 \end{bmatrix}$
(10)	2[1 0 1]	$\begin{bmatrix} 0 & 0 & 1 \\ 0 & -1 & 0 \\ 1 & 0 & 0 \end{bmatrix}$
(11)	2[0 1 -1]	$\begin{bmatrix} -1 & 0 & 0 \\ 0 & 0 & -1 \\ 0 & -1 & 0 \end{bmatrix}$
(12)	2[1 1 0]	$\begin{bmatrix} 0 & 1 & 0 \\ 1 & 0 & 0 \\ 0 & 0 & -1 \end{bmatrix}$

Table 2.4(b). The coincident symmetry elements in the dichromatic pattern based on C.S.L. of $\Sigma = 9(-2\ 2\ \ 1)$.

No.	W(c)[hkl]	W(c) Matrix
(1)	1	$\begin{bmatrix} 1 & 0 & 0 \\ 0 & 1 & 0 \\ 0 & 0 & 1 \end{bmatrix}$
(2)	m[1 1 0]	$\begin{bmatrix} 0 & -1 & 0 \\ -1 & 0 & 0 \\ 0 & 0 & 1 \end{bmatrix}$
(3)	$\bar{1}$[0 0 0]	$\begin{bmatrix} -1 & 0 & 0 \\ 0 & -1 & 0 \\ 0 & 0 & -1 \end{bmatrix}$
(4)	2[1 1 0]	$\begin{bmatrix} 0 & 1 & 0 \\ 1 & 0 & 0 \\ 0 & 0 & -1 \end{bmatrix}$

Table 2.4(c). The coincident symmetry elements of the dichromatic pattern based on C.S.L. of $\Sigma = 27(5\ -5\ -2)$.

No.	W(c)[hkl]	W(c) Matrix
(1)	1	$\begin{bmatrix} 1 & 0 & 0 \\ 0 & 1 & 0 \\ 0 & 0 & 1 \end{bmatrix}$
(2)	m[1 1 0]	$\begin{bmatrix} 0 & -1 & 0 \\ -1 & 0 & 0 \\ 0 & 0 & 1 \end{bmatrix}$
(3)	$\bar{1}$[0 0 0]	$\begin{bmatrix} -1 & 0 & 0 \\ 0 & -1 & 0 \\ 0 & 0 & -1 \end{bmatrix}$
(4)	2[1 1 0]	$\begin{bmatrix} 0 & 1 & 0 \\ 1 & 0 & 0 \\ 0 & 0 & -1 \end{bmatrix}$

$$W' = PW(\lambda) = W(\mu)P^{-1} \tag{2.3}$$

For the dichromatic pattern shown in Fig.2.3(a), it can be seen that there are twelve point antisymmetry elements, i.e. four antidiads (parallel to $[1\bar{1}\bar{1}]_\lambda$, $[211]_\lambda$, $[1\bar{1}2]_\lambda$ and $[12\bar{1}]_\lambda$), four antimirrors (perpendicular to $[1\bar{1}\bar{1}]_\lambda$, $[211]_\lambda$, $[1\bar{1}2]_\lambda$ and $[12\bar{1}]_\lambda$), two antihexads and two anti-roto-inversion hexads (along $[1\bar{1}\bar{1}]_\lambda$), Table 2.5(a).

Also, in Fig.2.3(b), there are four antisymmetry elements, i.e., two antidiads parallel to $[\bar{1}1\bar{4}]_\lambda$, and $[\bar{2}21]_\lambda$, and two antimirrors perpendicular to $[\bar{1}1\bar{4}]_\lambda$, and $[\bar{2}21]_\lambda$, Table 2.5(b).

Similarly, in Fig.2.3(c) there are four antisymmetry elements, i.e., two antidiads parallel to $[\bar{1}1\bar{5}]_\lambda$, and $[5\bar{5}\bar{2}]_\lambda$, and two antimirrors perpendicular to $[\bar{1}1\bar{5}]_\lambda$, and $[5\bar{5}\bar{2}]_\lambda$, Table 2.5(c).

The total symmetry (i.e., coincident and antisymmetry elements) of the dichromatic patterns of $\Sigma = 3$, 9, and 27 are expressed by their spacegroups, and correspond to P6'/m'mm', Imm'm', and Amm'm', respectively.

2.4. MATHEMATICAL ANALYSIS; GENERAL PRINCIPLES.

A mathematical formulation of the criteria for conservation of coincident and antisymmetry operations, exhibited by dichromatic patterns, with variation of the relative displacement of the black and white lattices can be obtained and is described in this section.

TABLE 2.5(a). The antisymmetry elements of the dichromatic pattern based on C.S.L. of $\Sigma = 3(1\ -1\ -1)$.

No.	W'[hkl]	W' Matrix
(1)	$6'^{+}[1\ -1\ -1]$	$1/3\begin{bmatrix} 2 & 1 & -2 \\ -2 & 2 & -1 \\ 1 & 2 & 2 \end{bmatrix}$
(2)	$6'^{-}[1\ -1\ -1]$	$1/3\begin{bmatrix} -2 & -2 & 1 \\ 1 & 2 & 2 \\ -2 & -1 & 2 \end{bmatrix}$
(3)	$\bar{6}^{+}{}'[1\ -1\ -1]$	$1/3\begin{bmatrix} -2 & -1 & 2 \\ 2 & -2 & 1 \\ -1 & -2 & -2 \end{bmatrix}$
(4)	$\bar{6}^{-}{}'[1\ -1\ -1]$	$1/3\begin{bmatrix} -2 & 2 & -1 \\ -1 & -2 & -2 \\ 2 & 1 & -2 \end{bmatrix}$
(5)	$m'[2\ 1\ 1]$	$1/3\begin{bmatrix} -1 & -2 & -2 \\ -2 & 2 & -1 \\ -2 & -1 & 2 \end{bmatrix}$
(6)	$m'[1\ -1\ 2]$	$1/3\begin{bmatrix} 2 & 1 & -2 \\ 1 & 2 & 2 \\ -2 & 2 & -1 \end{bmatrix}$
(7)	$m'[1\ 2\ -1]$	$1/3\begin{bmatrix} 2 & -2 & 1 \\ -2 & -1 & 2 \\ 1 & 2 & 2 \end{bmatrix}$
(8)	$m'[1\ -1\ -1]$	$1/3\begin{bmatrix} 1 & 2 & 2 \\ 2 & 1 & -2 \\ 2 & -2 & 1 \end{bmatrix}$
(9)	$2'[2\ 1\ 1]$	$1/3\begin{bmatrix} 1 & 2 & 2 \\ 2 & -2 & 1 \\ 2 & 1 & -2 \end{bmatrix}$
(10)	$2'[1\ -1\ 2]$	$1/3\begin{bmatrix} -2 & -1 & 2 \\ -1 & -2 & -2 \\ 2 & -2 & 1 \end{bmatrix}$
(11)	$2'[1\ 2\ -1]$	$1/3\begin{bmatrix} -2 & 2 & -1 \\ 2 & 1 & -2 \\ -1 & -2 & -2 \end{bmatrix}$
(12)	$2'[1\ -1\ -1]$	$1/3\begin{bmatrix} -1 & -2 & -2 \\ -2 & -1 & 2 \\ -2 & 2 & -1 \end{bmatrix}$

Table 2.5(b). The antisymmetry elements in the dichromatic pattern based on C.S.L. of $\Sigma=9(-2\ 2\ 1)$.

No.	W'	Matrix
(1)	2'[-1 1 -4]	$\frac{1}{9}\begin{bmatrix} -8 & -1 & 4 \\ -1 & -8 & -4 \\ 4 & -4 & 7 \end{bmatrix}$
(2)	2'[2 -2 -1]	$\frac{1}{9}\begin{bmatrix} -1 & -8 & -4 \\ -8 & -1 & 4 \\ -4 & 4 & -7 \end{bmatrix}$
(3)	m'[-1 1 -4]	$\frac{1}{9}\begin{bmatrix} 8 & 1 & -4 \\ 1 & 8 & 4 \\ -4 & 4 & -7 \end{bmatrix}$
(4)	m'[2 -2 -1]	$\frac{1}{9}\begin{bmatrix} 1 & 8 & 4 \\ 8 & 1 & -4 \\ 4 & -4 & 7 \end{bmatrix}$

Table 2.5(c). The antisymmetry elements in the dichromatic pattern based on C.S.L. of $\Sigma=27(5\ -5\ -2)$.

No.	W'	Matrix
(1)	2'[1 -1 5]	$\frac{1}{27}\begin{bmatrix} -25 & -2 & 10 \\ -2 & -25 & -10 \\ 10 & -10 & 23 \end{bmatrix}$
(2)	2'[5 -5 -2]	$\frac{1}{27}\begin{bmatrix} -2 & -25 & -10 \\ -25 & -2 & 10 \\ -10 & 10 & -23 \end{bmatrix}$
(3)	m'[1 -1 5]	$\frac{1}{27}\begin{bmatrix} 25 & 2 & -10 \\ 2 & 25 & 10 \\ -10 & 10 & -23 \end{bmatrix}$
(4)	m'[5 -5 -2]	$\frac{1}{27}\begin{bmatrix} 2 & 25 & 10 \\ 25 & 2 & -10 \\ 10 & -10 & 23 \end{bmatrix}$

In section 2.3 the three dichromatic patterns, Fig.2.3(a), (b), and (c), were created by a pure linear transformations, i.e. $\mathcal{P}$ = (P, p) with p = 0, where the F.C.C. lattices used have symmorphic spacegroups (i.e. $w(\lambda)_g = w(\mu)_g = 0$). Now, by substitution into equations (2.2) and (2.3), which describe the coincident and antisymmetry operations respectively, taking the values of p = 0, and $w(\lambda)_g = w(\mu)_g = 0$, we obtain

$$W_i(\lambda) = PW_j(\mu)P^{-1} = W(c) \qquad (2.4)$$

and

$$PW(\lambda) = W(\mu)P^{-1} = W' \qquad (2.5)$$

Now consider the relative displacement of the black lattice with respect to the white one by shifts $p \neq 0$. Now by substitution into equation (2.2) we obtain

$$(W(c), w(c)) = (PW(\mu)P^{-1}, -PW(\mu)P^{-1}p + p) \qquad (2.6)$$

Using equation (2.4) and equating the similar parts on both sides, the following expressions must be satisfied for coincident symmetry to be present,

$$W(c) = PW(\mu)P^{-1} \qquad (2.7a)$$

and

$$W(c)p = p \tag{2.7b}$$

Similarly, by substitution into equation (2.3), we obtain for the anti-operations

$$(PW(\lambda), p) = (W(\mu)P^{-1}, -W(\mu)P^{-1}p) \tag{2.8}$$

Using equation (2.5) and equating the similar parts on both sides, therefore,

$$PW(\lambda) = W(\mu)P^{-1} \tag{2.9a}$$

and

$$W'p = -p \tag{2.9b}$$

Equations (2.7b) and (2.9b) are the required criteria for conservation of coincident and antisymmetry operations, respectively. The former states that a coincident symmetry operation which leaves a shift vector p invariant will be conserved by this shift. The latter states that an antisymmetry operation which inverts a shift vector p will be conserved by this shift.

Some examples are given here to show the application of these two criteria for establishing the breaking and/or conservation of the symmetry elements in a dichromatic pattern.

(1) Consider first the $\Sigma = 9$ dichromatic pattern, Fig.2.3(b). It can

be seen by inspection that a shift $p = \frac{1}{18} [\bar{1}1\bar{4}]_\lambda$, as depicted in Fig.2.3(d), destroys two coincident symmetry elements, i.e. the centre and the diad along $[110]_\lambda$, and conserves two, i.e. the identity and the mirror perpendicular to $[110]_\lambda$. It is readily confirmed that the same result is obtained mathematically by using equation (2.7b). Also, this shift destroys two antisymmetry operations, i.e. the anti-mirror perpendicular to $[\bar{2}21]_\lambda$, and the anti-diad along $[\bar{1}1\bar{4}]_\lambda$, and conserves two, i.e. the anti-mirror perpendicular to $[\bar{1}1\bar{4}]_\lambda$, and the anti-diad along $[\bar{2}21]_\lambda$. Again this result is consistent with equation (2.9b).

(2) Fig.2.3(e) shows another example, similar to the one given above, but with a different shift, $p = \frac{1}{9} [\bar{2}21]_\lambda$, and one can observe the breaking of the antimirror perpendicular to $[\bar{1}1\bar{4}]_\lambda$, the antidiad along $[\bar{2}21]_\lambda$. and the conservation of the antimirror perpendicular to $[\bar{2}21]_\lambda$ and the antidiad along $[\bar{1}1\bar{4}]_\lambda$,

2.4.1. EQUIVALENT DISPLACEMENT AND WIGNER-SEITZ CELLS.

Whenever a dichromatic pattern with $p = 0$ has both translation symmetry and point symmetry higher than 1, there is a set of equivalent dichromatic patterns, obtained from the initial pattern by a set of equivalent displacements of the black lattice, which are related by the symmetry elements of the initial pattern. This set of displacements which reproduce the initial dichromatic pattern includes the three shortest independent vectors in the dichromatic pattern which join black sites to white ones and form a lattice called the d.s.c. lattice *(Pond et al. 1979)*. Fig.2.4(a), (b), and (c) show three d.s.c. lattices

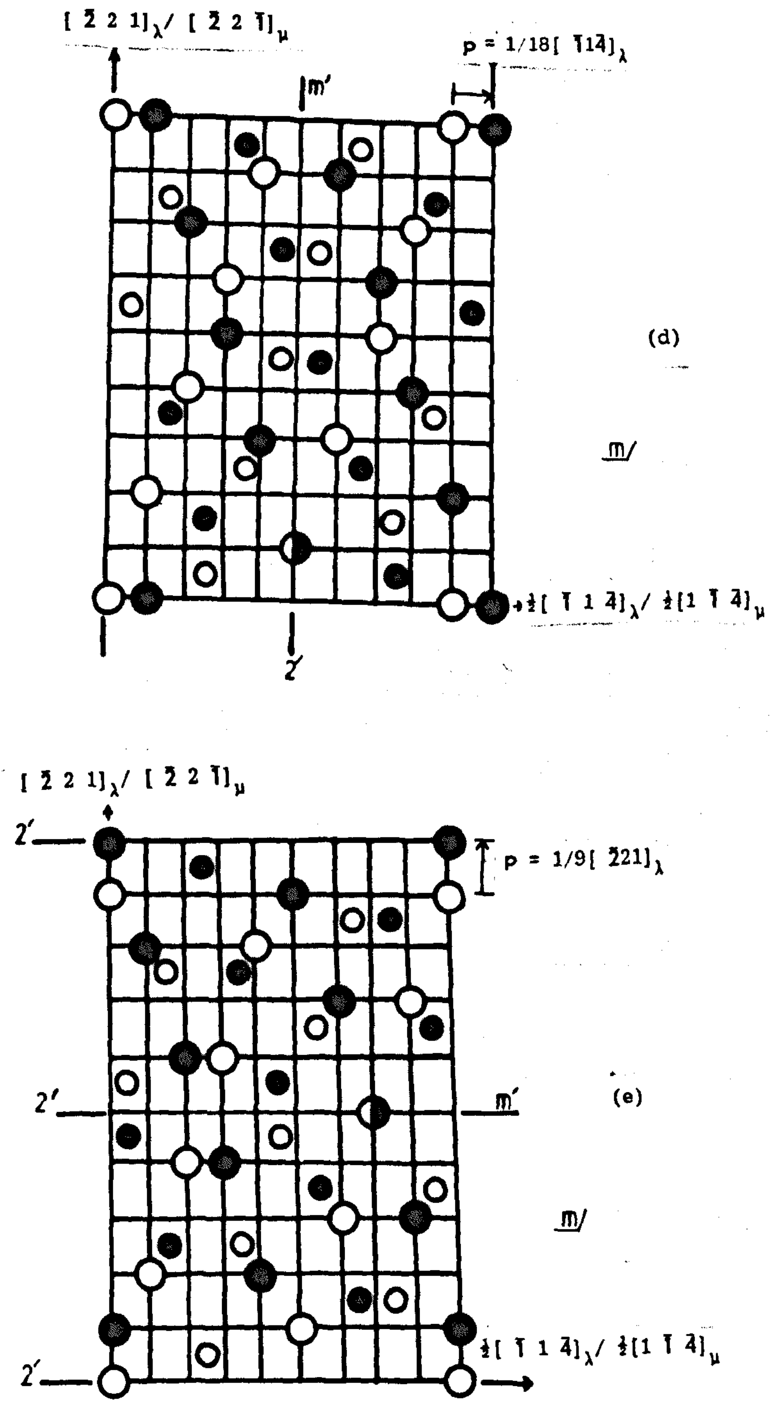

Fig. 2.3. (d) The projection along $[110]_\lambda$ of the $\Sigma=9$ dichromatic pattern, in Fig.2.3(b), but the black lattice is shifted by $p = 1/18[\bar{1}1\bar{4}]_\lambda$.

(e) The same as (d) but $p = 1/9[\bar{2}21]_\lambda$.

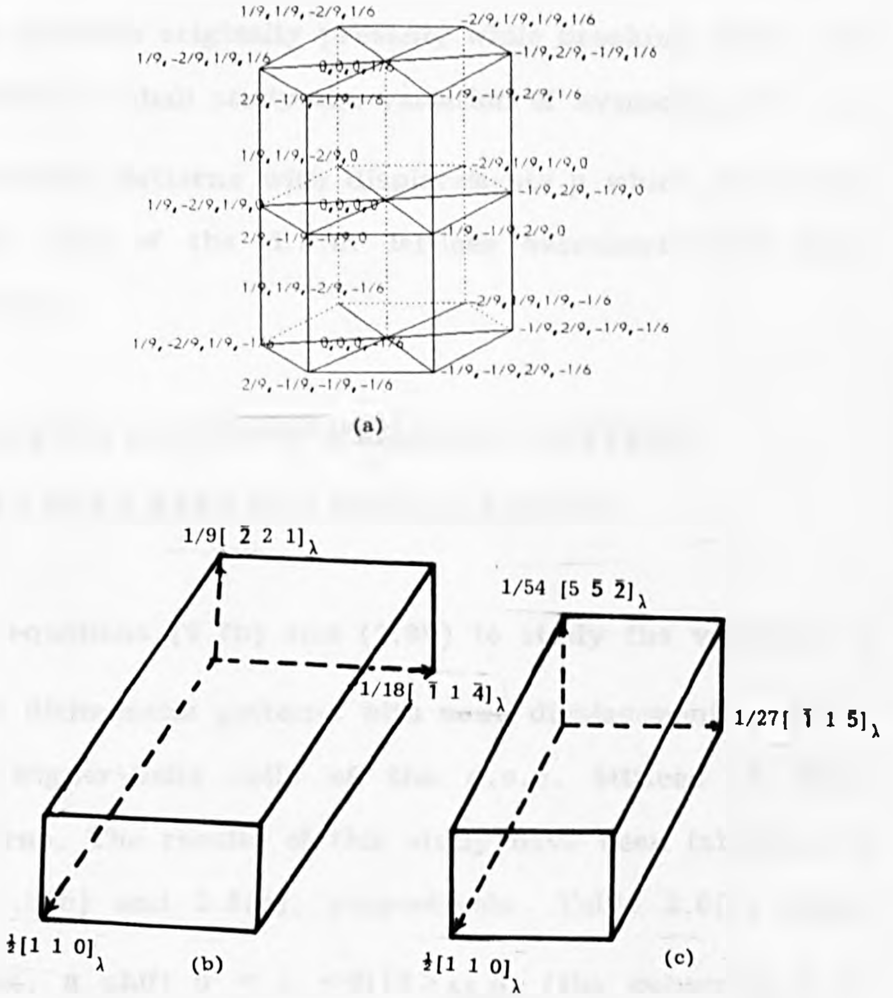

Fig. 2.4. (a) The Wigner-Seitz cell of the d.s.c. lattice associated with Σ=3 dichromatic pattern.

(b) The same as (a) but for Σ=9 dichromatic pattern.

(c) The same as (a) but for Σ=27 dichromatic pattern.

associated with $\Sigma = 3$, 9, and 27 dichromatic patterns.

Whereas displacements by d.s.c. vectors conserve all symmetry in a dichromatic pattern, displacement by other vectors can conserve some of the symmetry elements originally present, while breaking other, and in the next section we shall study the variation of symmetry of $\Sigma = 3$, 9, and 27 dichromatic patterns with displacements p which fall within the Wigner-Seitz cells of the d.s.c. lattices associated with these dichromatic patterns.

2.4.2. THE VARIATION OF THE DICHROMATIC PATTERN SYMMETRY WITH RELATIVE DISPLACEMENT.

We have used equations (2.7b) and (2.9b) to study the variation of $\Sigma = 3$, 9, and 27 dichromatic patterns with some displacements p which fall within the Wigner-Seitz cells of the d.s.c. lattices of these dichromatic patterns. The results of this study have been tabulated in Tables 2.6(a), 2.6(b) and 2.6(c), respectively. Table 2.6(a) shows that, for example, a shift $p = \frac{1}{18} <01\bar{1}0>_{\mathrm{M.B.}}$ (the subscript M.B. stands for Miller-Bravais hexagonal indexing system) breaks six of the 12 coincident point symmetry elements (Table 2.4(a)), e.g. two triads, two roto-inversion triads along $[0001]_{\mathrm{M.B.}}$, a centre of inversion at $[0000]_{\mathrm{M.B.}}$, a mirror parallel to $[2\bar{1}\bar{1}0]_{\mathrm{M.B.}}$, and six of the 12 antisymmetry elements (Table 2.5(a)), e.g. two antidiads along $[1\bar{1}00]_{\mathrm{M.B.}}$, and $[\bar{1}010]_{\mathrm{M.B.}}$, two antihexads along $[0001]_{\mathrm{M.B.}}$, and two anti-roto-inversion hexads along $[0001]_{\mathrm{M.B.}}$. So, this particular shift changes the spacegroup from P6'/m'mm' to P2'mm'. A shift $p = \alpha[0001]_{\mathrm{M.B.}}$, $\alpha < \frac{1}{6}$, similarly, change P6'/m'mm' to P$\bar{6}$'m2', and so on.

Table 2.6(a). The variation of $P6'/m'mm'$ with a shift p.

No.	p^*, M.B.	Spacegroup
(1)	$[0\ 0\ 0\ 0]$	$P6'/m'mm'$
(2)	$c[0\ 0\ 0\ \pm1]$	$P6'_3/m'mc'$
(3)	$c[0\ 0\ 0\ \pm1]$	$P\bar{6}'m2'$
(4)	$z\langle 0\ 1\bar{1}\ 0\rangle$	$P2'mm'$
(5)	$x\langle 2\bar{1}\ \bar{1}\ 0\rangle$	$P2'22'$
(6)	$x\langle 2\bar{1}\ \bar{1}\ 0\rangle + c[0\ 0\ 0\ \pm1]$	$P2_1'22_1'$
(7)	$z\langle 0\ 1\bar{1}\ 0\rangle + c[0\ 0\ 0\ \pm1]$	$P2_1'mc'$
(8)	$z\langle 0\ 1\bar{1}\ 0\rangle + c[0\ 0\ 0\ \pm1]$	Pm
(9)	$x\langle 2\bar{1}\ \bar{1}\ 0\rangle + c[0\ 0\ 0\ \pm1]$	$P2$
(10)	$x\langle 2\bar{1}\ \bar{1}\ 0\rangle + y\langle \bar{1}\ 2\bar{1}\ 0\rangle$	$P2'$
(11)	$x\langle 2\bar{1}\ \bar{1}\ 0\rangle + y\langle \bar{1}\ 2\bar{1}\ 0\rangle$ $+ c[0\ 0\ 0\ \pm1]$	$P2_1'$
(12)	$x\langle 2\bar{1}\ \bar{1}\ 0\rangle + y\langle \bar{1}\ 2\bar{1}\ 0\rangle$ $+ c[0\ 0\ 0\ \pm1]$	$P1$

* $x<1/18$, $y<1/18$, $z\leq1/9$, $c<1/6$.

Table 2.6(b). The variations of $Imm'm'$ with a shift p.

No.	p	Spacegroup
(1)	0,0,0	$Imm'm'$
(2)	1/8,0,0	$I112'$
(3)	0,1/8,0	$I12'1$
(4)	0,0,1/2	$I2'/m'$
(5)	x,x,0	$I12'2'$
(6)	x,-x,0 x=1/8	Imm'
(7)	x,-x,0 x=1/2	Imm'
(8)	x,-x,z x=1/36 ,z=1/9	$Imm'm'$
(9)	x,-x,z x=1/9 ,z=-1/18	$Imm'm'$
(10)	x,y,z x=2/9, y=5/18, and z=-1/18.	$I22'2'$

Table 2.6(c). The variations of $Amm'm'$ with a shift p.

No.	p	Spacegroup
(1)	0,0,0	$Amm'm'$
(2)	1/2,0,0	$A12'2'$
(3)	0,-1/2,0	$A12'2'$
(4)	0,0,z z≥1/10	$A2'/m'$
(5)	0,0,z z=-1/8	$A2'/m'$
(6)	x,x,0	$A22'2'$
(7)	x,-x,0 x=1/4	Amm'
(8)	x,-x,z x=1/54 ,z=5/54	$Amm'm'$
(9)	x,-x,z x=5/216,z=-1/108	$Amm'm'$
(10)	x,y,z x=59/216, y=49/216, and z=-1/108	$A2m'2'$

2.5. DICHROMATIC COMPLEXES.

A dichromatic complex can be created either by placing white and black motif (e.g. in case of germanium each motif contains two atoms displaced from each other by $\frac{1}{4}$ [111]), at lattice points of the corresponding dichromatic pattern or by misorienting two crystals by a certain axis/angle. In the latter method, the crystals after rotation are labelled white and black. The i^{th} white and the j^{th} black crystal symmetry operations have expressions similar to these in equations (2.1a) and (2.1b), respectively, except that w includes glide and/or screw translations. As in dichromatic pattern, the dichromatic complex exhibits coincident and antisymmetry operations. The former can be derived by substitution of equations (2.1a) and (2.1b) into equation (2.2). One obtains, for the l^{th} coincident operation

$$\begin{aligned}(W_l(c), w_l(c)) &= (W_i(\lambda), w_i(\lambda)) \\ &= (P, p)(W_j(\mu), w_j(\mu))(P, p)^{-1} \qquad (2.10)\end{aligned}$$

Two cases will be considered. First, consider a dichromatic complex created by only a pure linear transformation P, i.e. p = 0, so equation (2.10) becomes after rearranging and equating similar parts on both sides

$$W_l(c) = W_i(\lambda) = PW_j(\mu)P^{-1} \qquad (2.11a)$$

and

$$
\begin{aligned}
w_l(c) &= w_i(\lambda) + t_k(\lambda) \\
&= Pw_j(\mu) + t_k(\lambda) \qquad (2.11b)
\end{aligned}
$$

Secondly, consider a dichromatic complex created by a linear transformation P, and a shift p of a black crystal with respect to the white, i.e. $p \neq 0$. Rearranging equation (2.10), equating similar parts on both sides and using equation (2.11a) and (2.11b), we obtain

$$W_l(c)p = W_i(\lambda)p = p \qquad (2.11c)$$

Equation (2.11c) is the criterion for the conservation of the coincident symmetry operation, which states that the coincident symmetry operation which leaves a shift vector p invariant will be conserved by this vector.

Similarly, by substitution of equations (2.1a) and (2.1b) into equation (2.3), one obtains for the antisymmetry operation

$$
\begin{aligned}
(W', w') &= (P, p)(W_i(\lambda), w_i(\lambda)) \\
&= (W_j(\mu), w_j(\mu))(P, p)^{-1} \qquad (2.12)
\end{aligned}
$$

Rearranging and equating similar parts on both sides, we obtain

$$W' = PW_i(\lambda) = W_j(\mu)P^{-1} \qquad (2.13a)$$

and

$$w' = Pw_i(\lambda) + p = w_j(\mu) - W_j(\mu)P^{-1}p \qquad (2.13b)$$

For $p = 0$, we obtain

$$w' = Pw_i(\lambda) = w_j(\mu) \qquad (2.14a)$$

For $p \neq 0$, we obtain

$$W'p = -p \qquad (2.14b)$$

Equations (2.14a) and (2.14b) are the criteria for the conservation of the antisymmetry operation of a dichromatic complex.

The dichromatic complexes which are characterised by Σ = 3, 9, and 27 have been created by using the methods mentioned at the beginning of this section. The projection of the Σ = 3 dichromatic complex along $[0001]_{M.B.}$ is found identical to the dichromatic pattern shown in Fig.2.3(a), and therefore, it has a spacegroup similar to the pattern, i.e. P6'/m'mm'. The Σ = 9 and 27 complexes are shown in Fig.2.5(a) and 2.5(b), respectively. The symmetry operations and hence the spacegroups of these complexes have been derived as Imm'a', and Amm'a', respectively using equations (2.10) and (2.12). These symmetry operations are tabulated in Tables 2.7(a) and 2.7(b), respectively. From these Tables one can notice that the spacegroups Imm'a' and Amm'a' contain mirror glide planes, therefore they are non-symmorphic. Also, the spacegroups Imm'a' and Amm'a' are isomorphic to the spacegroups Imm'm' and Amm'm' of Σ = 9 and 27 dichromatic patterns.

2.5.1. THE VARIATION OF THE DICHROMATIC COMPLEX SYMMETRY WITH RELATIVE DISPLACEMENT.

Equations (2.11c) and (2.14b) have been used to study the

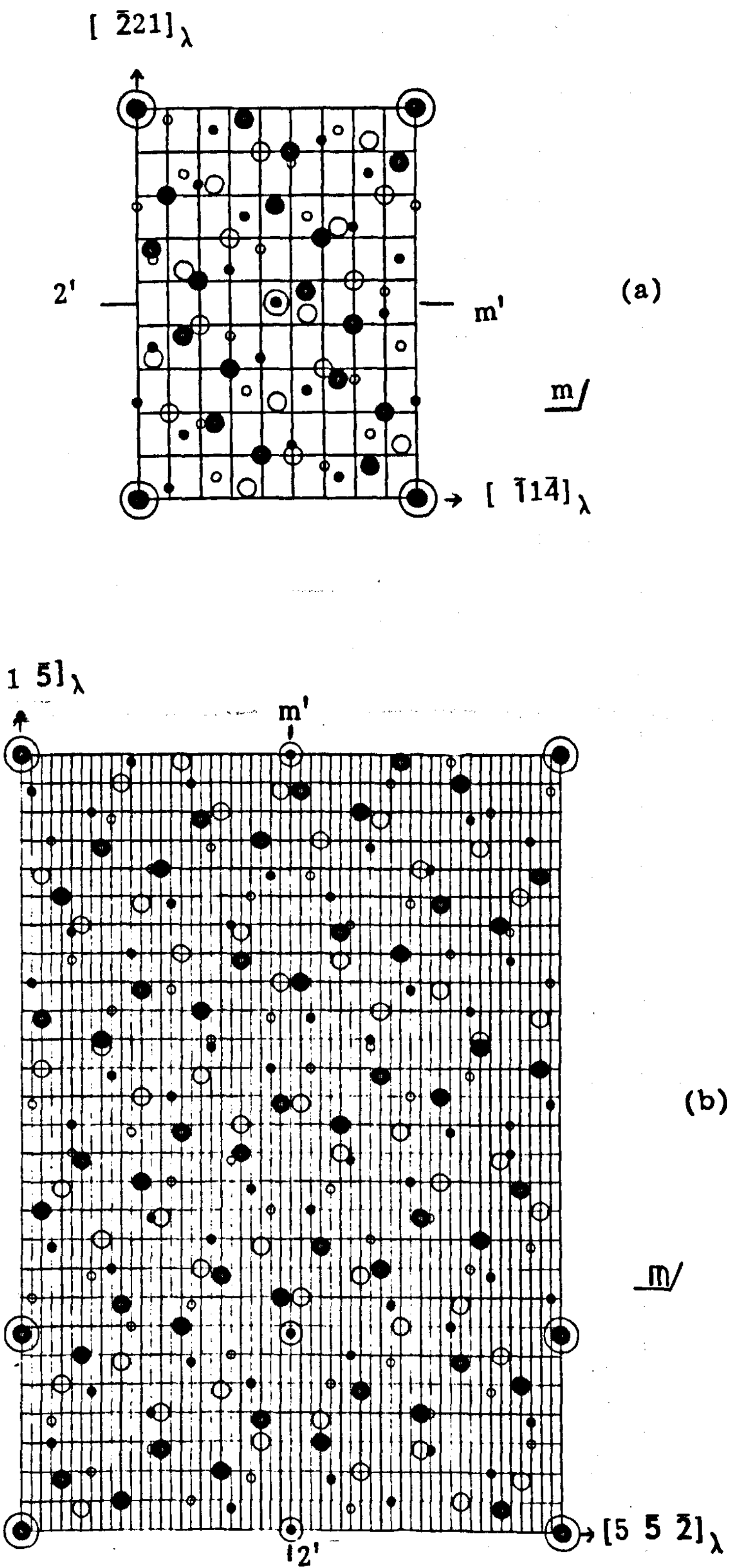

Fig. 2.5. (a) The projection along $[110]_\lambda$ of the $\Sigma=9$ dichromatic complex.

(b) The same as (a) but for $\Sigma=27$ dichromatic complex. The size of the symbols represents the...ABAB... stacking along $[110]_\lambda$.

Table 2.7(a). The elements of the spacegroup Imm'a' of the dichromatic complex of $\Sigma=9(-2\ 2\ 1)$.

(A)	Coincident Symmetry	
No.	$(W_1(c),\ w_1(c))$	$W(c)_1$ Matrix
(1)	(1, [000])	$\begin{bmatrix} 1 & 0 & 0 \\ 0 & 1 & 0 \\ 0 & 0 & 1 \end{bmatrix}$
(2)	(2[110], 3/4[110])	$\begin{bmatrix} 0 & 1 & 0 \\ 1 & 0 & 0 \\ 0 & 0 & -1 \end{bmatrix}$
(3)	($\bar{1}$[000], [000])	$\begin{bmatrix} -1 & 0 & 0 \\ 0 & -1 & 0 \\ 0 & 0 & -1 \end{bmatrix}$
(4)	(m[110], 1/4[110])	$\begin{bmatrix} 0 & -1 & 0 \\ -1 & 0 & 0 \\ 0 & 0 & 1 \end{bmatrix}$
(B)	Antisymmetry	
No.	(W', w')	W' Matrix
(5)	(2'[-1 1 -4], 1/4[110])	$1/9 \begin{bmatrix} -8 & -1 & 4 \\ -1 & -8 & -4 \\ 4 & -4 & 7 \end{bmatrix}$
(6)	(2'[-2 2 1], [000])	$1/9 \begin{bmatrix} -1 & -8 & -4 \\ -8 & -1 & 4 \\ -4 & 4 & -7 \end{bmatrix}$
(7)	(m'[-1 1 -4], 3/4[110])	$1/9 \begin{bmatrix} 8 & 1 & -4 \\ 1 & 8 & 4 \\ -4 & 4 & -7 \end{bmatrix}$
(8)	(m'[-2 2 1], [000])	$1/9 \begin{bmatrix} 1 & 8 & 4 \\ 8 & 1 & -4 \\ 4 & -4 & 7 \end{bmatrix}$

Table 2.7(b). The elements of the spacegroup Amm'a' of the dichromatic complex of Σ=27(5 -5 -2).

(A)	Coincident Symmetry	
No.	($W_1(c)$, $w_1(c)$)	$W(c)_1$ Matrix
(1)	(1, [000])	$\begin{bmatrix} 1 & 0 & 0 \\ 0 & 1 & 0 \\ 0 & 0 & 1 \end{bmatrix}$
(2)	(2[110], 3/4[110])	$\begin{bmatrix} 0 & 1 & 0 \\ 1 & 0 & 0 \\ 0 & 0 & -1 \end{bmatrix}$
(3)	($\bar{1}$[000], [000])	$\begin{bmatrix} -1 & 0 & 0 \\ 0 & -1 & 0 \\ 0 & 0 & -1 \end{bmatrix}$
(4)	(m[110], 1/4[110])	$\begin{bmatrix} 0 & -1 & 0 \\ -1 & 0 & 0 \\ 0 & 0 & 1 \end{bmatrix}$
(B)	Antisymmetry	
No.	(W', w')	W' Matrix
(5)	(2'[-1 1 -5], 1/4[110])	$1/27 \begin{bmatrix} -25 & -2 & 10 \\ -2 & -25 & -10 \\ 10 & -10 & 23 \end{bmatrix}$
(6)	(2'[5 -5 -2], [000])	$1/27 \begin{bmatrix} -2 & -25 & -10 \\ -25 & -2 & 10 \\ -10 & 10 & -23 \end{bmatrix}$
(7)	(m'[-1 1 -5], 3/4[110])	$1/27 \begin{bmatrix} 25 & 2 & -10 \\ 2 & 25 & 10 \\ -10 & 10 & -23 \end{bmatrix}$
(8)	(m'[5 -5 -2], [000])	$1/27 \begin{bmatrix} 2 & 25 & 10 \\ 25 & 2 & -10 \\ 10 & -10 & 23 \end{bmatrix}$

variation of the $\Sigma = 9$ and 27 dichromatic complexes symmetry with some shift vectors p and the results of this study tabulated in Tables 2.8(a) and 2.8(b), respectively.

2.6. BICRYSTAL SYMMETRY.

A bicrystal can be created from a dichromatic complex by following two steps; first, choose the orientation and location of the interfacial plane. Second, discard white crystal atoms on one side and black atoms on the other. Fig.2.6.(a), (b), and (c) shows three bicrystals created from $\Sigma = 3$, 9, and 27 dichromatic complexes (section 2.5.), by following this method. These bicrystals are called unrelaxed where $\mathbf{p} = 0$ while the relaxed bicrystals, i.e. $\mathbf{p} \neq 0$, will be considered in the next section. A bicrystal exhibits coincident symmetry and antisymmetry, and a bicrystal spacegroup can be assigned.

A coincident symmetry operator, $W(c)$, has the property that it leaves a vector, n, normal to the chosen interfacial plane ,and pointing into the white crystal, invariant. This property can be expressed mathematically as follows

$$W(c)\,\mathbf{n} = \mathbf{n} \qquad (2.15a)$$

While an antisymmetry operator, W', has the property that it inverts the vector n, and this property expressed mathematically as follows

Table 2.8(a). The variation of Imm'a' with p.

No.	p^*	Spacegroup
(1)	$[0\ 0\ 0]$	Imm'a'
(2)	$\frac{1}{4}[\ \bar{1}\ 1\ \bar{4}]_\lambda$	Imm'n'
(3)	$\alpha[\ \bar{1}\ 1\ \bar{4}]_\lambda$	Imm'1
(4)	$\frac{1}{2}[\ \bar{2}\ 2\ 1]_\lambda$	Ima'a'
(5)	$\beta[\ \bar{2}\ 2\ 1]_\lambda$	Im1a'
(6)	$\alpha[\ \bar{1}\ 1\ \bar{4}]_\lambda + \beta[\ \bar{2}\ 2\ 1]_\lambda$	Im11
(7)	$\frac{1}{4}[1\ 1\ 0]_\lambda$	Iam'a'
(8)	$\gamma[1\ 1\ 0]_\lambda$	I1m'a'
(9)	$\alpha[\ \bar{1}\ 1\bar{4}]_\lambda + \beta[\ \bar{2}\ 2\ 1]_\lambda + \frac{1}{4}[110]_\lambda$	Ia11
(10)	$\alpha[\ \bar{1}\ 1\bar{4}]_\lambda + \beta[\ \bar{2}\ 2\ 1]_\lambda + \gamma[110]_\lambda$	I111

* $0<\alpha<\frac{1}{4}$, $0<\beta<\frac{1}{2}$, and $0<\gamma<\frac{1}{4}$

Table 2.8(b). The variation of Amm'a' with p.

No.	$p^\#$	Spacegroup
(1)	$[0\ 0\ 0]$	Amm'a'
(2)	$\frac{1}{2}[\ \bar{1}\ 1\ \bar{5}]_\lambda$	Ama'a'
(3)	$\alpha[\ \bar{1}\ 1\ \bar{5}]_\lambda$	Am1a'
(4)	$\frac{1}{4}[5\ \bar{5}\ \bar{2}]_\lambda$	Amm'n'
(5)	$\beta[5\ \bar{5}\ \bar{2}]_\lambda$	Amm'1
(6)	$\alpha[\ \bar{1}\ 1\ \bar{5}]_\lambda + \beta[5\ \bar{5}\ \bar{2}]_\lambda$	Am11
(7)	$\frac{1}{4}[1\ 1\ 0]_\lambda$	Aam'a'
(8)	$\gamma[1\ 1\ 0]_\lambda$	A1m'a'
(9)	$\alpha[\ \bar{1}\ 1\bar{5}]_\lambda + \beta[5\ \bar{5}\ \bar{2}]_\lambda + \frac{1}{4}[110]_\lambda$	Aa11
(10)	$\alpha[\ \bar{1}\ 1\bar{5}]_\lambda + \beta[5\ \bar{5}\ \bar{2}]_\lambda + \gamma[110]_\lambda$	A111

$0<\alpha<\frac{1}{4}$, $0<\beta<\frac{1}{4}$, and $0<\gamma<\frac{1}{4}$

$$W' \mathbf{n} = -\mathbf{n} \qquad (2.15b)$$

A bicrystal symmetry operation can be determined by carrying out on n the symmetry operations of the corresponding dichromatic complex and making use of equations (2.15a) and (2.15b). For example, in Fig.2.6(a) the interfacial plane is chosen as $(\bar{1}1\bar{2})_\lambda$ and its normal is $[\bar{1}1\bar{2}]_\lambda$, by carrying out on n the operations of $\Sigma = 3$ dichromatic complex we found that only two coincident symmetry operations satisfy equation (2.15a) and two antioperations satisfy equation (2.15b). These operations are an identity, a mirror perpendicular to $[110]_\lambda$, an anti-diad parallel to $[1\bar{1}\bar{1}]_\lambda$, and an anti-mirror perpendicular to $[\bar{1}1\bar{2}]_\lambda$. These operations form the spacegroup p2'mm'. Similarly, the spacegroups of $\Sigma = 9$ and 27 bicrystals, Fig.2.6(b) and (c), have been derived and they are similar to $\Sigma = 3$ bicrystal, and Tables 2.9(a) and (b) show in detail their elements of symmetry.

2.7. RELAXED BICRYSTALS.

The bicrystals presented in the previous section are ideal and holosymmetric. The structure of the real bicrystals, which have thermodynamically favourable configurations, are related to the ideal structures by one or a combination of the following relaxation modes (Pond et al. 1983):

(i) rigid body translation,

(ii) migration of the interface plane,

(iii) local atomic relaxation, and

(iv) insertion or removal of additional material at the interface.

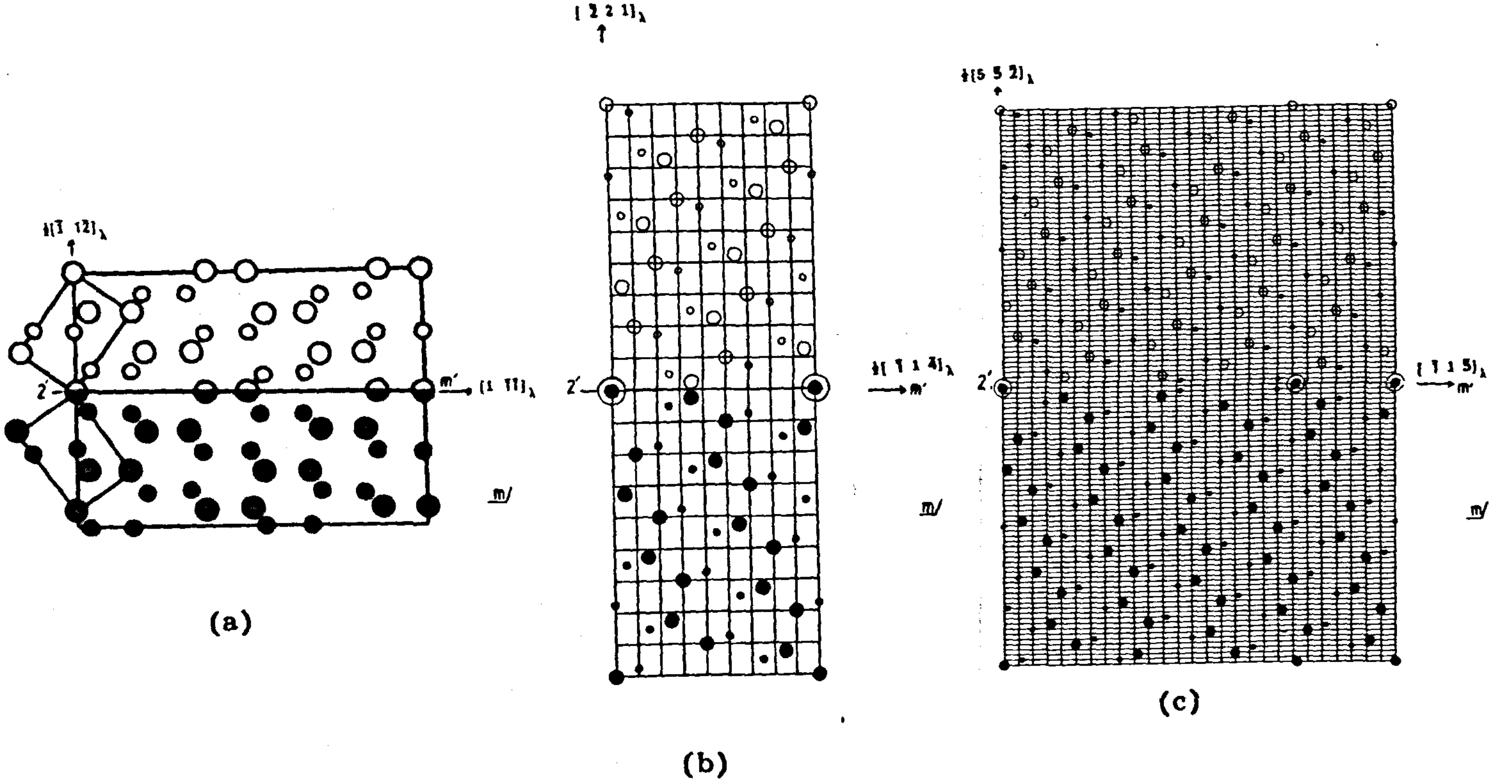

Fig. 2.6. (a) The projection along $[110]_\lambda$ of the $\Sigma=3(\bar{1}1\bar{2})_\lambda$ unrelaxed germanium bicrystal.

(b) The same as (a) but for $\Sigma=9(2\ \bar{2}\bar{1})_\lambda$ unrelaxed germanium bicrystal.

(c) The same as (a) but for $\Sigma=27(\bar{5}5\bar{2})_\lambda$ unrelaxed germanium bicrystal.

Table 2.9(a). The derivation of Ge bicrystal spacegroup of $\Sigma=9(\bar{2}\ 2\ 1)$, $n=[\bar{2}\ 2\ 1]$

No.	Imm'm'	Bicrystal symmetry
(A)	Coincident Symmetry	$W_1(c)n=n$
(1)	1[000]	1[000]
(2)	2[110]	
(3)	$\bar{1}[000]$	
(4)	m[110]	m[110]
(B)	Antisymmetry	W' n=-n
(5)	$2'[\bar{1}\ 1\ \bar{4}]$	$2'[\bar{1}\ 1\ \bar{4}]$
(6)	$2'[\bar{2}\ 2\ 1]$	
(7)	$m'[\bar{1}\ 1\ \bar{4}]$	
(8)	$m'[\bar{2}\ 2\ 1]$	$m'[\bar{2}\ 2\ 1]$

Table 2.9(b). The derivation of Ge bicrystal spacegroup of $\Sigma=27(5\ \bar{5}\ \bar{2})$, $n=[5\ \bar{5}\ \bar{2}]$

No.	Amm'm'	Bicrystal symmetry
(A)	Coincident Symmetry	$W_1(c)n=n$
(1)	1[000]	1[000]
(2)	2[110]	
(3)	$\bar{1}[000]$	
(4)	m[110]	m[110]
(B)	Antisymmetry	W' n=-n
(5)	$2'[\bar{1}\ 1\ \bar{5}]$	$2'[\bar{1}\ 1\ \bar{5}]$
(6)	$2'[5\ \bar{5}\ \bar{2}]$	
(7)	$m'[\bar{1}\ 1\ \bar{5}]$	
(8)	$m'[5\ \bar{5}\ \bar{2}]$	$m'[5\ \bar{5}\ \bar{2}]$

We consider here the first mode of relaxation in more detail. The conservation and/or breaking of coincident and antisymmetry operations with a shift p is expressed mathematically by the equations derived earlier (equation (2.11c) and (2.14b)), which are rewritten here for convenience

$$W(c)p = p \tag{2.16a}$$

and

$$W'p = -p \tag{2.16b}$$

The overall rigid body translation p at actual grain boundaries comprises two distinct components. One component corresponds to a physical displacement of one crystal, say the black crystal, in a direction perpendicular to the boundary plane. The other component corresponds to a displacement parallel to the boundary plane. In this study we consider only the relative displacements which are parallel to the boundary plane and fall within the in-plane Wigner-Seitz cells *(Pond 1977)*, which are planar and parallel to the bicrystal chosen interfaces. Fig.2.7(a),(b), and (c) show the in-plane Wigner-Seitz cells for the $\Sigma = 3(\bar{1}1\bar{2})_\lambda$, $9(\bar{2}21)_\lambda$ and $27(5\bar{5}\bar{2})_\lambda$ bicrystals. The holosymmetric structures which have the spacegroups p2'mm', are represented by the points O, in these cells. Other structures are designated A, B, and C. For example, the in-plane Wigner-Seitz cell of $\Sigma = 3$ bicrystal (Fig.2.7(a)) consists of the two vectors $\frac{1}{2}[1\bar{1}\bar{1}]_\lambda$ and $\frac{1}{2}[110]_\lambda$. The reference structure which is represented by O, has the holosymmetric spacegroup p2'mm'. Other structures can be obtained by considering certain in-plane displacements relative to the reference structure. Table 2.10(a) shows that an in-plane displacement equals, for example,

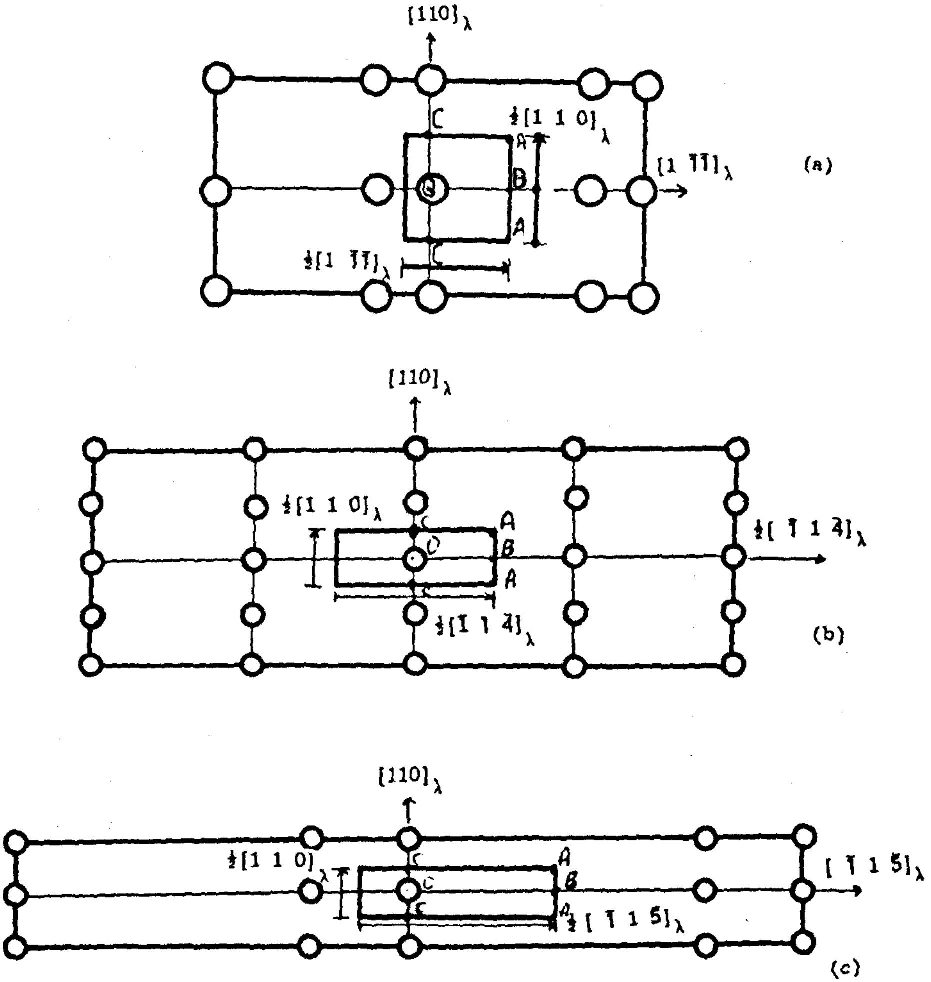

Fig. 2.7. (a) The vector digram for the in-plane Wigner-Seitz cell for $\Sigma=3(\bar{1}1\bar{2})_\lambda$ boundary.

(b) The same as (a) but for $\Sigma=9(2\bar{2}1)_\lambda$ unrelaxed germanium bicrystal.

(c) The same as (a) but for $\Sigma=27(55\bar{2})_\lambda$ unrelaxed germanium bicrystal.

Table 2.10(a). The variation of the spacegroup of $\Sigma=3(\bar{1}\ 1\ \bar{2})_\lambda$ bicrystal with p.

No.	p^*	Spacegroup
(1)	$[0\ 0\ 0]$	$p2'mm'$
(2)	$\frac{1}{2}[1\ \bar{1}\ \bar{1}]_\lambda$	$p2'_1ma'$
(3)	$\alpha[1\ \bar{1}\ \bar{1}]_\lambda$	$p1m1$
(4)	$\frac{1}{4}[1\ 1\ 0]_\lambda$	$p2'mb'$
(5)	$\beta[1\ 1\ 0]_\lambda$	$p2'11$
(6)	$\frac{1}{2}[1\ \bar{1}\ \bar{1}]_\lambda + \frac{1}{4}[1\ 1\ 0]_\lambda$	$p2'_1mn'$
(7)	$\alpha[1\ \bar{1}\ \bar{1}]_\lambda + \beta[1\ 1\ 0]_\lambda$	$p1$

Table 2.10(b). The variation of the spacegroup of $\Sigma=9(\bar{2}\ 2\ 1)_\lambda$ bicrystal with p.

No.	p^*	Spacegroup
(1)	$[0\ 0\ 0]$	$p2'mm'$
(2)	$\frac{1}{4}[\bar{1}\ 1\ \bar{4}]_\lambda$	$p2'_1ma'$
(3)	$\alpha[\bar{1}\ 1\ \bar{4}]_\lambda$	$p1m1$
(4)	$\frac{1}{4}[1\ 1\ 0]_\lambda$	$p2'mb'$
(5)	$\beta[1\ 1\ 0]_\lambda$	$p2'11$
(6)	$\frac{1}{2}[\bar{1}\ 1\ \bar{4}]_\lambda + \frac{1}{4}[1\ 1\ 0]_\lambda$	$p2'_1mn'$
(7)	$\alpha[\bar{1}\ 1\ \bar{4}]_\lambda + \beta[1\ 1\ 0]_\lambda$	$p1$

Table 2.10(c). The variation of the spacegroup of $\Sigma=27(5\ \bar{5}\ \bar{2})_\lambda$ bicrystal with p.

No.	p^*	Spacegroup
(1)	$[0\ 0\ 0]$	$p2'mm'$
(2)	$\frac{1}{2}[\bar{1}\ 1\ 5]_\lambda$	$p2'_1ma'$
(3)	$\alpha[\bar{1}\ 1\ 5]_\lambda$	$p1m1$
(4)	$\frac{1}{4}[1\ 1\ 0]_\lambda$	$p2'mb'$
(5)	$\beta[1\ 1\ 0]_\lambda$	$p2'11$
(6)	$\frac{1}{2}[\bar{1}\ 1\ 5]_\lambda + \frac{1}{4}[1\ 1\ 0]_\lambda$	$p2'_1mn'$
(7)	$\alpha[\bar{1}\ 1\ 5]_\lambda + \beta[1\ 1\ 0]_\lambda$	$p1$

* $0<\alpha<\frac{1}{2}$, $0<\beta<\frac{1}{4}$.

$\alpha[1\bar{1}\bar{1}]_\lambda$ is corresponding to the structure which has the spacegroup $p2_1$'ma' when $\alpha = \frac{1}{2}$ or p1m1 when $0 < \alpha < \frac{1}{2}$. Similarly, in-plane displacement equals, $\beta[110]_\lambda$, and $\beta = \frac{1}{4}$ or, $0 < \beta < \frac{1}{4}$ is corresponding to the structures which have the spacegroups p2'mb' or p2'11, respectively. The combinations of the above two in-plane displacements will result in structures which have spacegroups $p2_1$'mn' or p1, (see Table 2.10(a)). The possible in-plane displacements and the corresponding structure's spacegroups are tabulated in Tables 2.10(b) and (c) for $\Sigma = 9$ and 27 bicrystals, respectively.

CHAPTER THREE

Experimental Techniques

3.1. Specimen Preparation..............................3.2

  3.1.1. "Edge-on" Specimens........................3.3

  3.1.2. "Plan-View" Specimens......................3.4

3.2. Transmission Electron Microscopy Techniques........3.5

  3.2.1. Selected Area Diffraction..................3.5

  3.2.2. Convergent Beam Electron Diffraction.......3.13

  3.2.3. Large Angle Convergent Beam Electron Diffraction........................3.17

3.1. SPECIMEN PREPARATION.

The two pieces of germanium material used in this study have been obtained from *J.J.Bacmann (Department de Metallurgie/ SRM, CEN-Grenoble, France).* One piece has a cylindrical external shape with circular cross-section of diameter approximately 2.7 cm (Fig.5.1(a) in chapter 5). The other one has also cylindrical shape but with elliptical cross-section with major axis diameter about 2.7 cm (Fig.5.1(b) in chapter 5).

Two types of electron microscopy specimens have been prepared. "edge-on" specimens where the grain boundary plane is located perpendicular to the specimen surface, and "plan-view" specimens which have the boundary parallel to the specimen surfaces. The detailed method of preparation of these two types of specimens will be given in the next two sections, respectively. The method can be summarised here by the following four stages and shown schematically in Fig.(3.1):

stage one : slicing Ge bulk material,

stage two : chemical polishing of the slices to reveal the grain boundary,

stage three: cutting the slices into 3mm. discs,

stage four : mechanical, chemical and ion-beam thinning of the discs.

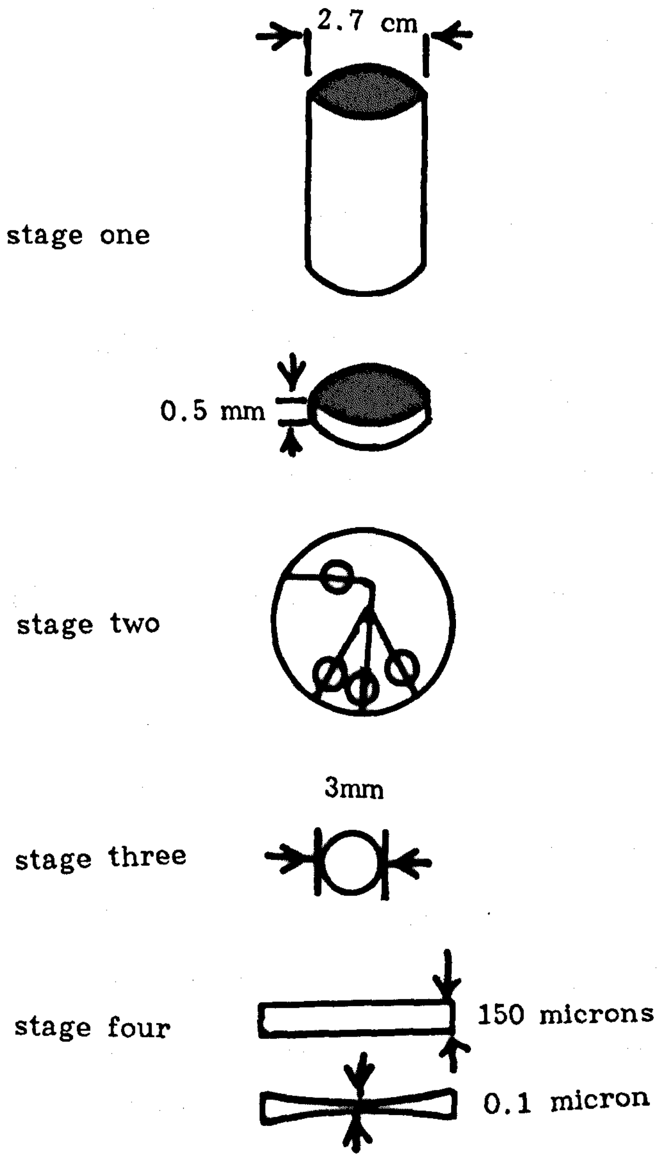

Fig. 3.1. Specimen preparation stages:
stage one: slicing Ge bulk material.
stage two: chemical polishing.
stage three: drilling the slice into 3mm discs.
stage four: mechanical and ion-beam thinning of the 3mm discs.

3.1.1. "EDGE-ON" SPECIMENS.

The preliminary step in the very long and difficult procedure for the preparation of germanium specimens for electron microscopy was cutting the germanium into slices. Difficulty arose from the fact that germanium is fragile and easy to break into small fragments under a slight stress. Because of the fragility of Ge material a diamond saw was used to slice the Ge material into 0.5 mm thick slices. The slices were manually polished by very fine emery papers to remove the effect of cutting on both sides of each slice. Then the slices were ready for the second stage, chemical polishing to reveal their grain boundaries. The polishing solution consisted of 20gm ferric chloride, 50ml distilled water and 50ml hydrochloric acid. The slices were immersed in the solution after bringing its temperature to boiling. After four minutes the slices are removed and washed thoroughly with acetone. This stage is very important because without being able to see the grain boundaries with the naked eye the next stage is impossible. The third stage was cutting or drilling the slices into 3mm diameter discs using an ultrasonic drill. Each disc contained the grain boundary (which had been revealed in the previous stage) edge-on and approximately situated at the middle of the disc. The fourth and the final stage is the thinning of the discs, and this consisted of three consecutive sub-stages. The first sub-stage was thinning using a mechanical dimpling machine. At the end of this sub-stage each disc was ground from 0.5mm down to 150 microns in thickness. The second sub-stage was chemical thinning which a mixture of 10% HF acid and 90% nitric acid was used in a chemical etching jet apparatus (Fig.3.2). The disc circumferences were protected against chemical solution attack by painting them with Lacomit varnish before

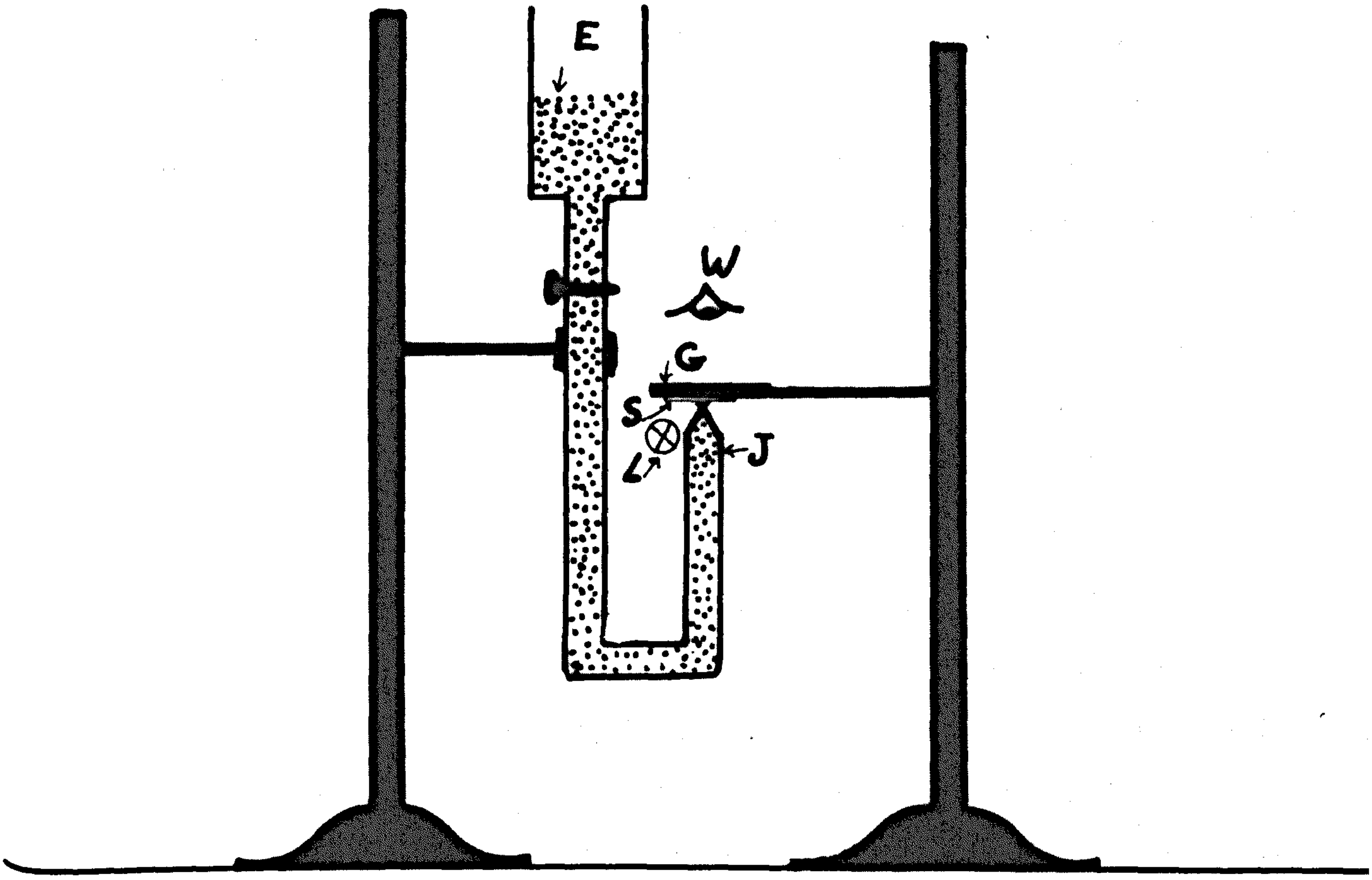

Fig. 3.2. The essential components of a jet chemical thinning apparatus. S-specimen, G-transparent glass slice to protect the observer's eyes and the specimen S is fixed on the other side away from the observer, L-light source, J-1mm diameter jet orifice, E-chemical etching solution (10% HF + 90% H_2NO_3) and W-the observer eye.

the thinning process. The jet nozzle was directed towards each disc and the chemical thinning process continued until a very small hole appeared as indicated by a light source located behind the specimen. Once the hole appeared the process needed to be stopped at once and the specimen washed first using plenty of distilled water to stop the etching process, then by acetone, and finally soaked in methanol for 24 hours. The final sub-stage of preparing the specimen is the ion beam thinning. In this stage Argon ions are accelerated by 8 KV in an ion miller machine to bombard the specimens and the beam inclination angle with respect to the specimen surface was 20 degrees. In each bombardment Ge material is removed layer by layer to reach the thickness approximately 0.1 micron. Then the specimens were ready for the electron microscope investigations.

3.1.2. "PLAN-VIEW" SPECIMENS.

The method of preparing the "plan-view" specimens is slightly different to that used for the case of "edge-on" ones. The main difference lies in the slicing step. While for the "edge-on" specimens the slicing step was straight forward, because already the boundaries were oriented edge-on, we found the slicing process in the case of "plan-view" specimens to be rather difficult. To overcome this difficulty the following preparation method was developed to suit this case. First, the Ge bulk materials were immersed in the polishing solution to reveal the grain boundaries on the top and bottom of the material as well as on the cylindrical surface then, the traces of the grain boundaries were marked by a sharp cutter. Secondly, the material was cut at a fixed distance on both sides of the marked traces, approximately 0.5 mm, so the boundary plane was parallel to the slice surface. The next procedures were typically the same as those for the "edge-on" case; drilling the slices into 3mm discs and thinning the discs mechanically, chemically and finally ion beam thinning.

3.2. TRANSMISSION ELECTRON MICROSCOPY (TEM) TECHNIQUES.

The three well-known techniques for obtaining diffraction patterns in electron microscopy are selected-area diffraction, SAD *(Hirsch et al. 1965)*, convergent beam electron diffraction, CBED *(Steeds 1979)*, and Tanaka or large-angle convergent beam electron diffraction, LACBED *(Tanaka et al. 1980)*, techniques. In the first technique, the electron beam incident on the specimen is broad and nearly parallel. It is focused below the specimen onto a distant viewing screen using the post-specimen lenses. In the second and third techniques the incident electron beam is focused on the specimen. The convergent angle of the incident beam in the case of CBED is less than the Bragg angle while in the case of LACBED it is equal to a Bragg angle. More details about these techniques will be given in the next three sections.

3.2.1. SELECTED AREA DIFFRACTION.

In this mode of operation a small area of a specimen can be selected for diffraction studies. Fig.3.3 shows a ray diagram of the formation of a SAD pattern in an electron microscope having two condenser lenses, one objective lens, and two projector lenses. The electron beam leaving the condenser lens is almost parallel and scattered by the

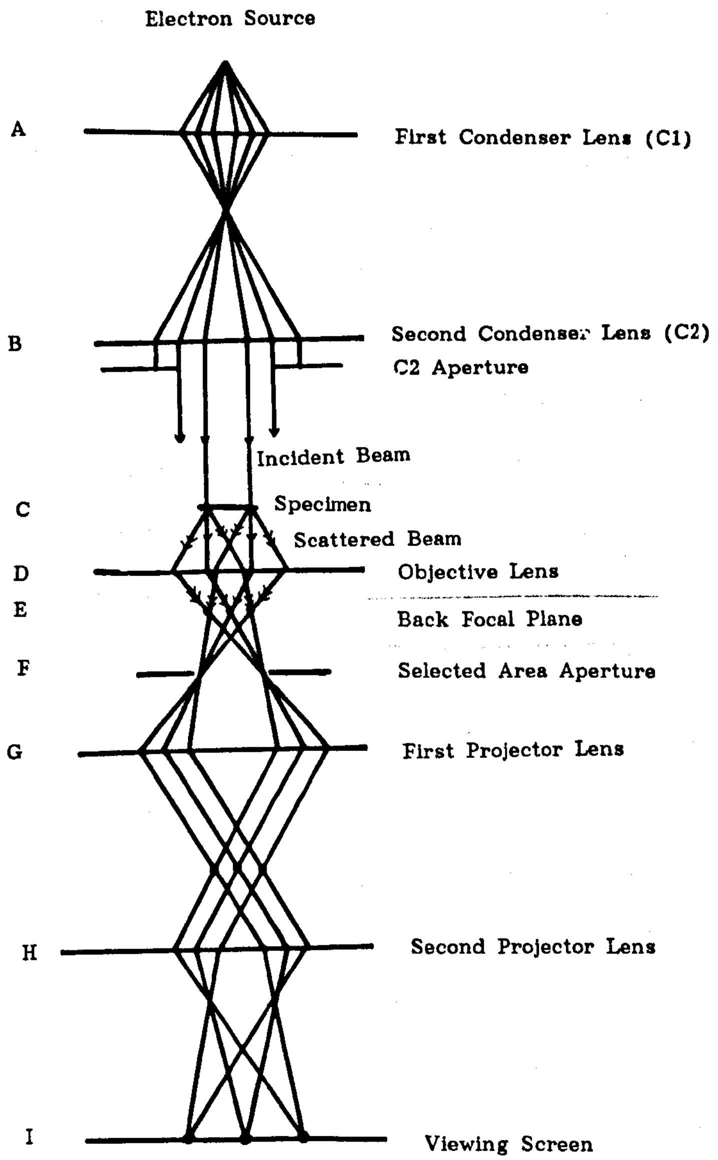

Fig. 3.3. A ray diagram showing the selected area diffraction mode in an electron microscope having 5 lenses.

specimen 'C'. The objective lens 'D' focused the incident and scattered beams (indicated by single and double arrows, respectively) in its back focal plane 'E' to form the diffraction pattern. The area from which the diffraction pattern is taken could be selected by placing a selected area aperture in the image plane 'F' of the objective lens. The function of the two projector lenses 'G' and 'H' which follow the objective lens is to transfer the SAD pattern formed by the objective lens on to the viewing screen 'I' at a high magnification.

As the electron beam passes through a selected area of a single crystal or bicrystal specimen (area selected by a selected area aperture 'F') in the microscope, some of the electrons are scattered from the main beam, in various directions and at various angles. Electrons scattered in phase from successive parallel planes lying at particular orientations, will combine constructively and peaks of intensity will occur in the form of regularly spaced diffraction spots. These intense spots obey Bragg law; $\lambda = 2d_{hkl}\sin\Theta_B$, where Θ_B is the angle between the incident electron beam and the plane of reflecting atoms and is called Bragg's angle, d_{hkl} is the spacing between the set of lattice planes and λ is the incident electron beam wavelength. While the electrons scattered from lattice planes lying at all other orientations will be out of phase and interact destructively, and no diffraction maxima will appear in the diffraction pattern from these scattered electrons. Fig. 3.4(a) is a SAD pattern obtained from Ge using a 120kv electron beam oriented along a <111> direction. The six spots closest to the origin (the most intense spot) of the pattern are 220 type as shown indexed in Fig. 3.4(b)

The understanding and interpretation of SAD patterns can be easily

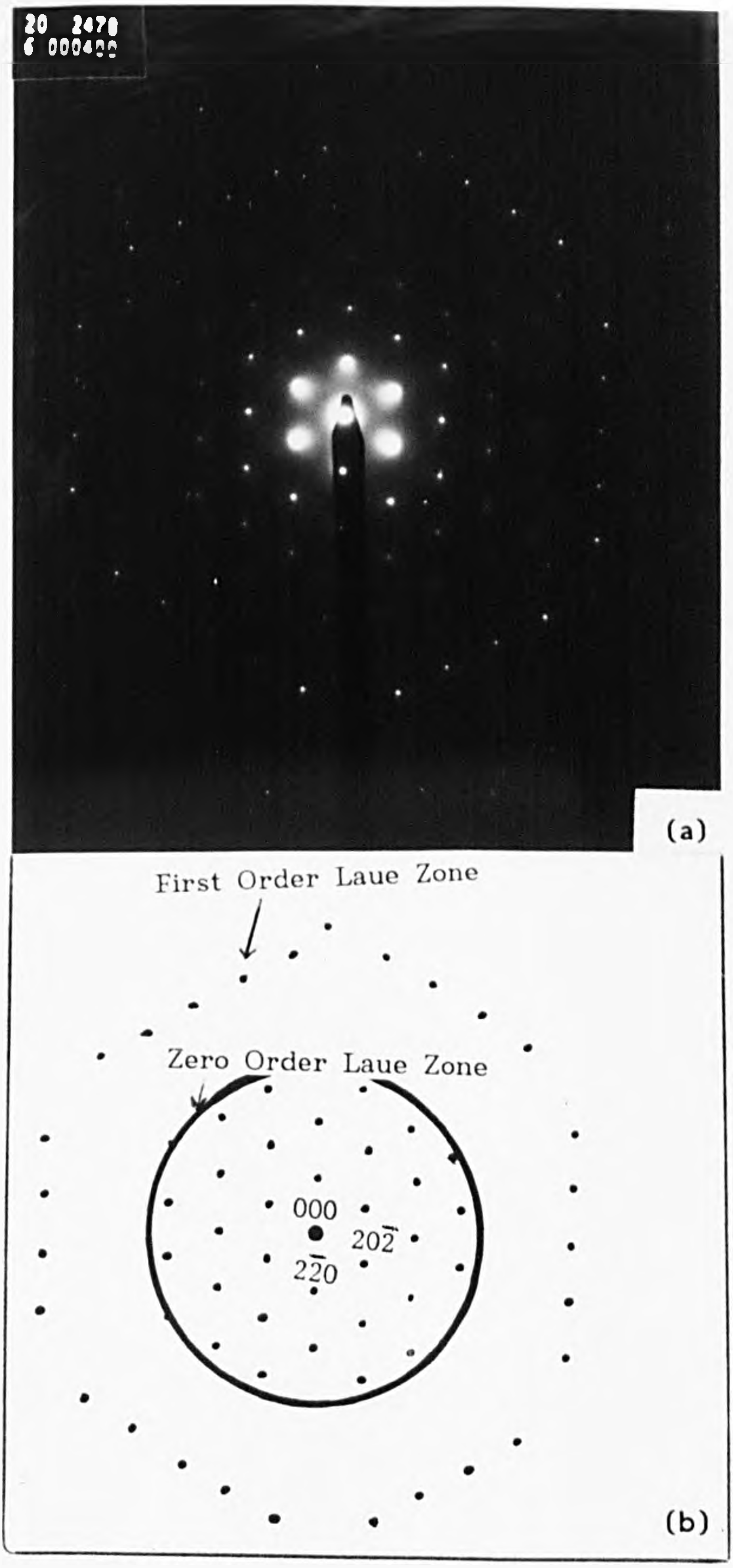

Fig. 3.4. (a) The [111] selected area diffraction pattern from germanium single crystal specimen with 120 Kv electron beam. It is taken at low camera length to show both the zero and first order laue reflections.

(b) A plan-view section showing the zero and first order laue reflection zones.

achieved by making use of the concept of the reciprocal lattice (RL), Ewald reflection sphere (ERS), Laue zones and structure factor.

First, the RL is related to the direct lattice, and is constructed by drawing a normal to each set of planes in the direct space lattice and marking off points along these normals at distances 1/d from the origin, where d is the interplanar spacing for each set of planes. A set of basis vectors, e_i, in direct space and their reciprocal vectors, e^*_j, in reciprocal space are related to each other by the vector dot product:

$$e_i \cdot e^*_j = \delta_{ij}$$

where

$$\delta_{ij} = 0 \quad \text{if} \quad i \neq j$$

and

$$\delta_{ij} = 1 \quad \text{if} \quad i = j \qquad (3.1)$$

For example the F.C.C. lattice shown in Fig.2.1(a) chapter two (its unit cell in direct space has the lattice points $000; \frac{1}{2}\frac{1}{2}0; 0\frac{1}{2}\frac{1}{2}; \frac{1}{2}0\frac{1}{2}$) its RL has lattice points at 000; 200; 020; 002; 111, i.e., a body centred cubic lattice. Fig.3.5 shows the RL corresponding to the F.C.C. lattice in Fig.2.1(a).

Secondly, the Ewald reflection sphere (ERS) can be constructed as shown in Fig.3.6, by drawing a sphere of radius OC = $1/\lambda$, where λ is the wavelength of the electron beam. The radius OC of the ERS is drawn from the origin 'O' of the RL in Fig.3.6 to a point 'C' which represents the centre of ERS. The radius of ERS, $\approx 30Å^{-1}$ at 120 KV, is so large compared with the lattice spacing that the ERS can be approximated to

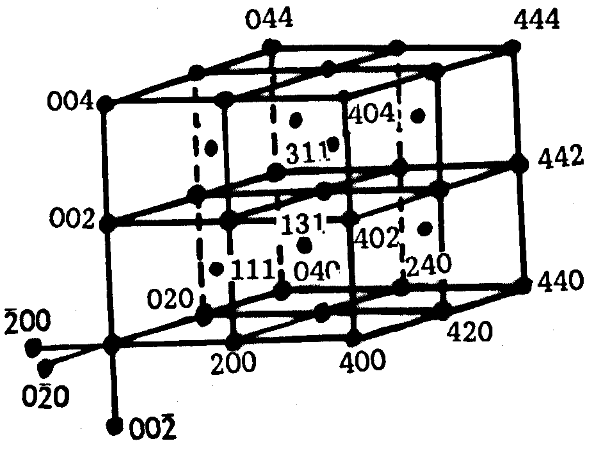

Fig. 3.5. The reciprocal lattice for a F.C.C. lattice.

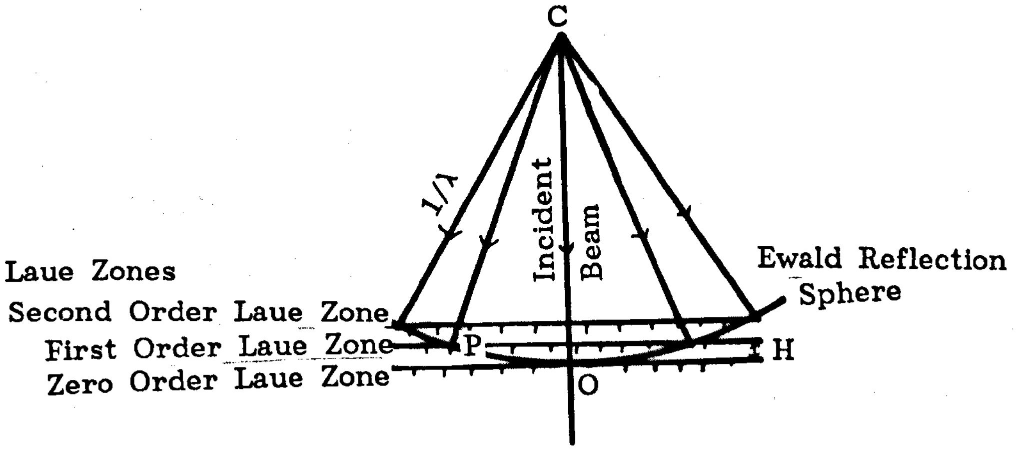

Fig. 3.6. The intersection between Ewald sphere and the reciprocal lattice planes and the position of the zero, first and second order laue zones.

a plane.

Whenever the ERS intersects a RL point, the Bragg equation will be satisfied, and diffraction will occur, and hence a spot will appear in a SAD pattern. The ERS in Fig.3.6 intersects, for example, the points O and P, so strong reflections will be produced, where the vectors CO and CP represent the incident and scattered beam directions, and an angle equal twice the Bragg angle, Θ_B, is enclosed between them. Since the angle Θ_B is small and from the geometry of the triangle OCP one can write

$$2\Theta_B = (1/d)/(1/\lambda) \text{ or } \lambda = 2\Theta_B d = 2d\sin\Theta_B$$

i.e., the Bragg equation is satisfied.

Thirdly, the Laue zone construction is very useful for indexing of SAD patterns. Because of the slight curvature of the ERS it intersects successive RL planes (Fig.3.6) so that reflection from these higher order RL planes as well as from the zero order RL plane will contribute to the corresponding SAD pattern. These spots will lie within circular bands called Laue zones. The <111> SAD pattern in Fig.3.4(a) contains reflection spots from zero and first order Laue zones.

Finally, the structure factor *(Hirsch et al. 1965)*, may be expressed more rigorously in terms of the atomic scattering factor and a path difference argument applied to scattering by each atom within a unit cell. For example, the wave scattered by the i^{th} atom is

$$f_i \exp(2\pi i g_i \,.\, r_i)$$

where f_i is the i^{th} atom scattering amplitude and the exponential argument corresponds to the phase difference between the wave scattered by the i^{th} atom which has the fractional coordinates $r_i = (u_i, v_i, w_i)$ and that scattered by an atom at the origin for the $g = hkl$, reflection. If a unit cell contains n atoms, then the resultant wave scattered by all the n atoms for the hkl reflection, is designated F_{hkl} and called the structure factor, equals

$$F_{hkl} = \Sigma_i f_i \exp(2\pi i g_i . r_i) \qquad (3.2)$$

where the summation extends over all the n atoms of the unit cell. The atomic scattering amplitude for germanium, $f_i = f_{Ge}$, is plotted in Fig.3.7 as a function of $\sin\Theta/\lambda(=1/2d)$. The values of f_{Ge} are taken from *Hirsch et al. (1965)* and multiplied by a correction factor $M = m_{120}/m_0$ where m_{120} is the mass of electron accelerated by 120kv and m_0 is the rest mass of the electron.

The intensity of a diffracted beam, I, is proportional to the magnitude of the product of the structure factor, F, and its complex conjugate, F^*, and can be written as follows

$$I \propto F.F^* \qquad (3.3)$$

The equation of the structure factor (Eq. 3.2) can be used to predict whether a reflection spot is allowed or forbidden in a RL and also to calculate the relative intensities of the RL points. Violation of the structure factor equation can occur as a result of double diffraction

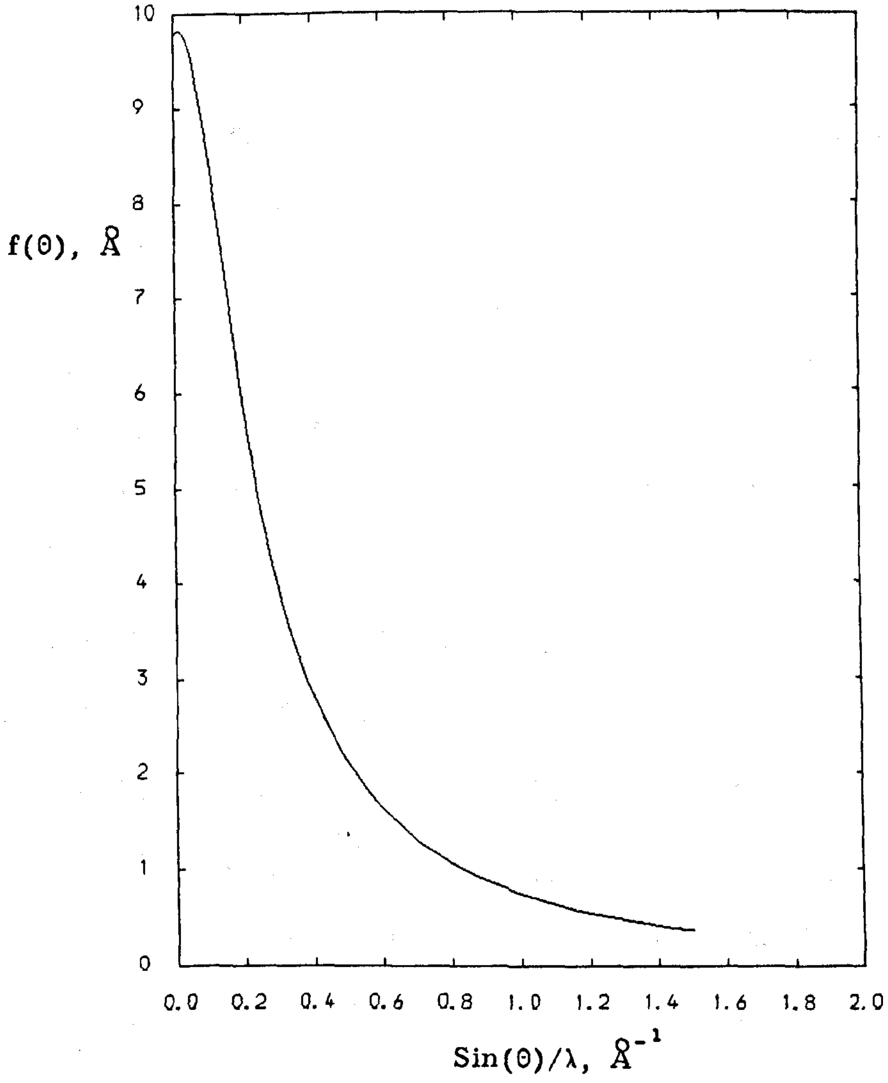

Fig. 3.7. The mean atomic scattering amplitude for germanium.

(Tu et al. 1978). For example, the structure factor for germanium crystal shown in Fig.2.2(a) may be calculated using equation (3.2) as follows. This crystal contains 8 atoms of the same kind, located at 000; $\frac{1}{2}\frac{1}{2}0$; $\frac{1}{2}0\frac{1}{2}$; $0\frac{1}{2}\frac{1}{2}$; $\frac{1}{4}\frac{1}{4}\frac{1}{4}$; $\frac{3}{4}\frac{3}{4}\frac{1}{4}$; $\frac{3}{4}\frac{1}{4}\frac{3}{4}$, and $\frac{1}{4}\frac{3}{4}\frac{3}{4}$. By substitution of these atom positions in equation (3.2) and factorize the lattice and basis terms, we obtain

$$F_{hkl} = f_{Ge}\left[1 + e^{\pi i(h+k)} + e^{\pi i(h+l)} + e^{\pi i(k+l)}\right]\left[1 + e^{\pi i(h+k+l)/2}\right] \qquad (3.4)$$

The first bracket on the right of the equality sign contains four terms corresponding to the four lattice sites in the Ge cell. The second bracket contains two terms corresponding to the two basis atoms. The atoms at the four lattice sites all scatter either in phase (constructive interference) or out of phase leading to $F_{hkl} = 0$ (destructive interference). The latter occurs if h, k, l are mixed (odd and even). The basis atoms scatter either partially in phase if h, k, l are all odd or out of phase if h, k, l are all even and $(h + k + l) = 4(n + \frac{1}{2})$, n is integer. These conditions after recombined together can be summarised as follows:

(1) $/F/^2 = 0$ if h, k, l mixed (odd and even) 3.5(a)

(2) $/F/^2 = 64f_{Ge}^2$ if h, k, l even and $(h + k + l) = 4n$, n is integer 3.5(b)

(3) $/F/^2 = 32f_{Ge}^2$ if h, k, l odd 3.5(c)

(4) $/F/^2 = 0$ if h, k, l even and $(h + k + l) = 4(n + ½)$, n is integer 3.5(d)

For example, Fig.3.4(a) shows the reflections of the type 220. According to the structure factor equation (3.4) and condition 3.5(b), these reflections are kinematically allowed. While reflections of the type 123 are not allowed kinematically because h, k, l are mixed (condition 3.5(a)), and consequently, they are absent in the diffraction pattern. Fig.3.8 shows a [110] SAD pattern is taken from a germanium single crystal. The reflection spots of the type 002, which are kinematically not allowed (condition 3.5(d)), can be observed with high intensity. This type of reflection violates the kinematical theory of electron diffraction and they can be interpreted by using the dynamical theory of electron diffraction *(Hirsch et al. 1965)* as a result of double diffraction *(Tu et al. 1978)* such as $\bar{1}11$ followed by $1\bar{1}1$, both of which are close to the ERS and also appear in the pattern. This anomaly in the kinematical electron diffraction theory arises because in this theory it was assumed that the wave incident on each atom is simply the primary wave falling on the crystal, and therefore that the total amplitude of the diffracted wave is proportional to the number of atoms in the crystal. This is not quite correct, for it is clear that the amplitude of the original wave will be diminished as it passes successive reflecting planes of atoms, because of the loss of electrons into the reflected wave. Also, the above mentioned double diffraction effect predicates that the diffracted beams act as new sources inside the specimen so that further diffraction can occur by the crystal.

The range of applicability of the kinematical electron diffraction theory

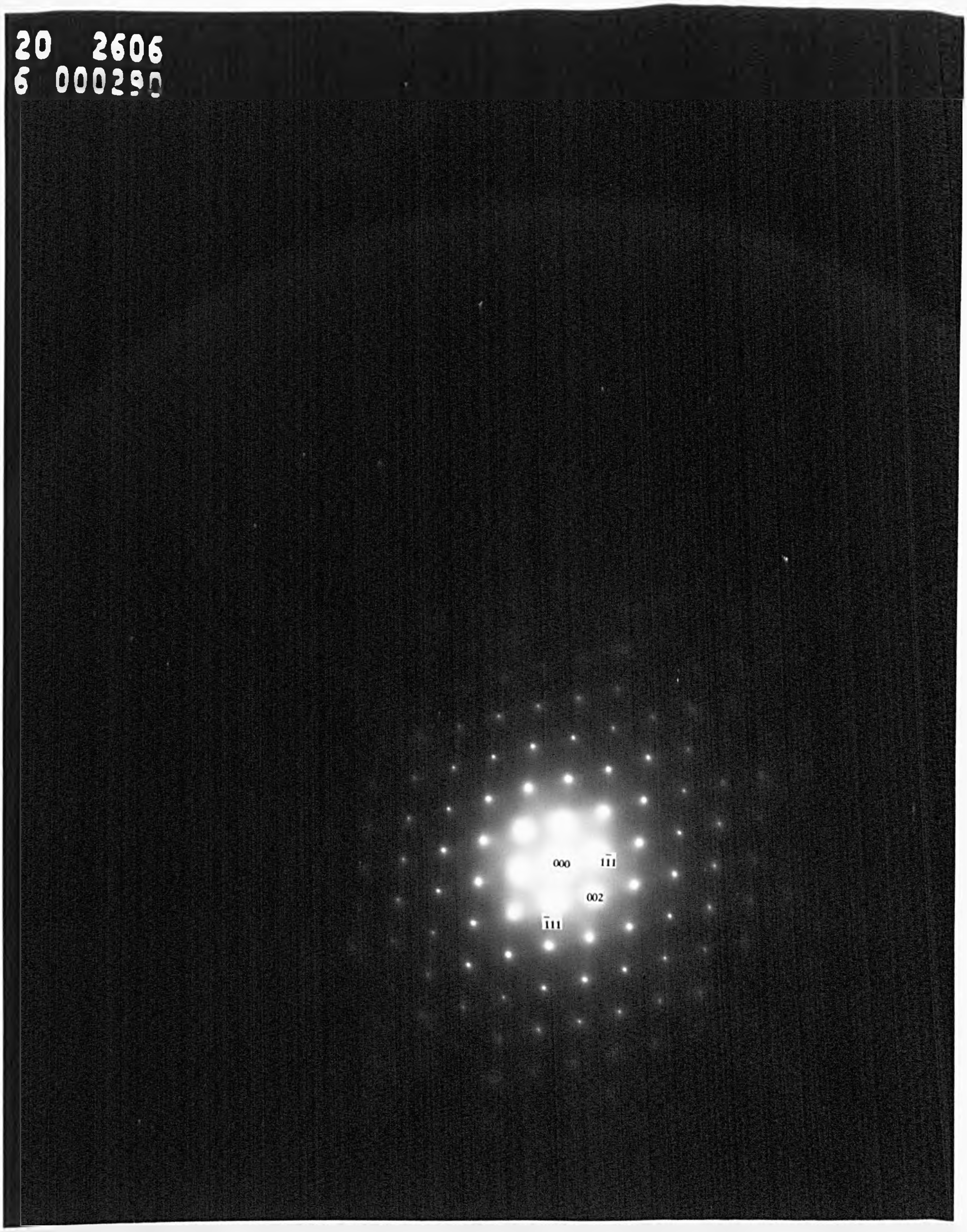

Fig. 3.8. The [110] SAD pattern was taken from a germanium single crystal (120Kv).

depends on the thickness, t, of the electron microscopy specimens. Thus specimens have to be very thin for this theory to be valid. All the SAD, CBED and LACBED patterns have been taken from the thinnest areas of Ge specimens prepared during this study. The thickness of these thin areas was within the values at which the kinematical theory is valid, so, this theory is sufficient to be used to interpret all the diffraction patterns presented here.

Thicker specimens need the dynamical diffraction theory which will take account of the repeated scattering and of the dynamical interaction of the incident and scattered electron beams with the material of the specimens. This theory has been explained at length by many authors, for example *Hirsch et al. (1965)*

The structure of interfaces in "edge-on" and "plan-view" grain boundaries has been studied considerably in the last decade using SAD technique. It is found that the interface in 'edge-on' specimens gives rise to an array of relrods along a direction parallel to both the specimen surface and the interface. These relrods are elongated normal to the interface *(Carter et al. 1980)*. The ERS can cut the relrods along their length and thus one can observe them in a SAD pattern as an array of streaks running normal to the boundary plane.

Also, the interface in the "plan-view" grain boundary gives rise to extra reflection spots (which result from the periodic structure of the boundary), besides the reflections from both grains (one and two). So, the SAD patterns taken from these specimens contain reflections from grains one and two and the grain boundary region. They also contain many spots due to double diffraction. It is therefore necessary to sort out those reflections which result from double diffraction from those which are singly diffracted. One can differentiate between grain boundary reflections and double diffraction by making use of the double diffraction cell. Such a cell consists of the shortest two vectors, say V_1 and V_2, of the RL in consideration. The vector, V (= V_1 or V_2), can be represented in terms of the reciprocal vectors g and h, as follows $V = (g - h)$ where g and h are any two reciprocal vectors connected to the origin of the RL with two spots in the zero or higher order laue zones for which the curvature of the ERS could be significant. In case of bicrystals the contribution to the double diffraction spots intensity is arising from multiple diffraction via spots, in the zero or higher order laue zones in one or both grains which constitute the bicrystal, that intersected or nearly intersected the ERS.

The SAD technique is useful in the determination of the orientation relationships between the grains in a specimen and the determination of the crystal class but it is unable to determine the point group or spacegroup of a crystal. We shall turn in the next section to consider another technique which will enable us to do so, and this technique is the CBED technique.

3.2.2. CONVERGENT BEAM ELECTRON DIFFRACTION.

The CBED is one of the most powerful techniques for investigations and determinations of crystal structure. Recently, the power of this technique has been appreciated in a wide variety of applications, such as the determination of crystal point groups and spacegroups

Using the SAD technique (section 3.2.1) a rather large area of the specimen contributes to the pattern because the specimen is illuminated with a parallel beam of electrons. On the other hand, using CBED, the electron beam is focused onto the specimen so that a small area of the specimen contributes to the pattern.

One can obtain a CBED pattern in a TEM by following this procedure *(Spence et al. 1986):*

(1) forming an image of the specimen,

(2) increase the strength of the first condenser lens C1 (Fig.3.3) to its maximum excitation while altering the second condenser lens C2 to produce a focused spot. This simply means that the illuminated area on the screen is minimised using the C2 fine control,

(3) the CBED pattern is observed by switching to diffraction mode.

Fig.3.9 shows a ray diagram depicting the formation of CBED patterns in the back focal plane. Fig.3.10 shows a [111] CBED pattern is taken from a germanium specimen following the above procedure. The central disc is 000 type, and the six next discs which are surrounding the zero one are of the type 220 and all are in the zero order Laue zone. Two types of information are available in the CBED patterns (e.g. Fig.3.10). The first is the detailed structure, within the direct beam, 000, and within the diffracted beams, 220, which shows certain symmetries. The second is information in the form of fine lines which are visible in the direct beam. These lines are called higher order laue zone

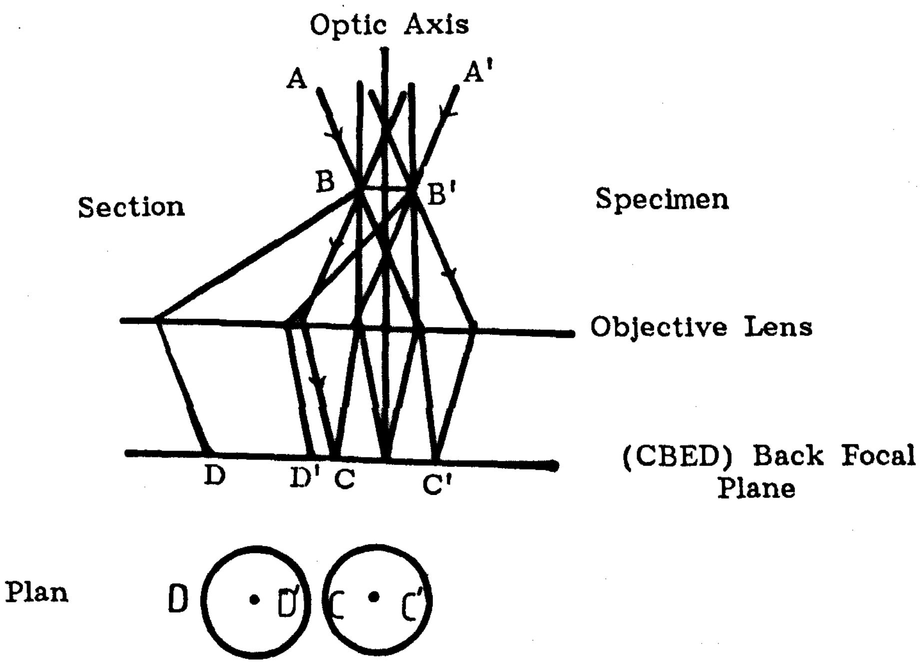

Fig. 3.9. A ray diagram illustrating the formation of the CBED pattern.

Fig. 3.10. The [111] CBED pattern was taken from a germanium single crystal (120Kv). The central disc is 000 type and the next discs around the centre are of the type 220.

lines (HOLZ lines) which arise as a result of elastic interactions between the electron beam and the HOLZ *(Jones et al. 1977)*. *Buxton et al. (1976)* classified the possible symmetry of the CBED patterns into 31 groups called the 31 diffraction groups. These groups consist of the ten two dimensional point groups, 1, 2, m, 2mm, 3, 3mm, 4, 4mm, 6, 6mm, *(Steeds 1979)* and 21 groups arising from the effect of inversion operation through one of the hkl maxima in the CBED pattern and designated by the subscript R, 1_R, 2_R, 21_R, m_R, $m1_R$, $2m_Rm_R$, 2_Rmm_R, $2mm1_R$, 4_R, 41_R, $4m_Rm_R$, 4_Rmm_R, $4mm1_R$, 31_R, $3m_R$, $3m1_R$, 6_R, 61_R, $6m_Rm_R$, 6_Rmm_R and $6mm1_R$. More detail about diffraction groups for single crystals and bicrystals will be given in chapter 4.

Tables 3.1 and 3.2 are reproduced from *Buxton et al. (1976)*. Table 3.1 lists, for each of the 31 diffraction groups, the symmetry of bright field, BF, the whole pattern, WP, dark field, DF, and ±G. The latter refers to the symmetry found when ±g reflections are observed using the displaced aperture method. Depending on the point group of the crystal +g and -g hkl discs may exhibit different internal symmetry. Table 3.2 connects the 31 diffraction groups to the 32 crystallographic point groups. Thus, if the diffraction group of a CBED pattern was found, then reference to Table 3.2 the point group could be determined for the material from which the CBED pattern was taken.

The spacegroup of a single crystal can be determined by observing the presence of what is called "lines of dynamic absence" which occur

Table 3.1 CBD Pattern Symmetries*
(Where a Dash Appears in Column 7, the Special Symmetries Can Be Deduced from Columns 5 and 6 of This Table (or from Table 1 in Buxton et al 1976).)

Diffraction Group	Bright Field	Whole Pattern	Dark Field		±G		Projection Diffraction Group
			General	Special	General	Special	
1	1	1	1	none	1	none	1_R
1_R	2	1	2	none	1	none	
2	2	2	1	none	2	none	21_R
2_R	1	1	1	none	2_R	none	
21_R	2	2	2	none	21_R	none	
m_R	m	1	1	m	1	m_R	$m1_R$
m	m	m	1	m	1	m	
$m1_R$	2mm	m	2	2mm	1	$m1_R$	
$2m_Rm_R$	2mm	2	1	m	2	—	$2mm1_R$
2mm	2mm	2mm	1	m	2	—	
2_Rmm_R	m	m	1	m	2_R	—	
$2mm1_R$	2mm	2mm	2	2mm	21_R	—	
4	4	4	1	none	2	none	41_R
4_R	4	2	1	none	2	none	
41_R	4	4	2	none	21_R	none	
$4m_Rm_R$	4mm	4	1	m	2	—	$4mm1_R$
4mm	4mm	4mm	1	m	2	—	
4_Rmm_R	4mm	2mm	1	m	2	—	
$4mm1_R$	4mm	4mm	2	2mm	21_R	—	
3	3	3	1	none	1	none	31_R
31_R	6	3	2	none	1	none	
$3m_R$	3m	3	1	m	1	m_R	$3m1_R$
3m	3m	3m	1	m	1	m	
$3m1_R$	6mm	3m	2	2mm	1	$m1_R$	
6	6	6	1	none	2	none	61_R
6_R	3	3	1	none	2_R	none	
61_R	6	6	2	none	21_R	none	
$6m_Rm_R$	6mm	6	1	m	2	—	$6mm1_R$
6mm	6mm	6mm	1	m	2	—	
6_Rmm_R	3m	3m	1	m	2_R	—	
$6mm1_R$	6mm	6mm	2	2mm	21_R	—	

Table 3.2
Relation Between the Diffraction Groups and the Crystal Point Groups

Diffraction Groups	Relation between the diffraction groups and the crystal point groups																														
$6mm1_R$																										X					
$3m1_R$																									X						
$6mm$																								X							
$6m_Rm_R$																							X								
61_R																						X									
31_R																					X										
6																				X											
6_Rmm_R																			X												X
$3m$																		X												X	
$3m_R$																	X												X		
6_R																X												X			
3															X												X				
$4mm1_R$														X																	X
4_Rmm_R													X																	X	
$4mm$												X																			
$4m_Rm_R$											X																		X		
41_R										X																					
4_R									X																						
4									X																							
$2mm1_R$								X							X												X		X			X
2_Rmm_R					X			X			X				X					X			X				X		X			X
$2mm$							X																			X						
$2m_Rm_R$						X						X		X										X				X		X		
$m1_R$							X						X	X											X	X					X	
m				X			X						X	X					X			X			X	X					X	
m_R			X			X	X		X	X		X	X	X				X			X			X	X	X		X		X	X	
21_R					X															X												
2_R		X			X			X			X				X		X			X			X				X		X			X
2			X															X														
1_R				X															X													
1	X		X	X		X	X		X	X		X	X	X		X		X	X		X	X		X	X	X		X		X	X	
Point Groups	1	$\bar{1}$	2	m	2/m	222	mm2	mmm	4	$\bar{4}$	4/m	422	4mm	$\bar{4}2m$	4/mmm	3	$\bar{3}$	32	3m	$\bar{3}m$	6	$\bar{6}$	6/m	622	6mm	$\bar{6}m2$	6/mmm	23	m3	432	$\bar{4}3m$	m3m

in the kinematically forbidden reflections *(Gjonnes and Moodie, 1965).* This effect indicates the presence of glide planes or screw axes in the crystal. An example will be considered next to show the usefulness of the above procedure for the determination the point group and the spacegroup for germanium single crystal. Fig.3.11(a), (b), (c), (d), (e) and (f) show six CBED patterns were taken in six different directions from Ge single crystal specimens. These patterns have been examined carefully, and to determine the diffraction group for each pattern their symmetries, WP, BF, DF and ±G, have been determined and tabulated in Table 3.3. Once the diffraction groups have been determined (8^{th} column in Table 3.3) one can make use of Table 3.2 to determine the point group which corresponds to each diffraction group and the results are listed in the last column of Table 3.3. Thus the point group of germanium is $m\bar{3}m$.

In order to determine the spacegroup of germanium it is necessary to identify forbidden reflections which occur due to double diffraction. In CBED patterns some of forbidden reflections reveal dynamic absences which take the form of dark bars or lines within the forbidden reflections. These dynamic absences are clearly seen in [011] and [013] CBED patterns Fig.3.11(b) and (e), respectively, for g = ±200 and this is a proof for the presence of a glide plane in Ge crystal parallel to the plane (100). So, one can assign $Fd\bar{3}m$ for the spacegroup of germanium.

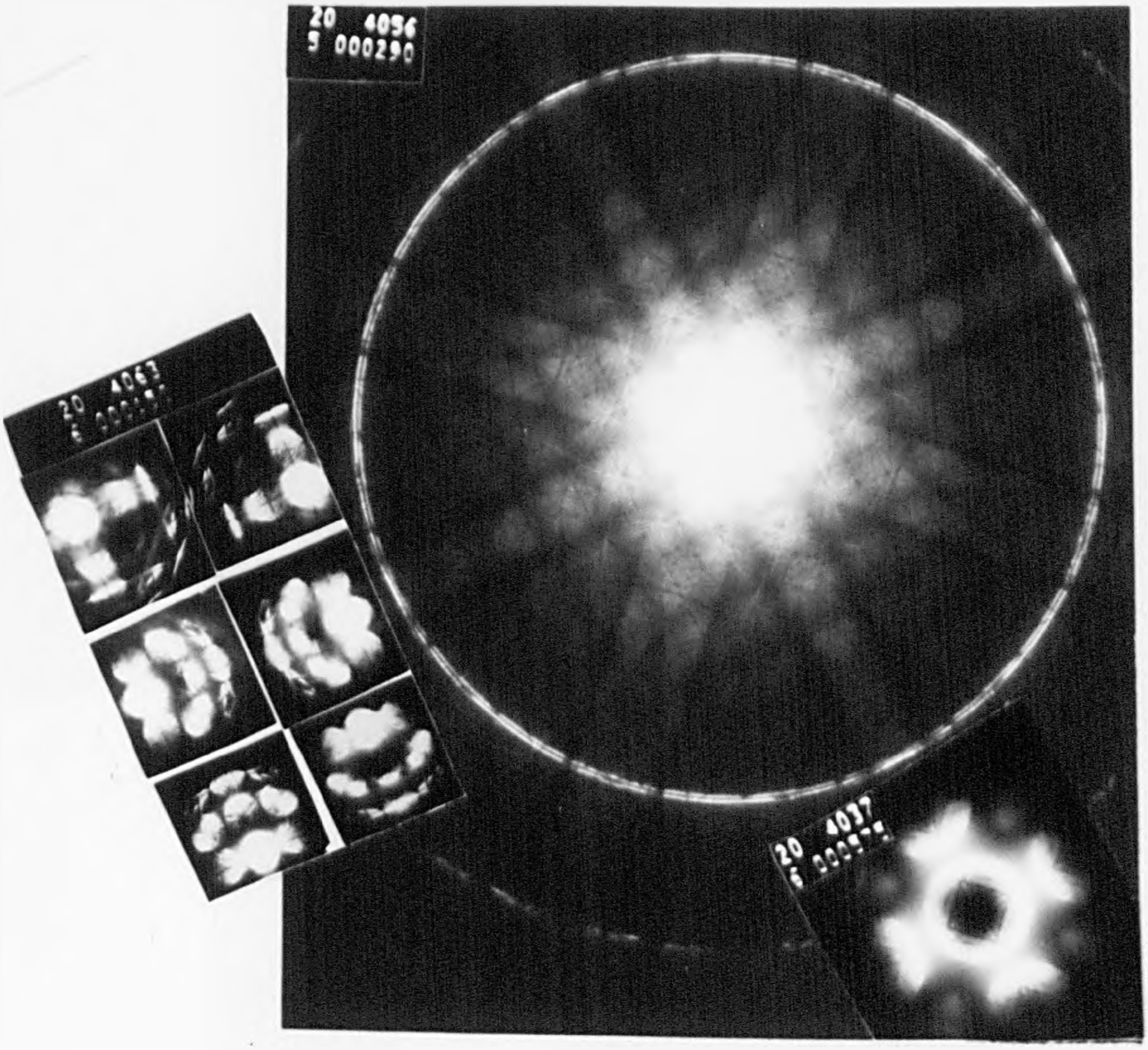

Fig. 3.11. (a) [001] low-, high-camera lengths and ±G CBED patterns.

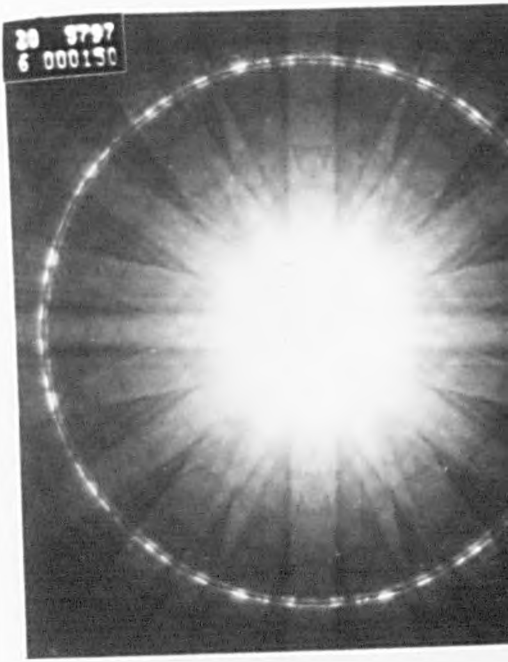

Fig. 3.11. (b) [011] low-

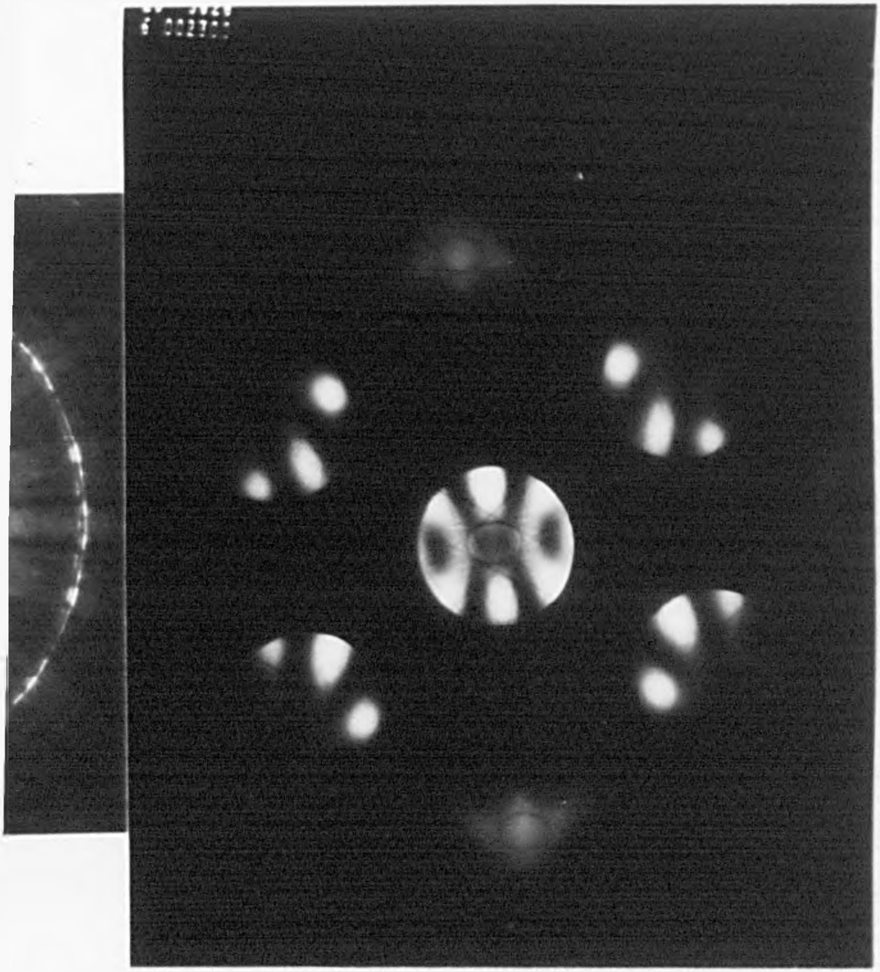

and high-camera lengths CBED patterns.

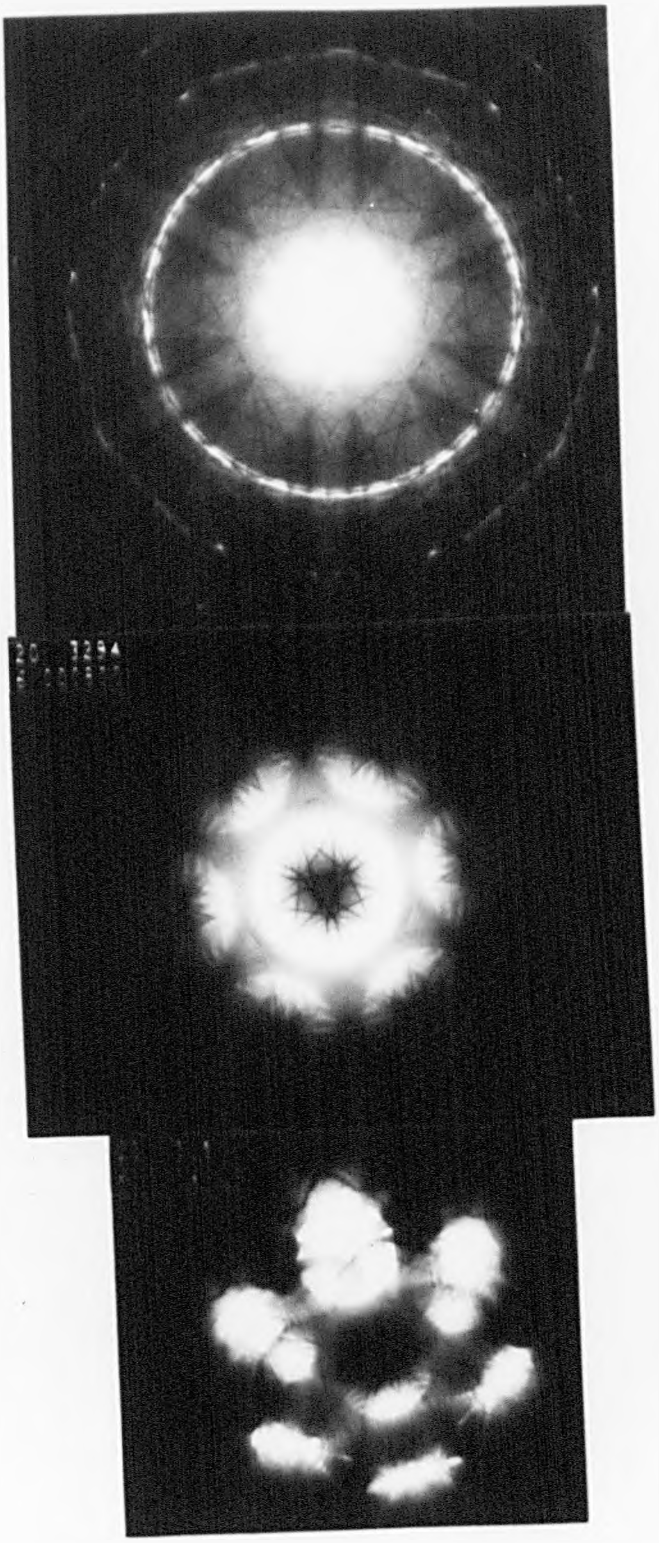

Fig. 3.11. (c) [111] low-, high-camera lengths and ±G CBED patterns.

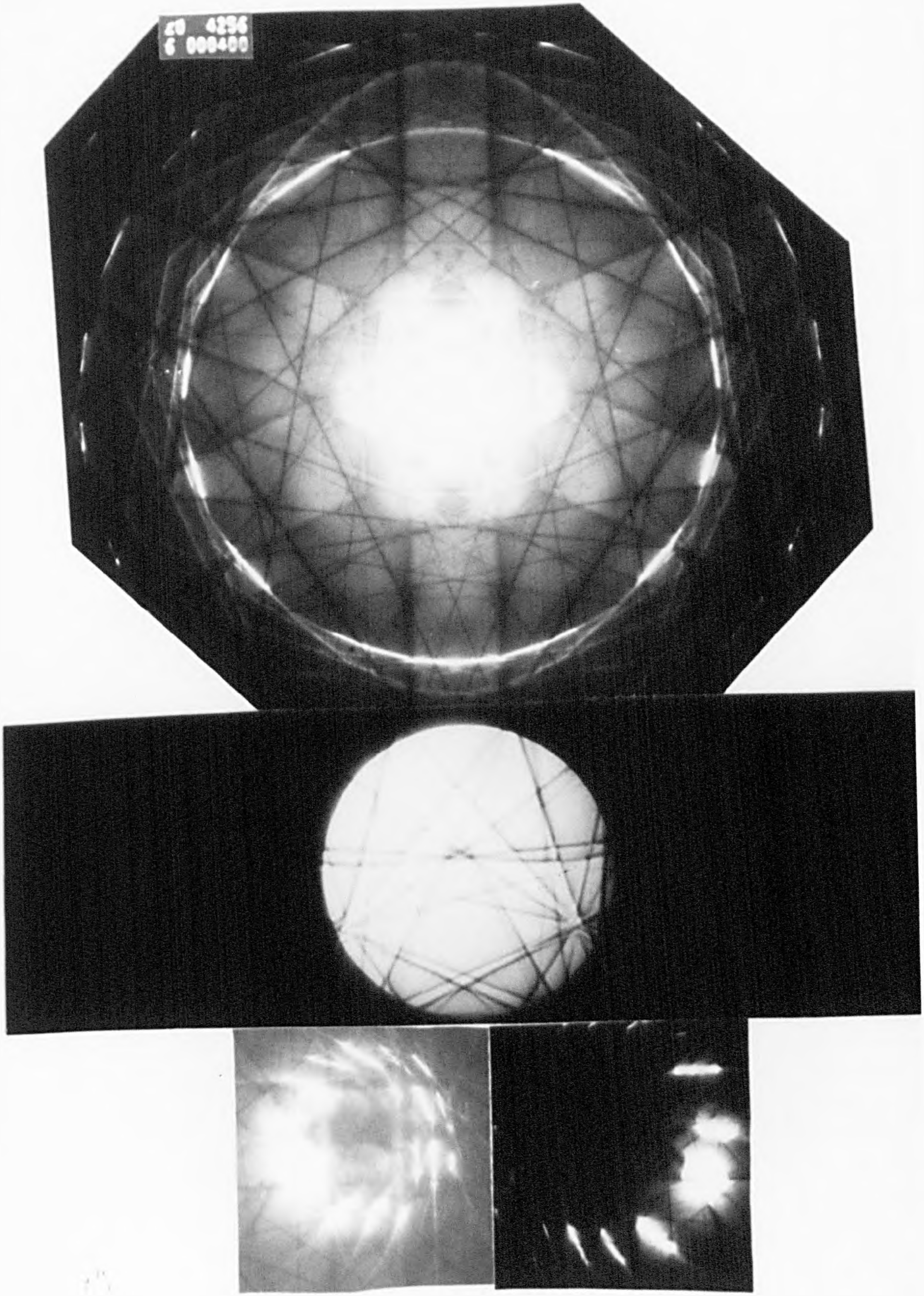

Fig. 3.11. (d) [012] low-, high-camera lengths and ±G CBED patterns.

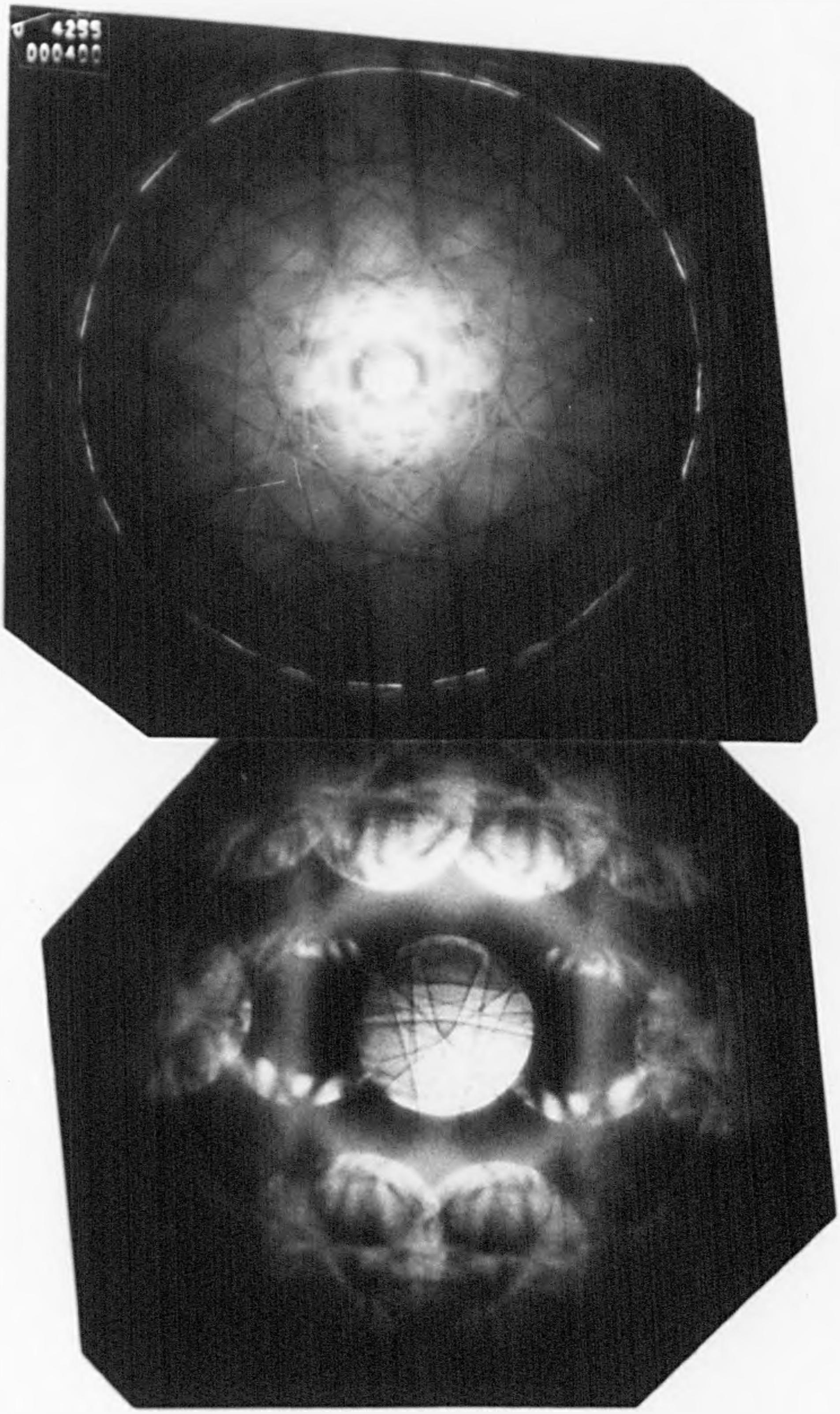

Fig. 3.11. (e) [013] low- and high-camera lengths CBED patterns.

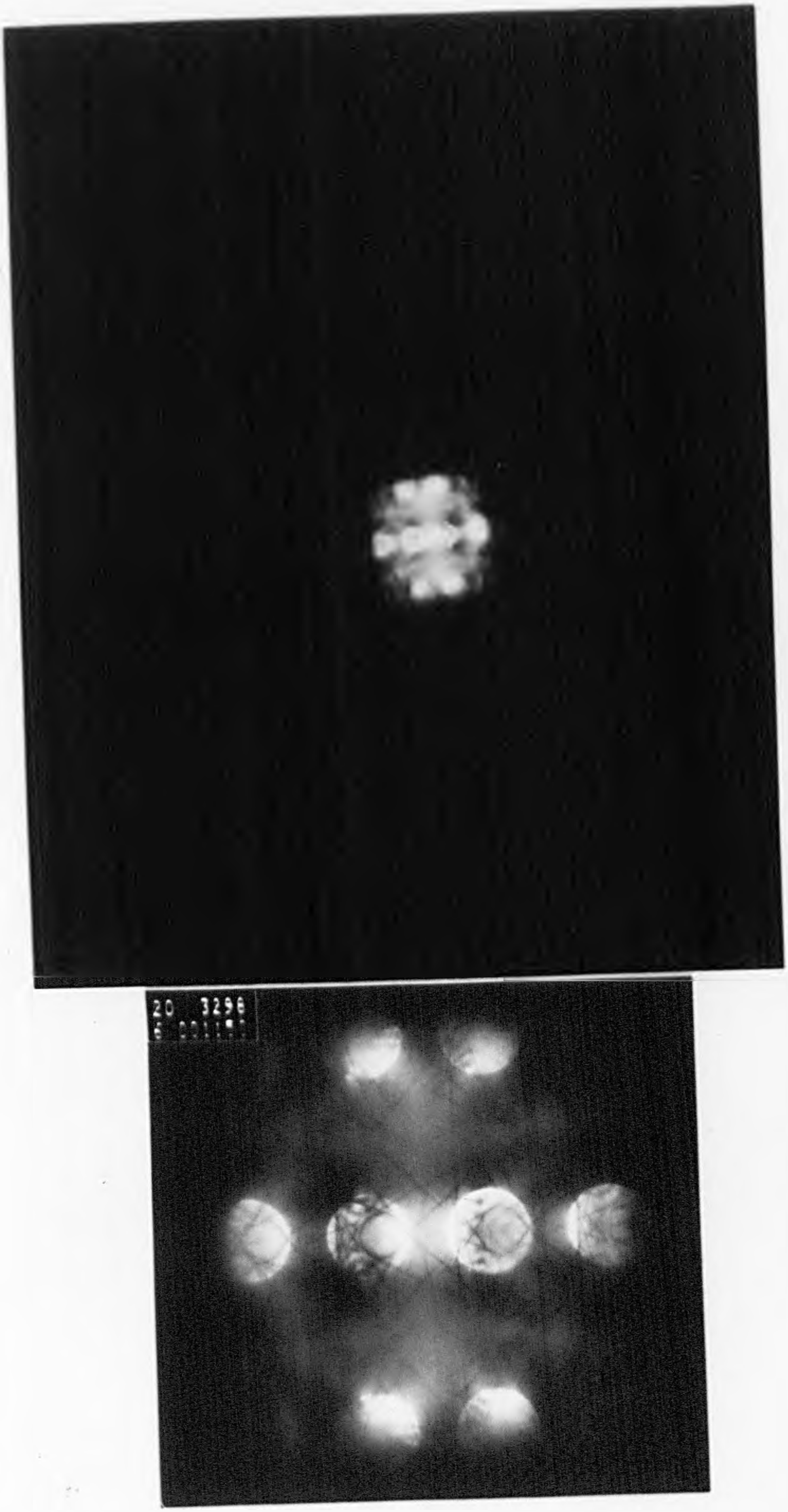

Fig. 3.11. (f) [112] low- and high-camera lengths CBED patterns.

Table 3.3. The symmetry of CBED patterns (Whole pattern, bright field, dark field, and ±G), possible diffraction groups for a germanium single crystal specimen.

No.	Figure	Zone Axis	Whole Pattern	Bright Field	Dark Field		±G		Possible Diffraction Groups	Point Groups
					General	Special	General	Special		
(1)	3.11(a)	[001]	4mm	4mm	2	2mm	—	—	$4mm1_R$	m3m
(2)	3.11(b)	[011]	2mm	2mm	2	2mm	2_R	—	6_Rmm_R	m3m
(3)	3.11(c)	[111]	3m	3m	1	m	—	—	$2mm1_R$	m3m
(4)	3.11(d)	[012]	m	m	1	m	2_R	—	2_Rmm_R	m3m
(5)	3.11(e)	[013]	m	m	1	m	2_R	—	2_Rmm_R	m3m
(6)	3.11(f)	[112]	m	m	1	m	2_R	—	2_Rmm_R	m3m

3.2.3. LARGE ANGLE CONVERGENT BEAM ELECTRON DIFFRACTION (TANAKA).

The diameter of a non-overlapping CBED pattern is limited by the Bragg angle. For large unit cell, i.e. has large lattice parameter, the CBED disc diameters become small, and the intensity distribution available in a small disc does not show clear symmetry so that the information in the disc is reduced severely.

The LACBED (Tanaka) technique is useful in the above case because it consists of large diameter non-overlapping discs. Another advantage of the LACBED technique is that it enables the electron microscopist to obtain patterns from relatively small areas, ~100 nm diameter *(Williams 1984)*. In the case of CBED technique four patterns (whole pattern, bright-field, dark-field, and ±G dark field patterns) are needed to determine a crystal point group, whereas, by using LACBED technique, a single pattern contains the above information simultaneously.

The procedure for obtaining a LACBED pattern for a PHILIPS EM400 is *(Williams 1984)*:

(1) Set up the microscope in the normal CBED mode (see section 3.2.2).

(2) Switch to image mode and focus the electron probe fully on the specimen surface.

(3) Use the specimen height control to increase the specimen height (i.e, move specimen toward electron gun) until the probe is seen split into many probe images, one for each Bragg beam.

(4) Isolate the order of interest by inserting the SAD aperture so that the order required passes through the aperture.

(5) Switch to diffraction pattern mode and remove the condenser aperture completely. A LACBED pattern with no overlap of order will be seen on the viewing screen.

Fig.3.12(a), (b), (c) and (d) show [001], [011], [111] and [112] LACBED patterns were taken from Ge single crystal specimens. Each pattern shows the WP, BF, DF and ±G symmetries, simultaneously, and they are equivalent to those listed before in Table 3.3 and recorded by four different pattern for each zone axis. Thus using the LACBED technique the procedure for determining the point group becomes shorter than using the CBED one.

Fig. 3.12(a). The [001] LACBED pattern was taken from a germanium single crystal (120Kv).

Fig. 3.12(b). The [011] LACBED pattern was taken from a germanium single crystal (120Kv).

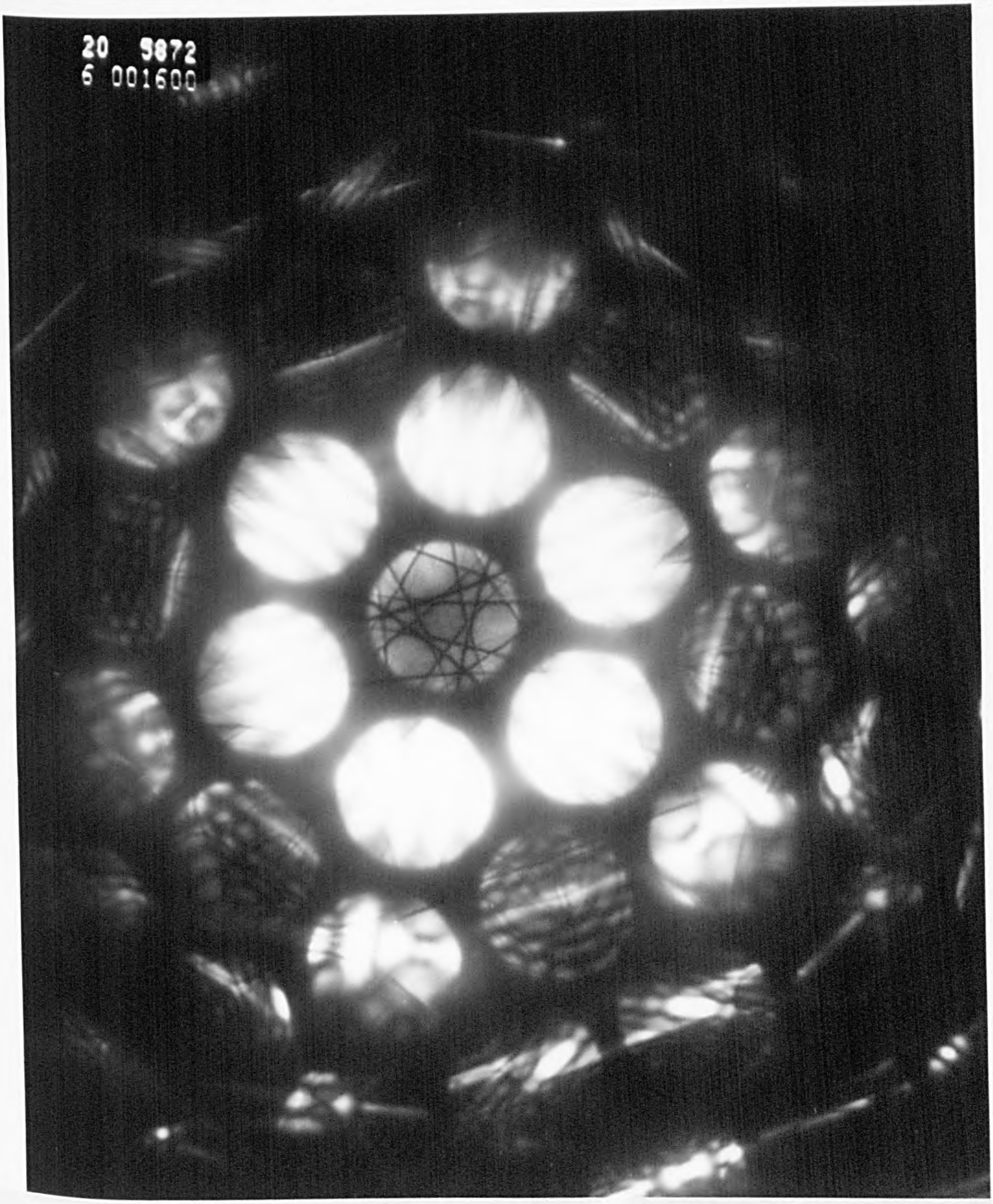

Fig. 3.12(c). The [111] LACBED pattern was taken from a germanium single crystal (120Kv).

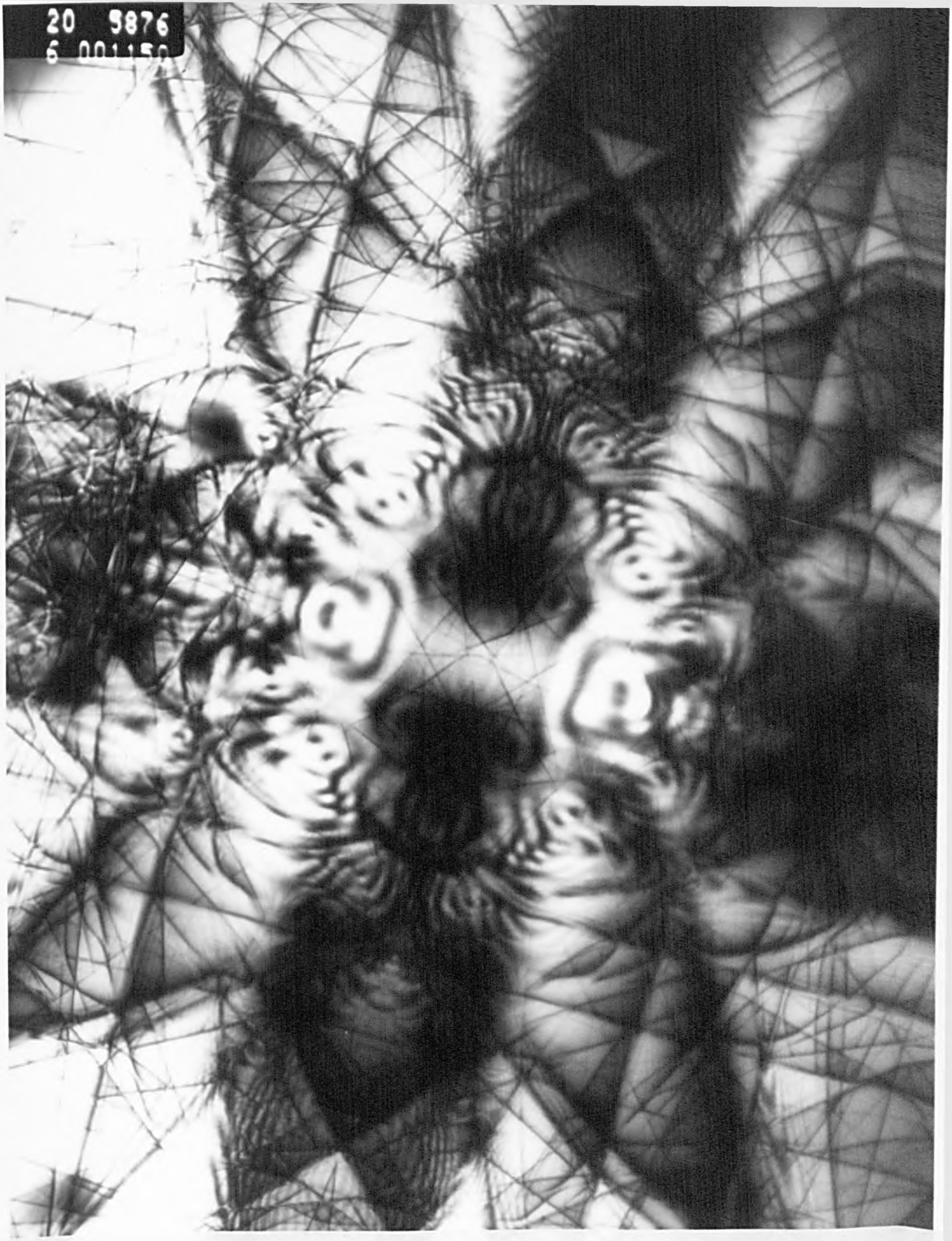

Fig. 3.12(d). The [112] LACBED pattern was taken from a germanium single crystal (120Kv).

CHAPTER FOUR

Diffraction Groups for Single Crystals and Bicrystals

4.1. Introduction..4.2

4.2. Types of symmetry..................................4.2

  4.2.1. The ordinary symmetry elements.............4.3

  4.2.2. The anti-symmetry elements.................4.3

4.3. Diffraction groups for single crystals..............4.3

4.4. The bright field, projection diffraction, and whole pattern groups.............................4.7

  4.4.1. The bright field groups...................4.8

  4.4.2. The projection diffraction groups.........4.10

  4.4.3. The whole pattern groups..................4.11

4.5. Bicrystal diffraction groups........................4.11

  4.5.1. Diffraction groups for "plan-view" bicrystals....................4.12

  4.5.2. Diffraction groups for "edge-on" bicrystals.....................4.14

4.6. Experimental determinations of relative displacement............................4.16

4.1. INTRODUCTION.

As mentioned in chapter 3, *Buxton et al.(1976)* classified the symmetry of CBED patterns taken from single crystal specimens into 31 groups which are called the diffraction groups. They also tabulated the relationship between these groups and the corresponding 32 crystallographic point groups (Table 3.2), hence the point groups of single crystal specimens can be determined. A complete example for the determination of the point and spacegroup of a Ge single crystal is given in the previous chapter.

This chapter is divided into two main parts. In the first part we present an alternative method for obtaining the 31 diffraction groups. We show that the 31 possible symmetries of CBED patterns from ideal plane single crystal parallel foils correspond, precisely, to the 31 permissible rosette groups *(Pond et al. 1983)*.

The second part of this chapter is devoted to the derivation of the "plan-view" and "edge-on" bicrystal diffraction groups by following the procedure adopted in part one, and making use of the 80 layer and 31 band permissible bicrystal groups *(Pond et al. 1983)* , respectively.

4.2. TYPES OF SYMMETRY.

Single crystal specimens, as mentioned before in chapter 2, may exhibit two types of symmetry elements: ordinary and/or antisymmetry. One can define an ordinary symmetry element in the present application as a symmetry element which leaves the normal to the specimen surface invariant, while an antisymmetry element inverts it.

4.2.1. THE ORDINARY SYMMETRY ELEMENTS.

The ordinary symmetry elements are:

(1) Ordinary rotation axis perpendicular to the specimen surface: 1-,2-,3-,4-,and 6-fold axes.

(2) Ordinary mirror perpendicular to the specimen surface: m

4.2.2. THE ANTISYMMETRY ELEMENTS.

The antisymmetry elements are:

(1) antirotation axis parallel to specimen surface: $2'$

(2) antimirror parallel to specimen surface: m'

(3) anti-inversion centre located in specimen: $\bar{1}\,'$

(4) anti-roto-inversion axis perpendicular to specimen surface: $\bar{3}\,'$, $\bar{4}'$, $\bar{6}'$

4.3. DIFFRACTION GROUPS FOR SINGLE CRYSTALS.

We shall determine the types of symmetry (ordinary and/or antisymmetry), and hence the point groups which an ideal parallel plane foil can have, and then, relate them to the diffraction groups:

(1) Let the specimen have the identity element of symmetry, 1. The ray diagram in Fig.4.1(a) depicts, graphically, this element of symmetry. The two horizontal lines represent the upper and lower

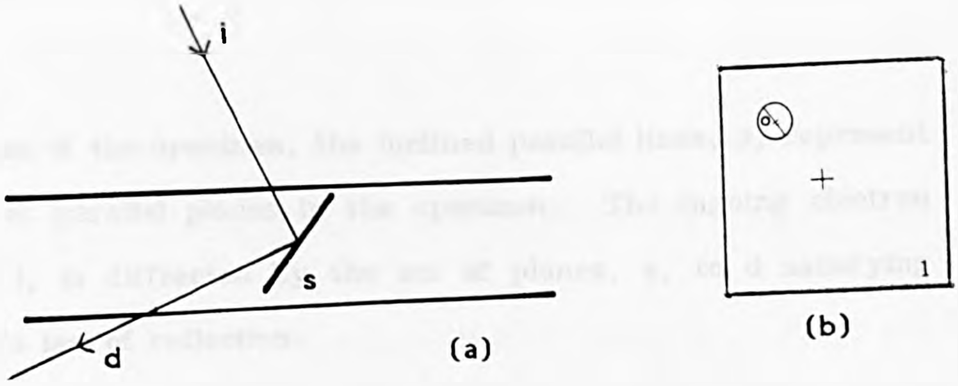

Fig. 4.1. (a) A ray diagram represents a specimen having the identity symmetry element.

(b) A stereographic projection represents the identity symmetry element (reproduced from Buxton et al. 1976).

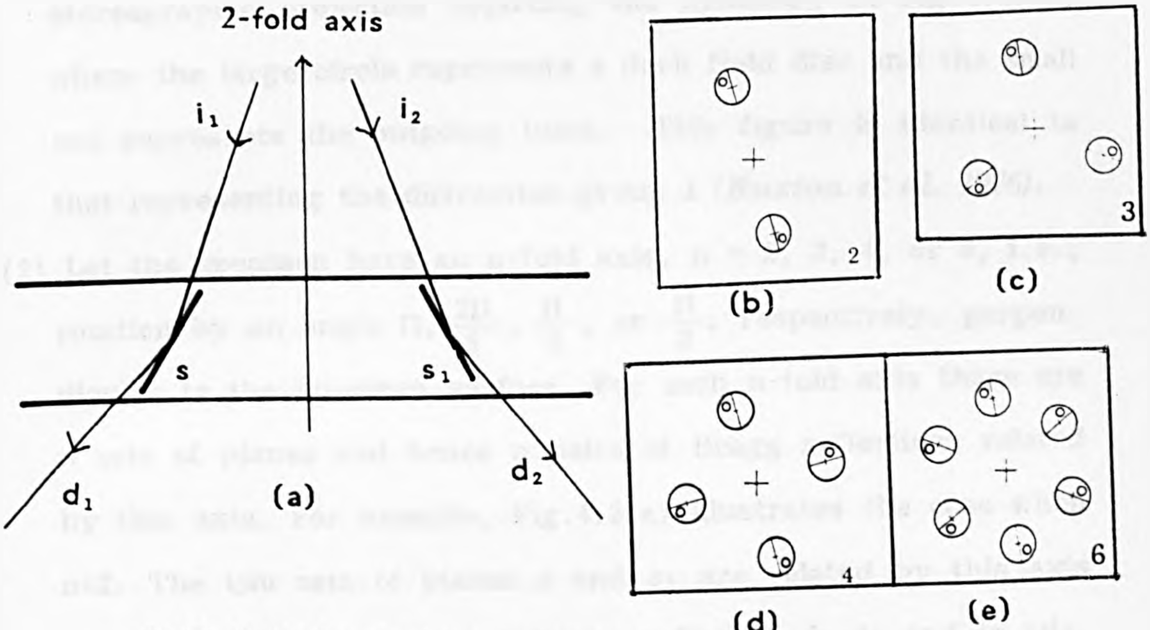

Fig. 4.2. (a) A ray diagram represents a specimen having a diad symmetry element perpendicular to its surface.

(b) A stereographic projection represents a diad symmetry element (reproduced from Buxton et al. 1976).

(c) As (b), but represents a triad symmetry element.

(d) As (b), but represents a tetrad symmetry element.

(e) As (b), but represents a hexad symmetry element.

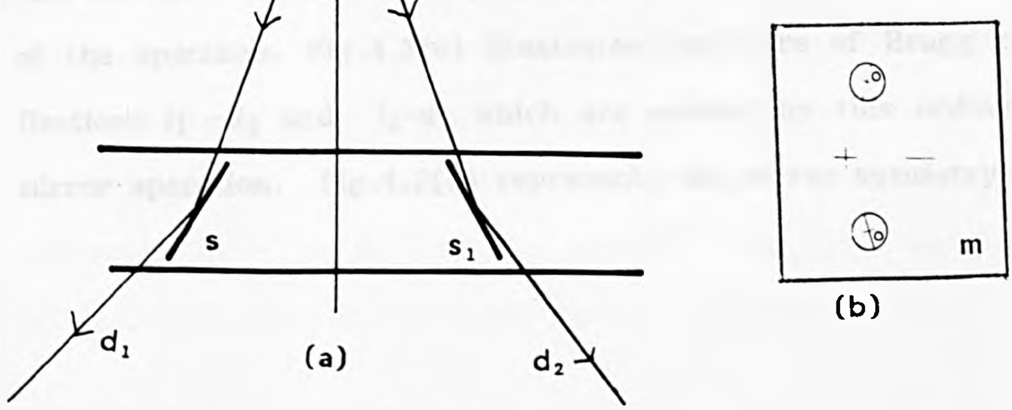

Fig. 4.3. (a) A ray diagram represents a specimen having a mirror symmetry element perpendicular to its surface.

(b) A stereographic projection represents the mirror symmetry element surfaces of the specimen, the inclined parallel lines, s, represent a set of parallel planes in the specimen. The ingoing electron beam, i, is diffracted by the set of planes, s, to d satisfying Bragg's law of reflection.

Alternatively, using the stereographic projection method *(Buxton et al. 1976)* one can represent the element of symmetry possessed by the above specimen. Fig.4.1(b), for example, is a stereographic projection depicting the symmetry in Fig.4.1(a), where the large circle represents a dark field disc and the small one represents the outgoing beam. This figure is identical to that representing the diffraction group 1 *(Buxton et al. 1976)*.

(2) Let the specimen have an n-fold axis, n = 2, 3, 4, or 6, i.e., rotation by an angle $\Pi, \frac{2\Pi}{3}, \frac{\Pi}{2}$, or $\frac{\Pi}{3}$, respectively, perpendicular to the specimen surface. For each n-fold axis there are n sets of planes and hence n pairs of Bragg reflections related by this axis. For example, Fig.4.2(a) illustrates the case when n=2. The two sets of planes s and s_1 are related by this axis as well as the two pairs of Bragg reflection i_1-d_1 and i_2 -d_2. Fig.4.2(b), (c), (d), and (e), show the symmetries of the n= 2-, 3-, 4-, and 6-fold axes, using the stereographic projection method, and they are similar to the figures representing the diffraction groups 2, 3, 4, and 6, respectively.

(3) Let the specimen have a mirror, m, perpendicular to the surface of the specimen. Fig.4.3(a) illustrates the pairs of Bragg reflections i_1 -d_1 and i_2-d_2 which are related by this ordinary mirror operation. Fig.4.3(b) represents the mirror symmetry of

Fig.4.3(a), using the stereographic projection method, and it can be seen that this represents the diffraction group m *(Buxton et al. 1976).*

(4) Let the specimen have an anti-inversion centre, $\bar{1}'$. Here, and in the following cases(5-7), the reciprocity theorem *(Howie 1978)* has been invoked. It states that the wave amplitude at a point, say a, originating from a point spherical source located at a point, say b, is equal to the amplitude at b when the source is placed at a.

Fig.4.4(a) is ray diagram representing the symmetry $\bar{1}'$. The ingoing beam, i_1, is incident on the upper surface of the specimen and is diffracted by the set of planes s to d_1. Similarly, and due to the presence of the symmetry element, $\bar{1}'$, an ingoing beam i_2, would be diffracted by the set of planes s_1 to d_2. Because of the reciprocity theorem, the diffracted beam d_2 can be regarded as the incident beam i_3 and the incident beam i_2 as the diffracted beam d_3. The diffracted beams d_1 and d_2 must have equal amplitudes to preserve the symmetry element, $\bar{1}'$. The stereographic projection of Fig.4.4(a) is shown in Fig.4.4(b). The latter is identical to that which represents the diffraction group 2_R, i.e. the symmetry element $\bar{1}'$ corresponds to the diffraction group 2_R. Note that the subscript R stands for the fact that we have invoked the reciprocity theorem.

(5) Let the specimen have an anti-diad axis parallel to its surface, $2'$, Fig.4.5(a). The two sets of planes s_1 and s_2 are related by this element of antisymmetry. The incident beam, i_1 , is diffracted by s to d_1 and the incident beam i_2 , would be diffracted by s_1 to d_2. By applying the reciprocity theorem,

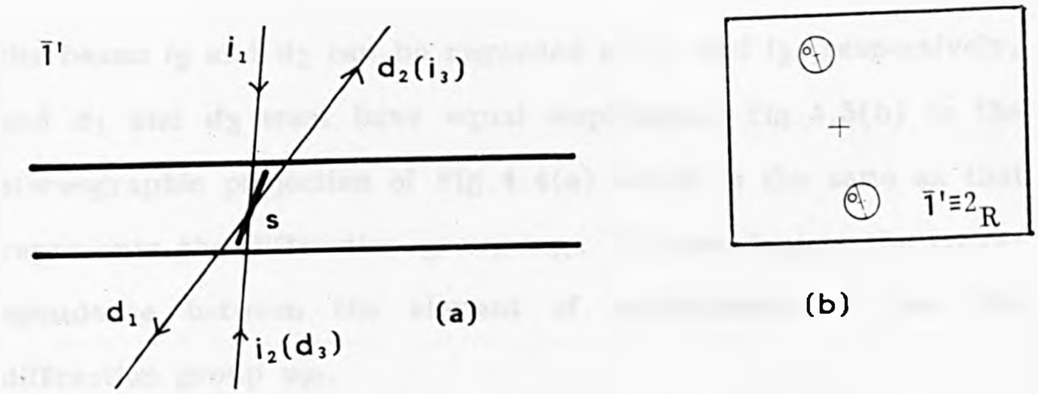

Fig. 4.4. (a) A ray diagram represents a specimen having an anti-inversion centre.

(b) A stereographic projection represents the symmetry element in (a) (reproduced from Buxton et al. 1976).

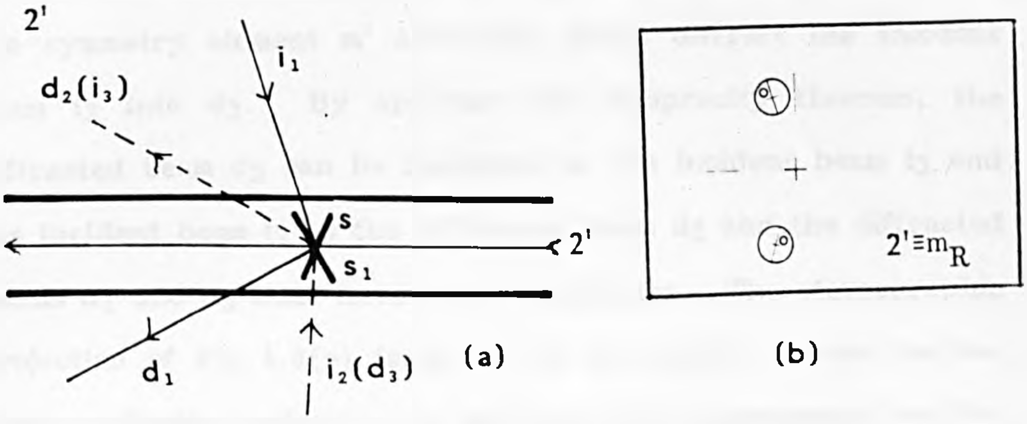

Fig 4.5. (a) A ray diagram represents a specimen having an anti-diad parallel to its surface.

(b) A stereographic projection represents the symmetry element in (a)

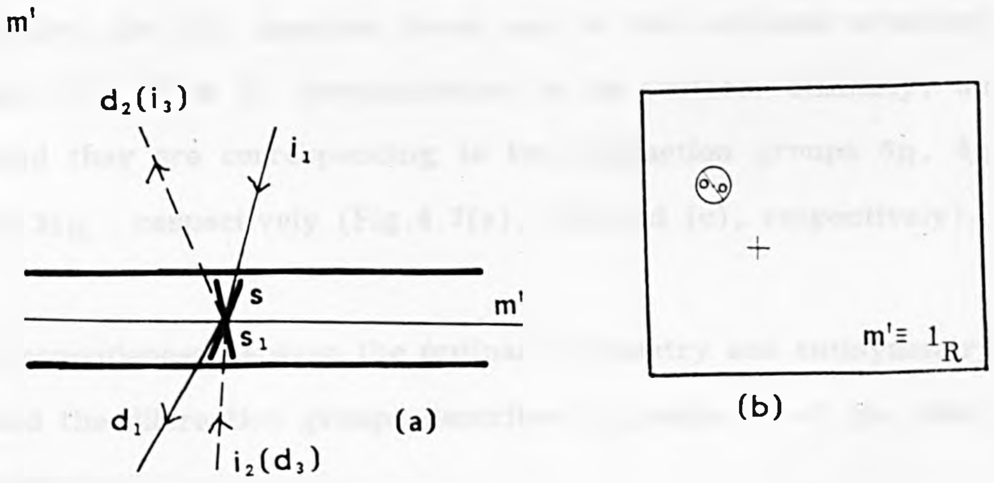

Fig 4.6. (a) A ray diagram represents a specimen having an anti-mirror parallel to its surface.

(b) A stereographic projection represents the symmetry element in (a) (reproduced from Buxton et al. 1976).

the beams i_2 and d_2 can be regarded as d_3 and i_3, respectively, and d_1 and d_3 must have equal amplitudes. Fig.4.5(b) is the stereographic projection of Fig.4.4(a) which is the same as that represents the diffraction group m_R. It also depicts the correspondence between the element of antisymmetry 2' and the diffraction group m_R.

(6) Let the specimen have an anti-mirror parallel to its surface, m', Fig.4.6(a). The incident beam i_1 is diffracted by the set of planes s to d_1 The set of planes s_1 is related to the set of planes s by the symmetry element m' and they would diffract the incident beam i_2 into d_2. By applying the reciprocity theorem, the diffracted beam d_2 can be regarded as the incident beam i_3 and the incident beam i_2 as the diffracted beam d_3 and the diffracted beams d_1 and d_3 must have equal amplitudes. The stereographic projection of Fig.4.6(a) is shown in Fig.4.6(b), where the two bragg reflection pairs i_1 -d_1 and i_3-d_3 are represented by two discs in complete coincidence because of the presence of the anti-mirror symmetry element, which has symmetry similar to that of the diffraction group 1_R, i.e. there is correspondence between m' and 1_R.

(7) Finally, let the specimen have one of the anti-roto-inversion axes, $\bar{3}$ ', $\bar{4}$' or $\bar{6}$', perpendicular to its surface. Similarly, we found they are corresponding to the diffraction groups 6_R, 4_R and 31_R , respectively (Fig.4.7(a), (b) and (c), respectively).

The correspondences between the ordinary symmetry and antisymmetry elements and the diffraction groups described in points 1 to 7 are tabulated in Table 4.1.

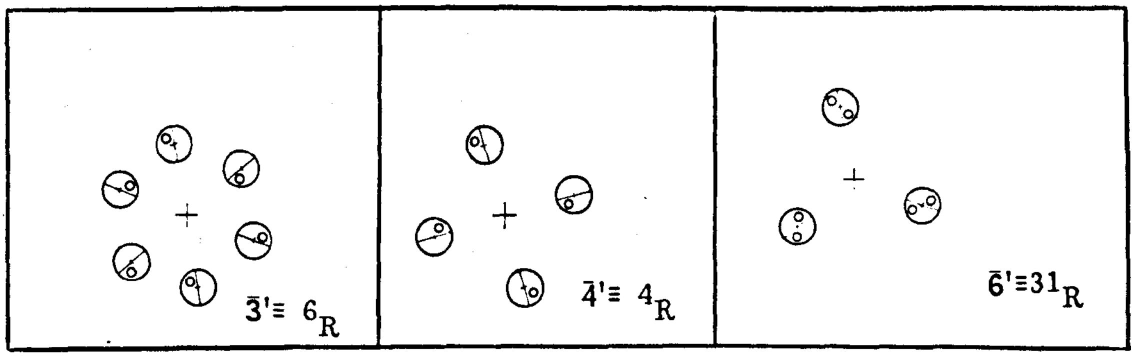

(a) **(b)** **(c)**

Fig. 4.7. A stereographic projection represents the symmetry elements: (a) $\bar{3}'$, (b) $\bar{4}'$ and (c) $\bar{6}'$.

Table 4.1. The correspondence between crystal symmetry elements (ordinary and antisymmetry) and diffraction groups.

	Crystal symmetry elements		Diffraction groups
No.	Ordinary	Antisymmetry	
(1)	1		1
(2)	2		2
(3)	3		3
(4)	4		4
(5)	6		6
(6)	m		m
(7)		$2'$	m_R
(8)		m'	1_R
(9)		$\bar{1}'$	2_R
(10)		$\bar{3}'$	6_R
(11)		$\bar{4}'$	4_R
(12)		$\bar{6}'$	31_R

The final step is the direct conversion of the 31 permissible rosette groups into their corresponding diffraction groups, using Table 4.1. Table 4.2 shows the correspondences between the 31 diffraction groups and their counterpart permissible rosette groups.

We believe that the method which we have used and illustrated in points 1 to 7, for the determination of the symmetry and hence the point groups of single crystal, is simpler than that used by ***Buxton et al. (1976).***

4.4. THE BRIGHT FIELD, PROJECTION DIFFRACTION, AND WHOLE PATTERN GROUPS.

It is well known now that a CBED pattern is composed of three inter-related patterns, i.e. the bright field, projection diffraction, and whole patterns *(Steeds 1979)*. The bright field pattern consists of the transmitted or direct beam disc, while the projection diffraction pattern comprises the direct and diffracted beam discs which form what is called the zero order laue zone (zolz). The whole pattern includes, beside the zolz reflection discs, the higher order laue zone (holz) discs. Consequently, the symmetry of a CBED pattern may be specified precisely by knowing the individual symmetry of its bright field, projection diffraction, and whole patterns. The possible symmetries of bright field, projection diffraction, and whole patterns belong to one of the set of ten of bright field, G_b , projection diffraction, G_p , and whole pattern, G_w , point groups, respectively, which were tabulated previously in Table 3.1 in chapter three. The importance of G_b , G_p and G_w point groups is, clearly, because of their role in the determination of the point group of a specimen.

Table 4.2. The correspondence between the 31 diffraction groups and the permissible rosette groups.

No.	Permissible rosette groups		Diffraction groups
	ordinary	Antisymmetry	
(1)	1		1
(2)		11m'	1_R
(3)	112		2
(4)		$\bar{1}'$	2_R
(5)		112/m'	21_R
(6)		2'11	m_R
(7)	m11		m
(8)		m2'm'	$m1_R$
(9)		2'2'2	$2m_Rm_R$
(10)	mm2		2mm
(11)		2'/m11	2_Rmm_R
(12)		mmm'	$2mm1_R$
(13)	4		4
(14)		$\bar{4}'$	4_R
(15)		4/m'	41_R
(16)		42'2'	$4m_Rm_R$
(17)	4mm		4mm
(18)		$\bar{4}'2'm$	4_Rmm_R
(19)		4/m'mm	$4mm1_R$
(20)	3		3
(21)		$\bar{6}'$	31_R
(22)		32'	$3m_R$
(23)	3m		3m
(24)		$\bar{6}'m2'$	$3m1_R$
(25)	6		6
(26)		$\bar{3}'$	6_R
(27)		6/m'	61_R
(28)		62'2'	$6m_Rm_R$
(29)	6mm		6mm
(30)		$\bar{3}'m$	6_Rmm_R
(31)		6/m'mm	$6mm1_R$

In the previous section we found there was a one to one correspondence between the 31 rosette groups, which describe the specimen symmetry, and the 31 diffraction groups. The 10 ordinary rosette groups (second column of Table 4.2) directly correspond to the 10 ordinary diffraction groups (last column of Table 4.2) while the 21 antisymmetry rosette groups correspond to the 21 diffraction groups (last column of Table 4.2) which we marked by a subscript R, indicating application of the reciprocity theorem.

The object of this section is to find a relation which may relate the specimen symmetry groups (the rosette groups) to the CBED pattern groups (G_b, G_p, G_w), considering the one to one correspondence between the rosette groups, G_r and the diffraction groups, G_d, which have already been emphasised previously (Table 4.2).

4.4.1. THE BRIGHT FIELD GROUPS.

The BF groups (see Table 3.1) envisage the possible symmetry of the transmitted beam, which form the internal disc of a CBED pattern. First, we consider the effect on the bright field disc of ordinary elements of symmetry in the specimen. If a specimen possesses one of the following ordinary symmetry 1, 2, 3, 4, 6 and m or a combination of them, e.g. 2mm, 4mm, 3m, or 6mm, then the resulting BF pattern will have symmetry similar to that possessed by the specimen itself as illustrated, stereographically, by patterns 1 to 10, respectively, in Fig.4.8. The dot and circle represent the incident and the transmitted beams, respectively and the cross represents the centre of the pattern.

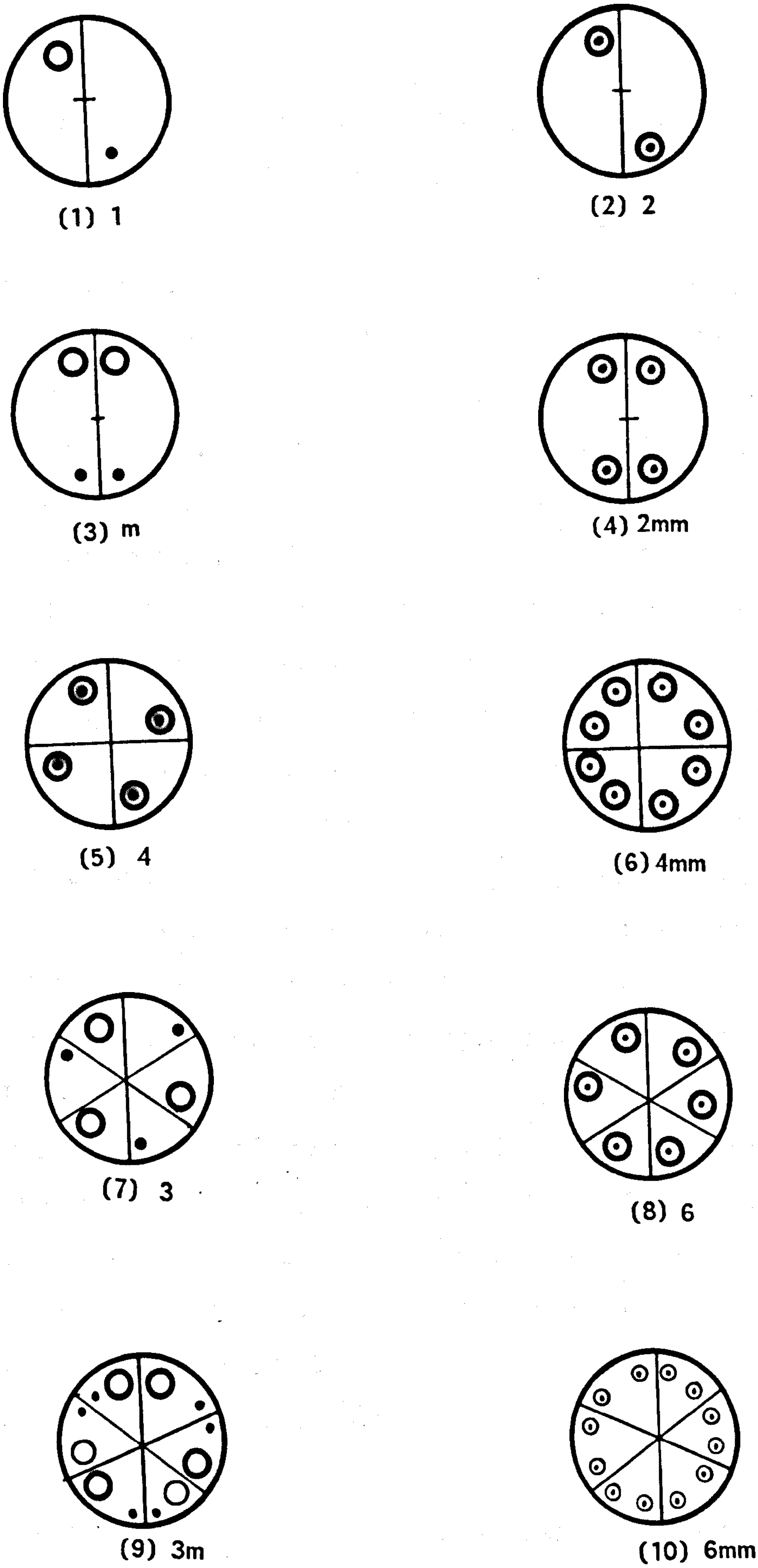

(1) 1

(2) 2

(3) m

(4) 2mm

(5) 4

(6) 4mm

(7) 3

(8) 6

(9) 3m

(10) 6mm

Fig. 4.8. The stereographic projections represent the ten 2-dimensional bright field point groups.

The symmetry assigned at the bottom of each pattern representing the symmetry of the transmitted beams only.

Secondly, we consider a specimen possessing antisymmetry. Fig.4.9(a) is a ray diagram for a specimen exhibiting an antidiad, 2'. In this case, the incident beam, i_1, is transmitted through the specimen to t_1 . Due to the presence of 2', the symmetry related incident beam, i_2, would be transmitted through the specimen to t_2 . Alternatively, and invoking the reciprocity theorem, the beams i_2 and t_2 can be regarded as i_2^R and t_2^R, respectively. The superscript R means that the reciprocity theorem has been invoked. The stereographic projection connected to Fig.4.9(a) is shown in Fig.4.9(b) and it is seen to exhibit mirror symmetry, where we have considered only the symmetry of the transmitted beams. In other words, if the specimen possesses an antidiad the resulting BF pattern will exhibit ordinary mirror symmetry. If the specimen possesses an antimirror, Fig.4.10(a), then the resulting BF pattern, Fig.4.10(b), will exhibit a diad symmetry, and if the specimen possesses an anticentre, $\bar{1}$ ', as illustrated in Fig.4.11(a), the resulting BF pattern, Fig.4.11(b), will exhibit a diad element of symmetry. Similarly, if a specimen possesses one of the following antisymmetry elements $\bar{3}$ ', $\bar{4}$' and $\bar{6}$', the resulting BF pattern will exhibit the ordinary symmetry 3, 4 or 6 respectively. One can conclude that the BF patterns (Table 4.3) possess only ordinary symmetry whether the specimen exhibits ordinary symmetry or antisymmetry, and this conclusion agrees with the symmetry of the BF patterns given in Table 3.1.

The above conclusion can be expressed mathematically as follows:

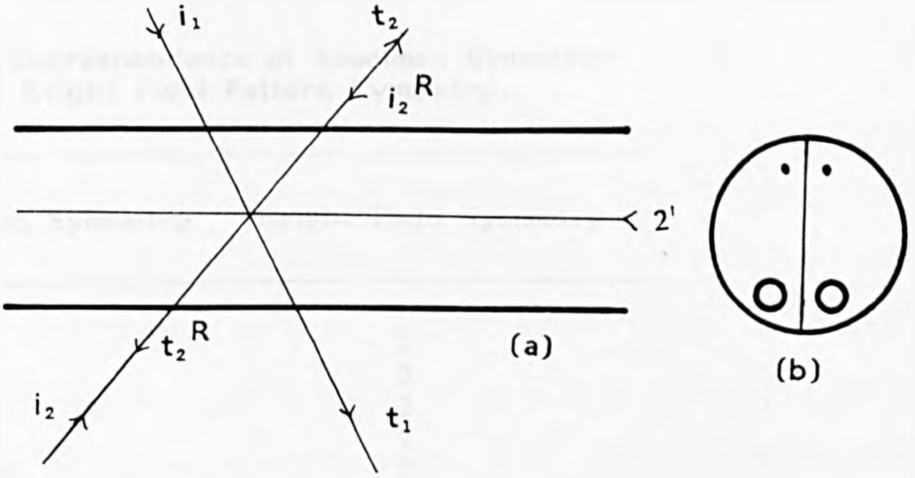

Fig. 4.9. (a) A ray diagram for a specimen exhibiting $2'$.
(b) A stereographic projection for $2'$ in (a).

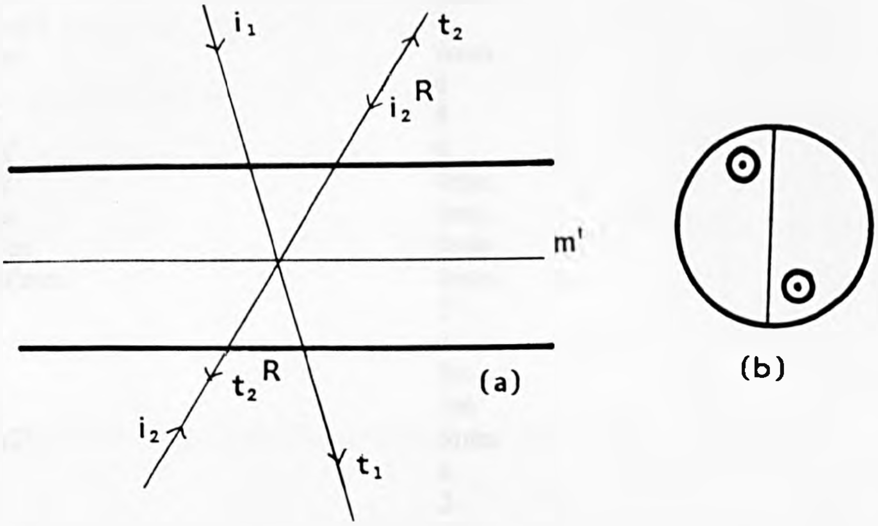

Fig. 4.10. (a) A ray diagram for a specimen exhibiting m'.
(b) A stereographic projection for m' in (a).

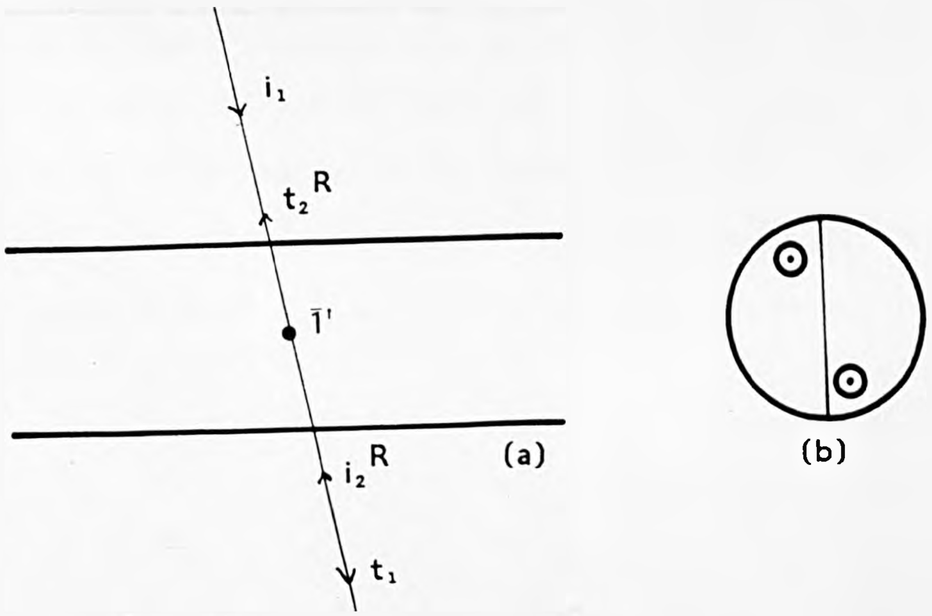

Fig. 4.11. (a) A ray diagram for a specimen exhibiting $\bar{1}'$.
(b) A stereographic projection for $\bar{1}'$ in (a).

Table 4.3. The Correspondence of Specimen Symmetry and Bright Field Pattern Symmetry.

No.	Specimen Symmetry	Bright Field Symmetry
(1)	1	1
(2)	11m'	2
(3)	112	2
(4)	$\bar{1}'$	2
(5)	112/m'	2
(6)	2'11	m
(7)	m11	m
(8)	m2'm'	2mm
(9)	2'2'2	2mm
(10)	mm2	2mm
(11)	2'/m11	2
(12)	mmm'	2mm
(13)	4	4
(14)	$\bar{4}'$	4
(15)	4/m'	4
(16)	42'2'	4mm
(17)	4mm	4mm
(18)	$\bar{4}'$2'm	4mm
(19)	4/m'mm	4mm
(20)	3	3
(21)	$\bar{6}'$	6
(22)	32'	3m
(23)	3m	3m
(24)	$\bar{6}'$m2'	6mm
(25)	6	6
(26)	$\bar{3}'$	3
(27)	6/m'	6
(28)	62'2'	6mm
(29)	6mm	6mm
(30)	$\bar{3}'$m	3m
(31)	6/m'mm	6mm

$$G_b = G_r^o \bigcup G_r^a \, . \, \bar{1}' \qquad (4.1)$$

where the rosette group G_r has been decomposed into two sets, one containing only the ordinary elements of symmetry, G_r^o, and the other containing the antisymmetry elements, G_r^a, (i.e. $G_r = G_r^o \bigcup G_r^a$). For example, consider the rosette group $G_r = 2'2'2 = \{ 1, 2, 2', 2' \}$, (No. 9 in Table 4.3), which can be expressed as the union of the sets of ordinary and antisymmetry elements $G_r = (1, 2) \bigcup (2', 2')$. Using Eq.(4.1) we obtain

$$\begin{aligned} G_b &= (1, 2) \bigcup (2', 2') \, . \, \bar{1}' \\ &= (1,2) \bigcup (m, m) \\ &= \{ 1, 2, m, m \} = 2mm. \end{aligned}$$

Thus the rosette group, $G_r = 2'2'2$ leads to the bright field group $G_b = 2mm$

4.4.2. THE PROJECTION DIFFRACTION GROUPS.

It has been shown that *(Buxton et al. 1976)* when the projection approximation is valid, the specimen behaves as though it has only two dimensional periodicity, and therefore, it exhibits an antimirror parallel to its surface. Also, the projection diffraction groups describe the symmetry present in the zolz of the CBED patterns. The consequence of the above two statements is that the projection diffraction groups can be expressed as the extension of the 31 diffraction groups by an antisymmetry group of index 2, i.e. $G' = \{ 1, m' \}$, which contains the identity and an antimirror parallel to the specimen surface. Table 4.4 shows that the extension of the 31 rosette groups (second column), by $G' = \{1, m'\}$ leads to the 10 groups shown in the last column. These 10 groups are identical to the 10 projection diffraction groups, G_p , of Table 3.1. This extension of G_r by G' is formulated mathematically by the following expression:

$$G_p = G_r \circ G', \qquad G' = \{1, m'\} \qquad (4.2)$$

4.4.3. THE WHOLE PATTERN GROUPS.

The whole pattern symmetry is the two dimensional point group symmetry of the CBED discs, including the symmetry of the zero and higher order laue zone discs. The whole pattern group, G_w , may be expressed mathematically as the intersection between G_r^o and G_b as follows:

$$G_w = G_r^o \cap G_b \qquad (4.3)$$

For example, the intersection of the rosette group and the bright field group listed in the first row of Table 4.5 results in the whole pattern point group listed in the same row and so on for the rest of the groups in the next rows. The whole pattern groups, G_w , which are listed in the last column of Table 4.5, are identical to these listed in Table 3.1 (third column).

4.5. DIFFRACTION GROUPS FOR BICRYSTALS.

Pond et al. (1983) indicated how all the possible bicrystal spatial groups, e.g., permissible bicrystal band and layer groups, can be

Table 4.4. Crystal Symmetry and the Projection Diffraction Groups.

No.	Rosette	Projection Diffraction Group
(1)	1	1_R
(2)	11m'	1_R
(3)	112	2_R
(4)	$\bar{1}'$	2_R
(5)	112/m'	2_R
(6)	2'11	2_R
(7)	m11	$m1_R$
(8)	m2'm'	$m1_R$
(9)	2'2'2	$2mm1_R$
(10)	mm2	$2mm1_R$
(11)	2'/m11	$2mm1_R$
(12)	mmm'	$2mm1_R$
(13)	4	41_R
(14)	$\bar{4}'$	41_R
(15)	4/m'	41_R
(16)	42'2'	$4mm1_R$
(17)	4mm	$4mm1_R$
(18)	$\bar{4}'2'm$	$4mm1_R$
(19)	4/m'mm	$4mm1_R$
(20)	3	31_R
(21)	$\bar{6}'$	31_R
(22)	32'	$3m1_R$
(23)	3m	$3m1_R$
(24)	$\bar{6}'m2'$	$3m1_R$
(25)	6	61_R
(26)	$\bar{3}'$	61_R
(27)	6/m'	61_R
(28)	62'2'	$6mm1_R$
(29)	6mm	$6mm1_R$
(30)	$\bar{3}'m$	$6mm1_R$
(31)	6/m'mm	$6mm1_R$

Table 4.5. Specimen Symmetry and the Whole Pattern Groups.

No.	Specimen Symmetry	Whole Pattern Symmetry
(1)	1	1
(2)	11m'	1
(3)	112	2
(4)	$\bar{1}'$	1
(5)	112/m'	2
(6)	2'11	1
(7)	m11	m
(8)	m2'm'	m
(9)	2'2'2	2
(10)	mm2	2mm
(11)	2'/m11	m
(12)	mmm'	2mm
(13)	4	4
(14)	$\bar{4}'$	2
(15)	4/m'	4
(16)	42'2'	4
(17)	4mm	4mm
(18)	$\bar{4}'2'm$	2mm
(19)	4/m'mm	4mm
(20)	3	3
(21)	$\bar{6}'$	3
(22)	32'	3
(23)	3m	3m
(24)	$\bar{6}'m2'$	3m
(25)	6	6
(26)	$\bar{3}'$	3
(27)	6/m'	6
(28)	62'2'	6
(29)	6mm	6mm
(30)	$\bar{3}'m$	3m
(31)	6/m'mm	6mm

established from first principles. They expressed the spatial bicrystal groups as extensions of the translation groups by means of ordinary and antisymmetry groups containing operations which leave the bicrystal invariant. In the case of bicrystal band groups the translation symmetry group is one dimensional and designated p. The ordinary and antisymmetry element sets which leave the translation symmetry p and the boundary plane invariant are (1, 2, m, a) and ($\bar{1}'$, 2', m', $2_1'$, a'), respectively. For the case of bicrystal layer groups, the translation group corresponds to one of the five 2-dimensional lattices and is designated p or c. The permissible ordinary and antisymmetry element sets are (1, 2, 3, 4, 6, m, a, b) and ($\bar{1}'$, 2', m', a', b', n'), respectively. They, also reported that a bicrystal band can have one of 31 band groups while a bicrystal layer can have one of 80 permissible bicrystal layer groups.

4.5.1. DIFFRACTION GROUPS FOR "PLAN-VIEW" BICRYSTALS.

The "plan-view" bicrystal has the interface parallel to its surface (see chapter 3). It can have 2-dimensional translation symmetry, or less, parallel to the boundary plane. It is pointed out in chapter 3 that the presence of non-symmorphic symmetry elements can be detected experimentally using CBED patterns: firstly, by means of equations 3.5(a) to (d) one can determine the kinematically forbidden reflections. Secondly, the dynamic absences, which have the form of dark bars or lines within the forbidden reflection disks, indicate the presence of these elements *(Gjonnes and Moodie 1965).*

The possible ordinary elements of point symmetry exhibited by a "plan-view" bicrystal:

(1) the identity, 1,

(2) a diad, a triad, a tetrad, and a hexad perpendicular to the specimen surface, 2, 3, 4, and 6,

(3) a mirror perpendicular to specimen surface, m.

The possible antisymmetry elements:

(1) an anti-inversion centre of symmetry in the boundary plane, $\bar{1}'$,

(2) an anti-diad parallel to the boundary plane, $2'$,

(3) an anti-roto-inversion triad, tetrad, and hexad perpendicular to the boundary plane, $\bar{3}'$, $\bar{4}'$ and $\bar{6}'$,

(4) an anti-mirror parallel to the boundary plane, m'.

It is illustrated in Fig.4.12, using the stereographic projection method, that "plan-view" bicrystal specimens can exhibit one of the 31 point groups. These 31 point groups are found to be equivalent to the 31 symmorphic layer point groups *(Pond et al. 1983)*. Hence the possible symmetry of the "plan-view" bicrystal specimens can be described precisely by the 31 symmorphic layer point groups *(Pond et al. 1983)*. The equivalence between the 31 symmorphic layer or "plan-view" bicrystal specimen point groups and the 31 diffraction groups is established and found identical to that which was tabulated in Table 4.2 for the equivalence between single crystal specimen point groups and the 31 diffraction groups. In other words, the point symmetries which can be exhibited by the two types of specimens are the same.

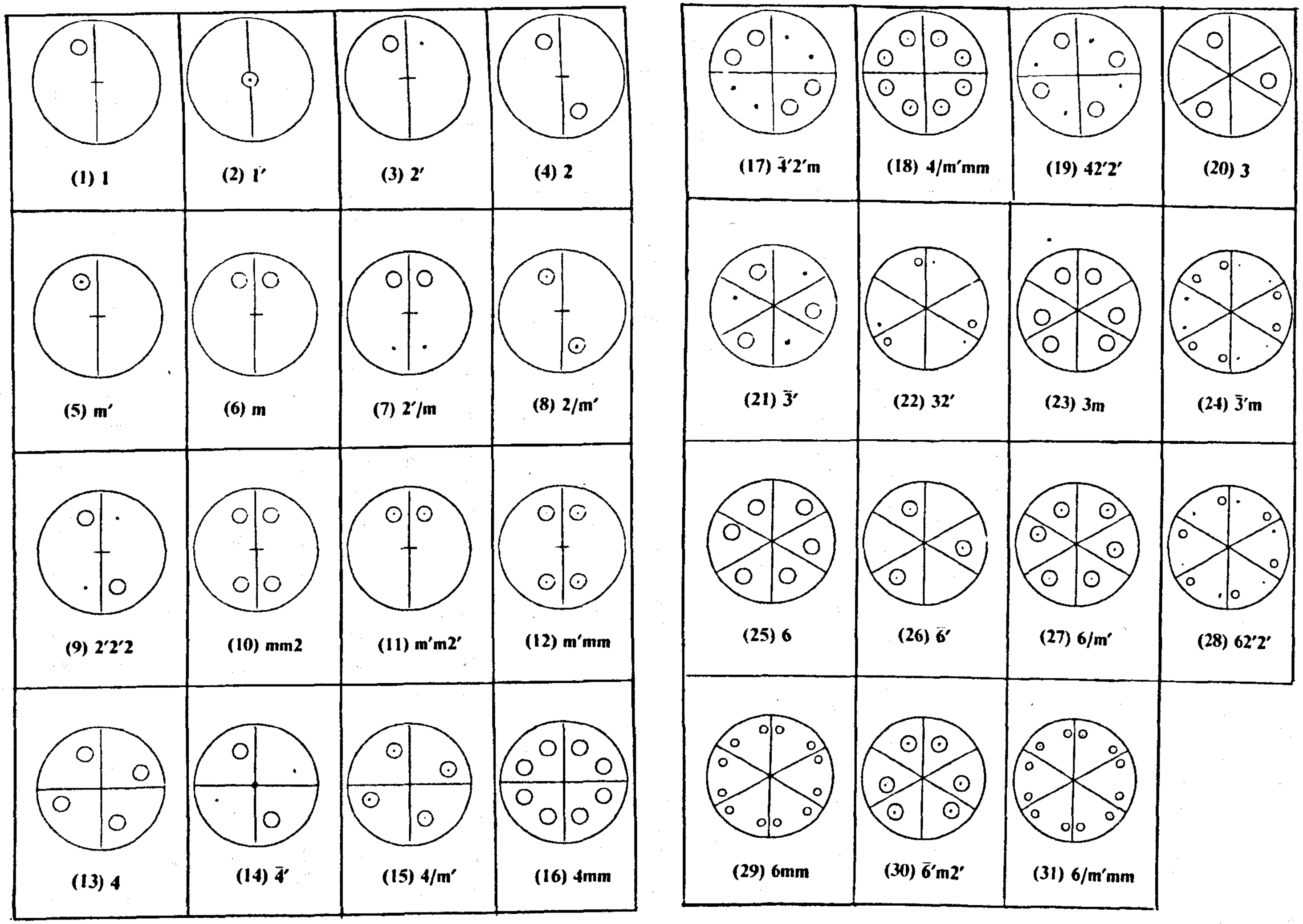

(1) 1 (2) 1′ (3) 2′ (4) 2 (5) m′ (6) m (7) 2′/m (8) 2/m′ (9) 2′2′2 (10) mm2 (11) m′m2′ (12) m′mm (13) 4 (14) $\bar{4}'$ (15) 4/m′ (16) 4mm (17) $\bar{4}'2'm$ (18) 4/m′mm (19) 42′2′ (20) 3 (21) $\bar{3}'$ (22) 32′ (23) 3m (24) $\bar{3}'m$ (25) 6 (26) $\bar{6}'$ (27) 6/m′ (28) 62′2′ (29) 6mm (30) $\bar{6}'m2'$ (31) 6/m′mm

Fig. 4.12. The stereographic projection patterns for the 31 "plan-view" bicrystal point groups. The dot and circle represent the incident and outgoing beams, respectively.

4.5.2. DIFFRACTION GROUPS FOR "EDGE-ON" BICRYSTALS.

In the case of "plan-view" bicrystal specimens the concept of anti-symmetry in bicrystal groups corresponded directly to symmetry which could be revealed in CBED patterns because anti-operations, g', correspond to those where the reciprocity theorem must be invoked. But this is not necessarily the case for the "edge-on" bicrystal specimens.

The objective of this section is to explain how we can identify those operations in the point group of an "edge-on" bicrystal, G(b), which lead to symmetry in CBED pattern when reciprocity is invoked. In other words, we describe a procedure for re-assigning the ordinary and anti-operations in G(b) into two sets, one corresponding to operations which lead to conventional symmetry, and the other containing the operations for which reciprocity must be invoked. We refer to such groups as revised groups, and designate them G^r(b). Thus, a group G(b), formally expressed as $G^o \bigcup G^a$ will now be re-expressed as G^r(b) $= G \bigcup G_R$, where the subscript R refers to the set of operations for which reciprocity must be invoked. The operations in the set G_R can be readily obtained as follows. Let $\underline{i}$ be a unit vector parallel to the incident beam direction, and $\underline{j}$ be the beam direction related to $\underline{i}$ by the operations g or g' belonging to G(b). If $\underline{i} \bullet \underline{j}$ is negative, then this operation must be assigned to the set G_R . Some examples of this procedure are illustrated below for the case of $\Sigma = 3$, 9, and 27 bicrystals. The first example chosen is for the $\Sigma = 3(\ \bar{1}1\bar{2}\ )_\lambda$ bicrystal which is shown in Fig.2.6(a) (chapter 2). It exhibits the following ordinary elements of symmetry (see chapter 2):

(1) the identity, 1,

(2) a mirror perpendicular to the interface and parallel to the specimen surface, $m(110)_\lambda$.

It exhibits the following antisymmetry elements:

(3) an anti-mirror parallel to the interface, $m'(\bar{1}1\bar{2})_\lambda$

(4) an anti-diad parallel to both the interface and the specimen surface, $2'[1\bar{1}\bar{1}]_\lambda$

Therefore, this specimen has the bicrystal point group 2′mm′. Now, consider $\underline{i} = [110]_\lambda$, i.e. the normal to the specimen surface, and operate on this direction by the 4 operations in the point group 2′mm′. One can find that only two operations arise such that $\underline{i} \bullet \underline{j}$ is negative; these operations are $m(110)_\lambda$ and $2'[1\bar{1}\bar{1}]_\lambda$, as shown in the third column of Table 4.6(a). Therefore the revised point group for $\Sigma = 3(\bar{1}1\bar{2})_\lambda$ bicrystal is:

$$G^r(b) = (1, m(\bar{1}1\bar{2})_\lambda) \cup (m'(110)_\lambda, 2'[1\bar{1}\bar{1}]_\lambda) = 2'm'm.$$

Similarly, for $\underline{i} = [53\bar{1}]_\lambda, [42\bar{1}]_\lambda, [31\bar{1}]_\lambda$, or $[51\bar{2}]_\lambda$, rows 4 to 7 in Table 4.6(a), the revised specimen point group is also, $G^r(b) = 2'm'm$, and for $\underline{i} = [20\bar{1}]_\lambda, [3\bar{1}\bar{2}]_\lambda, [1\bar{1}\bar{1}]_\lambda$, rows 8 to 10 in Table 4.6(a), $G^r(b) = 2mm$. Other examples are given in Tables 4.6(b), and (c) for $\Sigma = 9$, and 27, respectively.

The final step is converting the above revised point groups to their corresponding diffraction, bright field, projection diffraction and whole pattern point groups making use of Tables 4.2, 4.3, 4.4 and 4.5,

Table 4.6(a). Derivation of the revised point group for $\Sigma = 3(\bar{1}1\bar{2})_\lambda$ bicrystal.

Surface Normal	symmetry elements	I	$m(110)_\lambda$	$m'(\bar{1}1\bar{2})_\lambda$	$2'[1\bar{1}\bar{1}]_\lambda$
	2'mm'				
	Matrix	$\begin{bmatrix}1&0&0\\0&1&0\\0&0&1\end{bmatrix}$	$\begin{bmatrix}0&-1&0\\-1&0&0\\0&0&1\end{bmatrix}$	$1/3\begin{bmatrix}2&1&-2\\1&2&2\\-2&2&-1\end{bmatrix}$	$1/3\begin{bmatrix}-1&-2&-2\\-2&-1&2\\-2&2&-1\end{bmatrix}$
$[110]_\lambda$		$[110]_\lambda$	$[\bar{1}\bar{1}0]_\lambda$	$[110]_\lambda$	$[\bar{1}\bar{1}0]_\lambda$
$[53\bar{1}]_\lambda$		$[53\bar{1}]_\lambda$	$[\bar{3}\bar{5}\bar{1}]_\lambda$	$[53\bar{1}]_\lambda$	$[\bar{3}\bar{5}\bar{1}]_\lambda$
$[42\bar{1}]_\lambda$		$[42\bar{1}]_\lambda$	$[\bar{2}\bar{4}\bar{1}]_\lambda$	$[42\bar{1}]_\lambda$	$[\bar{2}\bar{4}\bar{1}]_\lambda$
$[31\bar{1}]_\lambda$		$[31\bar{1}]_\lambda$	$[\bar{1}\bar{3}\bar{1}]_\lambda$	$[31\bar{1}]_\lambda$	$[\bar{1}\bar{3}\bar{1}]_\lambda$
$[51\bar{2}]_\lambda$		$[51\bar{2}]_\lambda$	$[\bar{1}\bar{5}\bar{2}]_\lambda$	$[51\bar{2}]_\lambda$	$[\bar{1}\bar{5}\bar{2}]_\lambda$
$[20\bar{1}]_\lambda$		$[20\bar{1}]_\lambda$	$[0\bar{2}\bar{1}]_\lambda$	$[20\bar{1}]_\lambda$	$[0\bar{2}\bar{1}]_\lambda$
$[3\bar{1}\bar{2}]_\lambda$		$[3\bar{1}\bar{2}]_\lambda$	$[1\bar{3}\bar{2}]_\lambda$	$[3\bar{1}\bar{2}]_\lambda$	$[1\bar{3}\bar{2}]_\lambda$
$[1\bar{1}\bar{1}]_\lambda$		$[1\bar{1}\bar{1}]_\lambda$	$[1\bar{1}\bar{1}]_\lambda$	$[1\bar{1}\bar{1}]_\lambda$	$[1\bar{1}\bar{1}]_\lambda$

Table 4.6(b). Derivation of the revised point group for $\Sigma = 9(\bar{2}21)_\lambda$ bicrystal.

Surface Normal	symmetry elements	I	$m(110)_\lambda$	$m'(\bar{2}21)_\lambda$	$2'[\bar{1}1\bar{4}]_\lambda$
	2'mm'				
	Matrix	$\begin{bmatrix}1&0&0\\0&1&0\\0&0&1\end{bmatrix}$	$\begin{bmatrix}0&-1&0\\-1&0&0\\0&0&1\end{bmatrix}$	$1/9\begin{bmatrix}1&8&4\\8&1&-4\\4&-4&7\end{bmatrix}$	$1/9\begin{bmatrix}-1&-8&-4\\-8&-1&4\\-4&4&-7\end{bmatrix}$
$[110]_\lambda$		$[110]_\lambda$	$[\bar{1}\bar{1}0]_\lambda$	$[110]_\lambda$	$[\bar{1}\bar{1}0]_\lambda$
$[35\bar{4}]_\lambda$		$[35\bar{4}]_\lambda$	$[\bar{5}\bar{3}\bar{4}]_\lambda$	$[35\bar{4}]_\lambda$	$[\bar{5}\bar{3}\bar{4}]_\lambda$
$[13\bar{4}]_\lambda$		$[13\bar{4}]_\lambda$	$[\bar{3}\bar{1}\bar{4}]_\lambda$	$[13\bar{4}]_\lambda$	$[\bar{3}\bar{1}\bar{4}]_\lambda$
$[15\bar{4}]_\lambda$		$[15\bar{4}]_\lambda$	$[\bar{5}\bar{1}\bar{4}]_\lambda$	$[15\bar{4}]_\lambda$	$[\bar{5}\bar{1}\bar{4}]_\lambda$
$[01\bar{2}]_\lambda$		$[01\bar{2}]_\lambda$	$[\bar{1}0\bar{2}]_\lambda$	$[01\bar{2}]_\lambda$	$[\bar{1}0\bar{2}]_\lambda$
$[\bar{1}7\,\overline{16}]_\lambda$		$[\bar{1}7\,\overline{16}]_\lambda$	$[\bar{7}1\,\overline{16}]_\lambda$	$[\bar{1}7\,\overline{16}]_\lambda$	$[\bar{7}1\,\overline{16}]_\lambda$
$[\bar{3}5\overline{16}]_\lambda$		$[\bar{3}5\overline{16}]_\lambda$	$[\bar{5}3\overline{16}]_\lambda$	$[\bar{3}5\overline{16}]_\lambda$	$[\bar{5}3\overline{16}]_\lambda$
$[\bar{1}1\bar{4}]_\lambda$		$[\bar{1}1\bar{4}]_\lambda$	$[\bar{1}1\bar{4}]_\lambda$	$[\bar{1}1\bar{4}]_\lambda$	$[\bar{1}1\bar{4}]_\lambda$

Table 4.6(c). Derivation of the revised point group for $\Sigma = 27(55\bar{2})_\lambda$ bicrystal.

Surface Normal	symmetry elements	I	$m(110)_\lambda$	$m'(55\bar{2})_\lambda$	$2'[\bar{1}15]_\lambda$
	2'mm'				
	Matrix	$\begin{bmatrix}1&0&0\\0&1&0\\0&0&1\end{bmatrix}$	$\begin{bmatrix}0&-1&0\\-1&0&0\\0&0&1\end{bmatrix}$	$1/27\begin{bmatrix}2&25&10\\25&2&-10\\10&-10&23\end{bmatrix}$	$1/27\begin{bmatrix}-25&-2&10\\-2&-25&-10\\10&-10&23\end{bmatrix}$
$[110]_\lambda$		$[110]_\lambda$	$[\bar{1}\bar{1}0]_\lambda$	$[110]_\lambda$	$[\bar{1}\bar{1}0]_\lambda$
$[35\bar{5}]_\lambda$		$[35\bar{5}]_\lambda$	$[\bar{5}\bar{3}\bar{5}]_\lambda$	$[35\bar{5}]_\lambda$	$[\bar{5}\bar{3}\bar{5}]_\lambda$
$[23\bar{5}]_\lambda$		$[23\bar{5}]_\lambda$	$[\bar{3}\bar{2}\bar{5}]_\lambda$	$[23\bar{5}]_\lambda$	$[\bar{3}\bar{2}\bar{5}]_\lambda$
$[17\,\overline{15}]_\lambda$		$[17\,\overline{15}]_\lambda$	$[\bar{7}\bar{1}\,\overline{15}]_\lambda$	$[17\,\overline{15}]_\lambda$	$[\bar{7}\bar{1}\,\overline{15}]_\lambda$
$[\bar{1}7\,\overline{20}]_\lambda$		$[\bar{1}7\,\overline{20}]_\lambda$	$[\bar{7}1\overline{20}]_\lambda$	$[\bar{1}7\,\overline{20}]_\lambda$	$[\bar{7}1\overline{20}]_\lambda$
$[02\bar{5}]_\lambda$		$[02\bar{5}]_\lambda$	$[\bar{2}0\bar{5}]_\lambda$	$[02\bar{5}]_\lambda$	$[\bar{2}0\bar{5}]_\lambda$
$[\bar{1}3\overline{10}]_\lambda$		$[\bar{1}3\overline{10}]_\lambda$	$[\bar{3}1\overline{10}]_\lambda$	$[\bar{1}3\overline{10}]_\lambda$	$[\bar{3}1\overline{10}]_\lambda$
$[\bar{1}1\bar{5}]_\lambda$		$[\bar{1}1\bar{5}]_\lambda$	$[\bar{1}1\bar{5}]_\lambda$	$[\bar{1}1\bar{5}]_\lambda$	$[\bar{1}1\bar{5}]_\lambda$

respectively. For example, if an "edge-on" specimen has a revised point group $G^r(b)$ = mm2, then its corresponding G_r = 2mm, G_b = 2mm, G_p = 2mm1_R, and G_w = 2mm. Similarly, if an "edge-on" specimen has $G^r(b)$ = 2′m′m then its corresponding G_r = m1_R, G_b = 2mm, G_p = m1_R, and G_w = m.

4.6. EXPERIMENTAL DETERMINATIONS OF RELATIVE DISPLACEMENT.

In chapter 2 a theoretical study is given concerning the variation of the symmetry of three germanium bicrystals with rigid body translation p parallel to the boundary plane (section 2.7). It was deduced that a bicrystal's spacegroup is a function of the shift p. This conclusion was formulated mathematically through two equations expressing the criteria for conservation and/or breaking of coincident and antisymmetry operations (Eq. 2.16(a) and (b)).

In principle a rigid body translation p can be determined experimentally using SAD or CBED techniques (see chapter 3). The application of the former technique to determine p can be appreciated by considering the following points. Firstly, the structure factor equation (Eq.3.2 in chapter 3) can be rewritten for bicrystal interfacial reflections as

$$F_{hkl} = \Sigma_{j,q} \{f_j^{\lambda} e^{2\pi i(hx_j^{\lambda} + ky_j^{\lambda} + lz_j^{\lambda})} + f_q^{\mu} e^{2\pi i(hx_q^{\mu} + ky_q^{\mu} + lz_q^{\mu})} e^{2\pi i(hp_x + kp_y + lp_z)}\} \qquad (4.4)$$

where the sum is over all the white and black atoms in the bicrystal, f^{λ} and f^{μ} are the atomic scattering factors for the jth white and qth black atoms, $(x^{\lambda}, y^{\lambda}, z^{\lambda})$ and $(x^{\mu}, y^{\mu}, z^{\mu})$ are the fractional coordinates of the jth white and qth black atoms in the bicrystal and (p_x, p_y, p_z) are the x, y, z components of the the rigid body translation p of the black crystal with respect to the white one. Secondly, the absolute intensities, I_{hkl}, of the spots in a SAD pattern are given by $I_{hkl} = F_{hkl}F_{hkl}^{*}$ (Eq.(3.3) chapter 3).

Thus, if a rigid body translation is present in a given bicrystal, then a comparison of calculated intensities, I_{hkl}, and that measured from the SAD pattern from the bicrystal gives an insight into p. However, the SAD technique is not usually used for the determination of the rigid body translation because of the difficulty of the measurement of the absolute intensity, I_{hkl}.

Recently, *Cherns et al. (1986)* used the CBED technique to determine the interfacial rigid body displacement, p, in an Al/(001)GaAs "plan-view" specimen. Molecular beam epitaxy was used to grow 50nm of Al at 560°c on a fresh 1μm GaAs substrate. The projection symmetry of the observed [001] CBED pattern from this Al/(001)GaAs bicrystal, exhibited four-fold symmetry. Three possibilities for the rigid body shift, p, would be consistent with this as is described in more detail below.

GaAs crystal has the diamond structure (Fig.2.2(a)), where the Ga atoms have the coordinates *(Wyckoff 1963):*

000; 0½½ ; ½0½ ; ½½0

and As atoms have the coordinates:

$$\frac{1}{4}\frac{1}{4}\frac{1}{4};\frac{1}{4}\frac{3}{4}\frac{3}{4};\frac{3}{4}\frac{1}{4}\frac{3}{4};\frac{3}{4}\frac{3}{4}\frac{1}{4}$$

GaAs exhibits the symmetry of the spacegroup F$\bar{4}$3m (Table 4.7(a)). Al has the F.C.C. structure (Fig.2.1(a)) which exhibits symmetry identical to that of the spacegroup Fm$\bar{3}$m (Table 2.1). Consider GaAs as the white crystal and Al as the black one, and to distinguish between them the subscripts λ and μ, respectively, will be used. Now, if the Al/(001)GaAs "plan-view" bicrystal has the orientation where the 2-fold axes along $<001>_{\lambda,\mu}$ are coincident and the $(1\bar{1}0)_\lambda$ and $(110)_\lambda$ mirror planes in GaAs are coincident with the $(100)_\mu$ and $(010)_\mu$ mirror planes in Al, then the bicrystal exhibits only coincident symmetry elements identical to these in Table 4.7(a) under numbers (1) to (4) and (13) to (16) and listed in Table 4.7(b). Thus, the point symmetry of Al/(001)GaAs "plan-view" bicrystal is $\bar{4}$2m. Let us study the variation of that point group when the black crystal is displaced with respect to the white by shifts p which lie within the in-plane Wigner-Seitz cell for Al/(001)GaAs "plan-view" bicrystal, which has the dimensions $\frac{1}{2}[100]_\lambda \times \frac{1}{2}[010]_\lambda$, and is represented in Fig 4.13 by dashed lines. Now, a shift p parallel to $[100]_\lambda$ or $[010]_\lambda$, where $0 < p < \frac{1}{4}<100>_\lambda$, destroys all the symmetry elements in the point group $\bar{4}$2m except the identity and the 2-fold axis along $<100>_\lambda$ and the point group becomes G(b) = 121, while a shift $p = \frac{1}{4}<100>_\lambda$ makes G(b) = 222. Similarly, a shift p parallel to $[110]_\lambda$ or $[1\bar{1}0]_\lambda$, where $0 < p < \frac{1}{4}<110>_\lambda$ conserves the identity and the mirror plane parallel to $\{110\}_\lambda$, and G(b) becomes 11m and when $p = \frac{1}{4}<110>_\lambda$, G(b) = $\bar{4}$2m. A general shift p consists of a combination of the above two shifts, i.e.

Table 4.7(a). The symmetry operations in the spacegroup F$\bar{4}$3m (No. 216); origin at $\bar{4}$3m.

No.	Coordinate Triplets	W
(1)	x,y,z	1
(2)	-x,-y,z	2[001]
(3)	-x,y,-z	2[010]
(4)	x,-y,-z	2[100]
(5)	z,x,y	$3^{+}[111]$
(6)	z,-x,-y	$3^{+}[\bar{1}1\bar{1}]$
(7)	-z,x,-y	$3^{+}[1\bar{1}\bar{1}]$
(8)	-z,-x,y	$3^{+}[\bar{1}\bar{1}1]$
(9)	y,z,x	$3^{-}[111]$
(10)	y,-z,-x	$3^{-}[1\bar{1}\bar{1}]$
(11)	-y,z,-x	$3^{-}[\bar{1}\bar{1}1]$
(12)	-y,-z,x	$3^{-}[\bar{1}1\bar{1}]$
(13)	-y,-x,z	m[110]
(14)	y,x,z	m$[1\bar{1}0]$
(15)	y,-x,-z	$\bar{4}^{+}[001]$
(16)	-y,x,-z	$\bar{4}^{-}[001]$
(17)	x,-z,-y	m[011]
(18)	-x,z,-y	$\bar{4}^{+}[100]$
(19)	-x,-z,y	$\bar{4}^{-}[100]$
(20)	x,z,y	m$[01\bar{1}]$
(21)	-z,y,-x	m[101]
(22)	z,-y,-x	$\bar{4}^{-}[010]$
(23)	z,y,x	m$[\bar{1}01]$
(24)	-z,-y,x	$\bar{4}^{+}[010]$

Table 4.7(b). The symmetry operations in the point group $\bar{4}2m$.

No.	Coordinate Triplets	W
(1)	x,y,z	1
(2)	-x,-y,z	2[001]
(3)	y,-x,-z	$\bar{4}^{+}[001]$
(4)	-y,x,-z	$\bar{4}^{-}[001]$
(5)	-x,y,-z	2[010]
(6)	x,-y,-z	2[100]
(7)	y,x,z	$m[1\bar{1}0]$
(8)	-y,-x,z	m[110]

Table 4.7(c). The variation of the point group $\bar{4}2m$ with the shift p.

No.	The Shift p	Point Group	Projection Symmetry
(1)	0	$\bar{4}2m$	4mm
(2)	$0 < p < \frac{1}{4}[010]_{\lambda}$	121	2
(3)	$p = \frac{1}{4}[010]_{\lambda}$	222	4mm
(4)	$0 < p < \frac{1}{4}[110]_{\lambda}$	11m	m
(5)	$p = \frac{1}{4}[110]_{\lambda}$	$\bar{4}2m$	4mm
(6)	$0 < p < \frac{1}{4}[110]_{\lambda} + \frac{1}{4}[010]_{\lambda}$	111	1

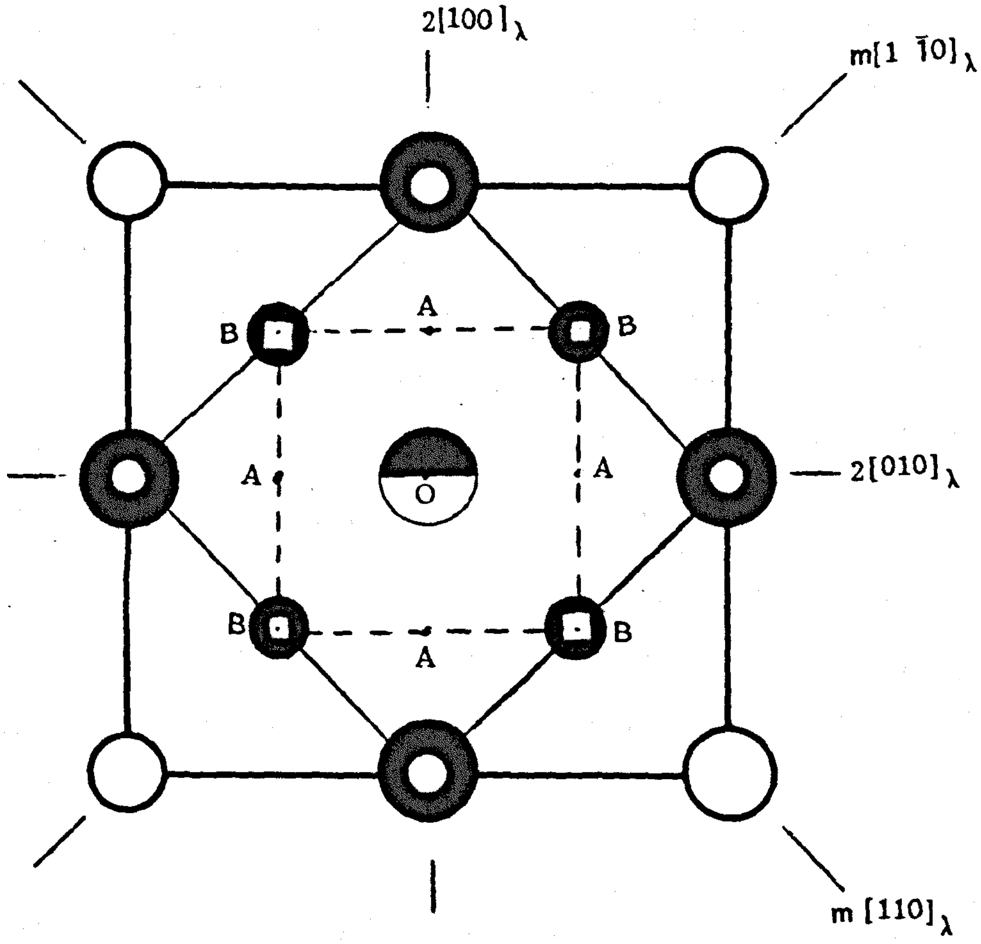

Fig. 4.13. Projection of Al/(001)GaAs structure along [001]$_\lambda$ Ga (open small and large circles, at heights $\frac{1}{2}$ and 0), As (open small and large squares, at heights 3/4 and $\frac{1}{4}$) and Al (filled small and large circles, at heights $\frac{1}{2}$ and 0). The coincident site is half shaded. The in-plane Wigner-Seitz cell is indicated by dashed lines.

$\frac{1}{4}<110>_\lambda$ and $\frac{1}{4}<100>_\lambda$, would destroy all the symmetry elements so that the point group becomes the identity (Table 4.7(c)).

The possibilities for the anticipated structure of Al/(001)GaAs "plan-view" bicrystal specimen are represented in Fig.4.13 by the letters O, A and B which correspond to the rigid body translations $p = 0$ and $\frac{1}{4}<100>_\lambda$ and $\frac{1}{4}<110>_\lambda$ respectively. In the structure O, as well as B, the columns of Al atoms sit on those of As and Ga atoms, and therefore both structures exhibit the symmetry of the point group G(b) = $\bar{4}2m$. This is no longer the case for the A structure where the Al strings are shifted with respect to those of Ga and As by a shift $p = \frac{1}{4}<100>_\lambda$ and, consequently, this structure possess the symmetry of the point group G(b) = 222. An important point is that the 3 structures, O, A and B, exhibit the same projection symmetry G_p = 4mm, as shown in the last column of Table 4.7(c).

The actual shift p was determined from among these three possibilities *(Cherns et al. 1986)* as follows. First, the comparison between segments of HOLZ rings obtained from Al/(001)GaAs and GaAs specimens revealed that these two specimens exhibited two different branch structures, where an extra branch was observed in the case of Al/(001)GaAs compared with GaAs. Secondly, the branch structures for both Al/(001)GaAs and GaAs were calculated using the dynamical theory of electron diffraction *(Hirsch et al. 1965)*. In the case of GaAs, the calculation resulted in two strongly excited branches represent 1s states of As and Ga (due to Bloch waves strongly localised on As and Ga strings of atoms) and one represents 2s state of Ga + As. In the case of Al/(001)GaAs a similar branch structure was obtained with two extra branches; one just outside that in the 2s state of Ga + As (may be due to a Bloch wave with maximum intensity at the mid-points between Ga or As strings), and another branch more strongly localised than that mentioned above, which showed more intensity in Al/(001)GaAs compared with GaAs. These two extra branches or Bloch states have been confirmed *(Cherns et al. 1986* , Eq.(3)) to be strongly excited in the lower crystal (GaAs) for the structure represented by the letter A, Fig. 4.13, and weakly excited for that represented by O. Thus , the structure of Al/(001)GaAs "plan-view" bicrystal specimen was determined to be that is represented in Fig. 4.13 by A where the Al crystals were shifted by a shift $p = \frac{1}{4}\langle 100\rangle_{\lambda}$ with respect to GaAs crystals.

CHAPTER FIVE

The Experimental Results

5.1. Macroscopic Investigations.............5.2

  5.1.1. Optical Microscopy......................5.2

  5.1.2. Scanning electron Microscopy...........5.3

  5.1.3. Laue Back-Reflection X-Ray Diffraction......5.3

5.2. Microscopic Investigations.............5.5

  5.2.1. $\Sigma = 3$ "edge-on" specimens, "ia", "iia" and "iiia".....5.6

  5.2.2. The "plan-view" $\Sigma = 3$ specimens, "ib", "iib" and "iiib"..5.7

  5.2.3. The "edge-on" $\Sigma = 3$ specimen, "iva".......5.8

5.3. $\Sigma = 3(\bar{1}1\bar{2})_\lambda$ grain boundary...5.9

  5.3.1. The $[\bar{1}1\bar{2}]_\lambda$ SAD and CBED patterns......5.10

  5.3.2. The $[110]_\lambda$ SAD and CBED patterns.....5.11

  5.3.3. The $[1\bar{1}\bar{1}]_\lambda$ SAD and CBED patterns........5.11

5.4. $\Sigma = 27$ grain boundary.............5.12

  5.4.1. The $\Sigma = 27$ "edge-on" specimen, "va"........5.12

  5.4.2. The $\Sigma = 27$ "plan-view" specimen, "vb"......5.14

This chapter contains an account of the experimental investigations of germanium (Ge) grain boundaries from both macroscopic and microscopic points of view. The macroscopic investigations include optical microscopy, scanning electron microscopy, and the back-reflection X-ray method. The microscopic investigations include SAD patterns, CBED patterns, and LACBED or Tanaka patterns.

5.1. MACROSCOPIC INVESTIGATIONS.

The aim of the macroscopic investigations is to investigate the germanium bulk materials received, for example the orientation relationships between the individual grains in Ge cylinders.

5.1.1. OPTICAL MICROSCOPY.

Fig.5.1(a) shows an optical micrograph for a polished Ge circular slice. It reveals the grains and the grain boundaries contained in the slice. It contains four grains marked by the letters A_c, B_c, C_c and D_c, (where the subscript c refers to the circular slice), separated by four straight grain boundaries, gm, gn, go and kl and a curved one, gk, as sketched in Fig.5.1(c). At g three of the straight and one of the curved grain boundaries meet. This point is enclosed by a circle in the figure. Similarly, Fig.5.1(b) is an optical micrograph for a polished Ge elliptical slice. It also, contains two junction points similar to g in Fig.5.1(a) with some slight differences (these junction points are enclosed by two circles, Fig.5.1(d), and each confines portions from four grains similar to grains A_c, B_c, C_c and D_c, in Fig.5.1(a) and marked by the letters A_e, B_e, C_e and D_e, where the subscript e refers to the elliptical slice. The first circle (from the left) encloses four straight

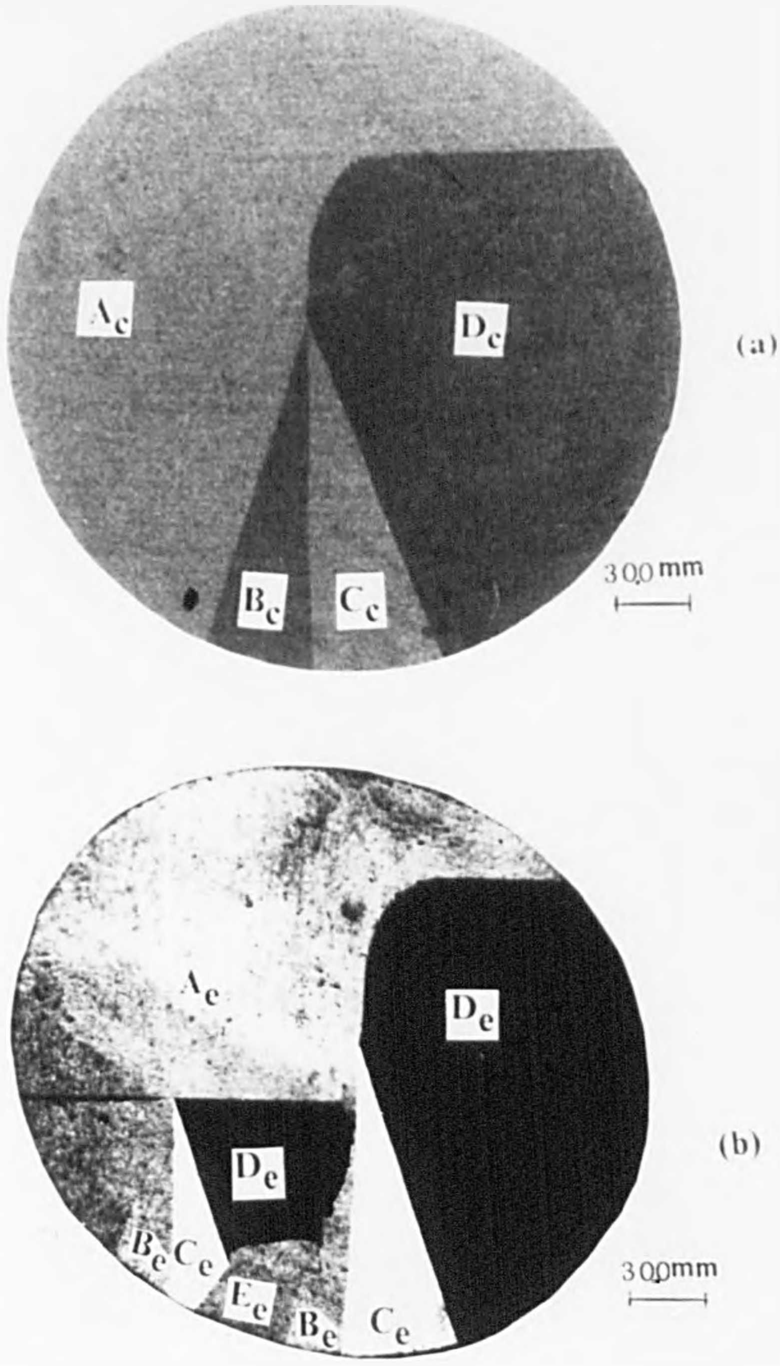

Fig. 5.1. (a) 3X optical micrograph showing a chemically polished germanium (circular cross section) slice, revealing four grains, A_e, B_e, C_e and D_e.

(b) 3X optical micrograph showing a chemically polished germanium (elliptical cross section) slice.

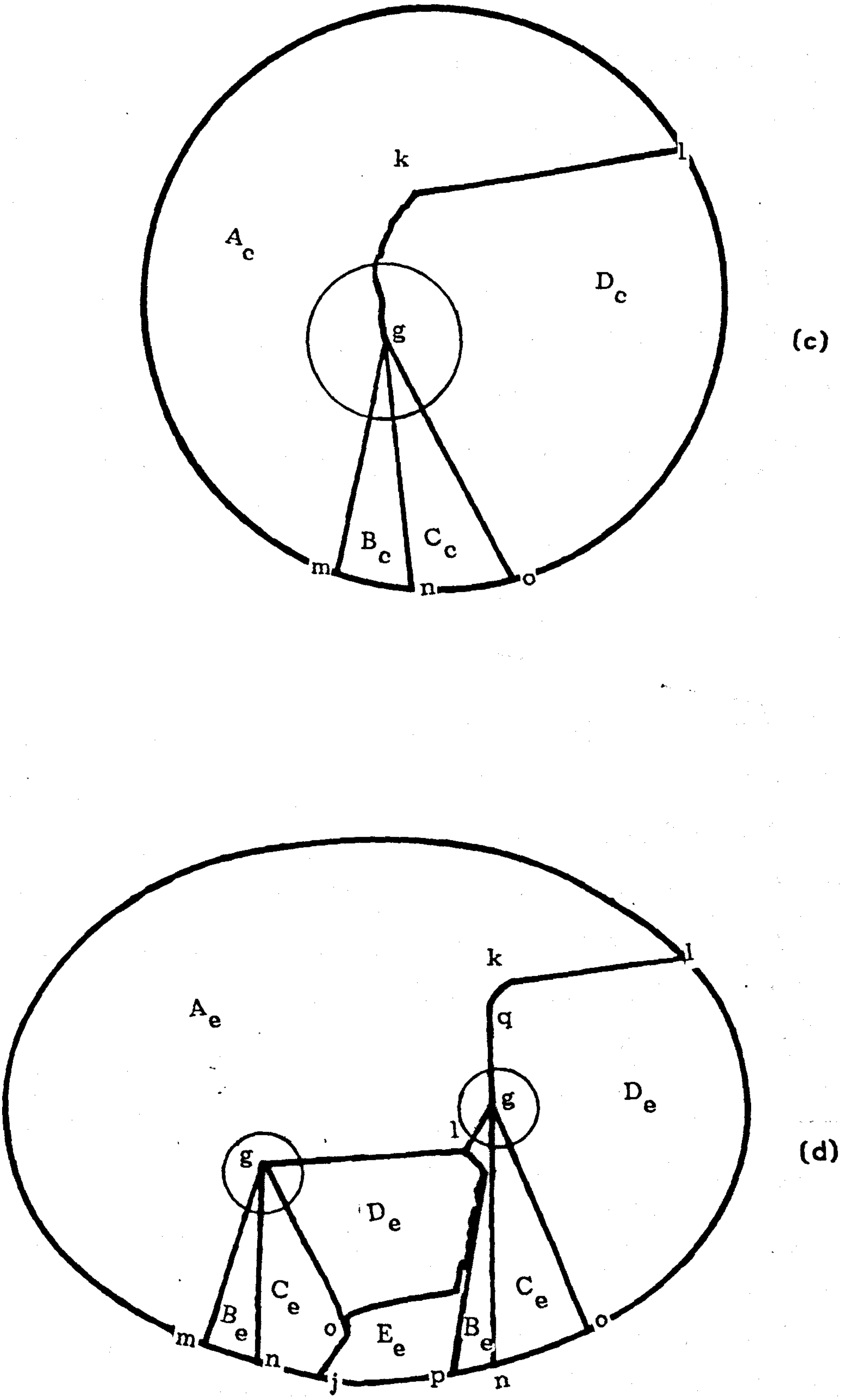

Fig. 5.1. (c) A schematic sketch for the grains observed in (a),
(d) A schematic sketch for the grains observed in (b).

grain boundaries, mg, ng, og and gl, joined at g, similarly, the second circle encloses the four straight grain boundaries, lg, qg, ng and og, which are joined at g.

The elliptical Ge slice contains also a grain E_e, enclosed by the straight grain boundaries jo, pl and a corrugated one ol. The grain boundaries are terminated at the circumference of the slice, at points m, n o, and l in the case of circular slice and at m, n, j, p, n, o and l for the elliptical one.

5.1.2. SCANNING ELECTRON MICROSCOPY.

A scanning electron microscope was used to observe the slices at higher magnification in order to reveal more about the shape of the grain boundaries, particularly the curved one. Fig.5.2 shows a scanning electron micrograph for the curved grain boundary, gk in Fig.5.1(c). It starts at k being straight, then it curves between b and c and then it is stepped as between d and g. So, the closer look to the curved grain boundary, gk, shows that it consists of faceted grain boundaries.

5.1.3. LAUE BACK-REFLECTION X-RAY DIFFRACTION.

The orientations between the four grains, A_c, B_c, C_c and D_c, in the slice (Fig.5.1(a)) were determined using the Laue back-reflection X-ray method *(Cullity, 1979)*. In this method a Ge slice was attached with plasticine to a two dimensional translatable holder, and a tungsten (35Kv, 25ma) X-ray beam was made incident for 30 minutes on one of the grains in the slice. The specimen-to-film distance was fixed at 3

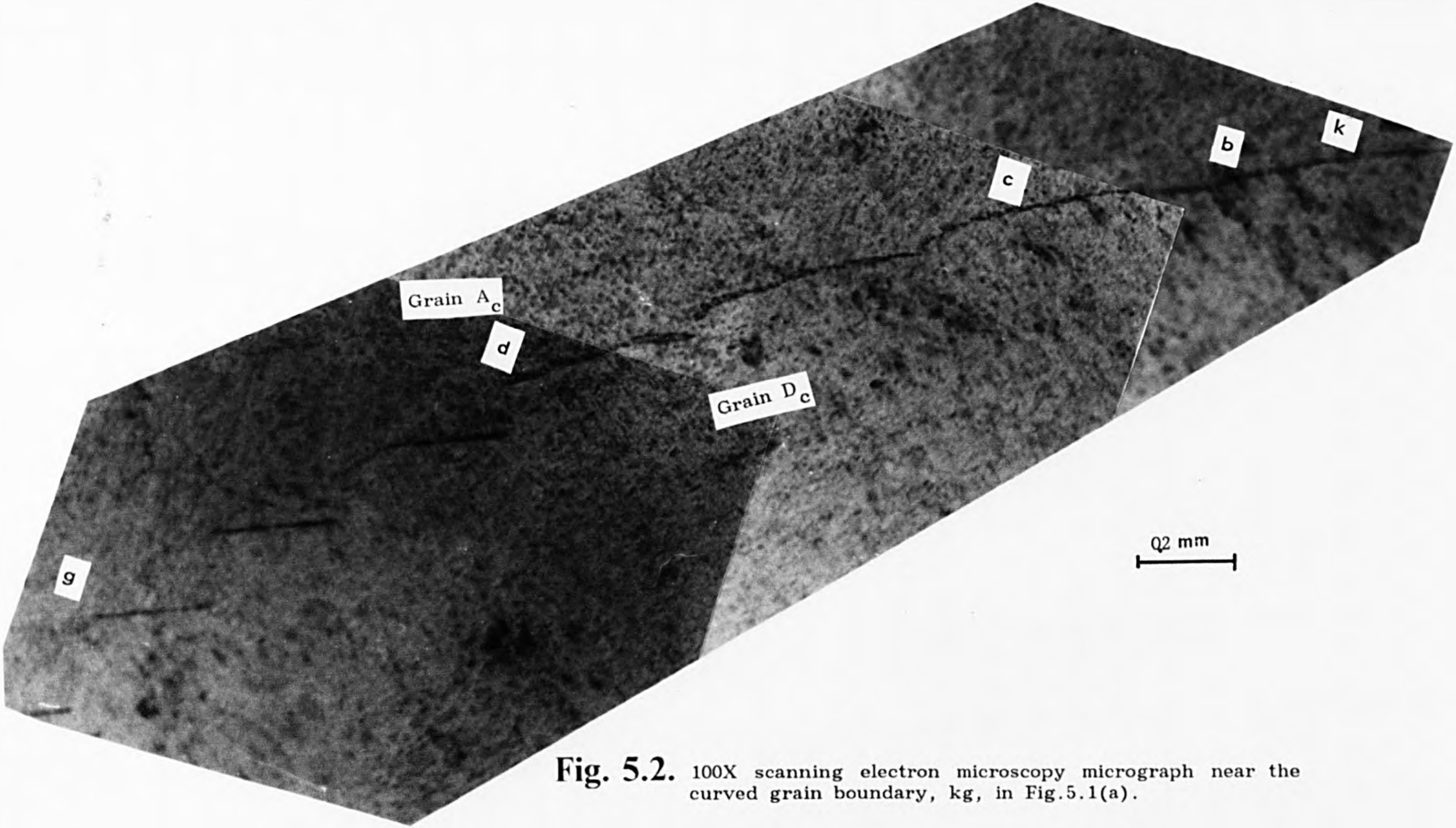

Fig. 5.2. 100X scanning electron microscopy micrograph near the curved grain boundary, kg, in Fig.5.1(a).

cm. Fig.5.3(a),(b),(c), and (d) show the diffraction patterns taken from grains A_c, B_c, C_c and D_c, respectively. These patterns have been obtained from the various grains by moving the specimen, between exposures, in two directions at right angles in the plane of the slice surface, this surface being perpendicular to the incident x-ray beam. Each diffraction pattern consists of spots lying on hyperbolae, or straight lines. This is due to the fact that Laue reflection spots from planes belonging to different zones lie on the surface of imaginary cones whose axes are the zones axes. Depending on the angles between those zone axes and the x-ray incident beam, the film, placed between the specimen and the x-ray source to record the diffraction pattern, intersects these cones in spots lying on hyperbolae or straight lines. Examination of these patterns showed that they are similar; each has two mirror elements of symmetry at right angles to each other and indicated by m_1 and m_2, respectively. The pattern pairs A_c-B_c, B_c-C_c, C_c-D_c, D_c-A_c are found to be rotated with respect to each other by the angles ($110.0^\circ \pm 0.5^\circ$), ($32.0^\circ \pm 0.41^\circ$), ($71.0^\circ \pm 0.5^\circ$) and ($71.0^\circ \pm 0.5^\circ$) respectively, about the direction normal to their planes. This normal will be determined by indexing the four patterns using the method explained by *(Cullity, 1979)*. Fig.5.4(a), for example, is a tracing of the photograph shown in Fig.5.3(a). It shows some of the important spots numbered for reference. The poles of the planes causing these numbered spots are plotted stereographically in Fig.5.4(b), using a Wulff net. The great circles W, X, Y and Z are drawn through 4 sets of poles corresponding to the hyperbolae of spots on the film. These circles connect planes of a zone and these zones are, P_W, P_X, P_Y and P_Z, respectively, and shown as open circles in the figure. The 4 zone axes, P_W, P_X, P_Y and P_Z, are indexed as $[2\bar{1}\bar{1}]$, $[2\bar{1}1]$, $[\bar{1}2\bar{1}]$ and

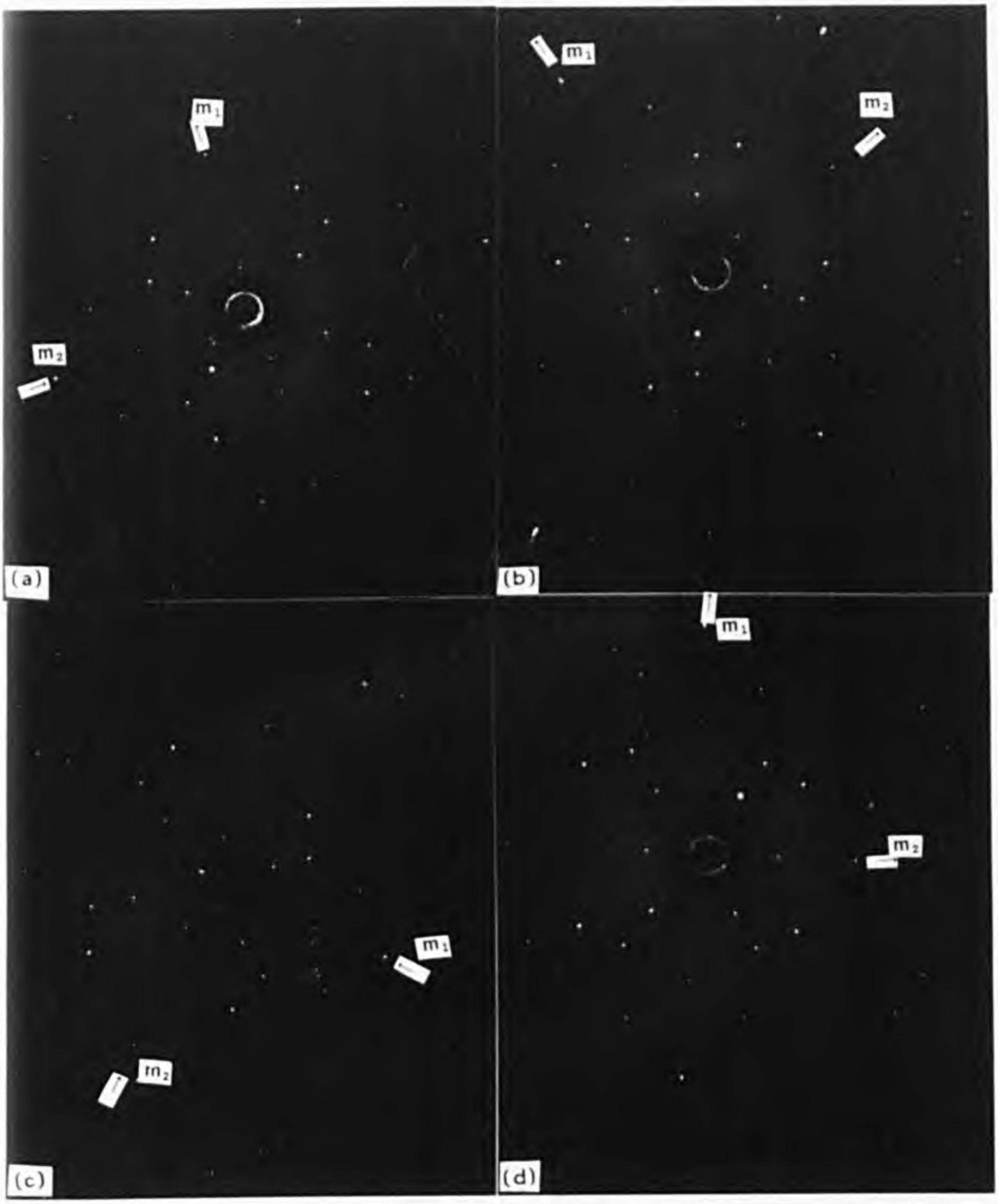

Fig. 5.3. The laue-back reflection x-ray diffraction patterns from Ge specimen in Fig.5.1(a): (a) Grain A_c, (b) Grain B_c, (c) Grain C_c, and (d) Grain D_c. m_1 and m_2 indicate the position of two mirror planes perpendicular to each other.

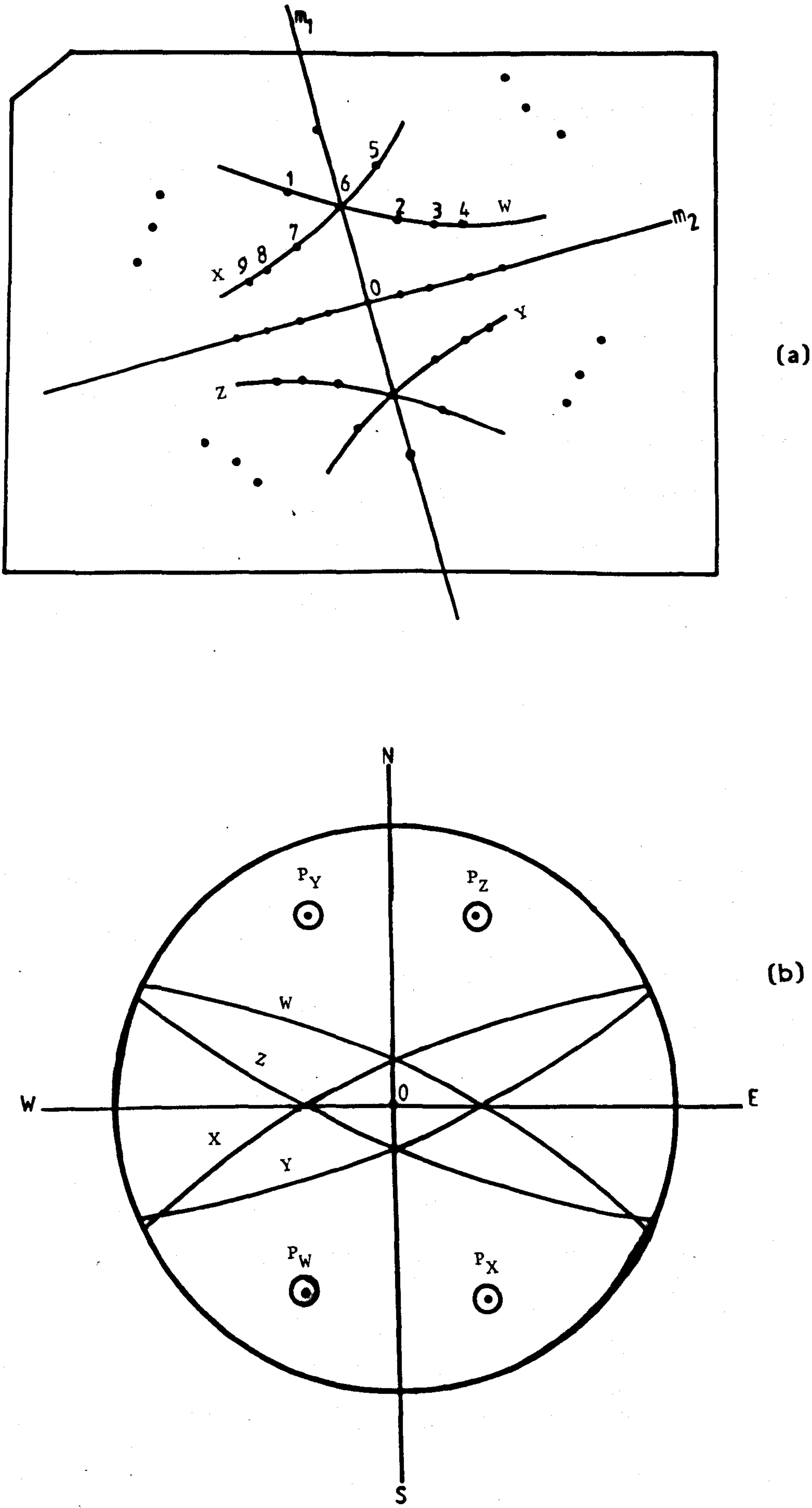

Fig. 5.4. (a) A tracing of the diffraction pattern spots in Fig.5.3(a),
(b) A stereographic projection corresponding to the laue back reflection pattern in (a).

[$\bar{1}21$], respectively. The pole number 0 is the centre of the projection and corresponds to the specimen normal and has the index [110].

From the orientation relationships which have been established above between the 4 diffraction patterns, one can assign $\Sigma = 3$, 27, 3 and 3 for the grain boundaries between grain pairs A_c-B_c, B_c-C_c, C_c-D_c and D_c-A_c, respectively, and the zone axis [110] is common for all the grains. The four grains, A_e, B_e, C_e and D_e, in Fig.5.1(b), have orientation relationships similar to those found for the four grains in Fig.5.1(a). Grain E_e and its border were not investigated during this study.

5.2. MICROSCOPIC INVESTIGATIONS.

The main aim of the next sections is to present the transmission electron microscope (TEM) investigations for the four grain boundaries identified in the previous section. Also they are concerned with the experimental study of Σ=3, and Σ=27 grain boundaries respectively using SAD, CBED and LACBED techniques.

Five electron microscopy specimens, listed in Table 5.1, four of the type assigned Σ=3 and one of the type Σ=27, were prepared to determine the precise orientation relationships between the grains. Each specimen contains two grains and the boundary plane between them is either "edge-on" or "plan-view". Specimens i, ii, iii contain the grain pairs A_c-B_c, B_c-C_c, C_c-D_c and D_c-A_c, respectively. Specimen iv contains grain pair A_e-D_e and specimen v contains grain pair B_c-C_c and the boundary assigned Σ=27.

Table 5.1. Types of the electron microscopy specimens.

	Grain	Specimen Type		Orientation	Surface
No.	Pair	Edge-on	Plan-view	relation	normal
(ia)	A_c-B_c	X		$\Sigma=3(1\ \bar{1}\bar{1})_\lambda$	$[110]_\lambda$
(ib)	A_c-B_c		X	$\Sigma=3(1\ \bar{1}\bar{1})_\lambda$	$[1\ \bar{1}\bar{1}]_\lambda$
(iia)	C_c-D_c	X		$\Sigma=3(1\ \bar{1}\bar{1})_\lambda$	$[110]_\lambda$
(iib)	C_c-D_c		X	$\Sigma=3(1\ \bar{1}\bar{1})_\lambda$	$[1\ \bar{1}\bar{1}]_\lambda$
(iiia)	D_c-A_c	X		$\Sigma=3(1\ \bar{1}\bar{1})_\lambda$	$[110]_\lambda$
(iiib)	D_c-A_c		X	$\Sigma=3(1\ \bar{1}\bar{1})_\lambda$	$[1\ \bar{1}\bar{1}]_\lambda$
(iva)	A_e-D_e	X		$\Sigma=3(\ \bar{1}1\bar{2})_\lambda$	$[110]_\lambda$
(ivb)	A_e-D_e	X		$\Sigma=3(\ \bar{1}1\bar{2})_\lambda$	$[1\ \bar{1}\bar{1}]_\lambda$
(ivc)	A_e-D_e		X	$\Sigma=3(\ \bar{1}1\bar{2})_\lambda$	$[\ \bar{1}1\bar{2}]_\lambda$
(va)	B_c-C_c	X		$\Sigma=27(5\ \bar{5}\bar{2})_\lambda$	$[110]_\lambda$
(vb)	B_c-C_c		X	$\Sigma=27(5\ \bar{5}\bar{2})_\lambda$	$[5\ \bar{5}\bar{2}]_\lambda$

Each specimen has been studied in a PHILIPS EM400 electron microscope operating at 120 KV(or otherwise stated). A cold stage double-tilt specimen holder was used to hold the specimen and to keep its temperature down to liquid nitrogen temperature to minimise diffuse electron scattering. The grains have been imaged and SAD, CBED and LACBED patterns taken from each grain and the grain boundary region. The patterns and images were then carefully studied.

5.2.1. $\Sigma = 3$ "EDGE-ON" SPECIMENS "ia", "iia" AND "iiia".

The bright-field (BF) micrographs which have been taken from the "edge-on" specimens "ia", "iia", "iiia" showed that the grain boundary of each specimen is quite flat. For each specimen of the above three the SAD, CBED, and LACBED patterns were taken from each grain and from the grain boundary. These patterns are of the type <110>. λ and μ will be used from now on to refer, respectively, to the two grains in each specimen. Fig.5.5 is a BF image taken from specimen "ia". Fig.5.6, 5.7 and 5.8 are the SAD, CBED, and LACBED patterns, respectively, taken from the specimen "ia" grain pair and from the grain boundary.

The SAD patterns in Fig.5.6 have been solved and indexed for both grains and grain boundary. The careful study of these patterns showed that the SAD patterns from grains A_c and B_c are of the type <110> and rotated by an angle 70.5^0 (or its complement) with respect to each other about the common zone axis $[110]_\lambda$. In fact the author has chosen to index the <110> zone axes as $[110]_\lambda$ and $[101]_\mu$ with respect to the two crystal coordinate frames. This implies that the orientation relationship

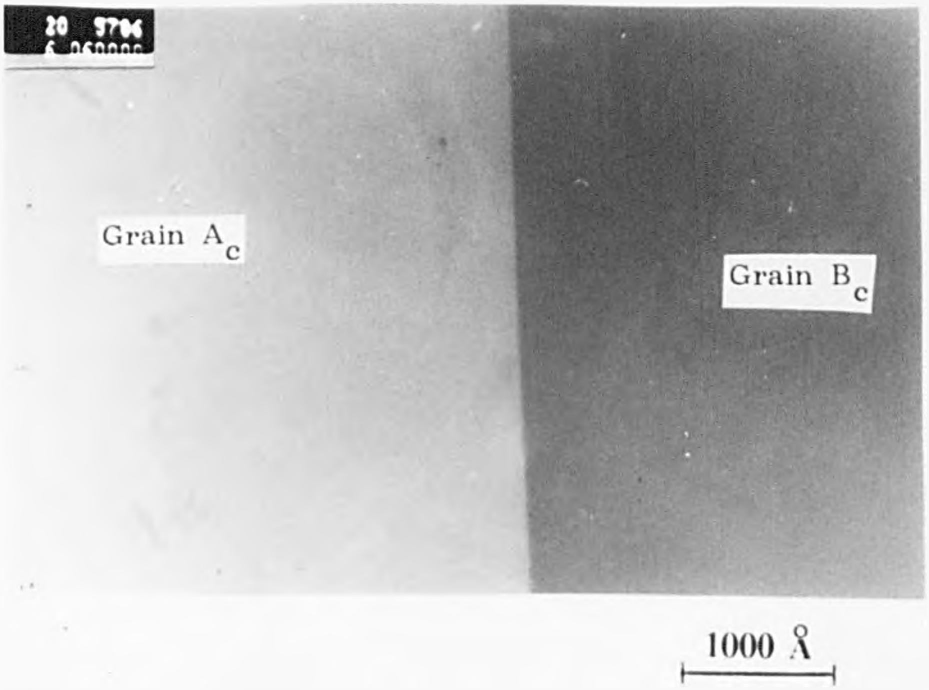

Fig. 5.5. A bright field micrograph taken from Ge specimen "ia" from an area containing $\Sigma = 3(1\,\bar{1}\bar{1})$, boundary.

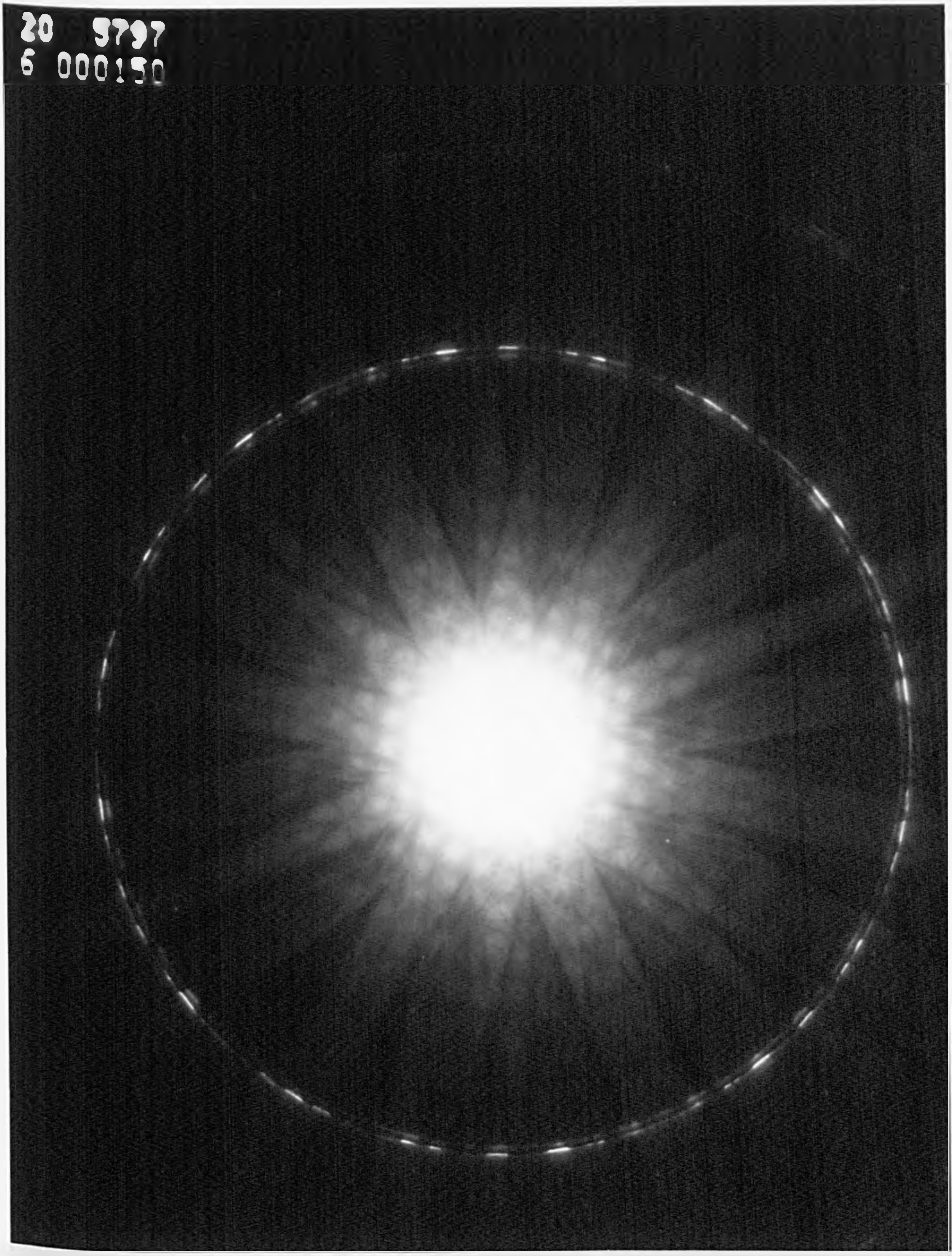

Fig. 5.6(a). 1-$[110]_{\gamma}$ Low-camera length SAD pattern was taken from Grain A_c.

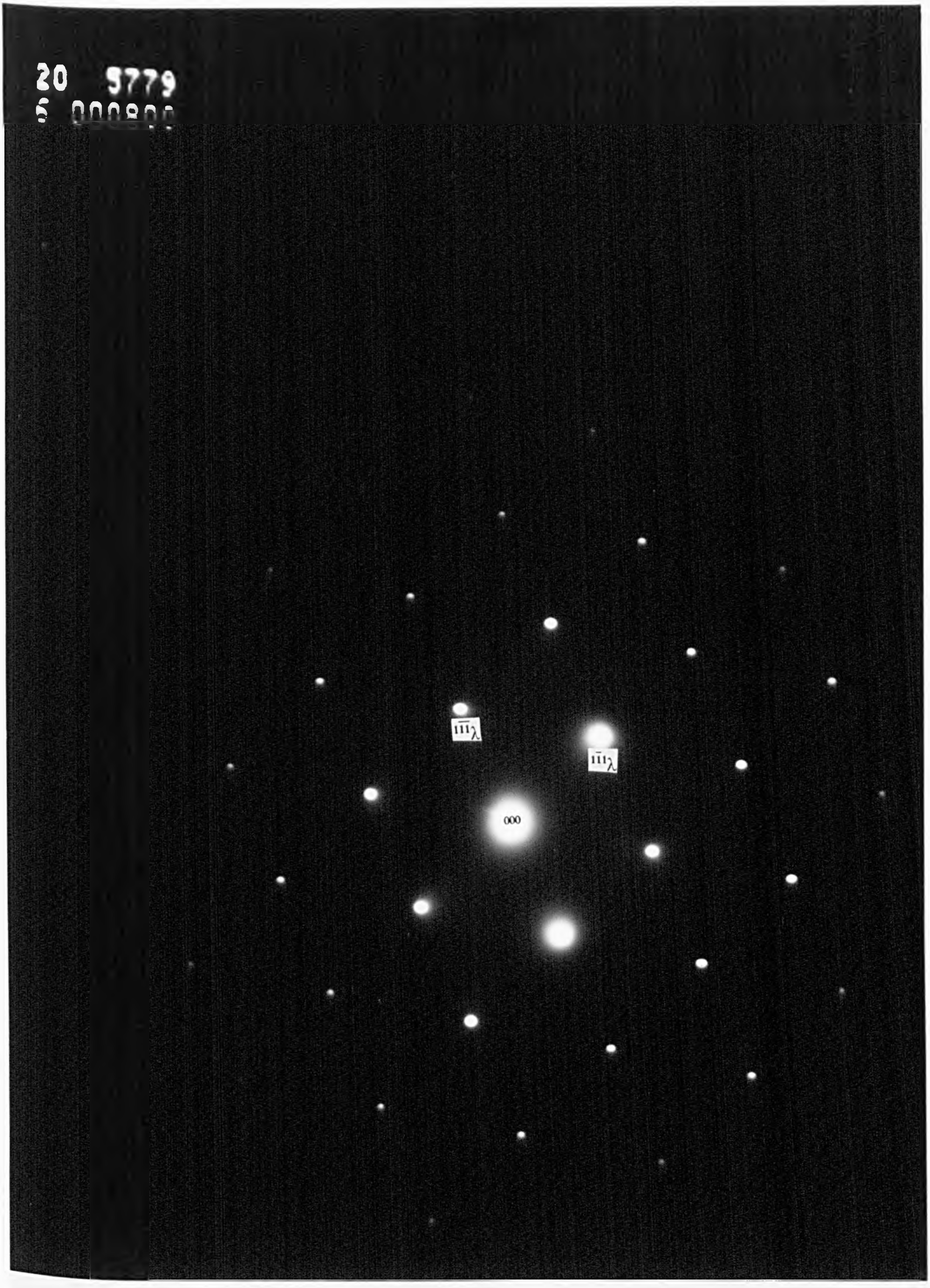

Fig. 5.6(a). 2-[110]$_\lambda$ High-camera length SAD pattern was taken from Grain A_c.

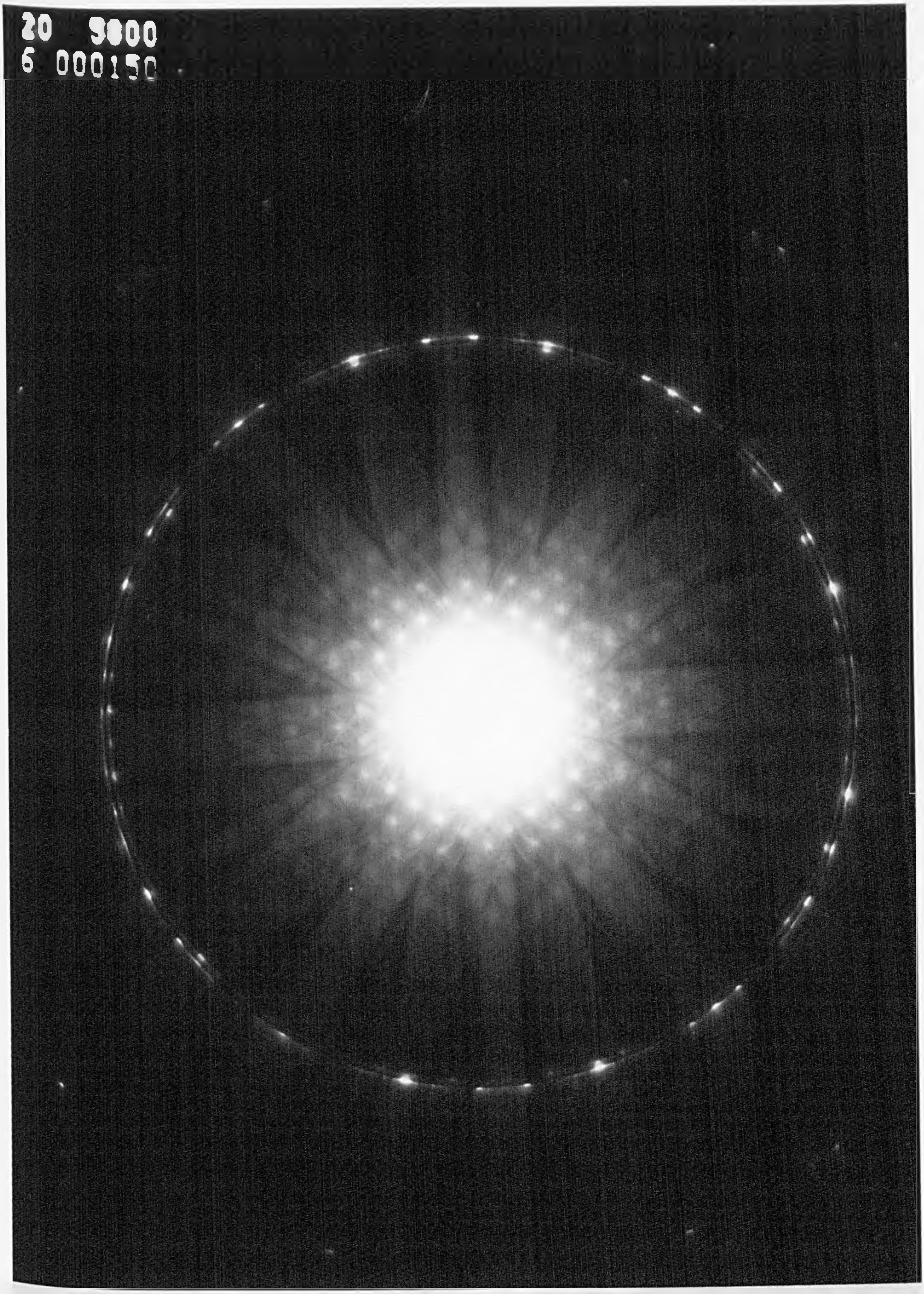

Fig. 5.6(b). 1-$[101]_\mu$ Low-camera length SAD pattern was taken from Grain B_c.

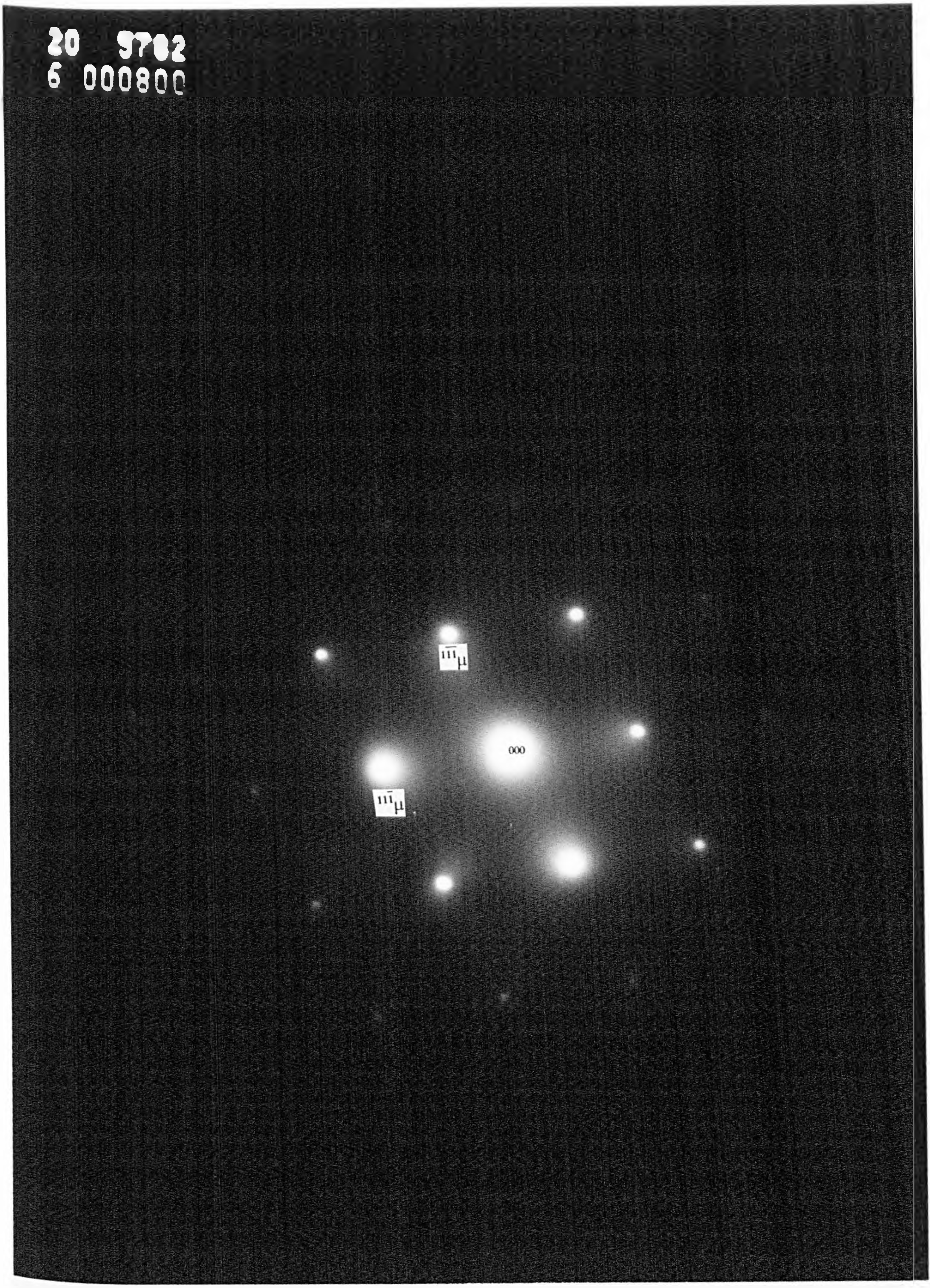

Fig. 5.6(b). 2-$[101]_{\mu}$ High-camera length SAD pattern was taken from Grain B_c.

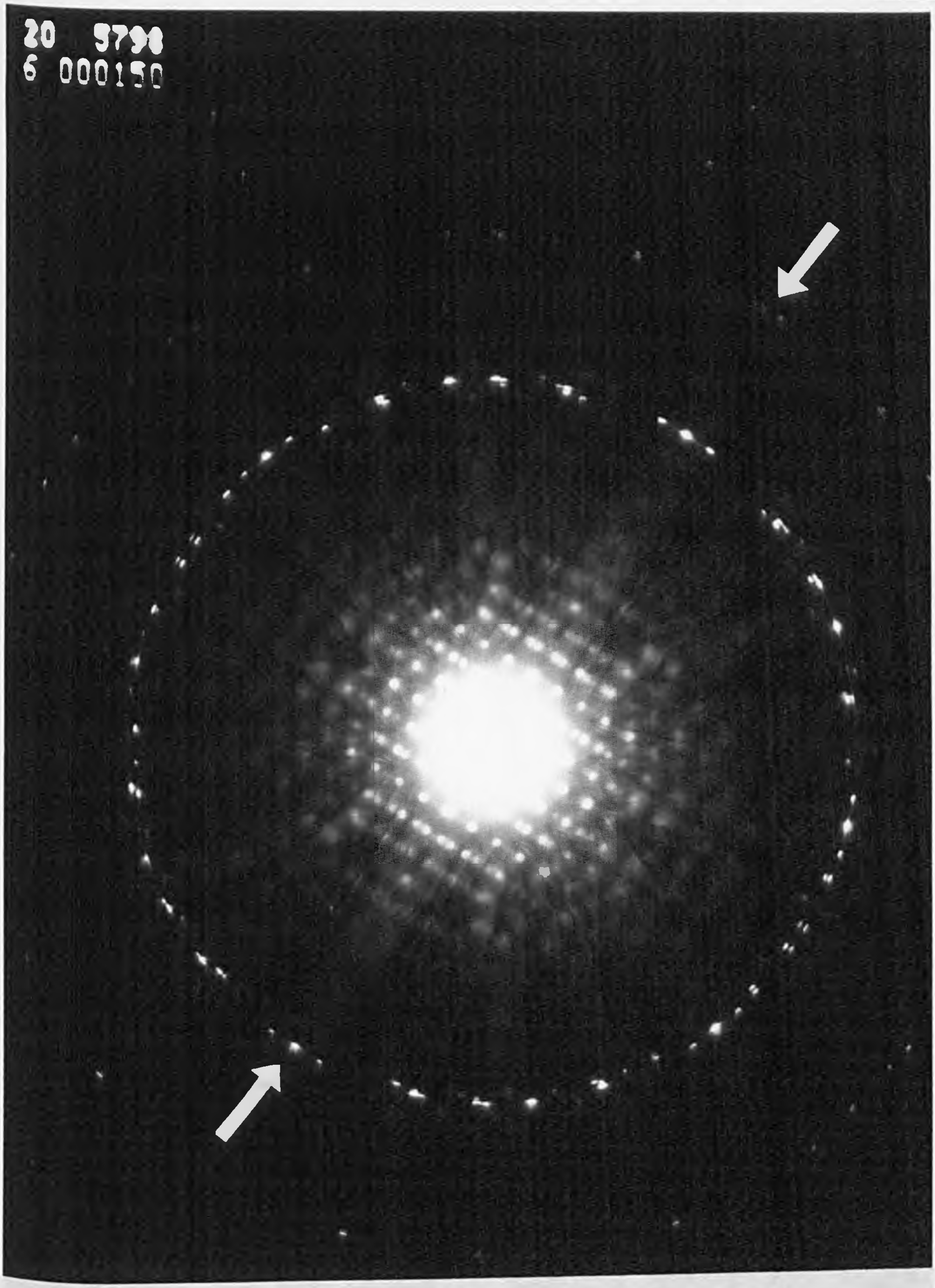

Fig. 5.6(c). 1-$[110]_\lambda/[101]_\mu$ Low-camera length SAD pattern was taken from grain boundary between Grains A_c and B_c. A trace of the boundary plane $(1\bar{1}\bar{1})_\lambda$ is indicated.

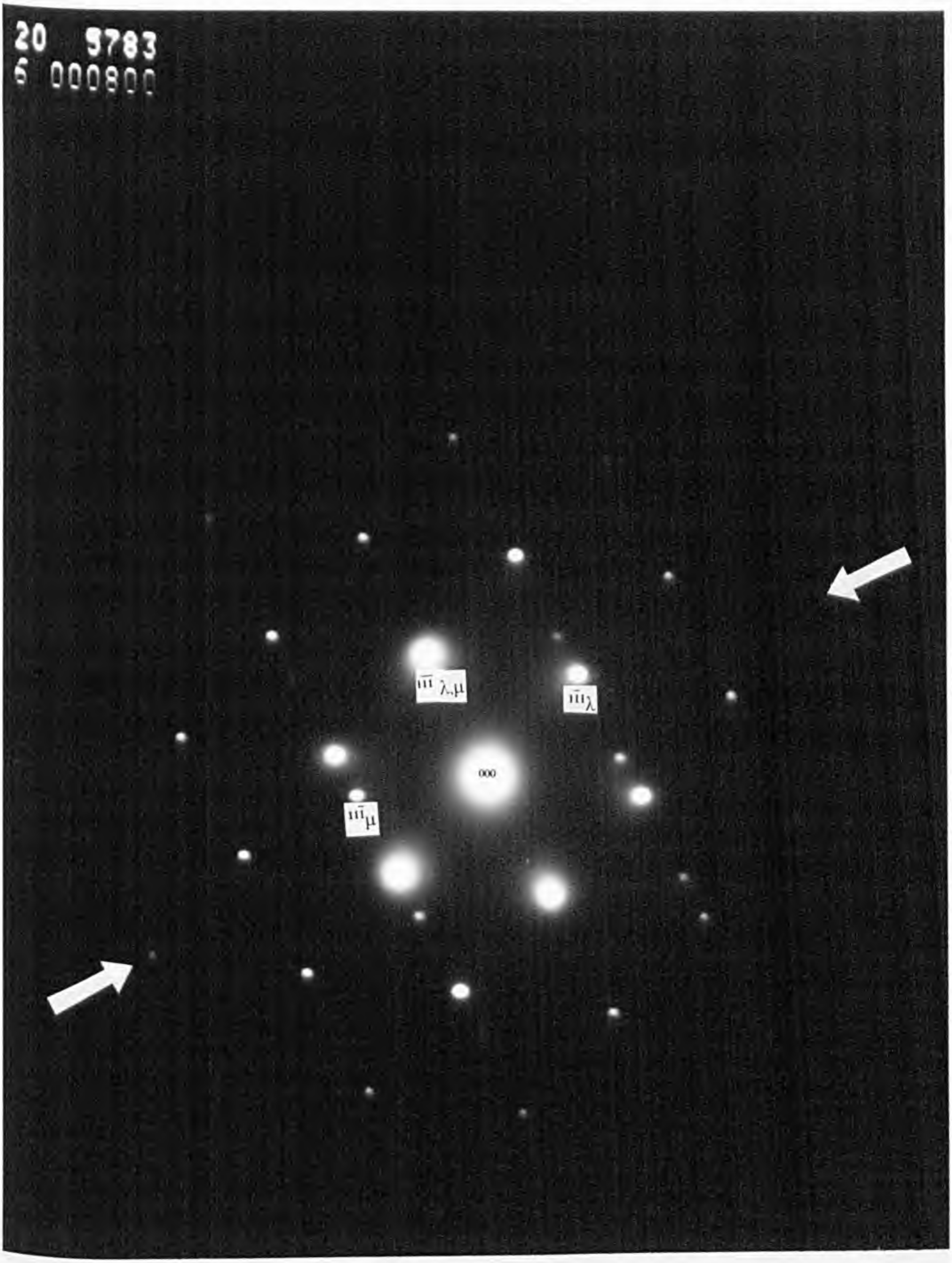

Fig. 5.6(c). 2-$[110]_\lambda/[101]_\mu$ High-camera length SAD pattern was taken from grain boundary between Grains A_c and B_c. A trace of the boundary plane $(1\overline{11})_\lambda$ is indicated.

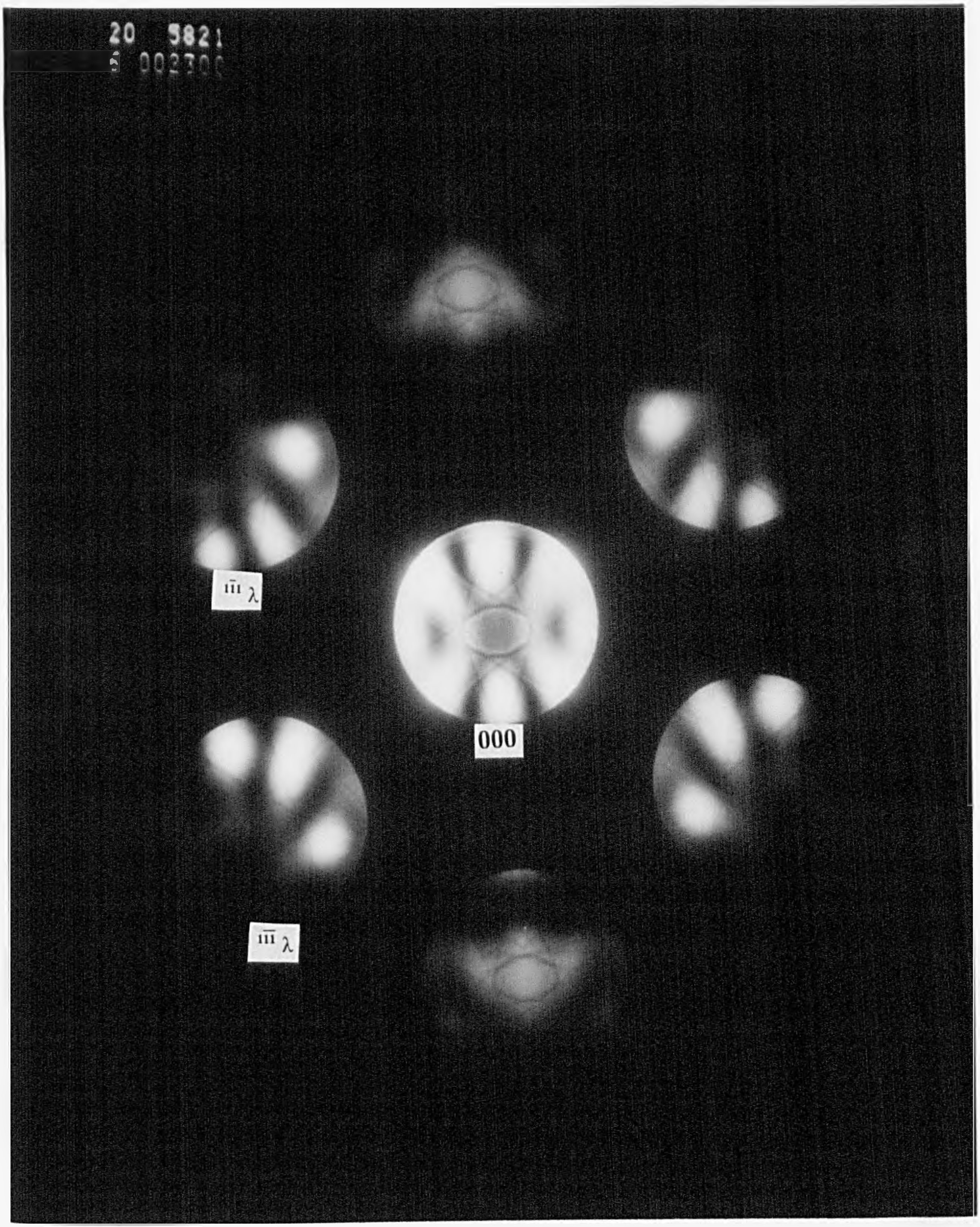

Fig. 5.7(a). $[110]_\lambda$ High-camera length CBED pattern was taken from Grain A_c.

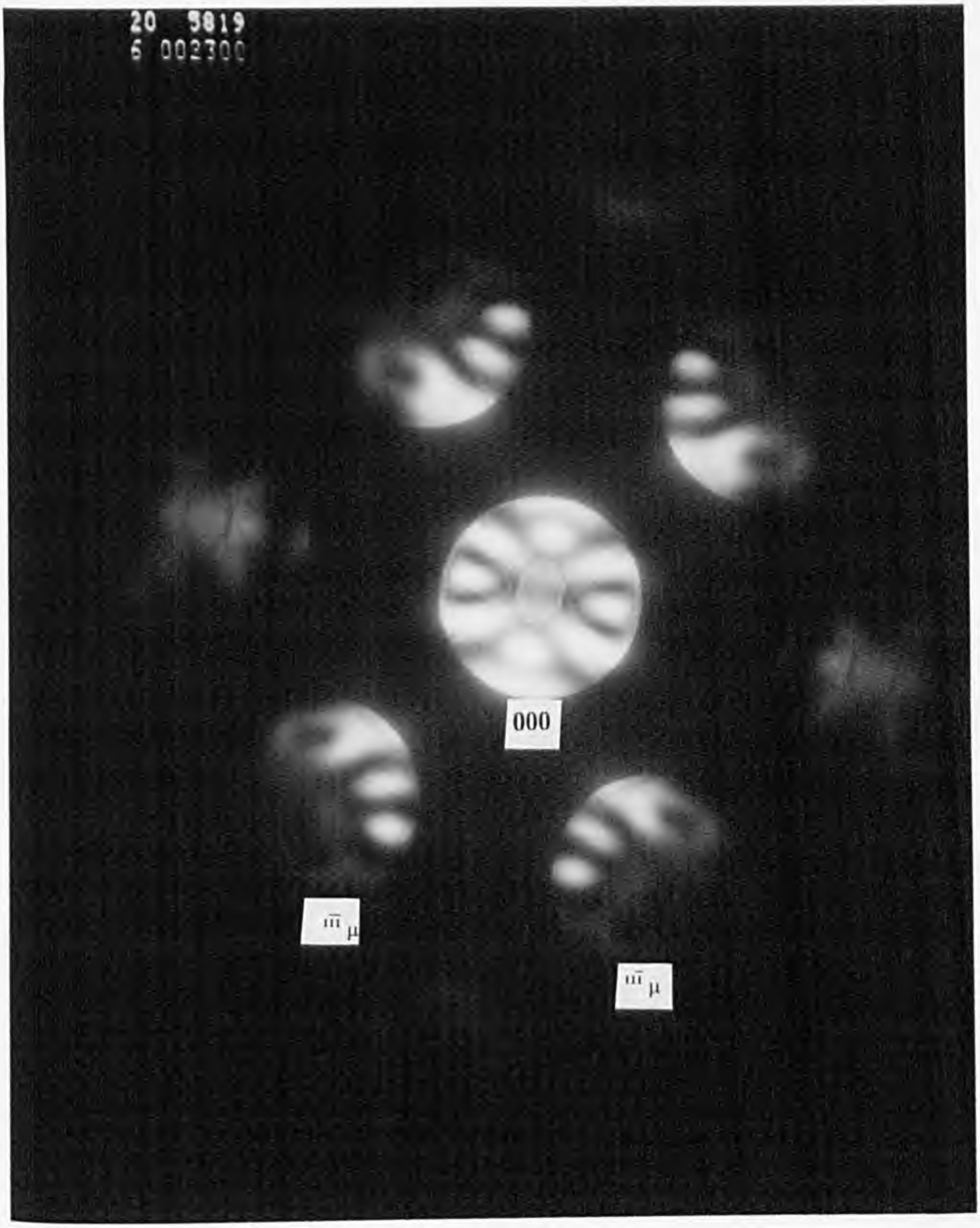

Fig. 5.7(b). $[101]_\mu$ High-camera length CBED pattern was taken from Grain B_c.

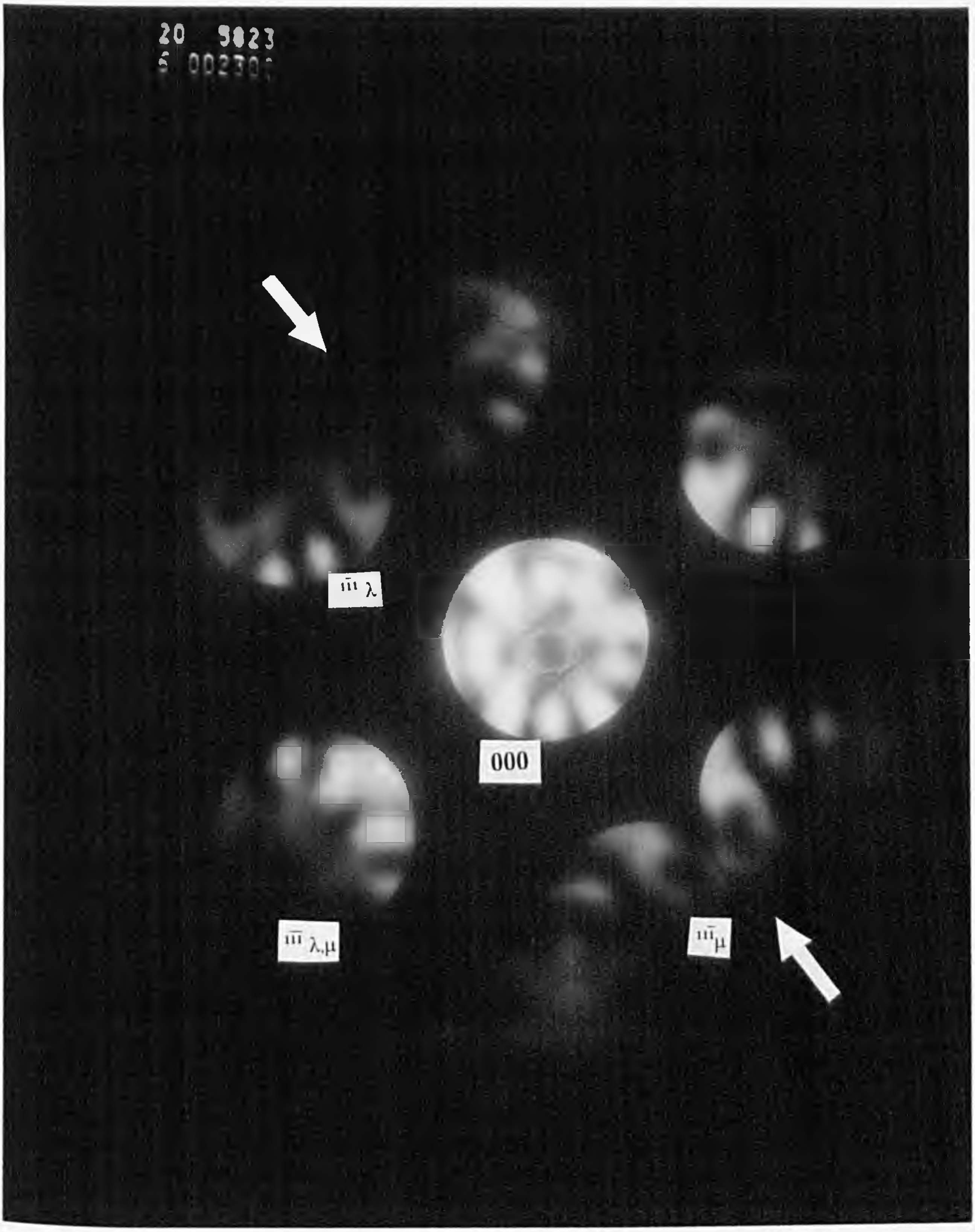

Fig. 5.7(c). $[110]_\lambda/[101]_\mu$ High-camera length CBED pattern was taken from grain boundary between Grains A_c and B_c. A trace of the boundary plane $(1\overline{11})_\lambda$ is indicated.

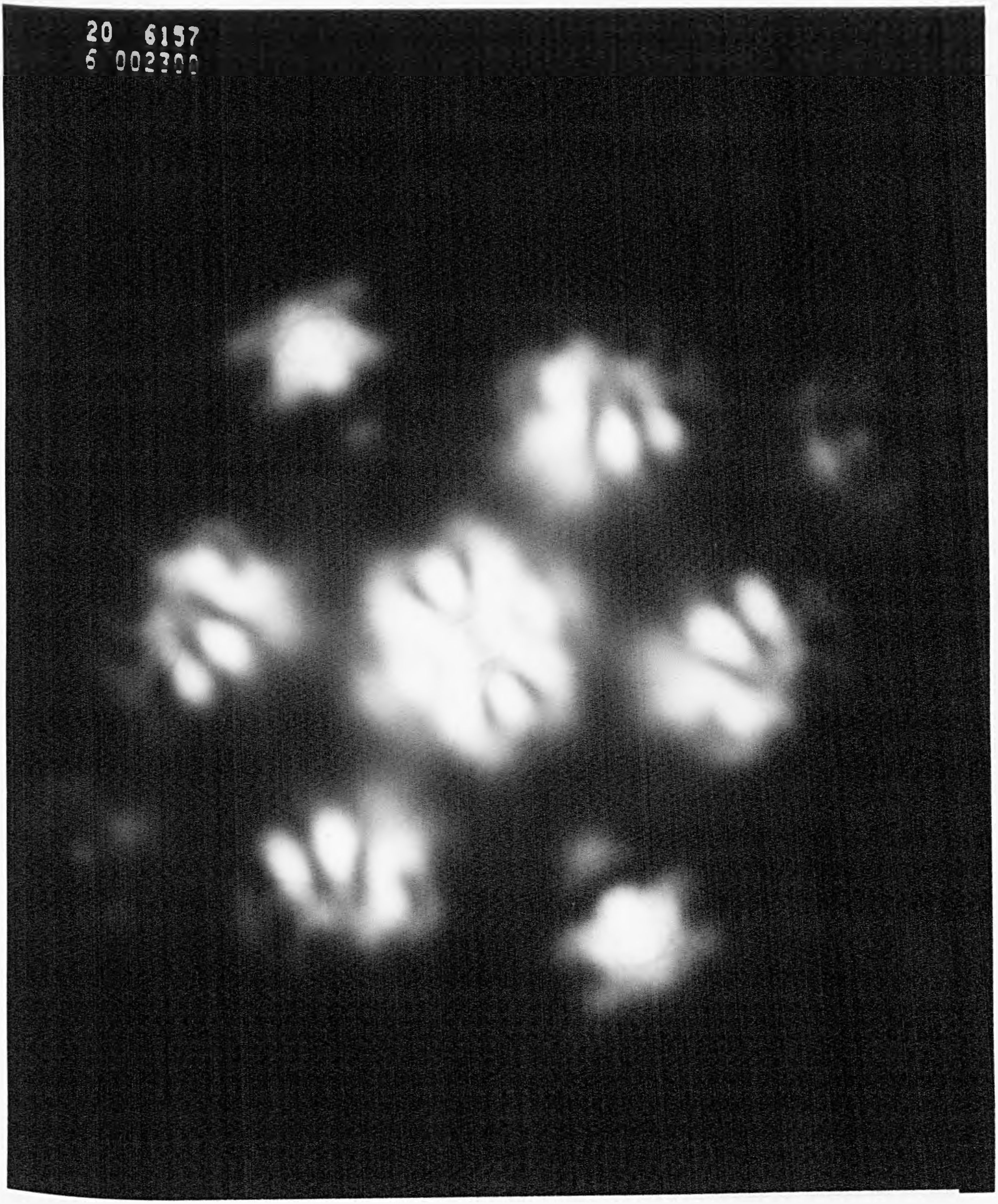

Fig. 5.8(a). $[110]_{\lambda}$ LACBED pattern was taken from Grain A_c.

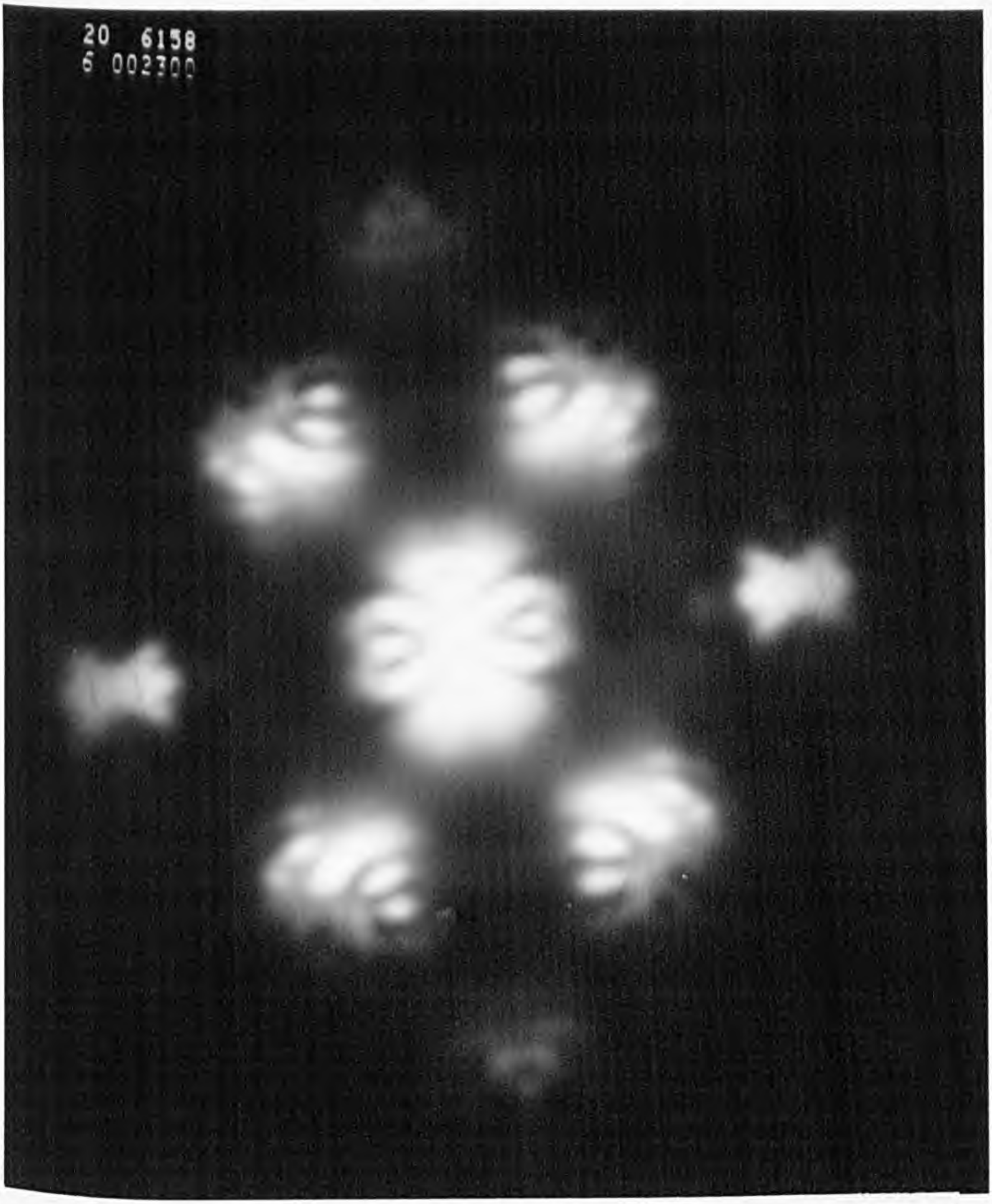

Fig. 5.8(b). $[101]_{\mu}$ LACBED pattern was taken from Grain B_c.

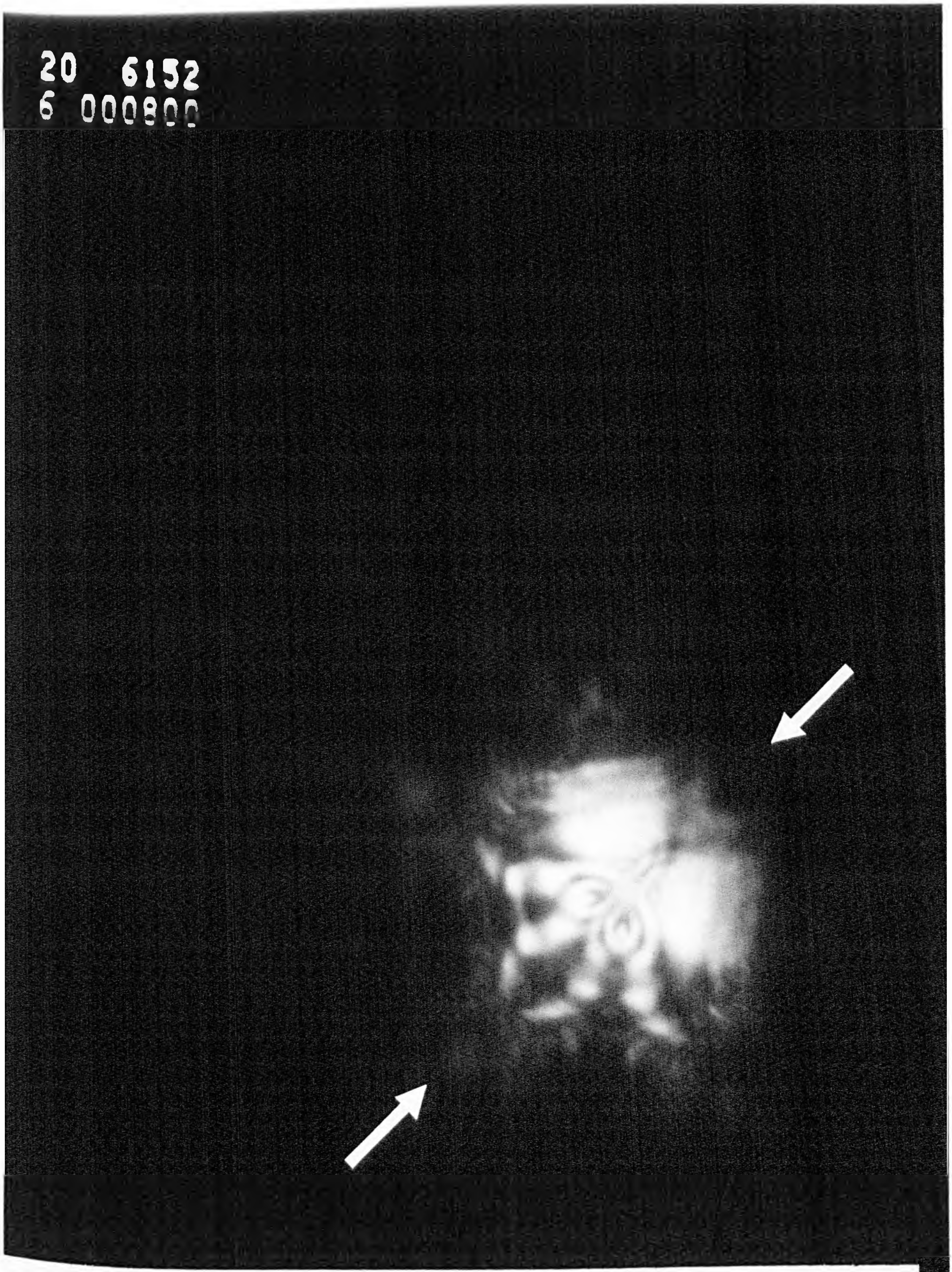

Fig. 5.8(c). $[110]_\lambda/[101]_\mu$ LACBED pattern was taken from grain boundary between Grains A_c and B_c. A trace of the boundary plane $(1\bar{1}\bar{1})_\lambda$ is indicated.

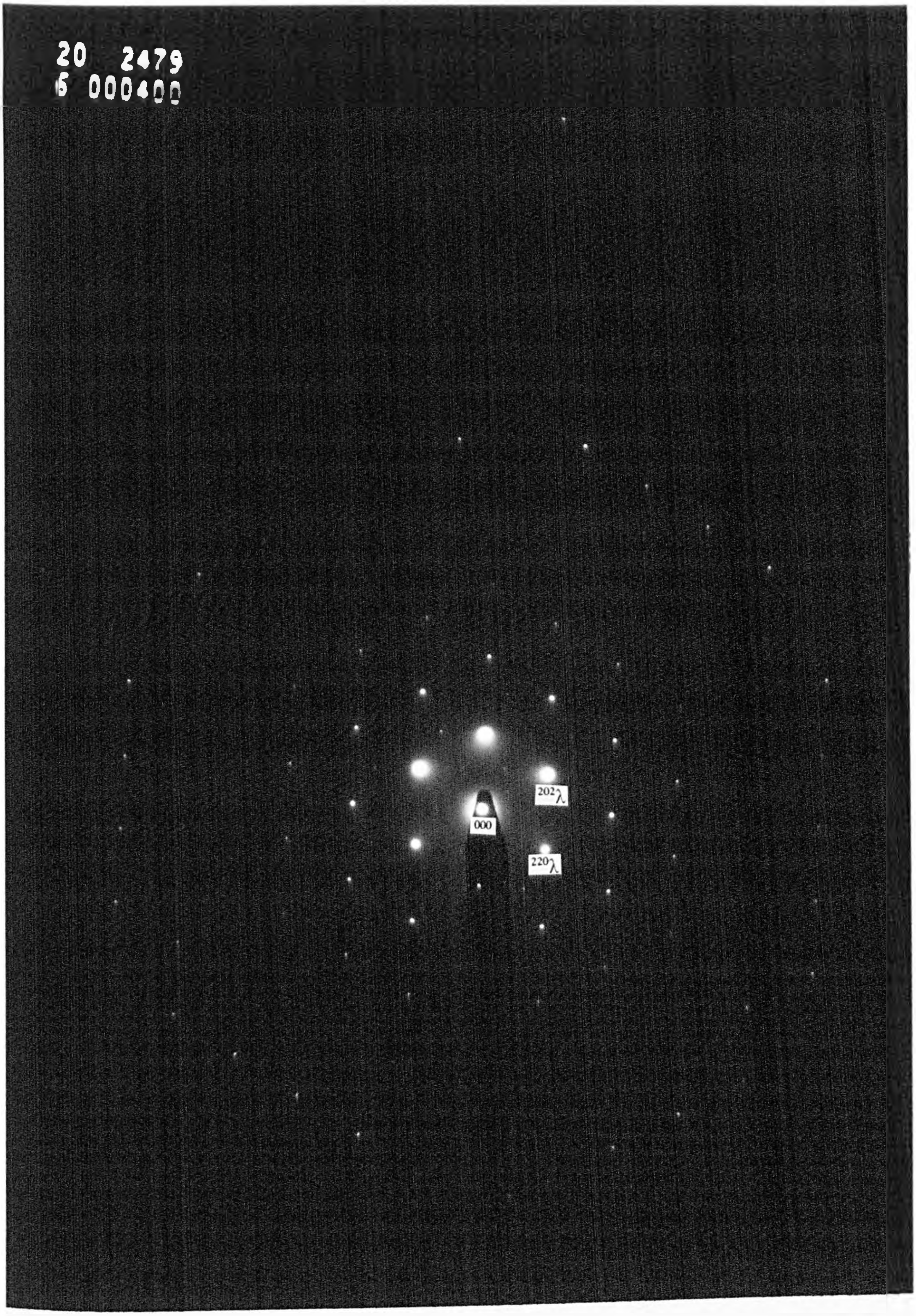

Fig. 5.8(d). $[1\bar{1}\bar{1}]_\lambda$ SAD pattern was taken from a $\Sigma = 3(1\bar{1}\bar{1})_\lambda$ "plan-view" specimen.

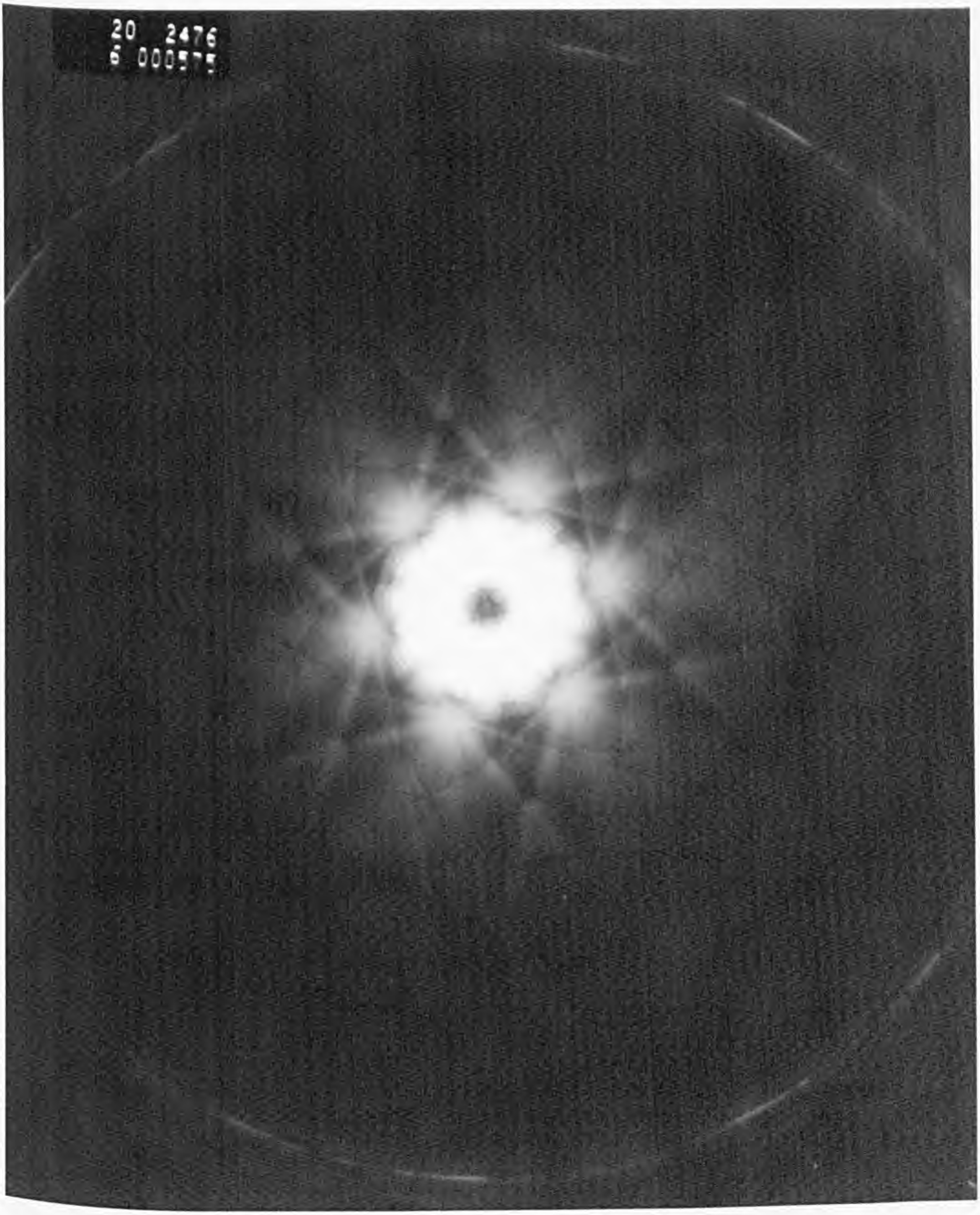

Fig. 5.8(e). $[\,1\bar{1}\bar{1}\,]_\lambda$ CBED pattern was taken from a $\Sigma = 3(\,1\bar{1}\bar{1}\,)_\lambda$ "plan-view" specimen.

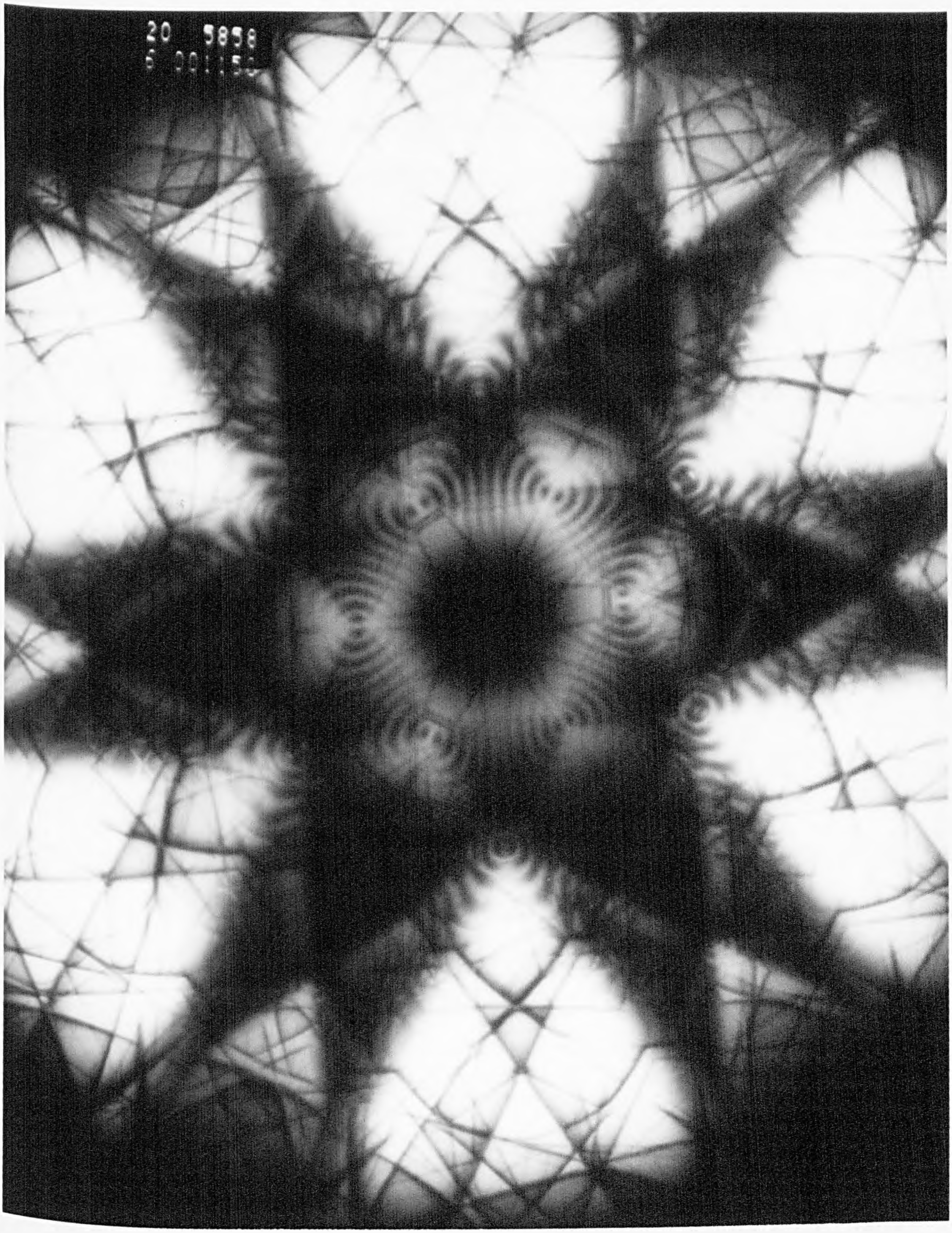

Fig. 5.8(f). [$1\bar{1}\bar{1}$]$_\lambda$ LACBED pattern was taken from a $\Sigma = 3(1\bar{1}\bar{1})_\lambda$ "plan-view" specimen.

5.2.3. THE $\Sigma = 3$ "EDGE-ON" SPECIMEN "iva".

Fig.5.9 is a BF image taken from specimen "iva" from an area containing the grain boundary. The low- and high-camera lengths SAD patterns taken from grains A_e and D_e and grain boundary are shown in Fig.5.10(a), (b) and (c), respectively. The SAD pattern from grain A_e can be indexed as $[110]_\lambda$. The angle of rotation of these two patterns about the axis $[110]_\lambda$ is 70.5^0. The SAD pattern from the grain boundary have been indexed and some of the indices of the diffraction spots indicated as well as the trace of the boundary plane which in this case has the index $(\bar{1}1\bar{2})_\lambda$. So, the boundary plane in the case of "iva" specimen is of the type $\Sigma = 3(\bar{1}1\bar{2})_\lambda$. Fig.5.10(d), (e) and (f) are the CBED patterns taken from the grain pairs A_e and D_e and the grain boundary plane (see section 5.3.2 for the explanation of the symmetry of these patterns).

Fig.5.9 was taken from an area containing the $\Sigma = 3(\bar{1}1\bar{2})_\lambda$ grain boundary where it appeared to be flat at lower magnification. In fact this grain boundary was not exactly flat as shown in the figure but it is observed microscopically stepped in some areas. Fig.5.11 is one of our observations which is taken from an area containing the grain boundary where it is microscopically stepped. Also, the $\Sigma = 3(\bar{1}1\bar{2})_\lambda$ grain boundary is found to be unstable in some areas and dissociated into $\Sigma = 3(\bar{1}12)_\lambda$, $\Sigma = 3(1\bar{1}1)_\lambda$, $\Sigma = 9(\bar{2}\bar{1}2)_\mu$ and $\Sigma = 9(1\bar{4}\bar{1})_\mu$ as observed and recorded in the BF image shown in Fig.5.12(a). Fig.5.12(b) shows the SAD pattern taken from the dissociated boundary (fig.5.12(a)).

Fig. 5.9. A bright field micrograph taken from "iva" Ge "edge-on" specimen.

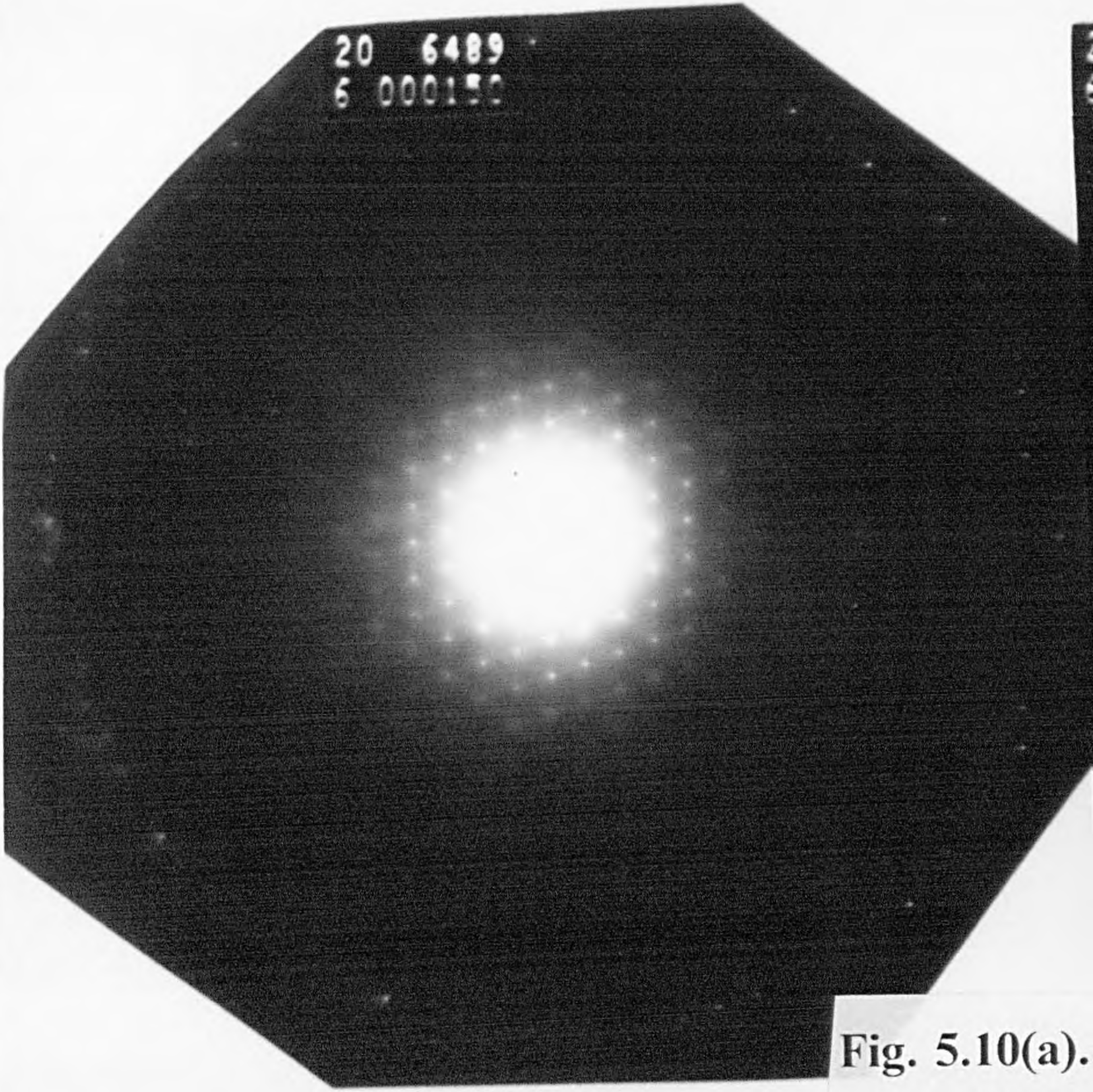

Fig. 5.10(a).

(a)

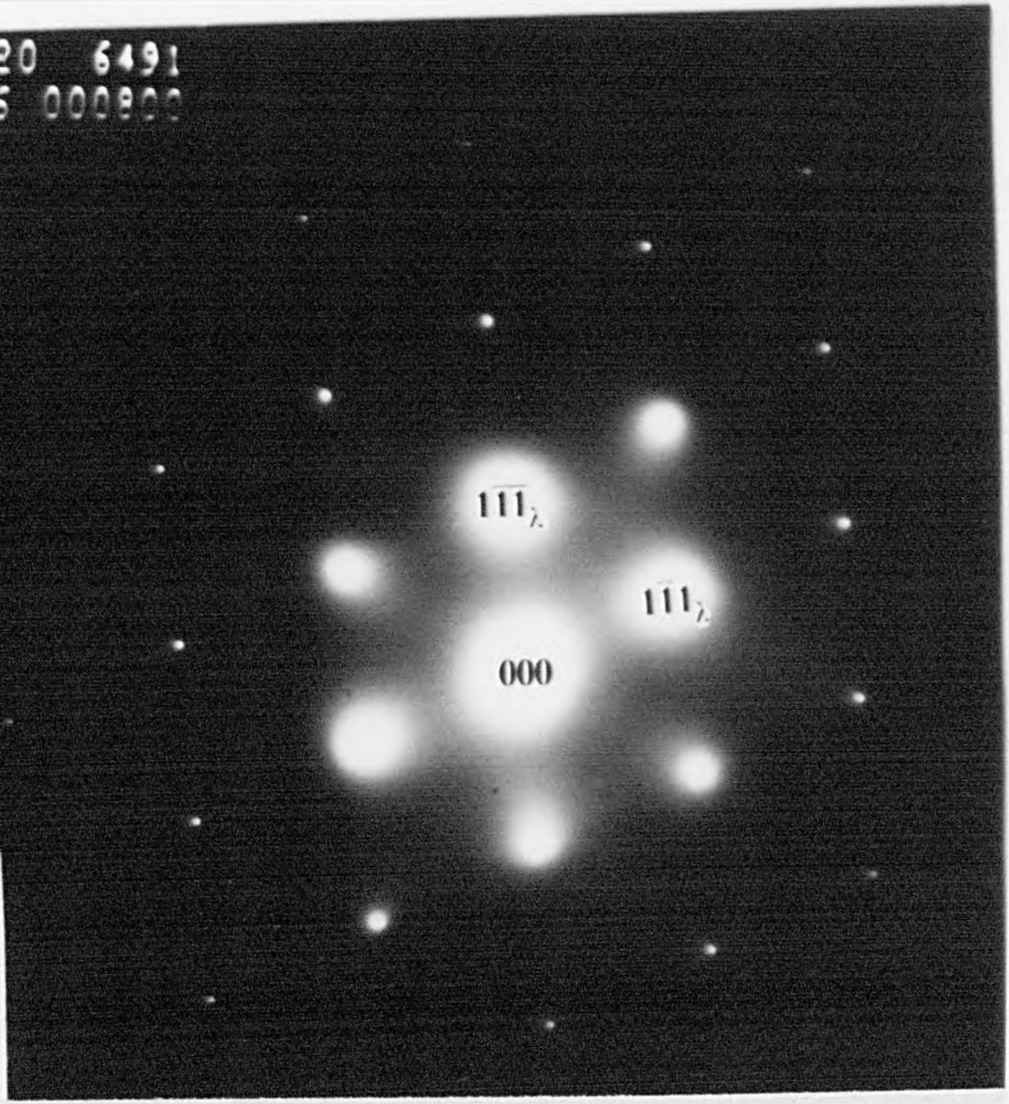

$[110]_\gamma$ Low- and High-camera lengths SAD patterns were taken from Grain A_e.

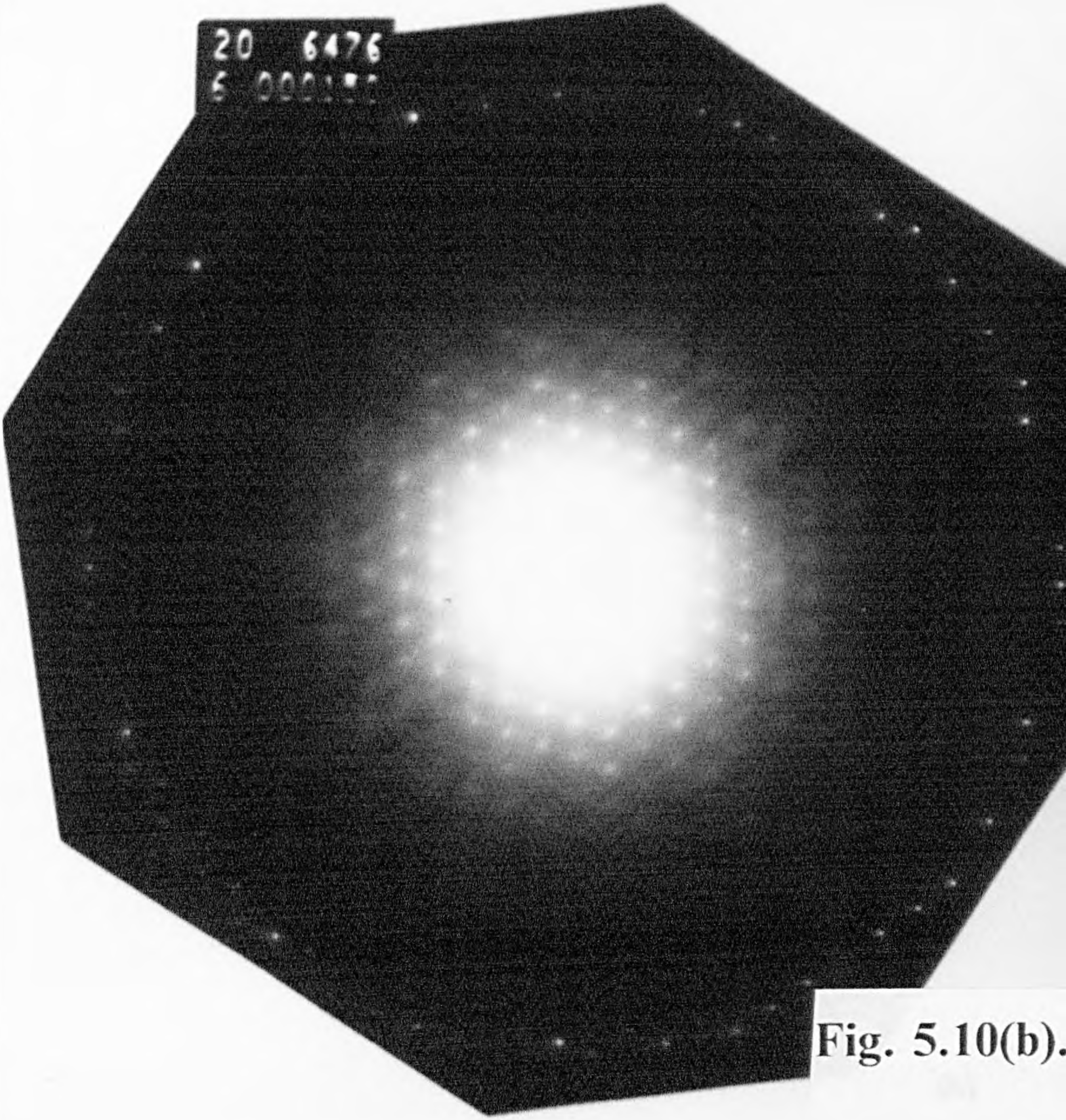

Fig. 5.10(b).

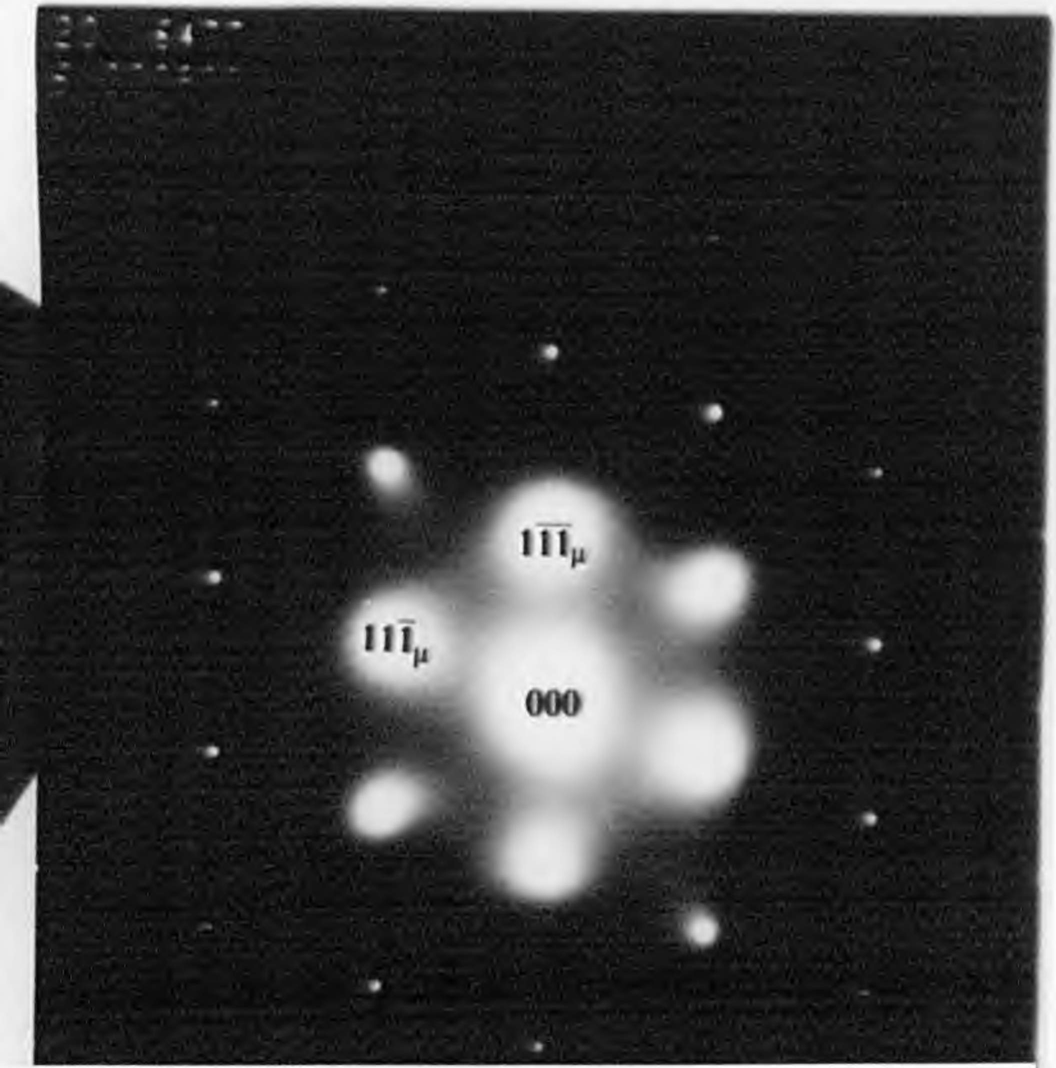

$[101]_{\mu}$ Low- and High-camera lengths SAD patterns were taken from Grain B_e.

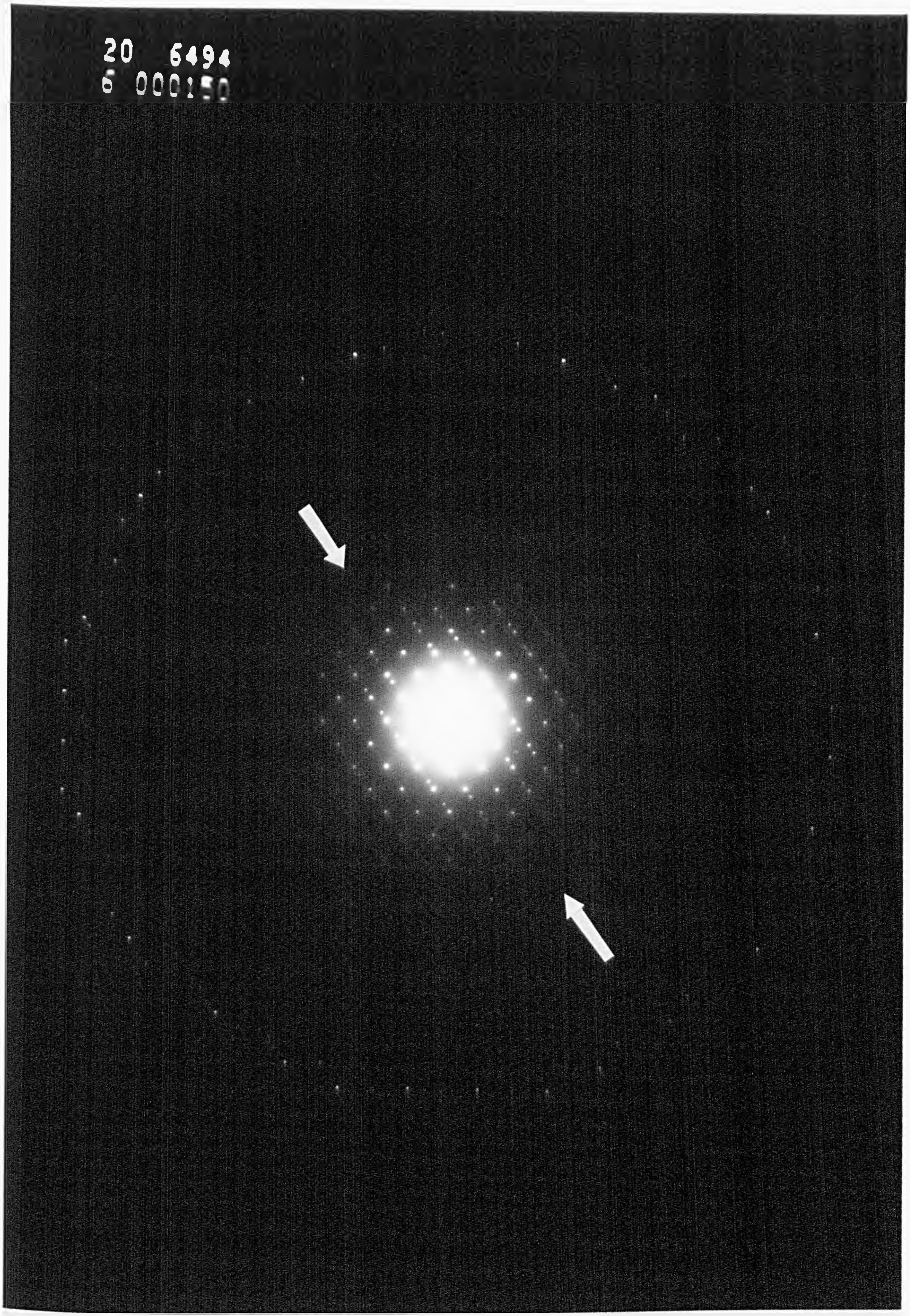

Fig. 5.10(c). 1-$[110]_\lambda/[101]_\mu$ Low-camera length SAD pattern was taken from grain boundary between Grains A_e and B_e. A trace of the boundary plane $(\bar{1}1\bar{2})_\lambda$ is indicated.

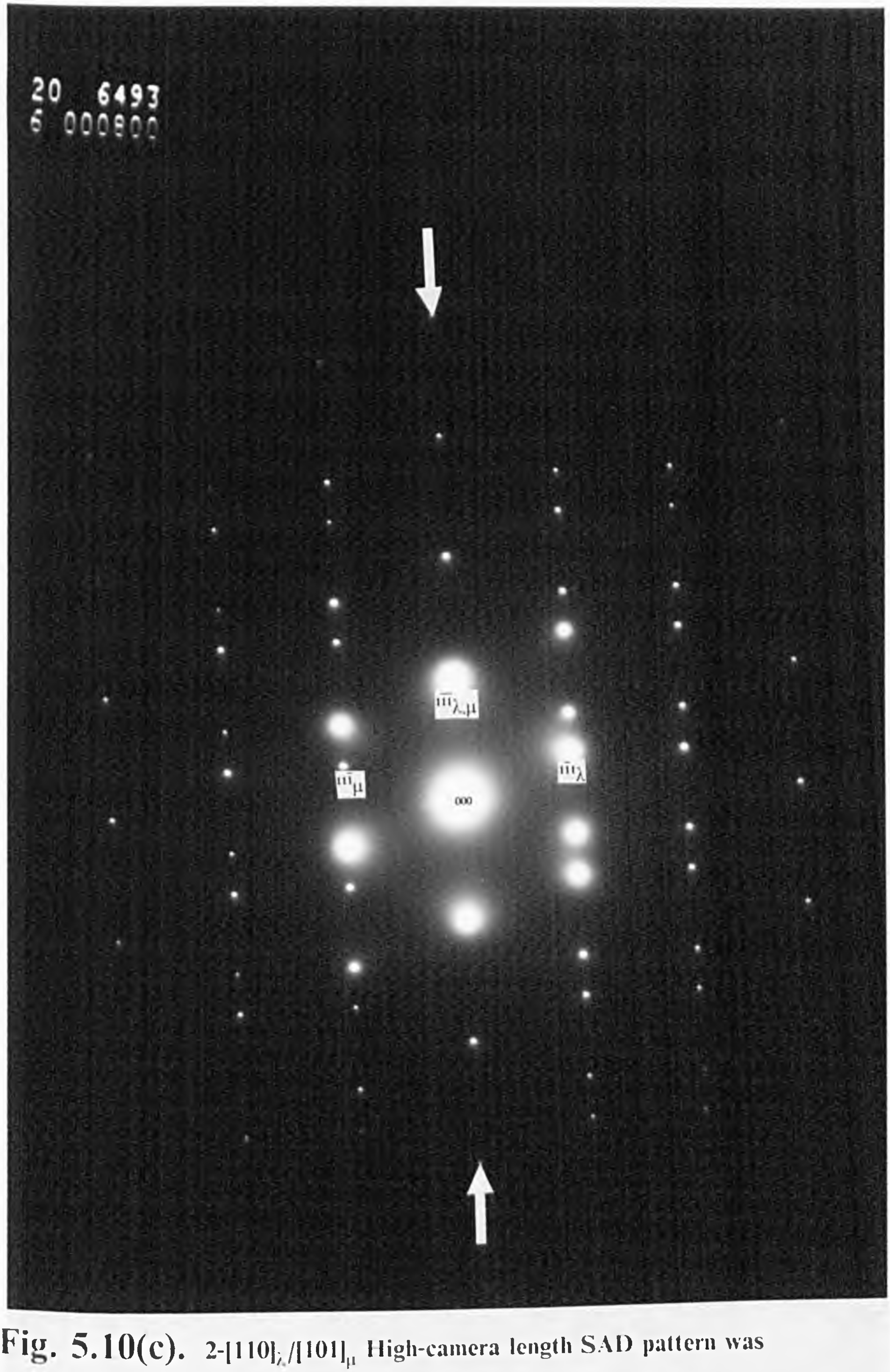

Fig. 5.10(c). 2-$[110]_{\lambda}/[101]_{\mu}$ High-camera length SAD pattern was taken from grain boundary between Grains A_e and B_e. A trace of the boundary plane $(\bar{1}1\bar{2})_{\lambda}$ is indicated.

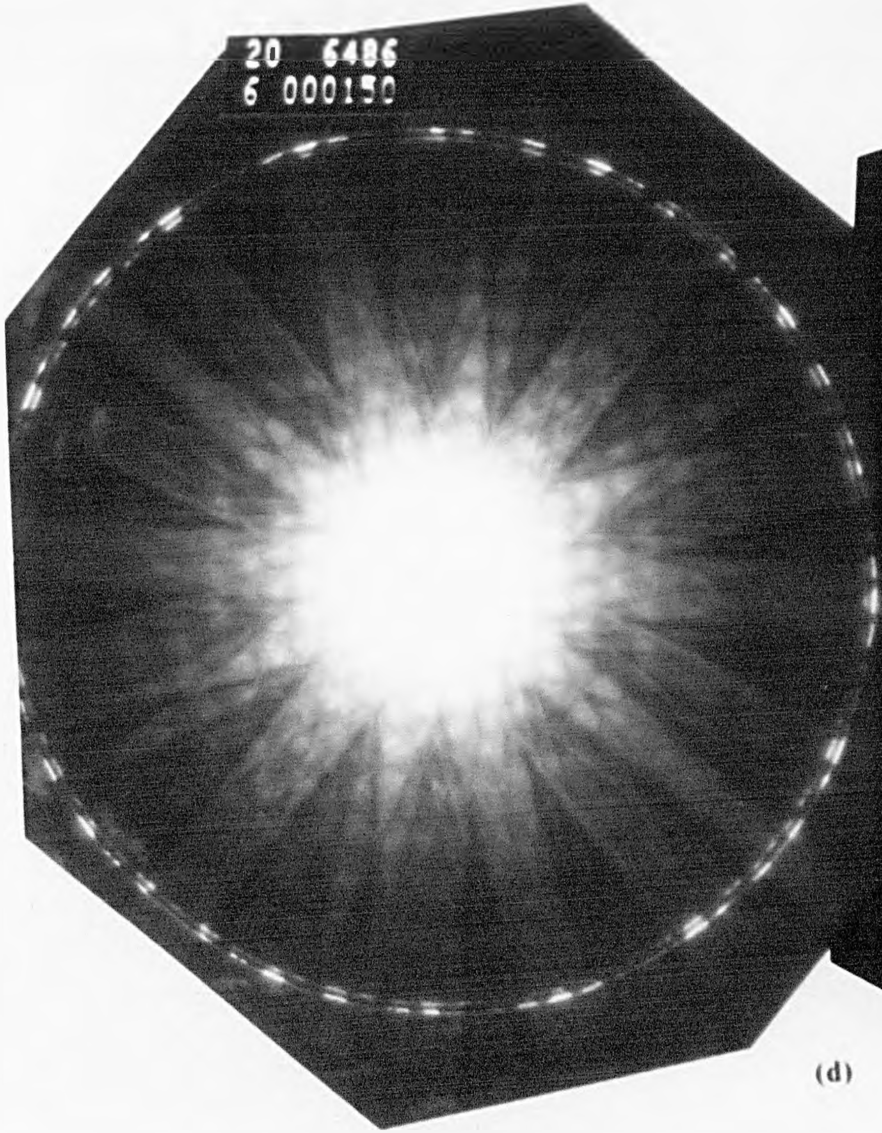

(d)

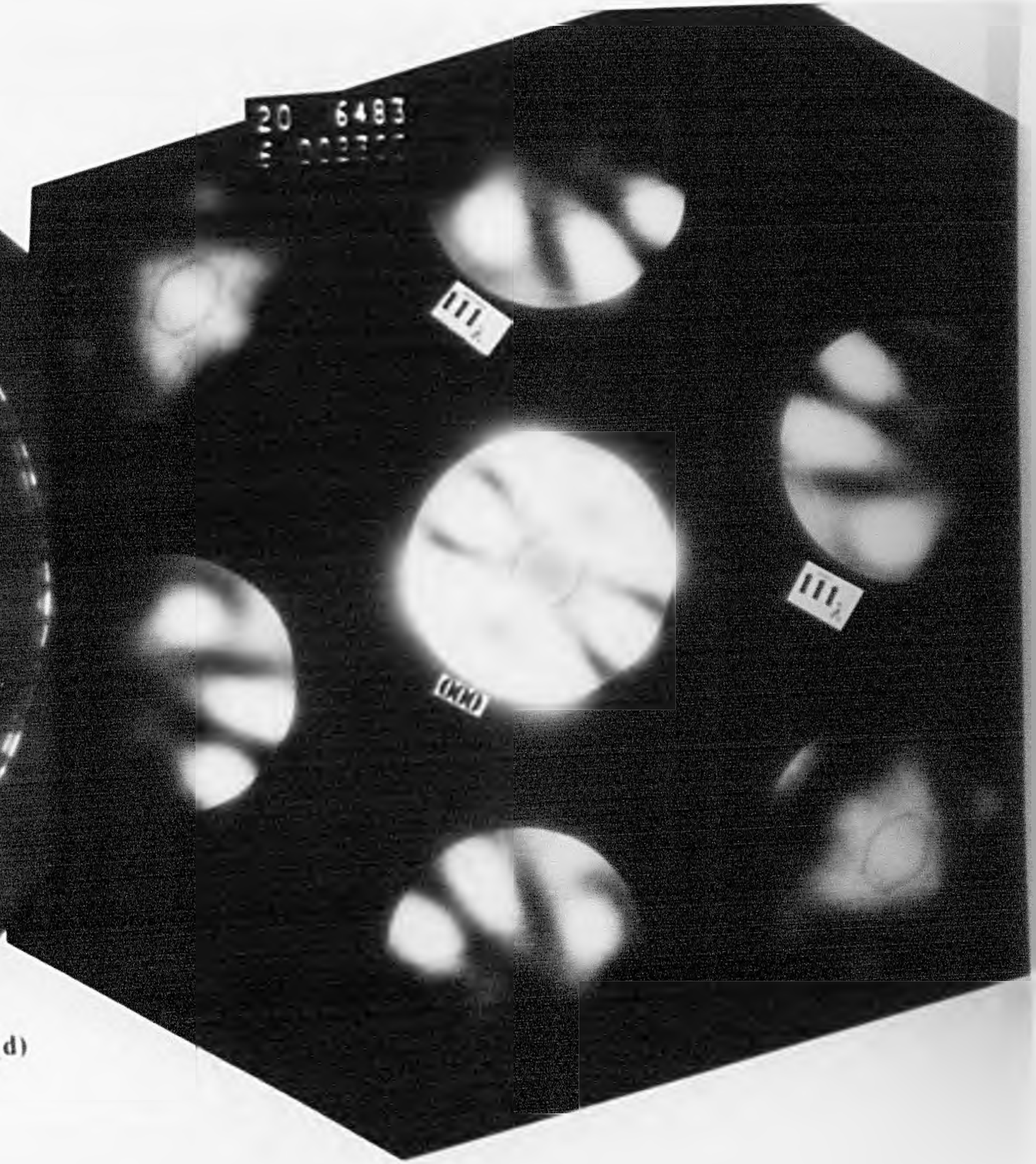

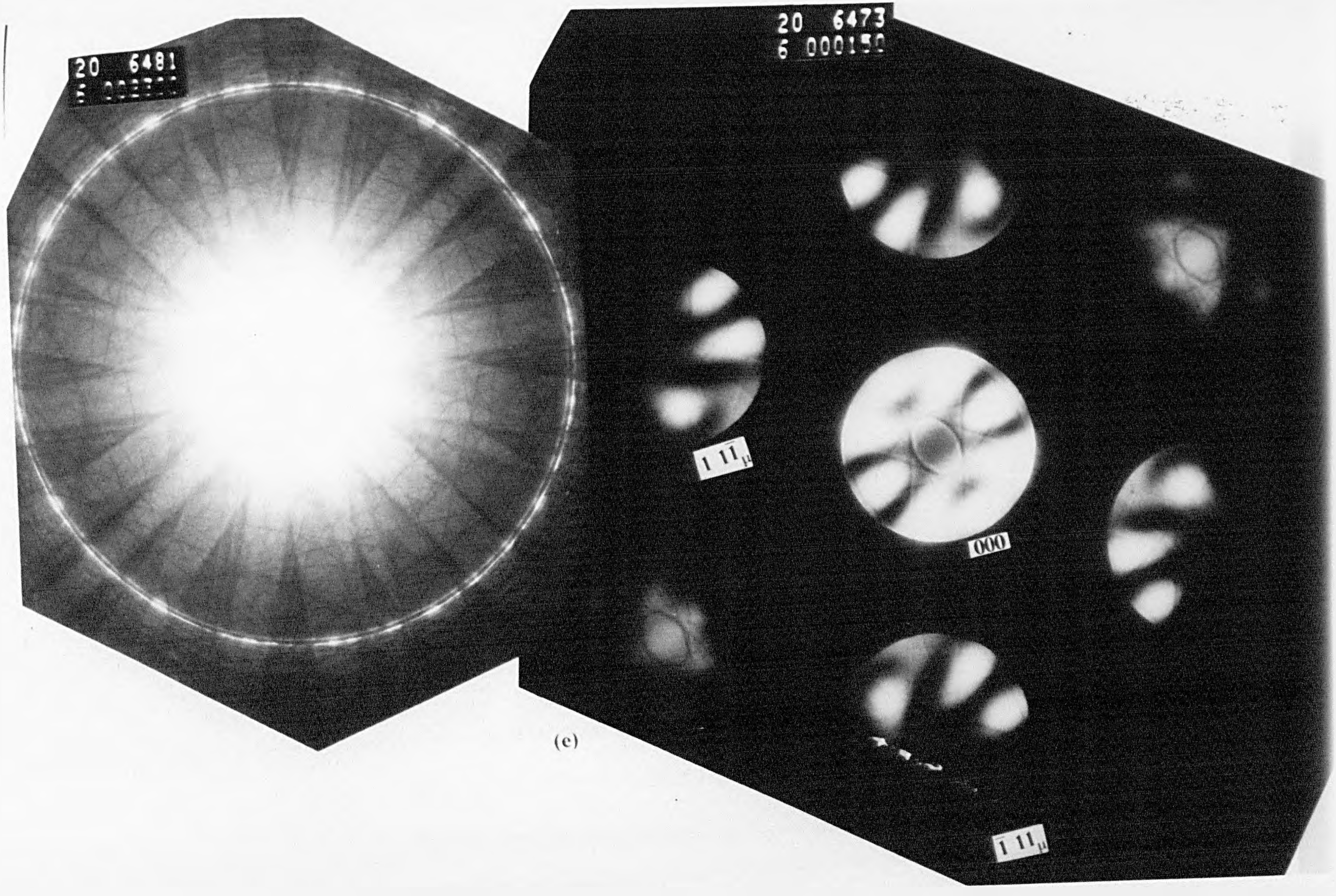

(e)

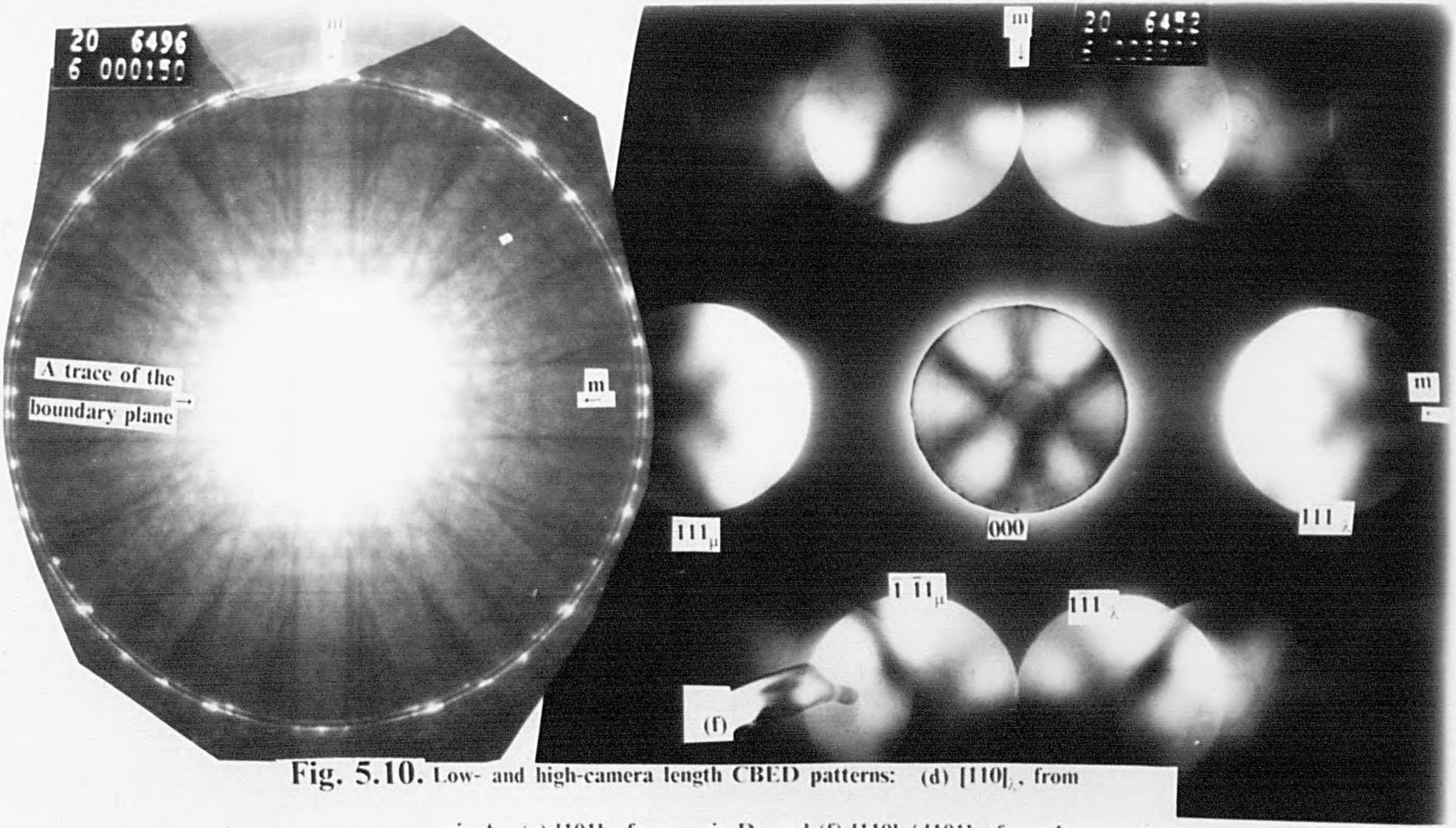

Fig. 5.10. Low- and high-camera length CBED patterns: (d) $[110]_\lambda$, from grain A_e, (e) $[101]_\mu$, from grain D_e and (f) $[110]_\lambda$ / $[101]_\mu$, from the boundary between the grain pair A_e-D_e. A trace of the boundary plane $(112)_\lambda$ is indicated.

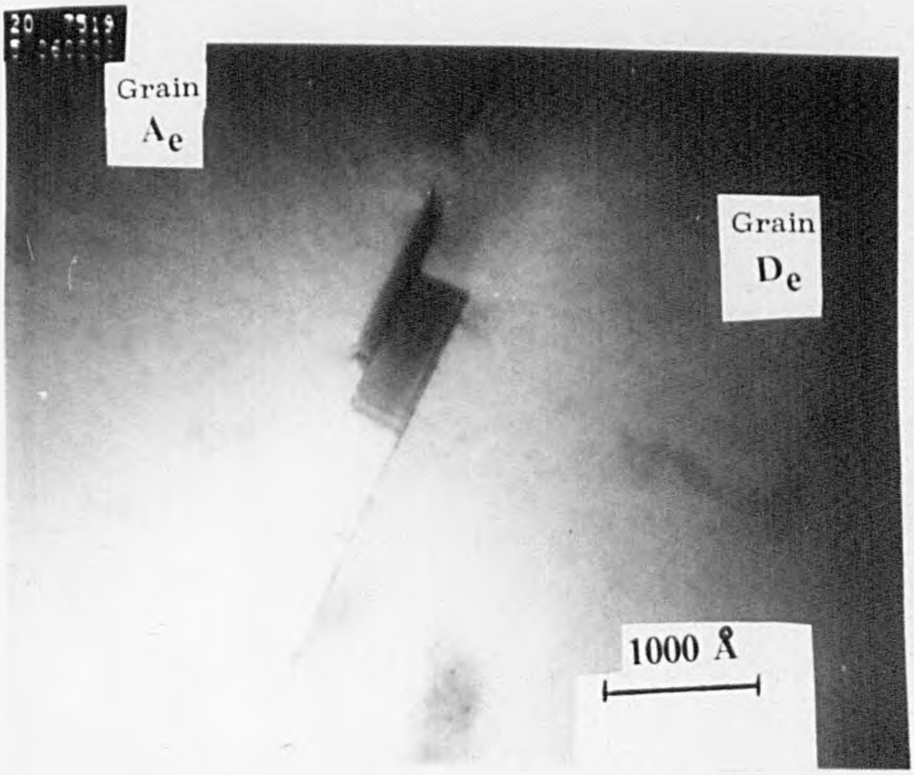

Fig. 5.11. A bright field micrograph of the stepped $\Sigma = 3(\bar{1}1\bar{2})_A$ "edge-on" grain boundary.

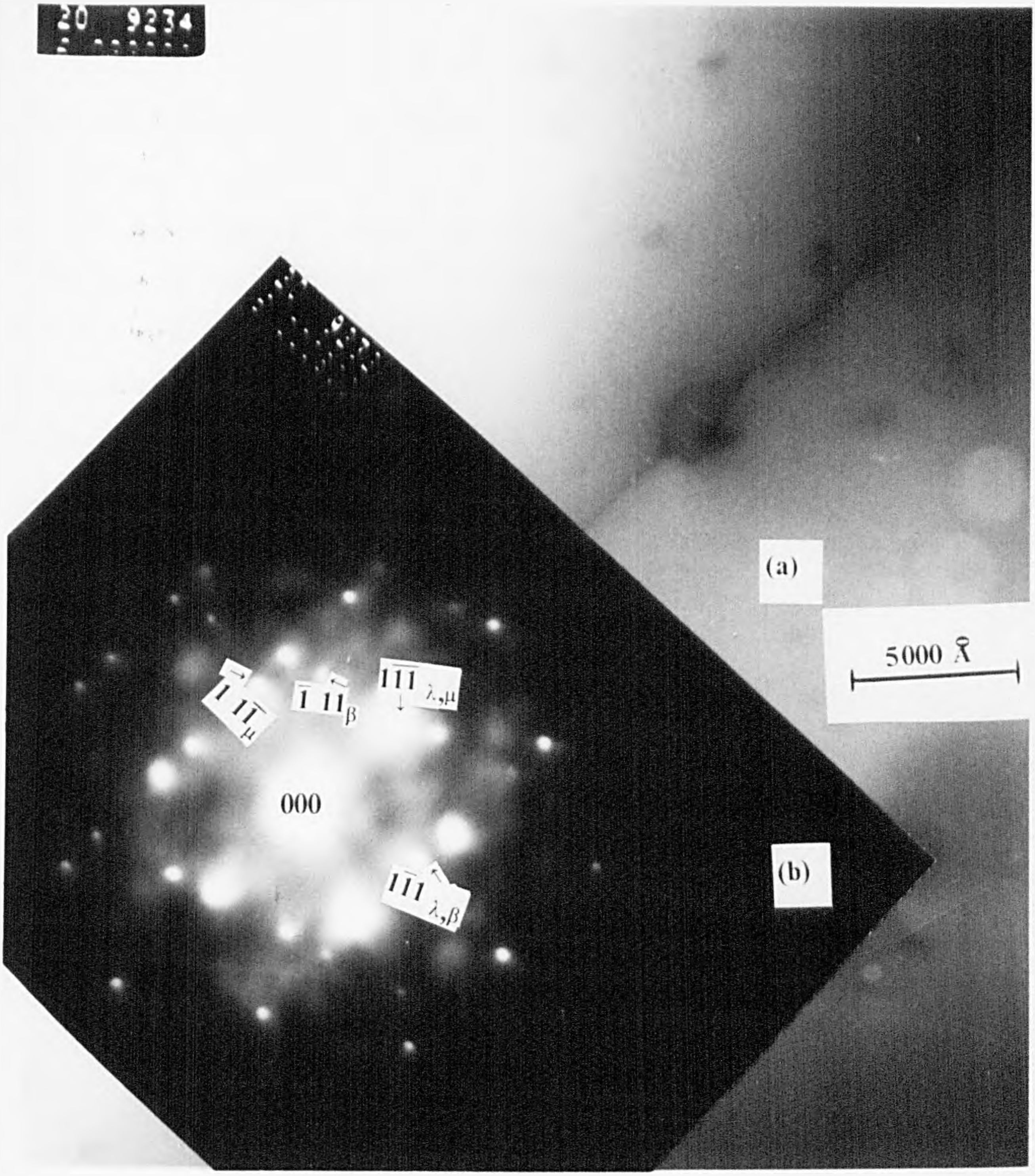

Fig. 5.12. (a) A bright field micrograph of the facetted $\Sigma = 3(\bar{1}1\bar{2})_{\lambda}$ "edge-on" grain boundary.

(b) SAD pattern from the facetted grain boundary in (a).

5.3. $\Sigma = 3(\bar{1}1\bar{2})_\lambda$ GRAIN BOUNDARY.

The comprehensive study of the structure of the $\Sigma = 3(\bar{1}1\bar{2})_\lambda$ grain boundary in Ge has required the preparation of three different types of thin specimens for TEM *investigations*. One was a "plan-view" specimen where the direction $[\bar{1}1\bar{2}]_\lambda$ was normal to the boundary plane (as shown schematically in Fig.5.13(a)). The other two were "edge-on" specimens where the directions $[110]_\lambda$ and $[1\bar{1}\bar{1}]_\lambda$ were perpendicular to the specimen surfaces and lie in the boundary plane $(\bar{1}1\bar{2})_\lambda$ (Fig.5.13(b)).

The advantage of preparing the above mentioned three specimens was that, using a double-tilt specimen holder, one has the facility to make the electron beam sweep a wide range of incident angles with respect to the boundary. For example, making use of the two "edge-on" specimens, one can make the electron beam parallel to the directions indicated in Fig.5.13(c) keeping the boundary plane edge-on all the time to avoid double diffraction.

Extensive SAD and CBED techniques have been used to accomplish this study. In the case of "edge-on" specimens SAD and CBED patterns have been taken from both grains and grain boundary for some of the low index zones lying between the directions $[110]_\lambda$ and $[1\bar{1}\bar{1}]_\lambda$ (Fig.5.13(c)). Also in the case of the "plan-view" specimen the $[\bar{1}1\bar{2}]_\lambda$ SAD and CBED patterns have been obtained.

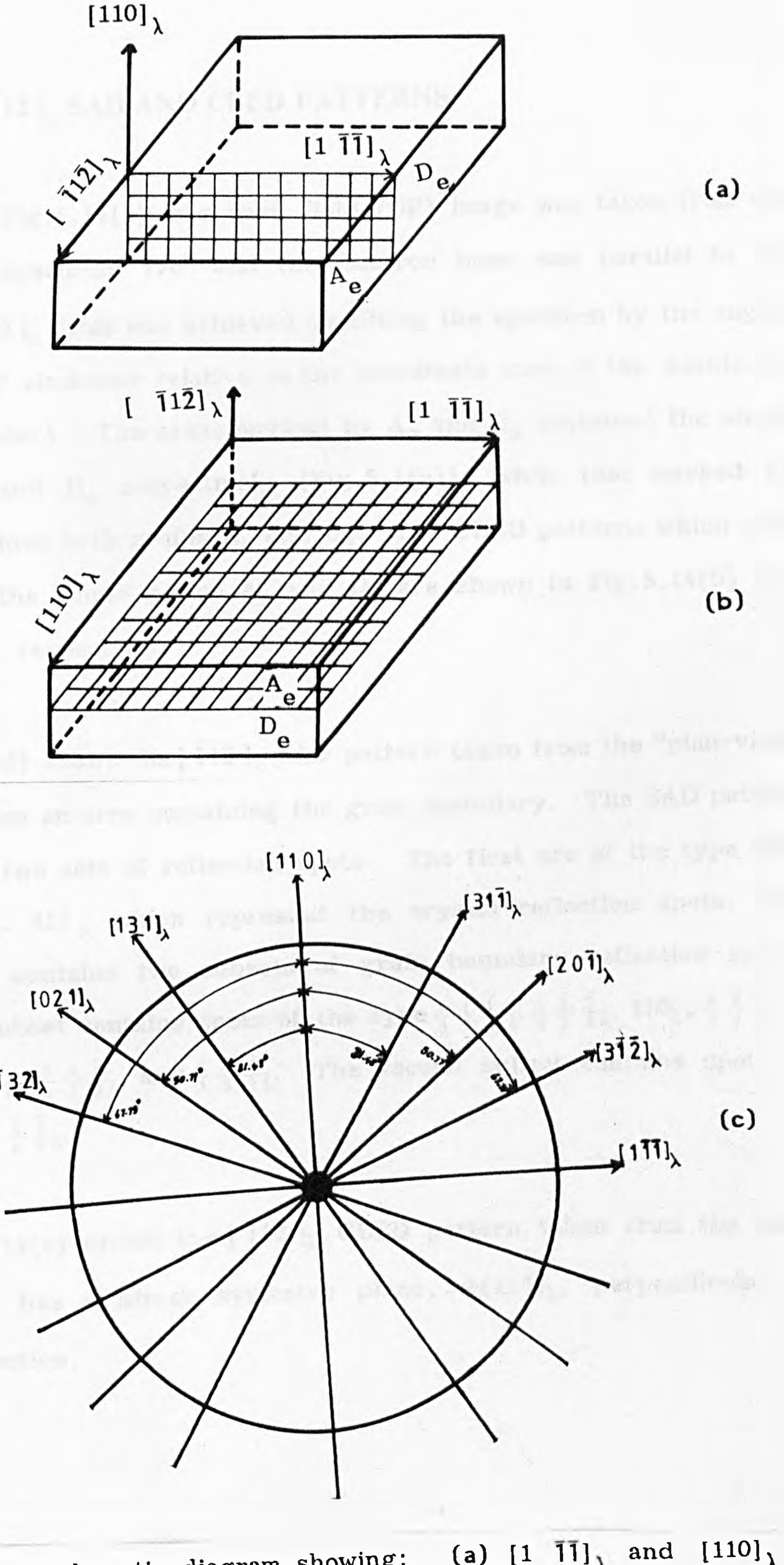

Fig. 5.13. A schematic diagram showing: (a) $[1\ \bar{1}\bar{1}]_\lambda$ and $[110]_\lambda$ surface normal "edge-on" specimens, and (b) $[\ \bar{1}1\bar{2}]_\lambda$ surface normal "plan-view" specimens. (c) A schematic diagram showing some of the directions enclosed between $[1\ \bar{1}\bar{1}]_\lambda$ and $[110]_\lambda$ directions and lie in the boundary plane $(\bar{1}1\bar{2})_\lambda$.

5.3.1. THE $[\bar{1}1\bar{2}]_\lambda$ SAD AND CBED PATTERNS.

Shown in Fig.5.14(a) is a dark field (DF) image was taken from the "plan-view" specimen "ivc" and the electron beam was parallel to the direction $[\bar{1}1\bar{2}]_\lambda$ (this was achieved by tilting the specimen by the angles 8.5° and 3.0° clockwise relative to the coordinate axes of the double tilt specimen holder). The areas marked by A_e and D_e contained the single grains A_e and D_e respectively (Fig.5.1(a)), while that marked by A_e-D_e contained both grains A_e and D_e. The CBED patterns which were taken from the single grains A_e and D_e are shown in Fig.5.14(b) and *Fig.5.14(c)*, respectively.

Fig.5.14(d) shows the $[\bar{1}1\bar{2}]_\lambda$ SAD pattern taken from the "plan-view" specimen from an area containing the grain boundary. The SAD pattern consists of two sets of reflection spots. The first are of the type 000, $1\bar{1}\bar{1}_\lambda$, 220_λ, $31\bar{1}_\lambda$ which represent the crystal reflection spots. The second set contains two subsets of grain boundary reflection spots. The first subset contains spots of the type $\frac{1}{3}\frac{\bar{1}}{3}\frac{\bar{1}}{3}{}_\lambda$, $\frac{2}{3}\frac{\bar{2}}{3}\frac{\bar{2}}{3}{}_\lambda$, 110_λ, $\frac{4}{3}\frac{2}{3}\frac{7}{3}{}_\lambda$, $\frac{5}{3}\frac{\bar{1}}{3}\frac{\bar{2}}{3}{}_\lambda$, $20\bar{1}_\lambda$, $\frac{7}{3}\frac{5}{3}\frac{\bar{1}}{3}{}_\lambda$, and $\frac{8}{3}\frac{4}{3}\frac{\bar{2}}{3}{}_\lambda$. The second subset contains spots of the type $\frac{4}{6}\frac{2}{6}\frac{\bar{1}}{6}{}_\lambda$.

Fig. 5.14(e) shows the $[\bar{1}1\bar{2}]_\lambda$ CBED pattern taken from the same area. It has a mirror symmetry plane, $m(110)_\lambda$, perpendicular to $[220]_\lambda$ direction.

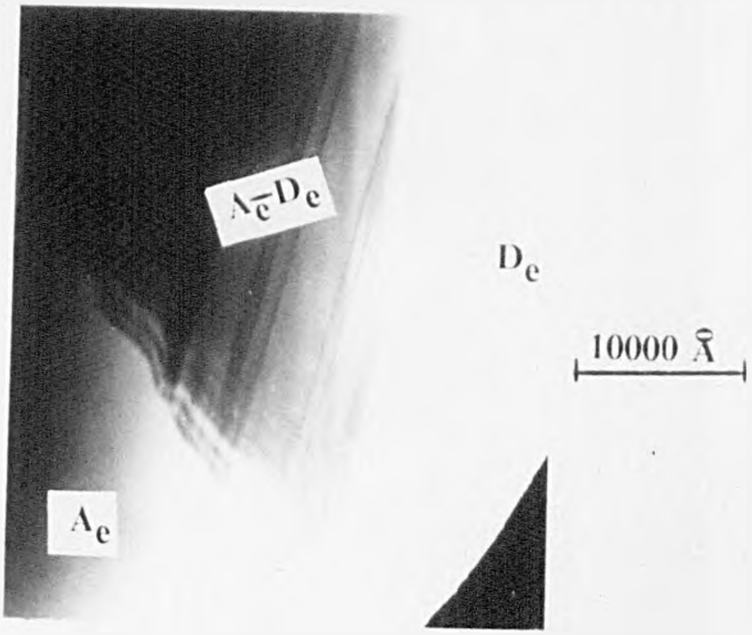

Fig. 5.14. (a) A dark field (DF) micrograph taken from the specimen "ive" from an area contained the single grains A_e, D_e and a "plan-view" area contained the grains A_e-D_e. The electron beam was parallel to the direction $[\,112\,]$.

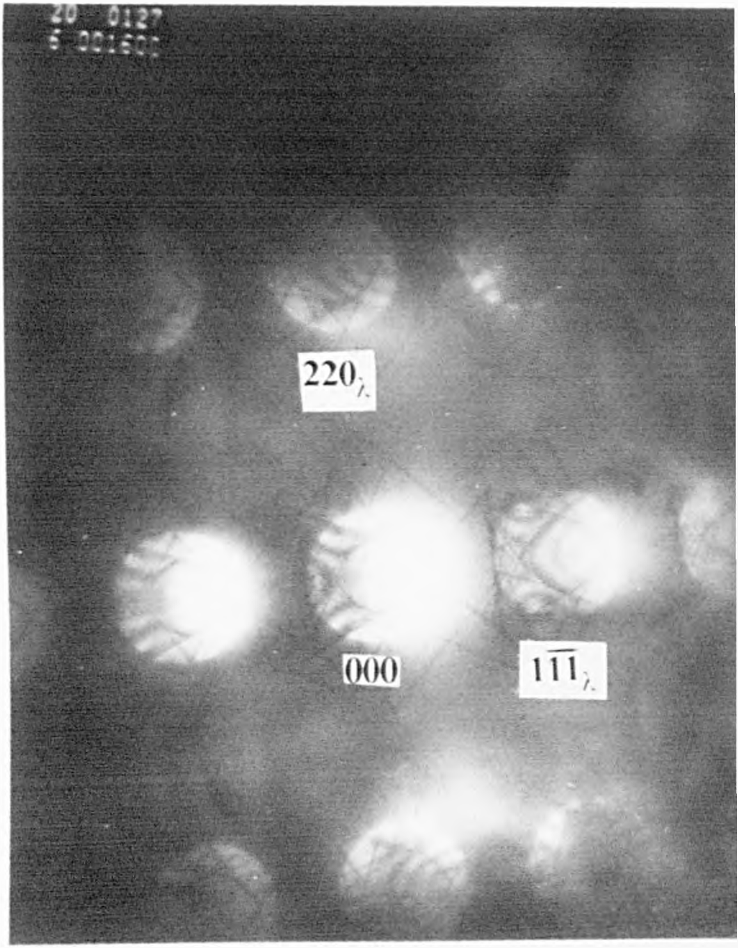

(b)

Fig. 5.14. CBED patterns: (b) [1 grain D_e.

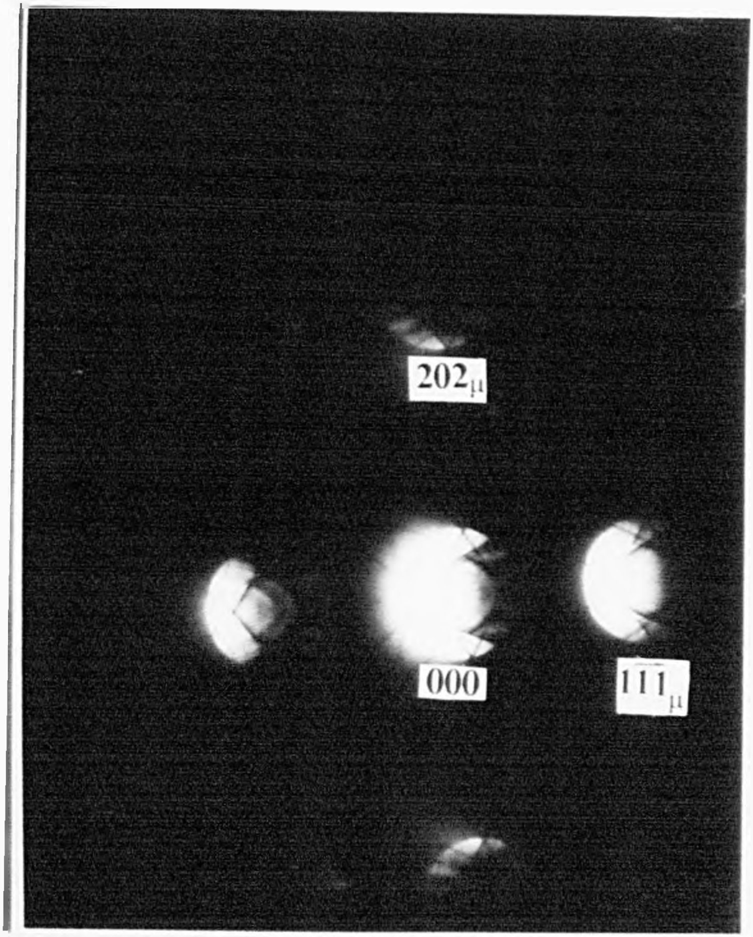

(c)

$1\bar{2}\ ]_{\epsilon}$, from grain A_{e}, (c) $[12\ 1\ ]_{\mu}$ from

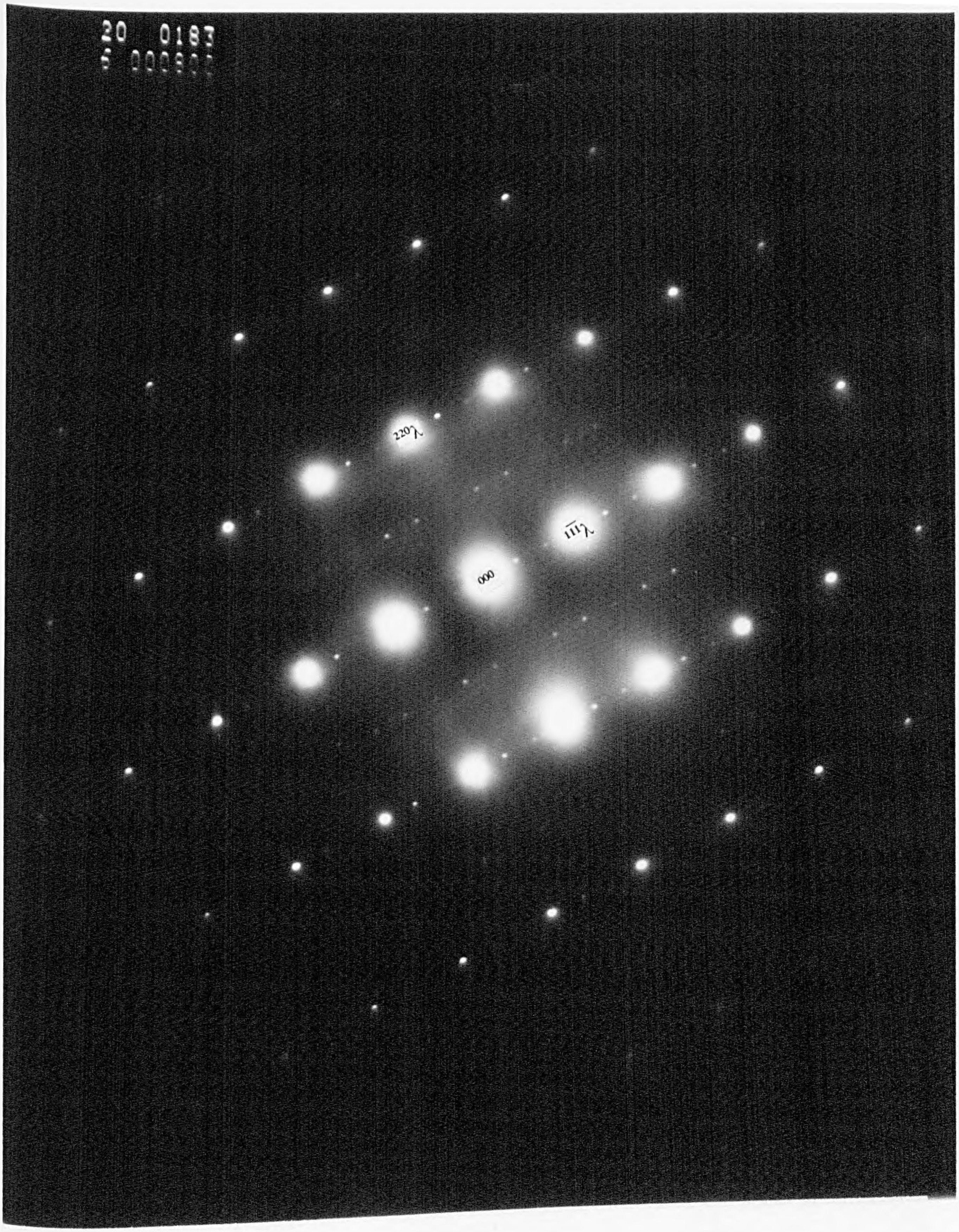

Fig. 5.14(d). $[\bar{1}1\bar{2}]_\lambda$ SAD pattern was taken from a $\Sigma = 3(\bar{1}1\bar{2})_\lambda$ "plan-view" specimen.

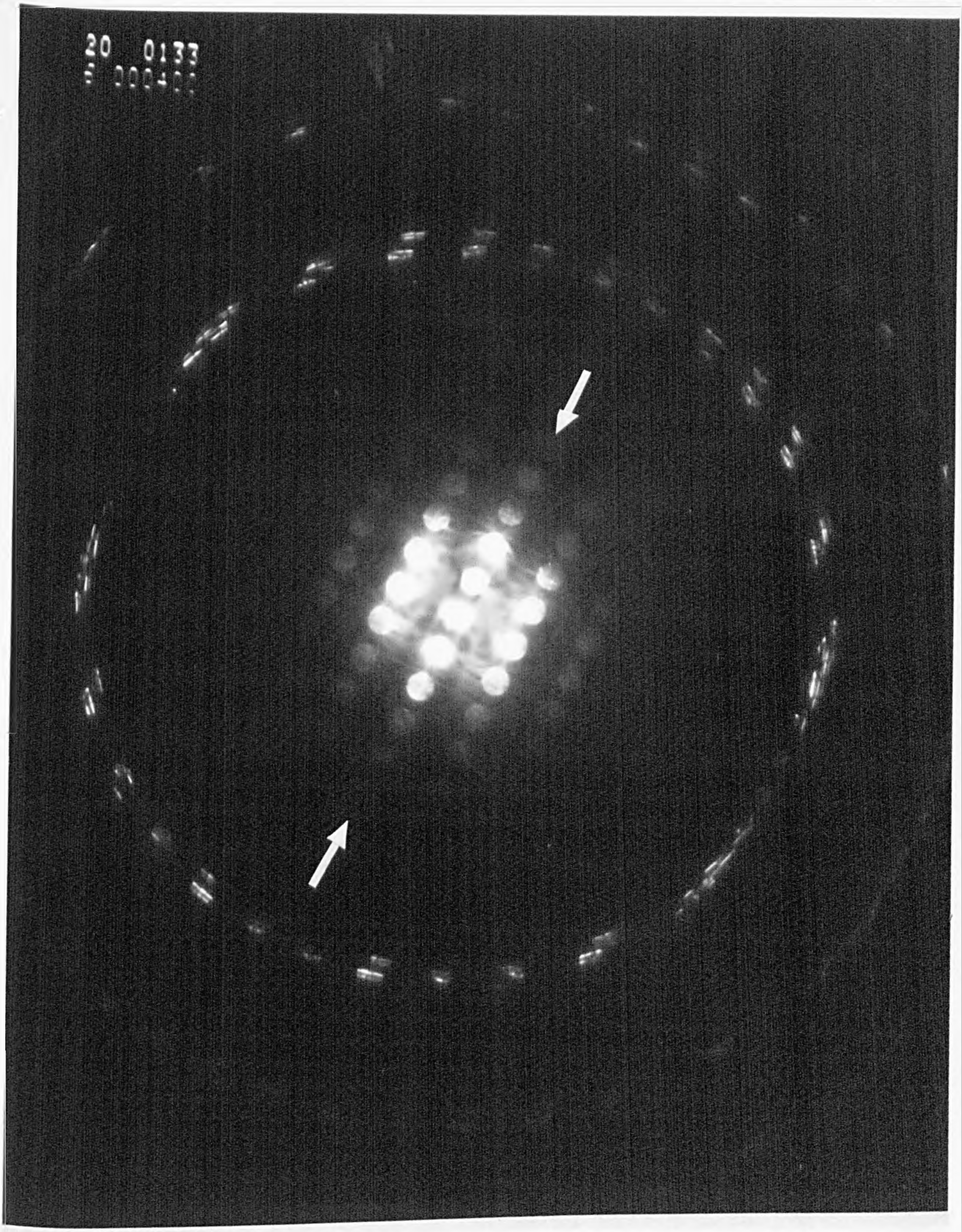

Fig. 5.14(e). 1-[$\bar{1}1\bar{2}$]$_\lambda$ low-camera length CBED pattern was taken from a $\Sigma = 3(\bar{1}1\bar{2})_\lambda$ "plan-view" specimen.
The arrows indicate to the trace of the mirror m$(110)_\lambda$.

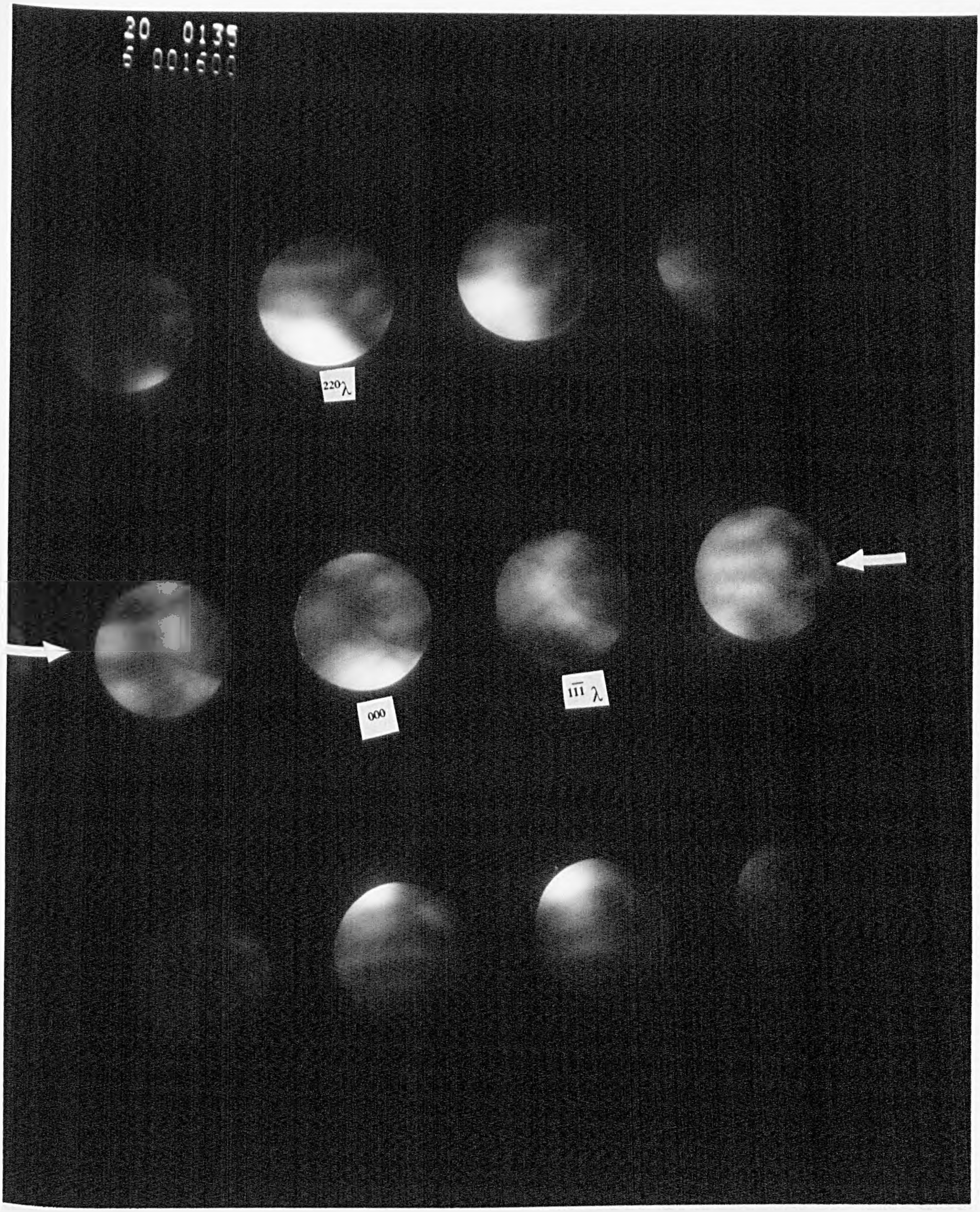

Fig. 5.14(e). 2-$[\bar{1}1\bar{2}]_\lambda$ high-camera length CBED pattern was taken from a $\Sigma = 3(\bar{1}1\bar{2})_\lambda$ "plan-view" specimen.

The arrows indicate to the trace of the mirror $m(110)_\lambda$.

5.3.2. THE $[110]_\lambda$ SAD AND CBED PATTERNS.

The SAD patterns which were taken from specimen "iva" grains A_e and D_e are shown, previously, in Fig.5.10(a) and (b), respectively. They are based on the $1\bar{1}1_\lambda$ and $2\bar{2}0_\lambda$ types reflections and the forbidden 002_λ type reflection. Fig.5.10(c) was taken from an area containing the boundary plane. The crystal reflection spots are indexed. Fig.5.10(c) shows no evidence of the grain boundary reflection spots. Fig.5.10(d) and (e) are the $[110]_\lambda$ and $[101]_\mu$ low- and high-camera lengths CBED patterns taken from the same grains above. Fig.5.10(f) is the $[110]_\lambda$ CBED pattern taken from the grain boundary. It exhibits a mirror symmetry perpendicular to the boundary plane, $m(1\bar{1}\bar{1})_\lambda$, a mirror parallel to the boundary plane, $m(\bar{1}1\bar{2})_\lambda$, and a diad perpendicular to the pattern plane, $2[110]_\lambda$.

5.3.3. THE $[1\bar{1}\bar{1}]_\lambda$ SAD AND CBED PATTERNS.

Fig.5.15 shows the CBED and SAD patterns, which were taken from the $[1\bar{1}\bar{1}]_\lambda$ surface normal "edge-on" specimen, "ivb", when the electron beam was parallel to the zone axis $[1\bar{1}\bar{1}]_\lambda$. Fig.5.15(a) was taken from grain A_e, Fig.5.15(b) from grain D_e and Fig.5.15(c) from the grain boundary. The SAD pattern, which was taken from the grain boundary, is shown in Fig.5.15(d). The crystal reflection spots from both grains were in complete coincidence and undistinguishable from each other. Also, Fig.5.15(d) shows no evidence of the grain boundary reflection spots or streaks. The symmetry exhibited by the low- and high-camera length CBED patterns, Fig.5.15(c), are 3m (BF and whole pattern), i.e. a triad perpendicular to the pattern plane, $3[1\bar{1}\bar{1}]_\lambda$, and three mirror

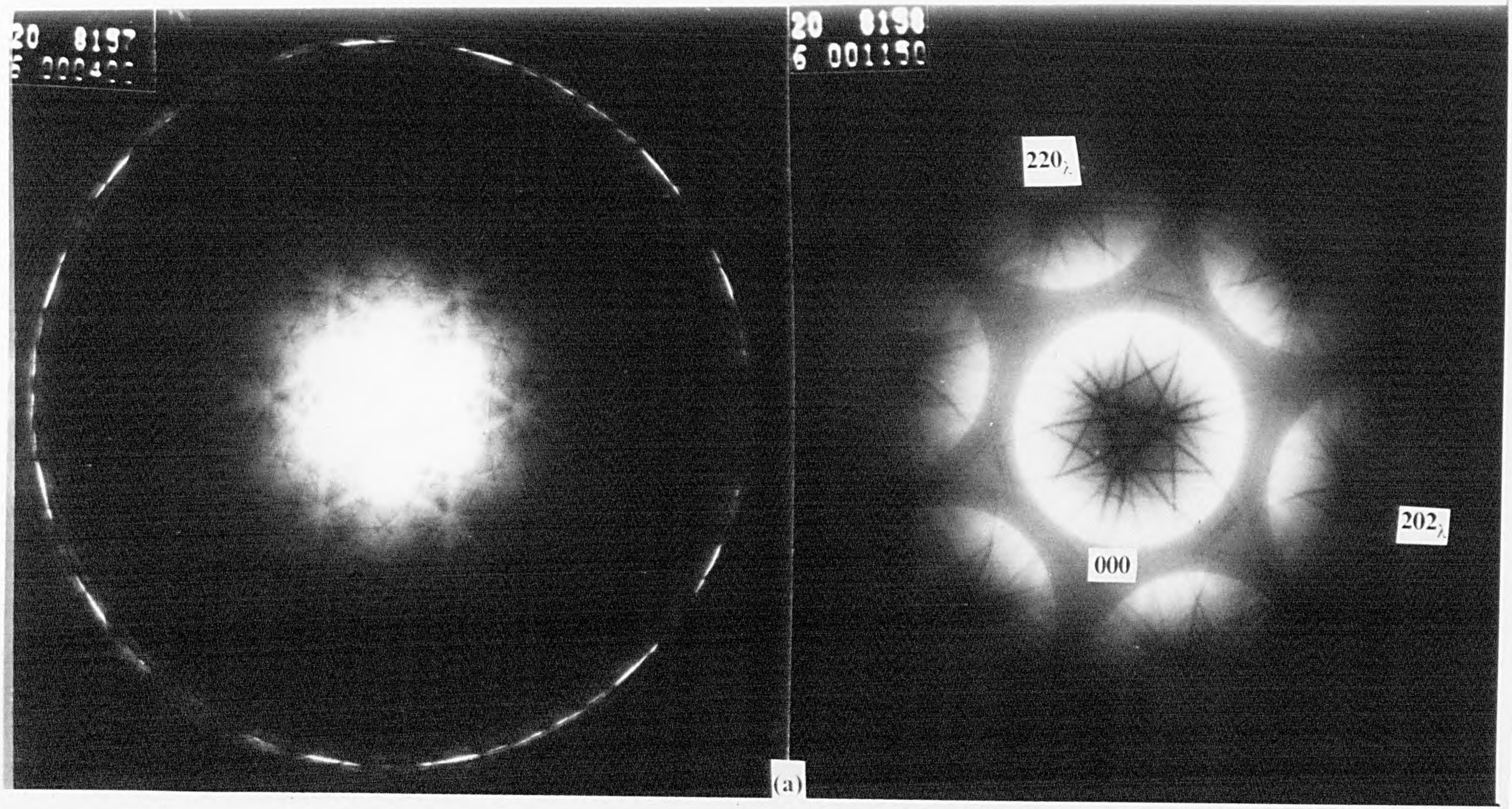
20 8197
6 000400
20 8198
6 001150
220_λ
202_λ
000
(a)

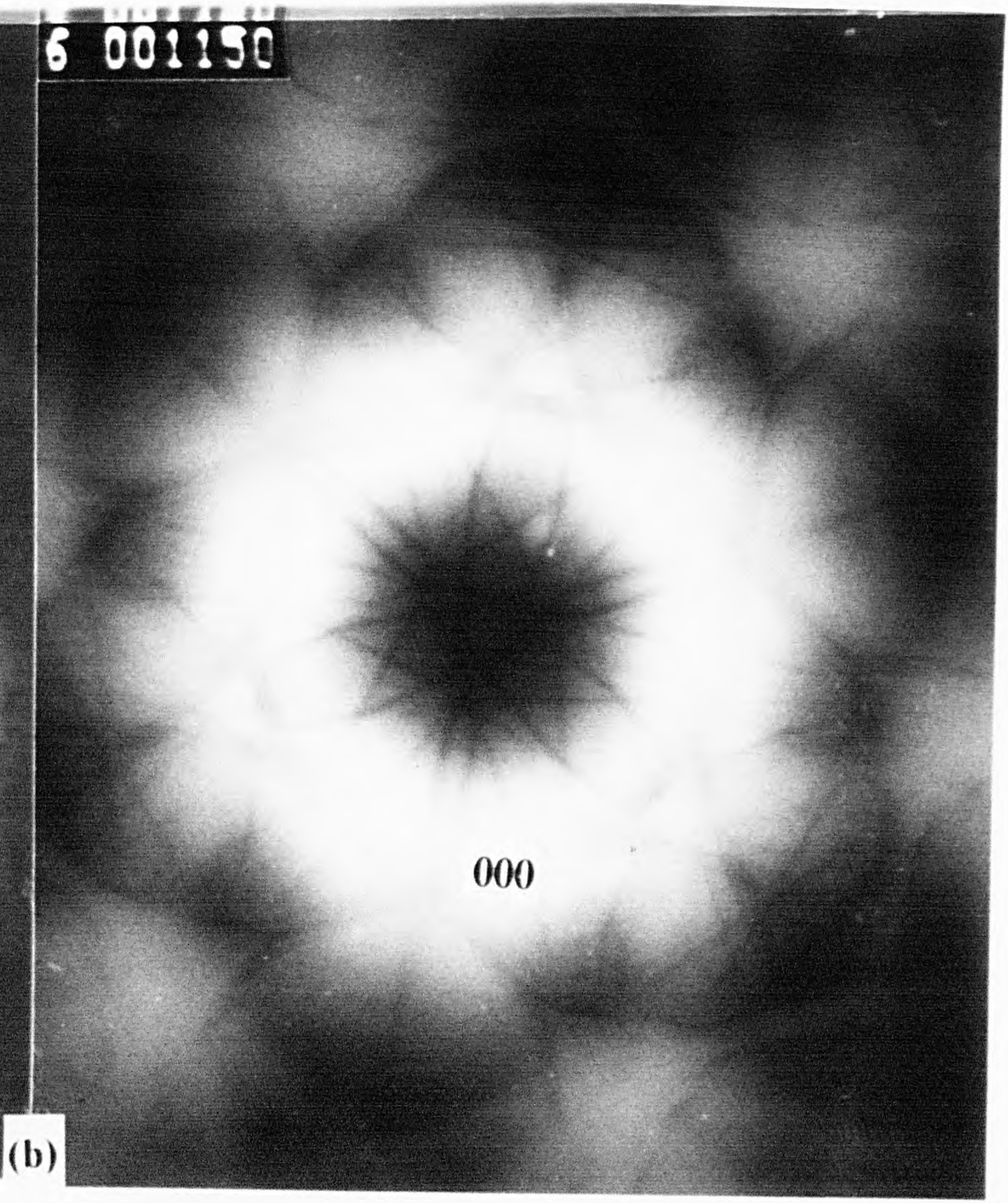
6 001150
000
(b)

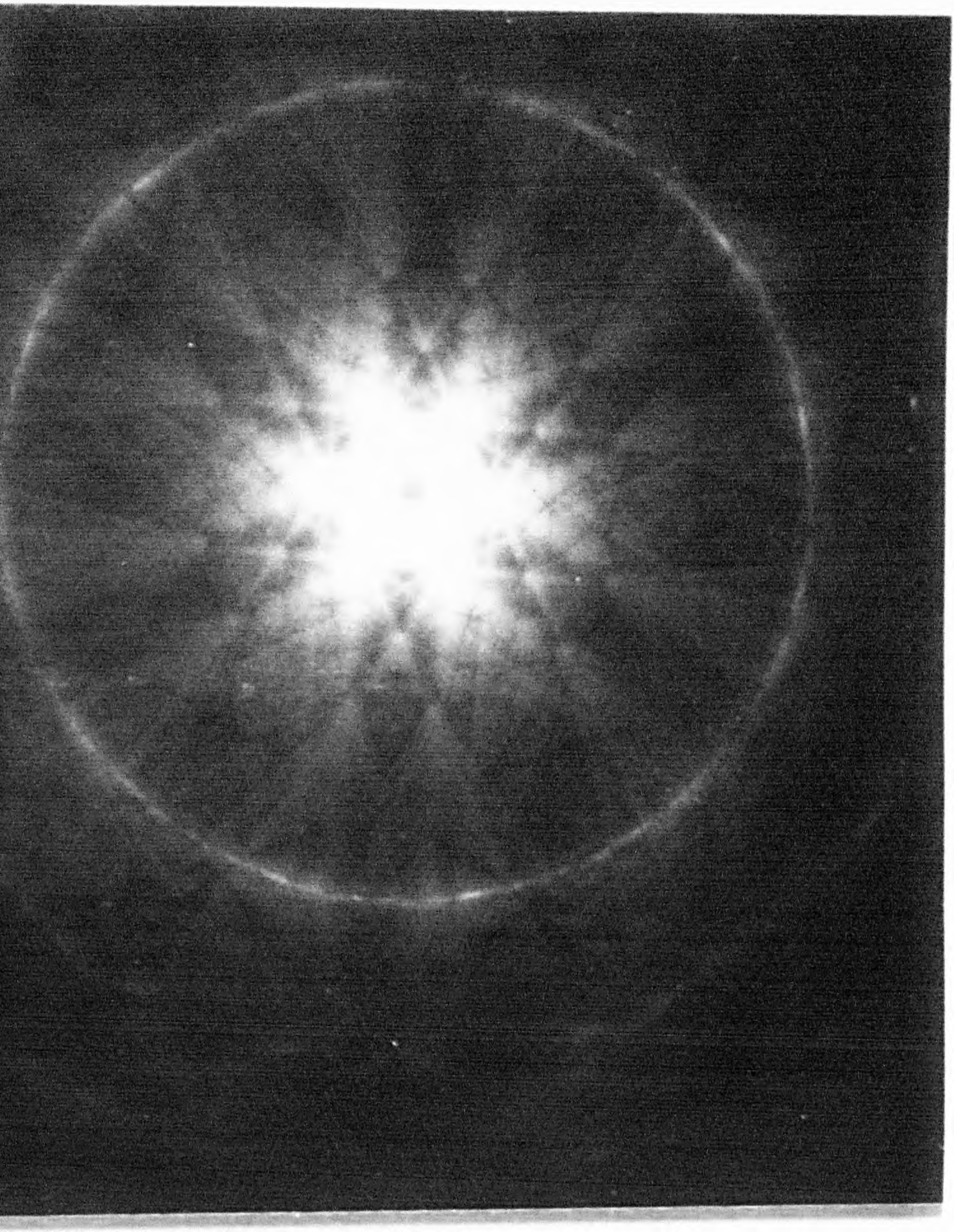

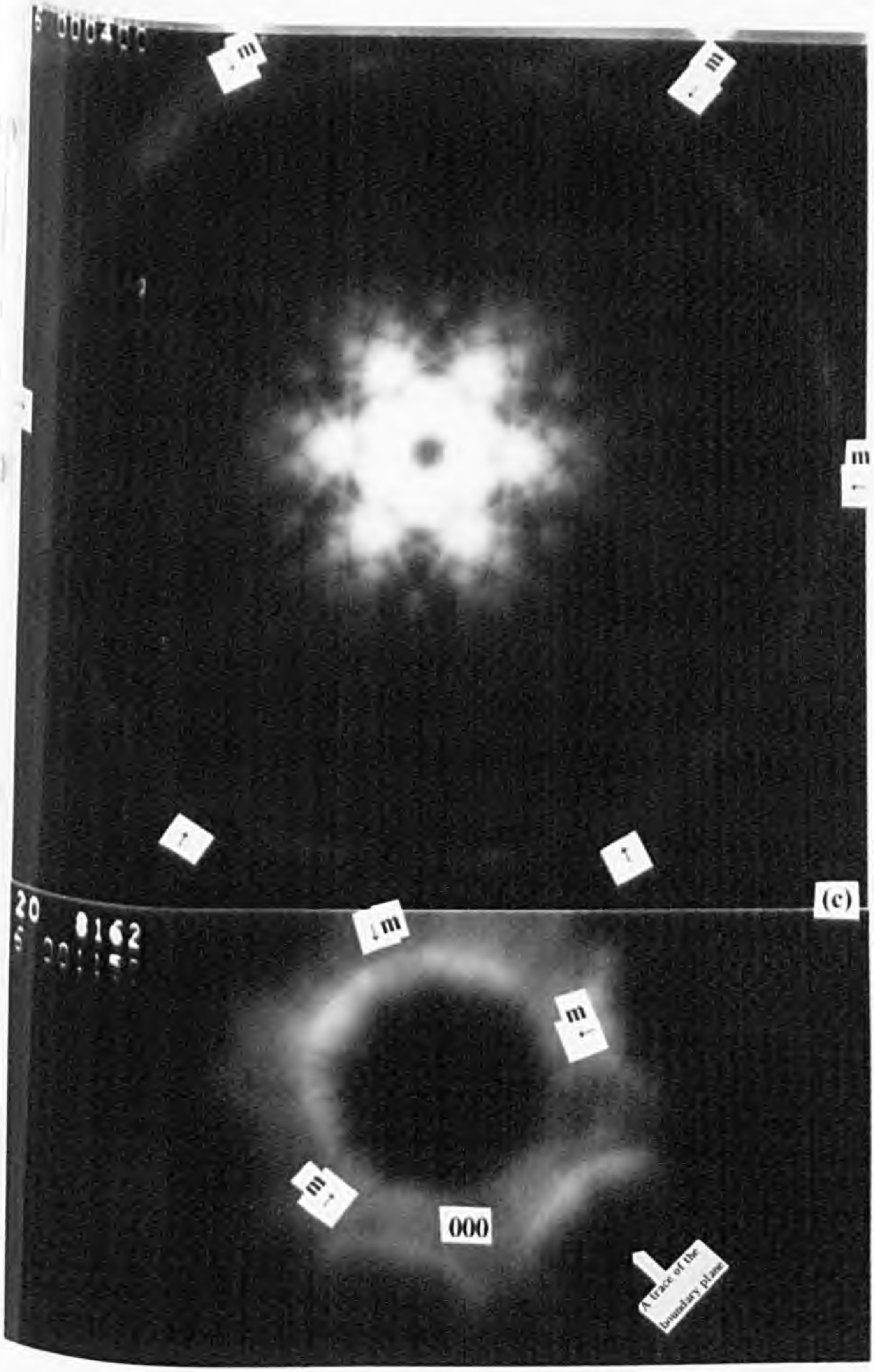

Fig. 5.15. $[1\,11]$[illegible] Low- and high-camera length CBED patterns taken from the "ivb" "edge-on" specimen from grains: (a) A_e, (b) D_e and (c) A_e-D_e. A trace of the boundary plane is indicated.

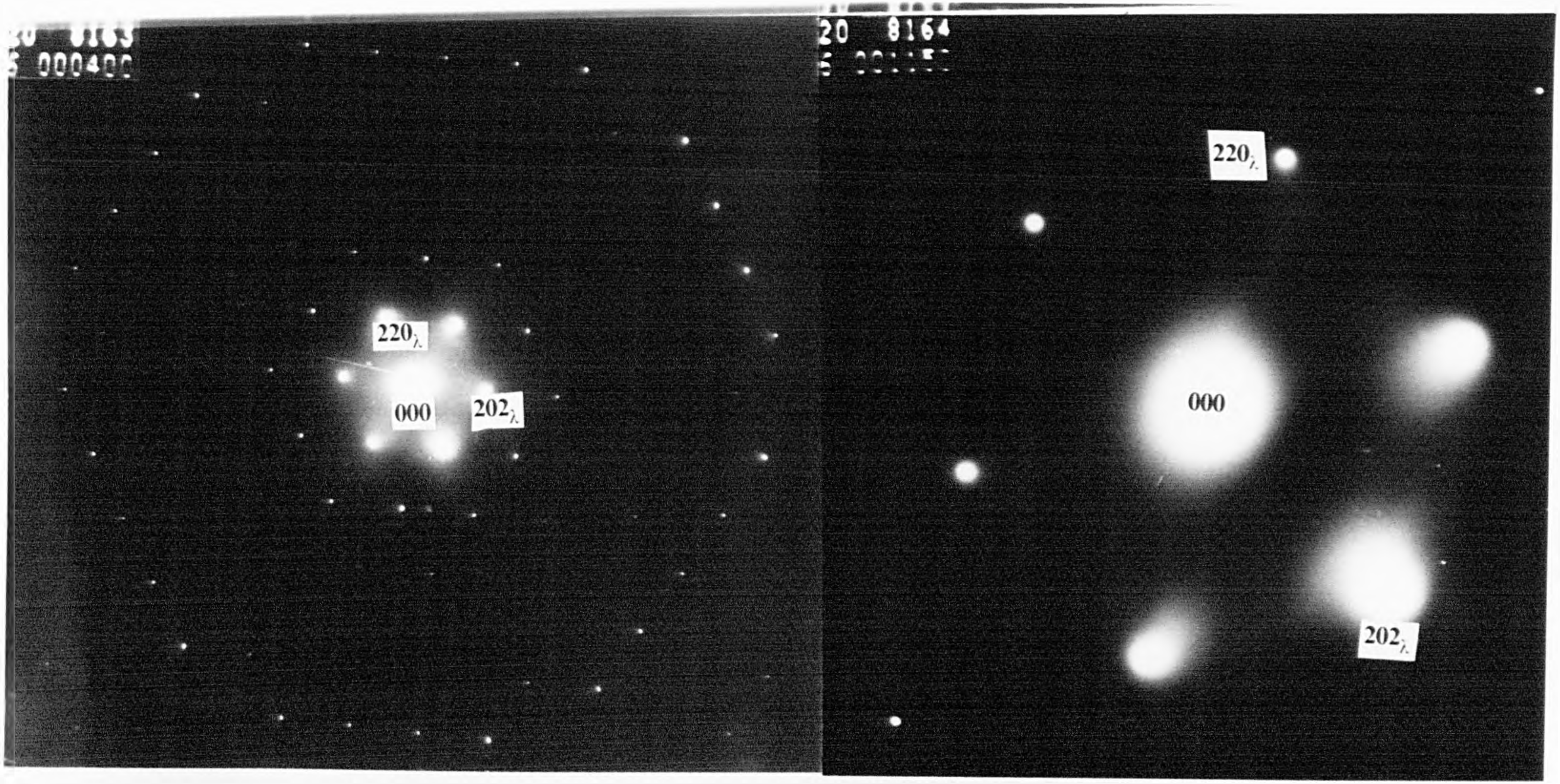

Fig. 5.15. (d) Low- and high-camera length SAD patterns taken from the "ivb" "edge-on" specimen from the grain boundary area.

planes, $m(110)_\lambda$, $m(101)_\lambda$, and $m(0\bar{1}1)_\lambda$, perpendicular to the directions $[220]_\lambda$, $[202]_\lambda$, and $[0\bar{2}2]_\lambda$, respectively.

5.4. $\Sigma=27$ GRAIN BOUNDARY.

5.4.1. THE $\Sigma = 27$ "edge-on" specimen "va".

A bright-field image for an area containing the $\Sigma=27$ grain boundary in the "edge-on" specimen "va" is shown in Fig.5.16, where the electron beam direction was exactly parallel to the $[110]_\lambda$ direction. The figure shows that the boundary is not flat as was shown before in the optical micrograph in Fig.5.1(a), (the boundary plane between grains B_c and C_c), but has a complex microscopic structure. It is corrugated between points g&h, o&n, and it was also unstable between points h&o, where the $\Sigma=27$ boundary was dissociated into first and second order symmetric tilt boundary, $\Sigma=3$ and 9, respectively as listed in Table 5.2.

Beside grains B_c and C_c, Fig.5.16 shows two other big microscopic grains E_c and F_c. There are some tiny subgrains, e.g. G_c, left unidentified in this study.

The SAD and CBED patterns have been taken from both grains B_c and C_c and from the grain boundary (the segments marked "gh" and "on" in Fig.5.16), and shown in Fig.5.17 and 5.18, respectively. The electron beam direction was exactly parallel to the common zone axis $[110]_\lambda$ and the patterns from B_c and C_c were found to be misoriented by an angle $\Theta=31.6^\circ$ and the boundary plane index was $(5\bar{5}\bar{2})_\lambda$. A trace

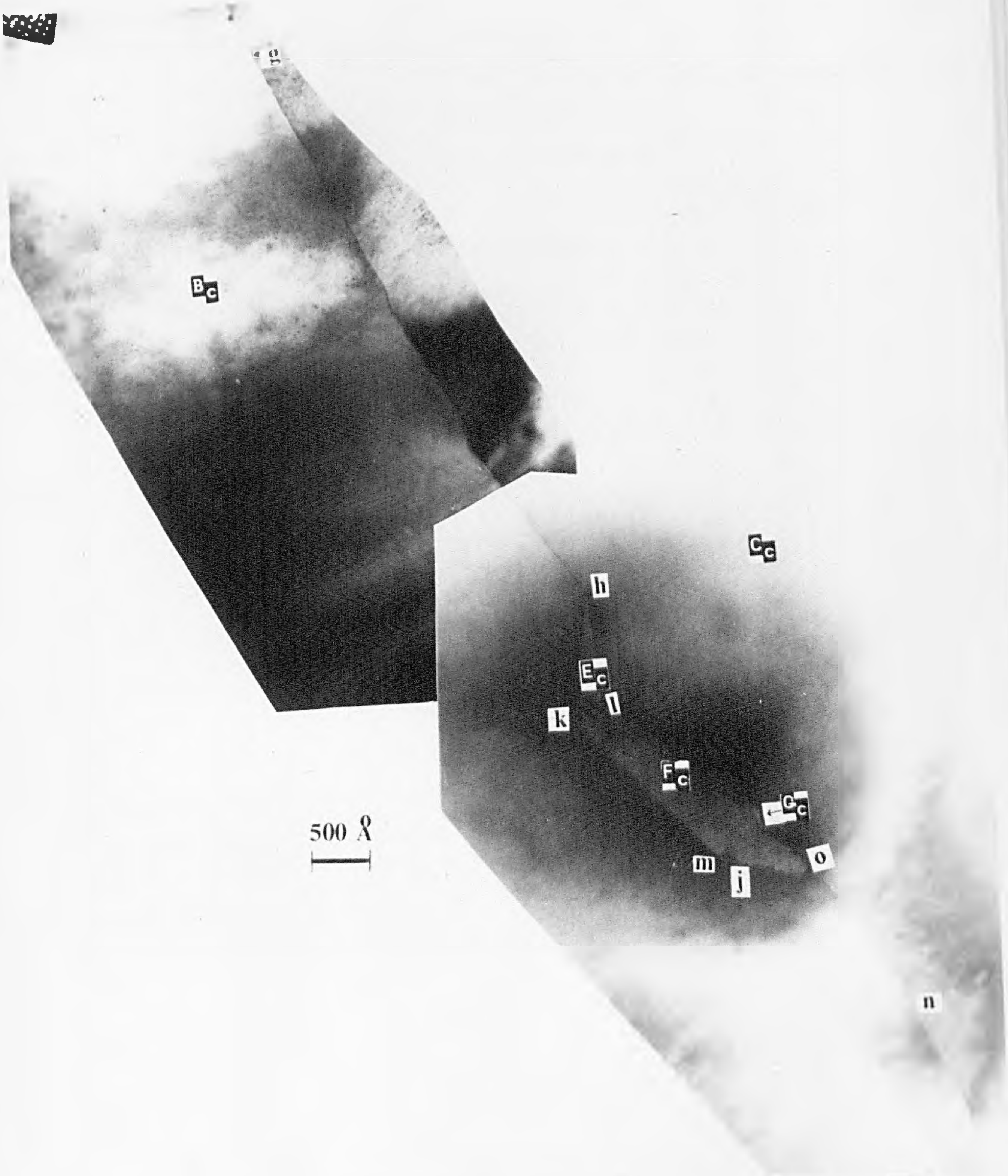

Fig. 5.16. A bright field micrograph of the dissociated $\Sigma=27(5\ \overline{52}\ )_{\lambda}$ symmetric tilt boundary from the "va" "edge-on" Ge specimen. It contained grains B_c, C_c and the microscopic grains E_c and F_c.

Table 5.2. The dissociated $\Sigma=27(5\ \bar{5}\bar{2})$ tilt boundary.

Segment	Grains	Figure	Orientation relation and interface plane*
gh	B-C	5.18	$\Sigma=27(5\ \bar{5}\bar{2})_{\lambda}$
on	B-C	as 5.18	$\Sigma=27(5\ \bar{5}\bar{2})_{\lambda}$
hk	C-E	5.21	$\Sigma=9(\ \bar{2}21)_{\lambda}$
hl	B-E	5.19	$\Sigma=3(\ \bar{1}11)_{\lambda}$
lk	E-F	5.20	$\Sigma=3(\ \bar{1}11)_{\lambda}$
km	C-F	5.22	$\Sigma=3(1\ \bar{1}1)_{\lambda}$
zj	C-F	as 5.22	$\Sigma=3(1\ \bar{1}1)_{\lambda}$
mz	C-F	as 5.22	$\Sigma=3(1\ \bar{1}\bar{2})_{\lambda}$
lw	B-F	5.23	$\Sigma=9(2\ \bar{2}1)_{\lambda}$
jo#	C-F		
wo#	B-F-G		

* The indexing of the planes are quoted with respect to the first grain in each grain pair of the second column.

unidentified

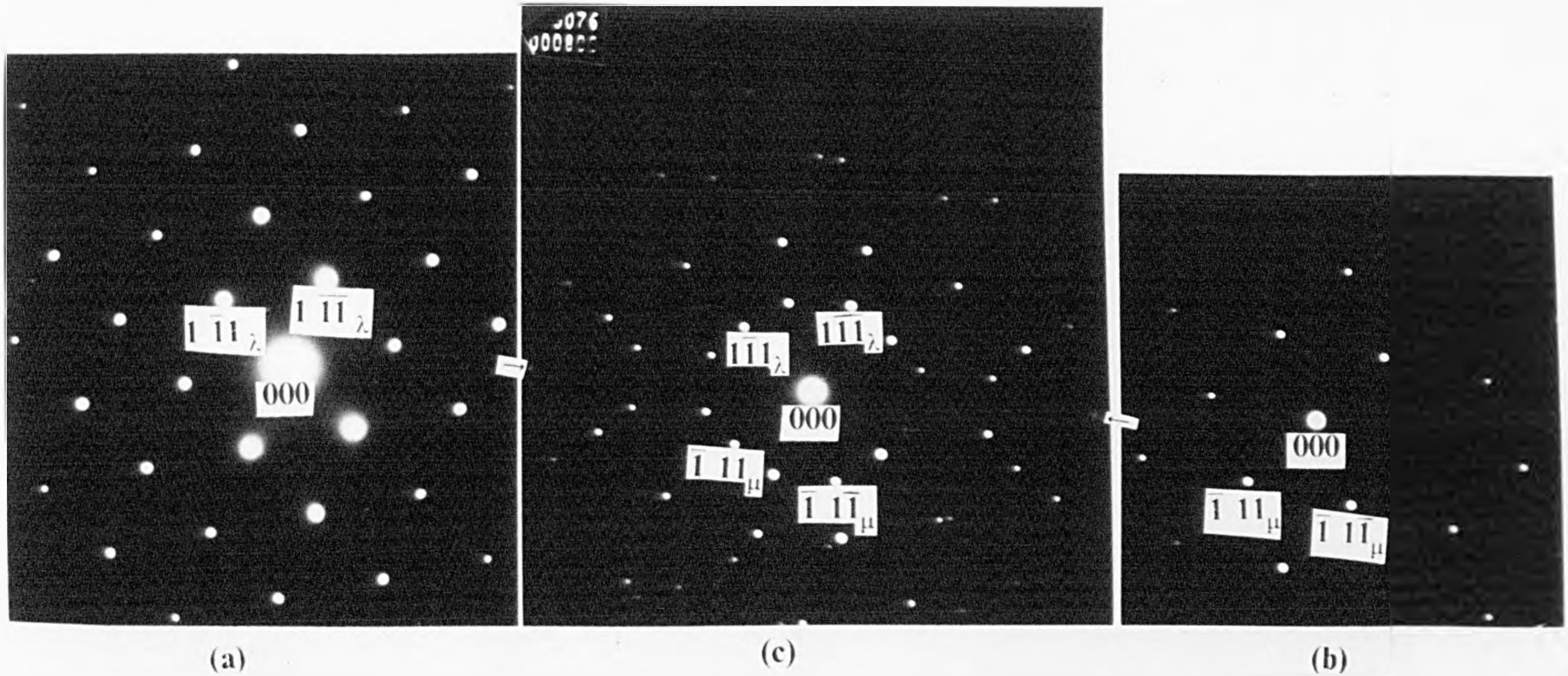

Fig. 5.17. $[110]_{\lambda}$ SAD patterns were taken from the "edge-on" specimen "va":

(a) from grain B_c, (b) from grain C_c, and (c) from the boundary of the grain pair B_c-C_c. A trace of the boundary plane is indicated.

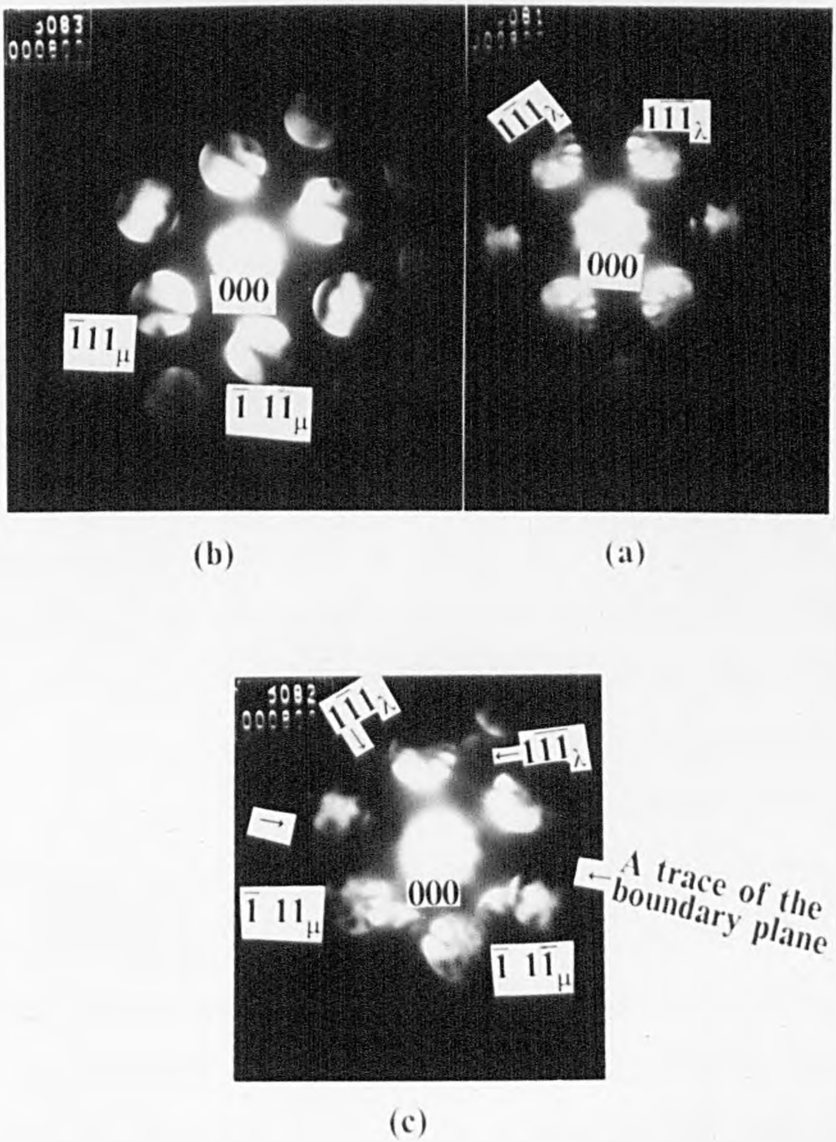

Fig. 5.18. $[110]_\lambda$ CBED patterns were taken from the "edge-on" specimen "va": (a) from grain B_c, (b) from grain C_c, and (c) from Grain boundary segments "gh" and "on". A trace of the boundary plane is indicated.

of the plane $(5\bar{5}\bar{2})_\lambda$ is indicated in Fig.5.17(c) and 5.18(c). Since the grains B_c and C_c were misoriented by the angle $\Theta=31.6^0$ about $[110]_\lambda$ and the boundary plane was of the type $(5\bar{5}\bar{2})_\lambda$, thus segments "gh" and "on" were traces of grain boundaries of the type $\Sigma = 27(5\bar{5}\bar{2})_\lambda$.

The symmetry exhibited by the CBED pattern in Fig.5.18(c), which was taken from the grain boundary $\Sigma = 27(5\bar{5}\bar{2})_\lambda$, are a mirror symmetry perpendicular to the boundary plane, $m(5\bar{5}\bar{2})_\lambda$, a mirror parallel to the boundary plane, $m(\bar{1}1\bar{5})_\lambda$, and a diad perpendicular to the pattern plane, $2[110]_\lambda$.

Similarly, the CBED patterns in Fig.5.19, 5.20, 5.21, 5.22 and 5.23 have been taken from the grain boundary segments "hl", "lk", "hk", "km" and "lw", respectively, and the grain pairs on both sides of each segment. At point "h" the $\Sigma = 27(5\bar{5}\bar{2})_\lambda$ boundary dissociated into $\Sigma = 3(\bar{1}11)_\lambda$ (segment hl) and $\Sigma = 9(\bar{2}21)_\lambda$ (segment hk). At point "l" the $\Sigma = 9(\bar{2}21)_\lambda$ (segment lw) dissociated into $\Sigma = 3(\bar{1}11)_\lambda$ (segment lh) and $\Sigma = 3(\bar{1}11)_\lambda$ (segment lk). At point "k" the $\Sigma = 9(\bar{2}21)_\lambda$ (segment hk) dissociated into $\Sigma = 3(1\bar{1}1)_\lambda$ (segment km) and $\Sigma = 3(\bar{1}11)_\lambda$ (segment kl). Segment mz was of the boundary type $\Sigma = 3$ as km but formed on $(1\bar{1}\bar{2})_\lambda$ plane. Segment "zj" was identical to "km". The examination of the boundaries between j&o and w&o revealed the presence of a number of tiny steps, and left for future study. A sketch of the $\Sigma = 27(5\bar{5}\bar{2})_\lambda$ boundary is shown in Fig.5.24, where each segment has been indexed and identified, except the segments "jo" and "wo".

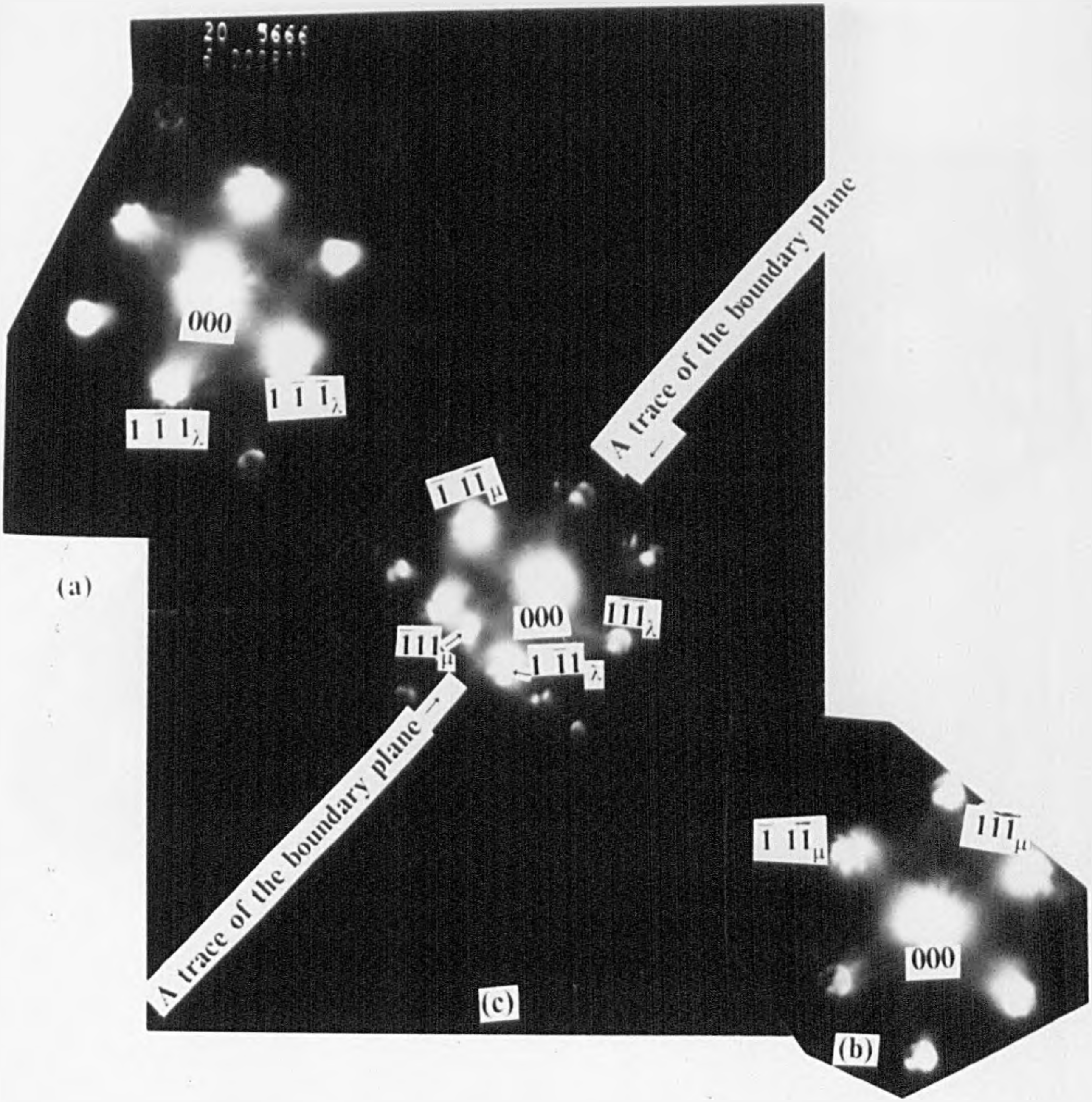

Fig. 5.19. CBED patterns were taken from the "edge-on" specimen "va" from grains: (a) B_c, (b) E_c, and (c) Grain boundary segments "hl". A trace of the boundary plane is indicated.

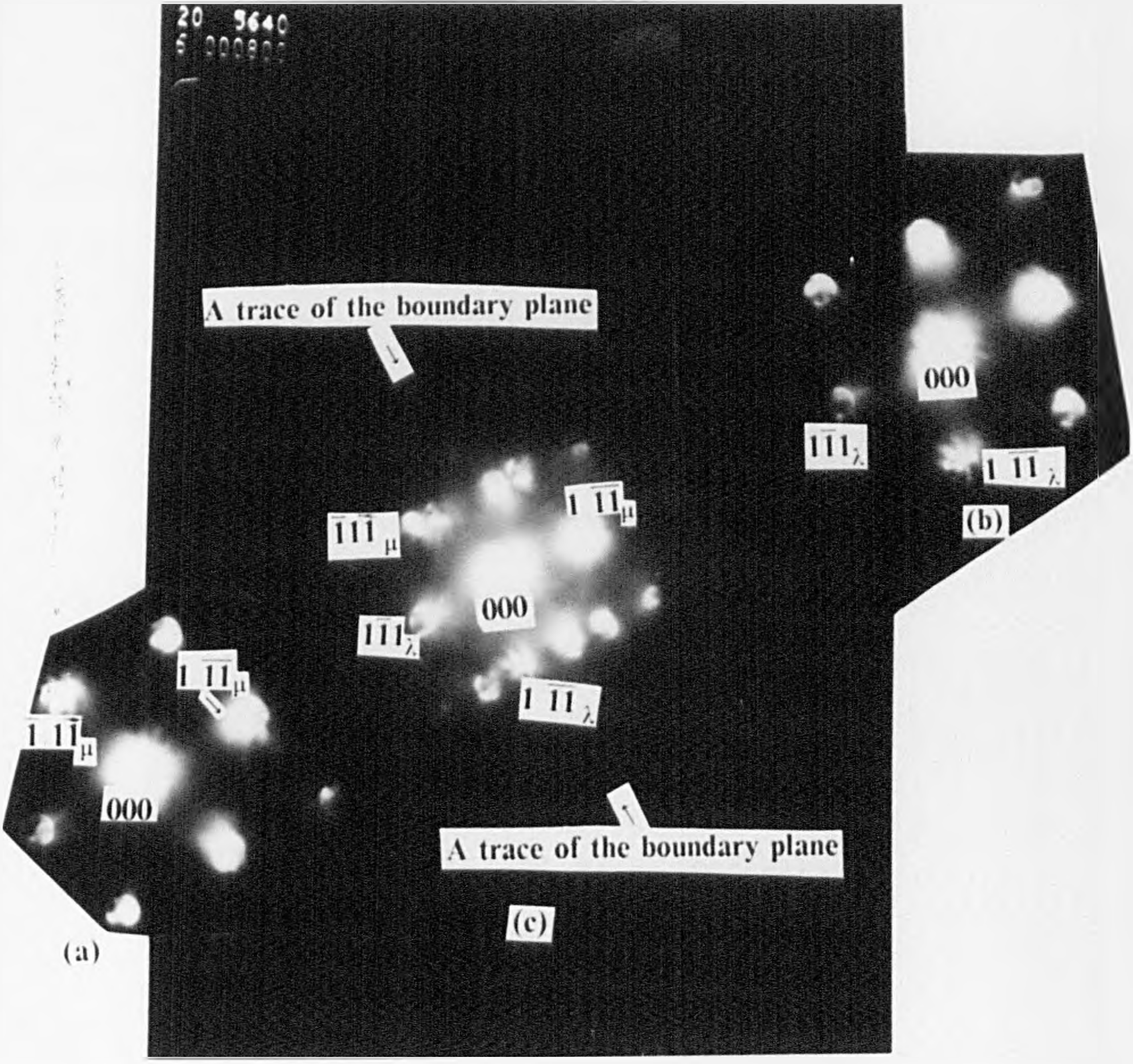

Fig. 5.20. CBED patterns were taken from the "edge-on" specimen "va" from grains: (a) E_c, (b) F_c, and (c) Grain boundary segments "lk". A trace of the boundary plane is indicated.

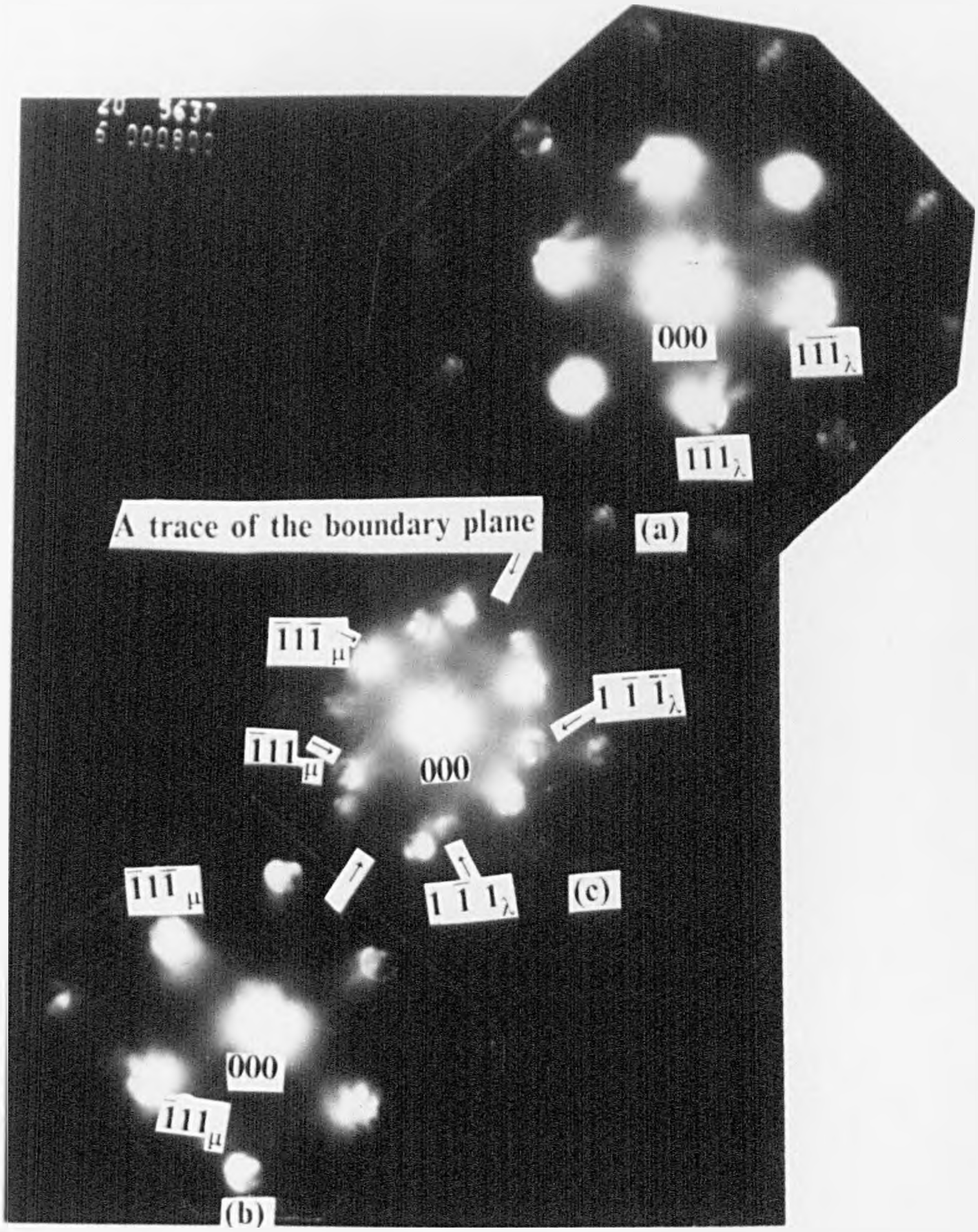

Fig. 5.21. CBED patterns were taken from the "edge-on" specimen "va" from grains: (a) C_e, (b) E_e, and (c) Grain boundary segments "hk". A trace of the boundary plane is indicated.

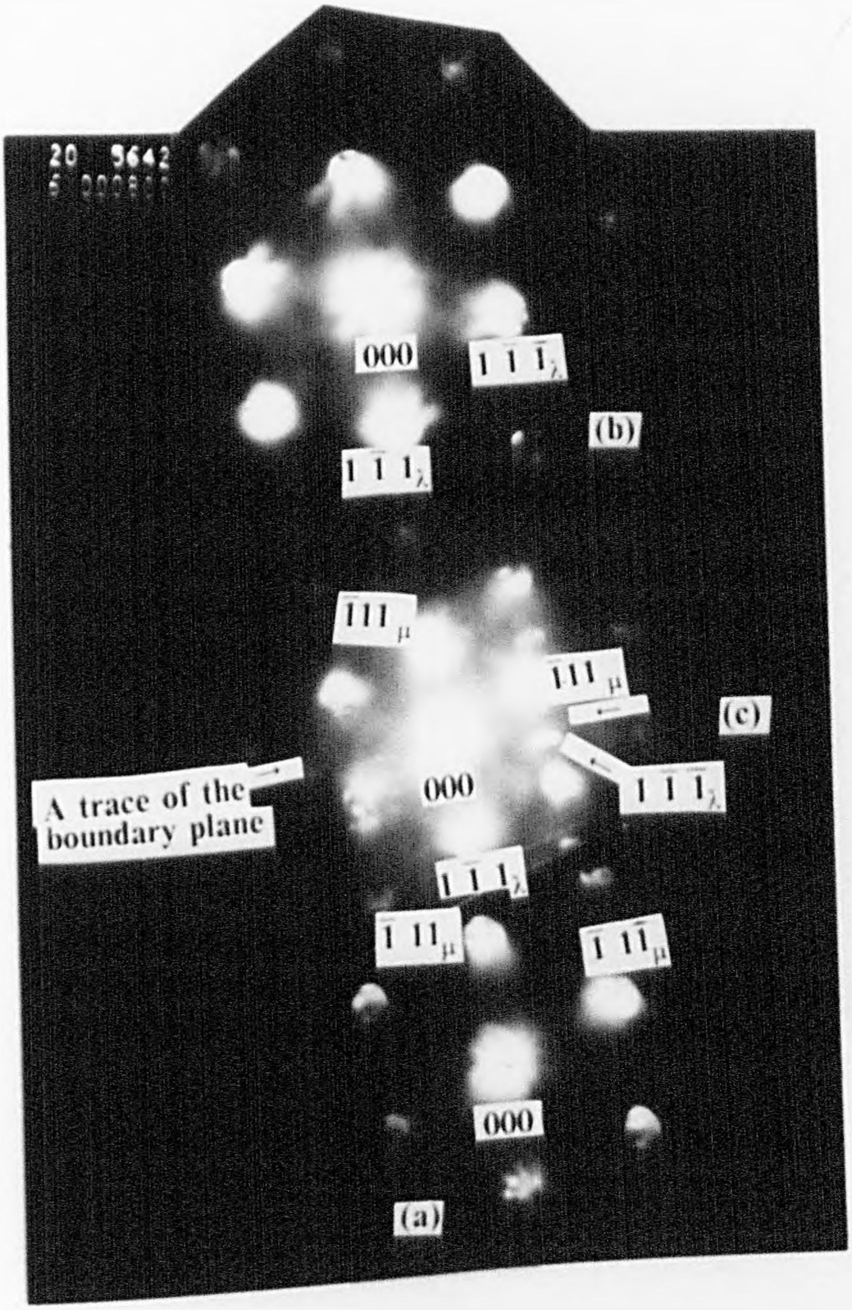

Fig. 5.22. CBED patterns were taken from the "edge-on" specimen "va" from grains: (a) C_e, (b) F_e, and (c) Grain boundary segments "km". A trace of the boundary plane is indicated.

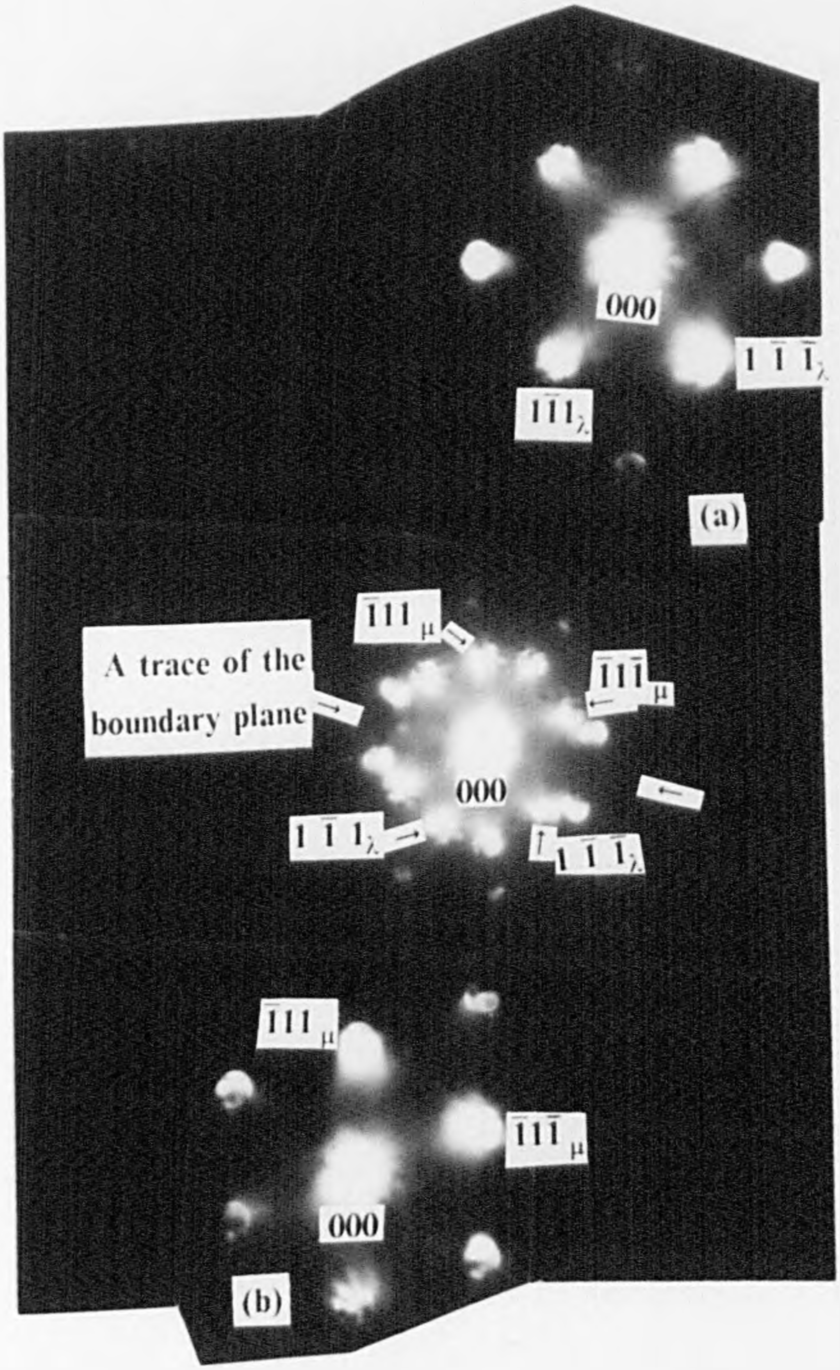

Fig. 5.23. CBED patterns were taken from the "edge-on" specimen "va" from grains: (a) B_c, (b) F_c, and (c) Grain boundary segments "lw". A trace of the boundary plane is indicated.

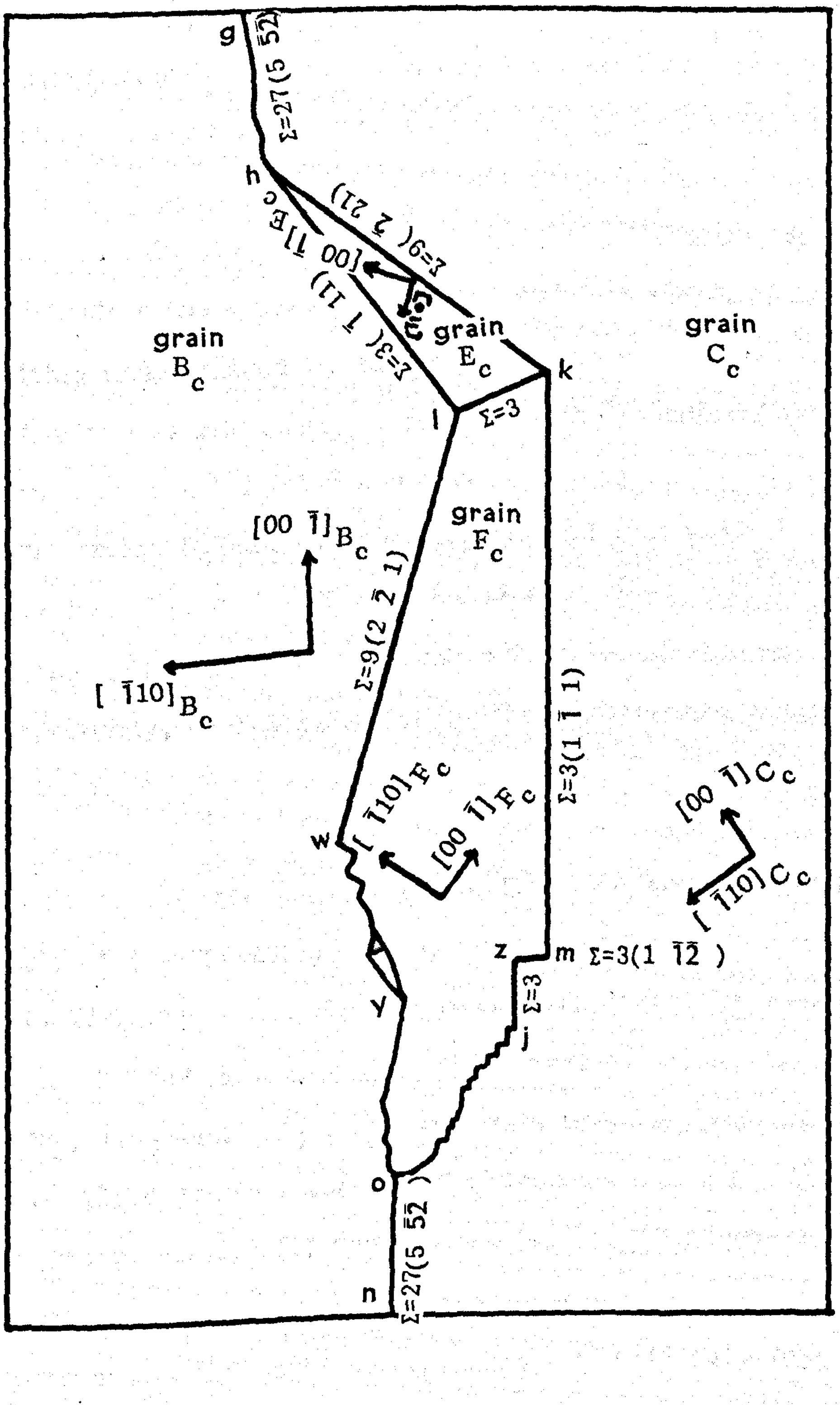

Fig. 5.24. A sketch of the grain boundary geometry of the dissociated $\Sigma=27(5\ \bar{5}\bar{2})_\lambda$ symmetric tilt boundary. The traces of the boundary planes are indexed.

5.4.2. THE $\Sigma = 27$ "PLAN-VIEW" SPECIMEN "vb".

A "plan-view" specimen, where the axis $[\,5\overline{52}\,]_\lambda$ was perpendicular to both the surface of the specimen and the boundary plane, as shown schematically in Fig.5.25, was prepared.

Fig.5.26 is a BF image taken from $\Sigma = 27(\,5\overline{52}\,)_\lambda$ "plane-view" specimen "vb" where the electron beam was parallel to the direction $[\,5\overline{52}\,]_\lambda$ (this was achieved by tilting the specimen by the angles 1.5° anticlock wise and 1.0° clockwise relative to the coordinate axes of the double tilt specimen holder). The area marked by B_c and C_c contained the single grains B_c and C_c (Fig.5.1(a)), and that marked by B_c-C_c contained both the grains B_c and C_c in plan-view. Fig.5.27(a) and (b) are the $[\,5\overline{52}\,]_\lambda$ CBED patterns taken from the single grains B_c and C_c, respectively, and Fig.5.27(c) is the high-camera length CBED pattern taken from B_c.

Fig.5.28 is a SAD pattern taken from an area containing the undissociated $\Sigma = 27(\,5\overline{52}\,)_\lambda$ "plane-view" boundary (area marked by B_c-C_c in Fig.5.26. The electron beam (accelerated by 100kv), was exactly parallel to $[\,5\overline{52}\,]_\lambda$ direction. It is based on the crystal reflection spots 220_λ, $\bar{1}1\bar{5}_\lambda$ and $13\bar{5}_\lambda$ and some grain boundary reflections spots and/or double diffraction spots coming from higher order Laue zones in both grains. Fig.5.29(a) and (b) are low- and high-camera lengths $[\,5\overline{52}\,]_\lambda$ CBED patterns taken from the same area defined above. The whole pattern and BF exhibit no symmetry other than the identity element of symmetry.

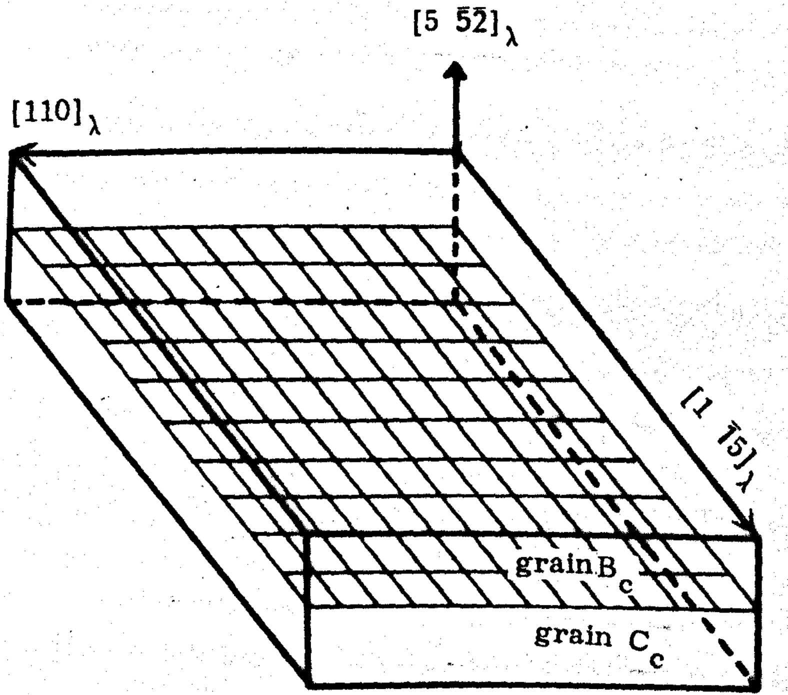

Fig. 5.25. A schematic diagram for the $\Sigma=27(5\ \bar{5}\bar{2})_\lambda$ bicrystal.

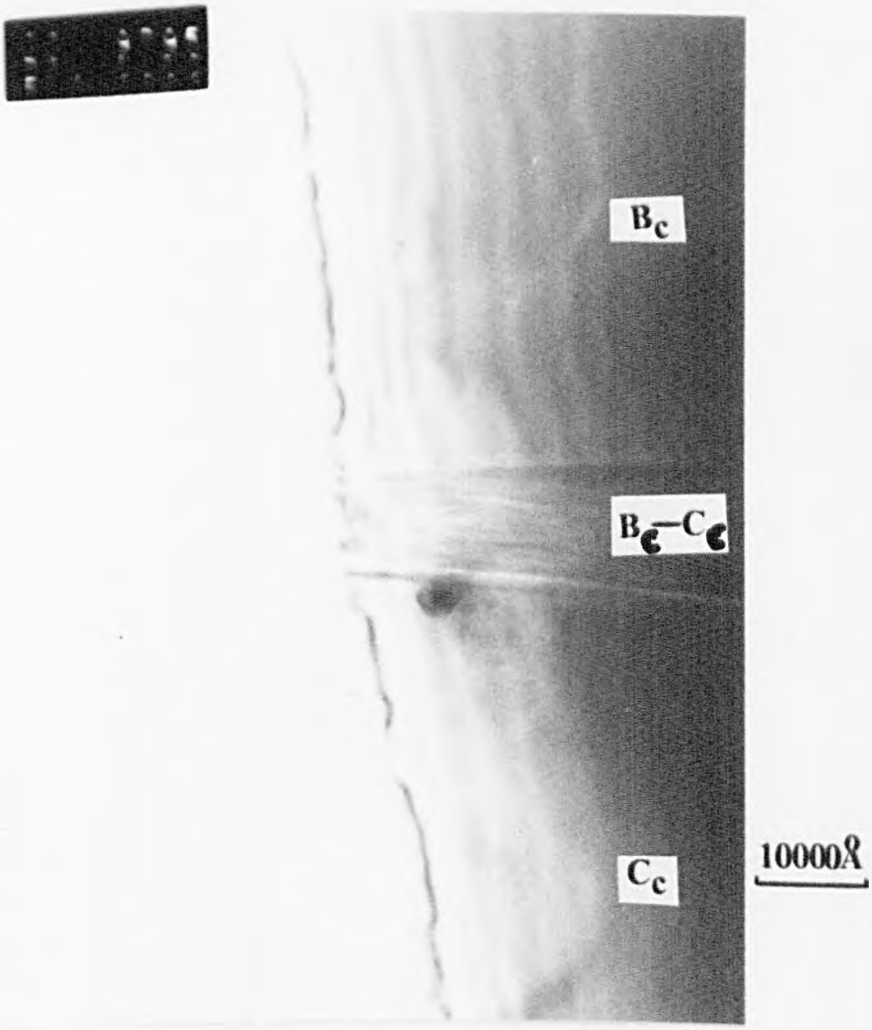

Fig. 5.26. A bright field micrograph taken from the $\Sigma = 27(5\,\overline{52}\,)_\lambda$ "plan-view" Ge specimen.

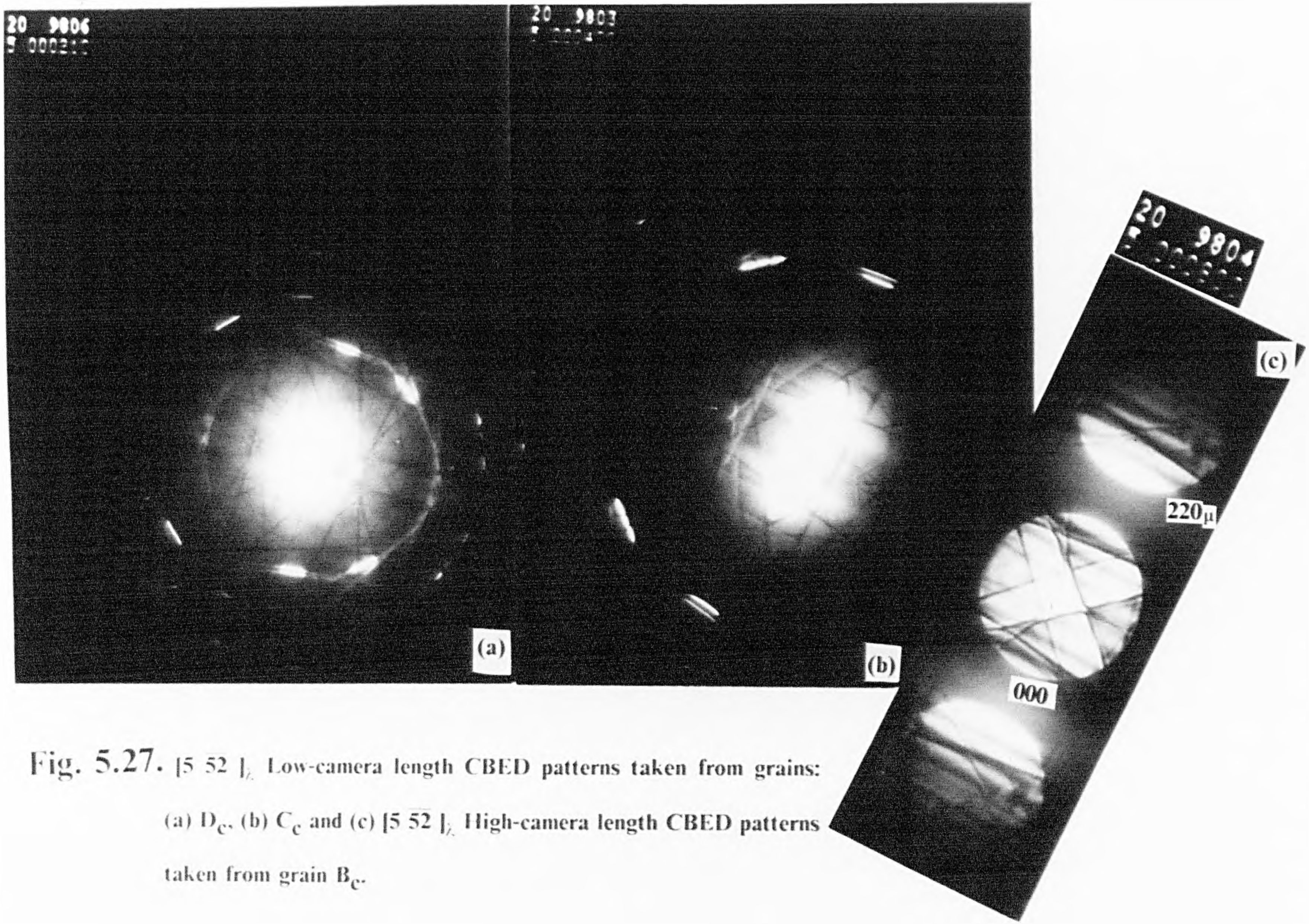

Fig. 5.27. $[5\ \overline{52}\ ]_Z$ Low-camera length CBED patterns taken from grains: (a) D_c, (b) C_c and (c) $[5\ \overline{52}\ ]_Z$ High-camera length CBED patterns taken from grain B_c.

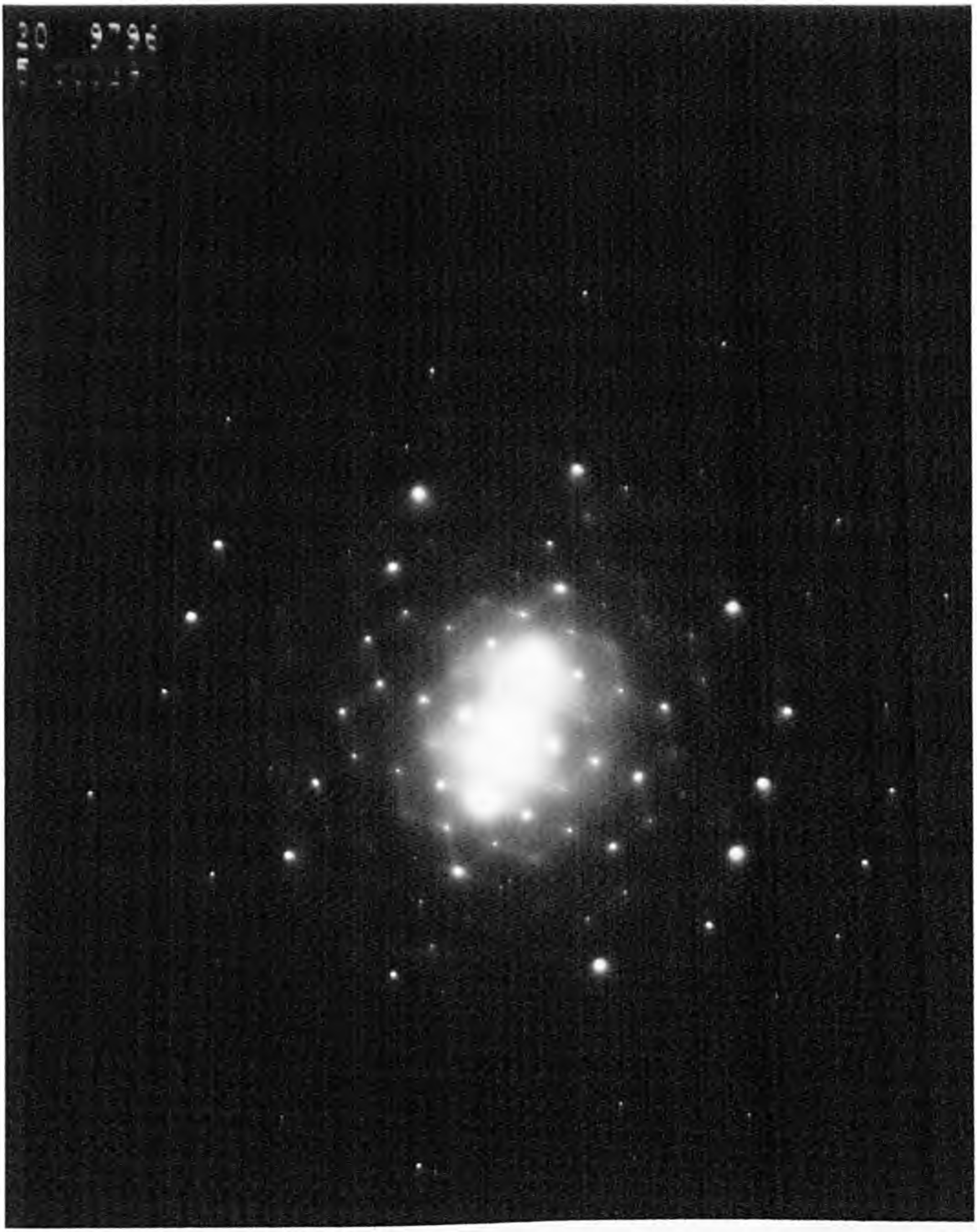

Fig. 5.28. 1-[$5\overline{52}$]$_\lambda$ low-camera length SAD pattern was taken from a $\Sigma = 27$ $(5\overline{52})_\lambda$ "plan-view" specimen.

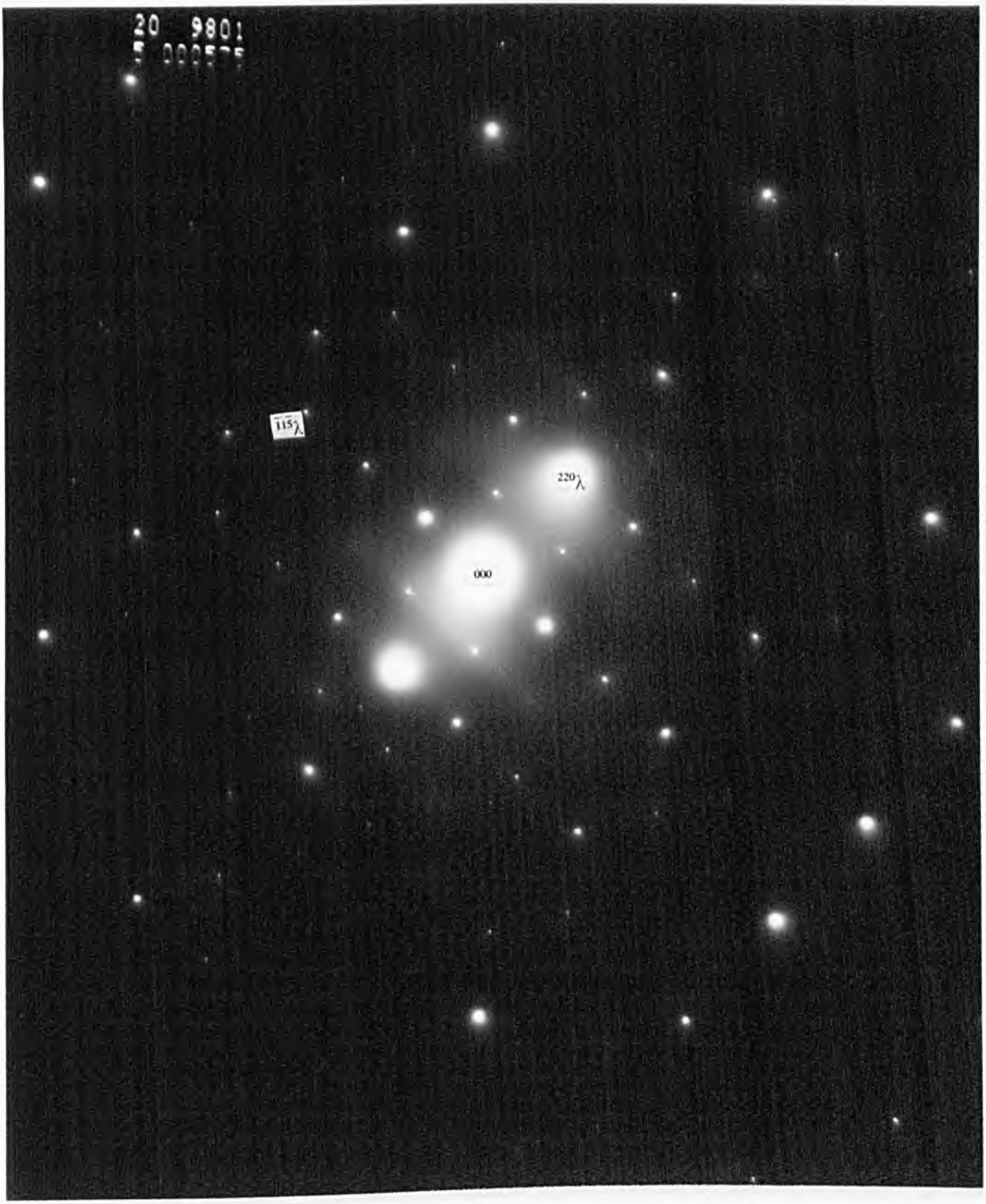

Fig. 5.28. 2-$[5\bar{5}\bar{2}]_\lambda$ High-camera length SAD pattern was taken from a $\Sigma = 27(5\bar{5}\bar{2})_\lambda$ "plan-view" specimen.

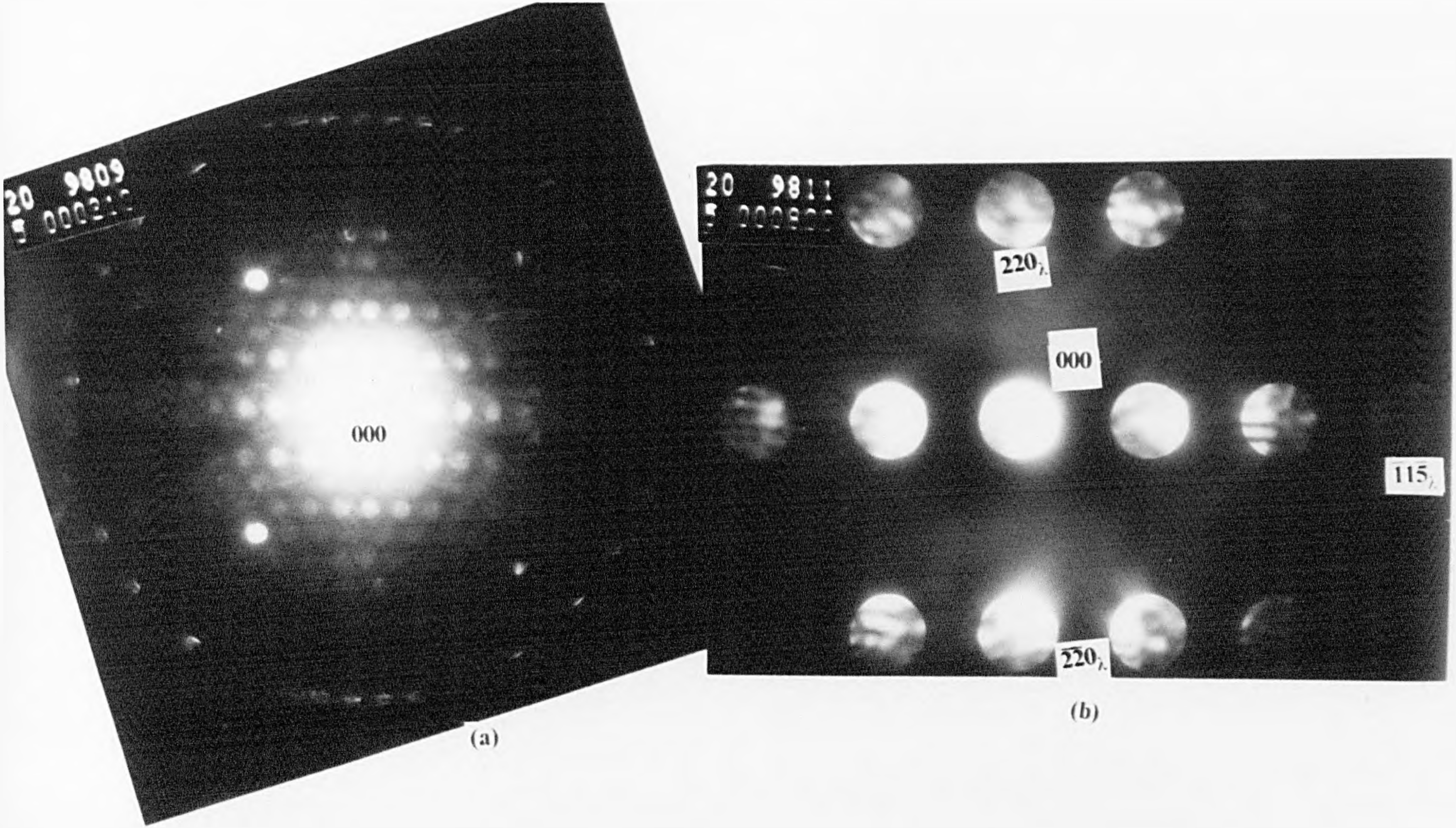

(a)

(b)

Fig. 5.29. $[5\,52]_L$ CBED patterns: (a) Low-camera length and (b) High-camera length.

CHAPTER SIX

Discussion

6.1. General remarks..................6.3

6.2. Interfacial facetting and dissociation........6.4

6.3. Interpretation of CBED and LACBED patterns from "plan-view" and "edge-on" specimens.......6.7

6.4. Interpretation of SAD patterns................6.10

6.5. Observation of $\Sigma = 3(1\bar{1}\bar{1})_\lambda$ boundary...6.13

- 6.5.1 Previous experimental observations and theoretical models of $\Sigma = 3(1\bar{1}\bar{1})_\lambda$ boundary...6.13
- 6.5.2. SAD patterns from "edge-on" and "plan-view" specimens................6.14
- 6.5.3. CBED patterns from "edge-on" specimen.....6.15
- 6.5.4. CBED patterns from "plan-view" specimen.....6.16
- 6.5.5. LACBED patterns from "edge-on" and "plan-view" specimen................6.17
- 6.5.6. Summary of observations.................6.18

6.6. Previous experimental observations and theoretical models of $\Sigma = 3(\bar{1}1\bar{2})_\lambda$ boundary...6.19

- 6.6.1. SAD patterns from "edge-on" and "plan-view" specimens................6.20
- 6.6.2. CBED patterns from "edge-on" and "plan-view" specimens...............6.24
- 6.6.3. Summary of observations................6.26
- 6.6.4. Observation of dissociation in $\Sigma = 3(\bar{1}1\bar{2})_\lambda$

"edge-on" specimen....................6.27

6.7. Previous experimental observations and theoretical models of $\Sigma=27(5\bar{5}\bar{2})_\lambda$ boundary...6.28

6.7.1. Dissociation of $\Sigma=27(5\bar{5}\bar{2})_\lambda$ boundary......6.29

6.7.2. SAD patterns from "edge-on" and "plan-view" specimens........6.30

6.7.3. CBED patterns from "edge-on" and "plan-view" specimens........6.31

6.7.4. Summary of observations.................6.33

6.1. GENERAL REMARKS.

The objective of this study can be restated here briefly as follows. The experimental work programme was divided into two parts. The first part was concerned with the preparation of germanium bicrystal specimens for electron microscopy. The second part was devoted to obtaining SAD, CBED and LACBED patterns from these bicrystal specimens. Many difficulties were faced in the specimen preparation process; for example, the fragility of germanium was one of the major obstacles and required modifications of the methodology of specimen preparation in order to be overcome. Also, a new method has been adopted and used successfully for preparing $\Sigma=3(\ 1\bar{1}\bar{1}\ )_{\lambda}$, $\Sigma=3(\ \bar{1}1\bar{2}\ )_{\lambda}$ and $\Sigma=27(\ 5\bar{5}\bar{2}\ )_{\lambda}$ "edge-on" and "plan-view" specimens (see chapter 3). Hence, the first part of the experimental work has been carried out completely as planned.

SAD, CBED, and LACBED patterns have been obtained and photographed from the above specimens, i.e. 3 "edge-on" and 3 "plan-view" specimens. In the case of "edge-on" specimens 3 different patterns (SAD or CBED) have been taken from each specimen; one straddling the grain boundary and one from each of the adjacent grains. A discussion of these patterns might be expected next, but complications arose which need to be discussed first. These unforeseen difficulties are concerned with the fact that the $\Sigma=3(\ \bar{1}1\bar{2}\ )_{\lambda}$ and $\Sigma=27(\ 5\bar{5}\bar{2}\ )_{\lambda}$ boundaries were found not to be planar, but were generally facetted or dissociated. Secondly, the interpretation of CBED from "plan-view" and "edge-on" bicrystal specimens is not as straight forward as was originally envisaged. These two topics will be considered before discussing the experimental results described in chapter 5.

6.2. INTERFACIAL FACETTING AND DISSOCIATION.

The words facetting and dissociation imply the change in the atomic structure of a boundary to produce special configurations in order to lower the total contribution of this boundary to the free energy of the grains present on either side of the boundary. Indeed, if a boundary produces a lower energy configuration without creation of new grains, other than the parent grains, it is called a facetted boundary whereas, if a boundary produces a lower energy configuration with creation of new grains, in addition to parent grains, it is called a dissociated boundary. In the case of CSL boundaries it has been suggested that interfacial energy is inversely correlated to the density of coincident sites *(Grimmer et al. 1974)*. Therefore, the interfacial energy would be expected also to depend on the type of the boundary plane, so that different facets of the same boundary have different energies. This model implies that, for example, the grain boundaries $\Sigma = 3$, 9, or 27 are stable when they form on the dense planes $\{1\bar{1}\bar{1}\}$, $\{\bar{2}21\}$ or $\{5\bar{5}\bar{2}\}$ (see Fig. 2.6(a), (b) and (c) in chapter 2), respectively, and also that a $\Sigma = 3$ boundary which has formed on a $\{\bar{1}1\bar{2}\}$ plane would have relatively higher energy than that for the boundary formed on a $\{1\bar{1}\bar{1}\}$ plane.

The facetting and dissociation behaviour of grain boundaries illustrates that the thermodynamic driving force is acting in such a way as to reduce or minimise interfacial energy. Let us consider that a boundary has facetted in order to attain a lower energy configuration. Hence, the sum of the energies of the two facets must be less than or equal to the parent boundary energy, i.e.

$$\gamma_1 A_1 \geq \gamma_2 A_2 + \gamma_3 A_3 \qquad (6.1)$$

where γ is the grain boundary energy per unit area and A is the area of the boundary plane. From the experimental point of view, A can be measured easily, but determinations of the energies γ are difficult and only relative values can be obtained by standard techniques *(e.g. Goodhew 1980).* For this reason, observations of facetting and dissociation are useful since they can provide some information concerning γ.

The tendency of a grain boundary to acquire low energy configurations by facetting or dissociation mechanisms mentioned above has been appreciated and confirmed experimentally. For example, in the last decade significant transmission electron microscopy (TEM) and high resolution electron microscopy (HREM) observations have been made of facetted and dissociated boundaries in the second and third order twins (see e.g. *Cunningham et al. 1982, Vaudin et al. 1983, Bourret et al. 1985, 1986 and Garg et al. 1988).*

Some experimental evidence, reported by *Goodhew (1980),* showed that grain boundary energy varied with misorientation, inclination, impurity levels and temperature. Recently, a review of possible geometric criteria for low interfacial energy has been given *(Sutton et al. 1987).* Those criteria comprise:

(1) low reciprocal volume density of coincidences sites;

(2) high planar density of coincidences sites;

(3) large interplanar spacing;

(4) high density of locked-in rows of atoms; and

(5) high planar density of coincidence sites at constant interplanar spacing.

These authors also made use of the available experimental observations to test these criteria, and found a significant number of experimental observations violating the first four of the criteria above. The last criterion is applicable for a limited number of cases, e.g. metal/metal or ionic/ionic interfaces but fails for metal/ionic interfaces.

In summary, we can say that there is no general and reliable theory available which can be used to predict grain boundary energies, and only a relatively small body of experimental observations has been recorded.

Now, we present and discuss some examples of specific observations, published by other workers, which are relevant to our work. First, we present some examples concerning dissociation and facetting. For example, $\Sigma=27$ interfaces could dissociate into $\Sigma=3$ and 9 boundaries which have higher planar densities of coincidence sites. A specific example is the $\Sigma=3\{111\}_\lambda/\{115\}_\mu$ boundary, which has low planar density of coincidence sites, and is observed to be facetted to $\Sigma=3\{111\}_\lambda/\{111\}_\mu$, $\Sigma=3\{112\}_\lambda/\{112\}_\mu$ boundaries, which have higher planar densities of coincidence sites *(Sutton et al. 1987)*. Also, the $\Sigma=9\{111\}_\lambda/\{115\}_\mu$ boundary is observed to be dissociated into $\Sigma=3\{111\}_\lambda/\{111\}_\mu$ plus $\Sigma=3\{112\}_\lambda/\{112\}_\mu$ boundaries for the same reason *(Sutton et al. 1987)*. Secondly, we show how one can estimate relative grain boundary energies from such observations. *Bourret and Bacmann (1985b)* observed a $\Sigma=3(\ 21\bar{1}\ )$ boundary which dissociated into $\Sigma=3(\ 11\bar{1}\ )$ and $\Sigma=9(\ \bar{1}2\bar{2}\ )$ boundaries, and, in another paper *(Bourret et al. 1985)*, gave a calculated value for the energy of $\Sigma=3(\ 21\bar{1}\ )$ boundary as $\gamma_1=0.29\mathrm{Jm}^2$. The measured areas of the boundary planes of $\Sigma=3(\ 21\bar{1}\ )$, $\Sigma=3(\ 11\bar{1}\ )$ and $\Sigma=9(\ \bar{1}2\bar{2}\ )$ boundaries, respectively, are $A_1=0.82a^2$, $A_2=2.31a^2$ and $A_3=0.67a^2$. Substituting into relation (6.1) one can therefore obtain

$$0.29 \times 0.82a^2 \geq 2.31a^2\gamma_2 + 0.67a^2\gamma_3$$

or

$$\gamma_2 \geq (1.0 - 2.8\ \gamma_3/9.714) \qquad (6.2)$$

6.3. INTERPRETATION OF CBED AND LACBED PATTERNS FROM "PLAN-VIEW" AND "EDGE-ON" SPECIMENS.

In the course of this work it has been noticed that the observed symmetry of CBED and LACBED patterns, which were obtained experimentally from $\Sigma = 3$, and 27 grain boundaries in germanium "plan-view" and "edge-on" bicrystal specimens, did not always correspond to the anticipated bicrystal symmetry. We believe that these discrepancies have arisen for two reasons; firstly due to effects associated with an extended focal spot size, and secondly due to symmetry breaking inherent in the specimen preparation. These aspects are discussed separately below.

In previously published accounts of the interpretation of CBED symmetry from "edge-on" bicrystal specimens, *Schapink and Co-workers (Caron et al. (1985), Schapink et al. (1986) and Schapink (1986))*, it was assumed that the incident convergent beam has a point focus centred in the boundary plane as depicted in Fig.6.1(a). It can be seen from the figure that the range of angles of incidence of the electron beam in this case is not equivalent in the adjacent crystals. As a consequence, the symmetry of CBED and LACBED patterns may not therefore correspond directly to that of the bicrystal. However, in the present work, we note that the incident beam in fact has an extended focus or "spot size", due to, firstly, the electron source not being a point source but an extended one, and secondly, the lens aberrations (see for example *Edington (1976) and Chescoe et al. (1984)*), and we believe that this is a most important

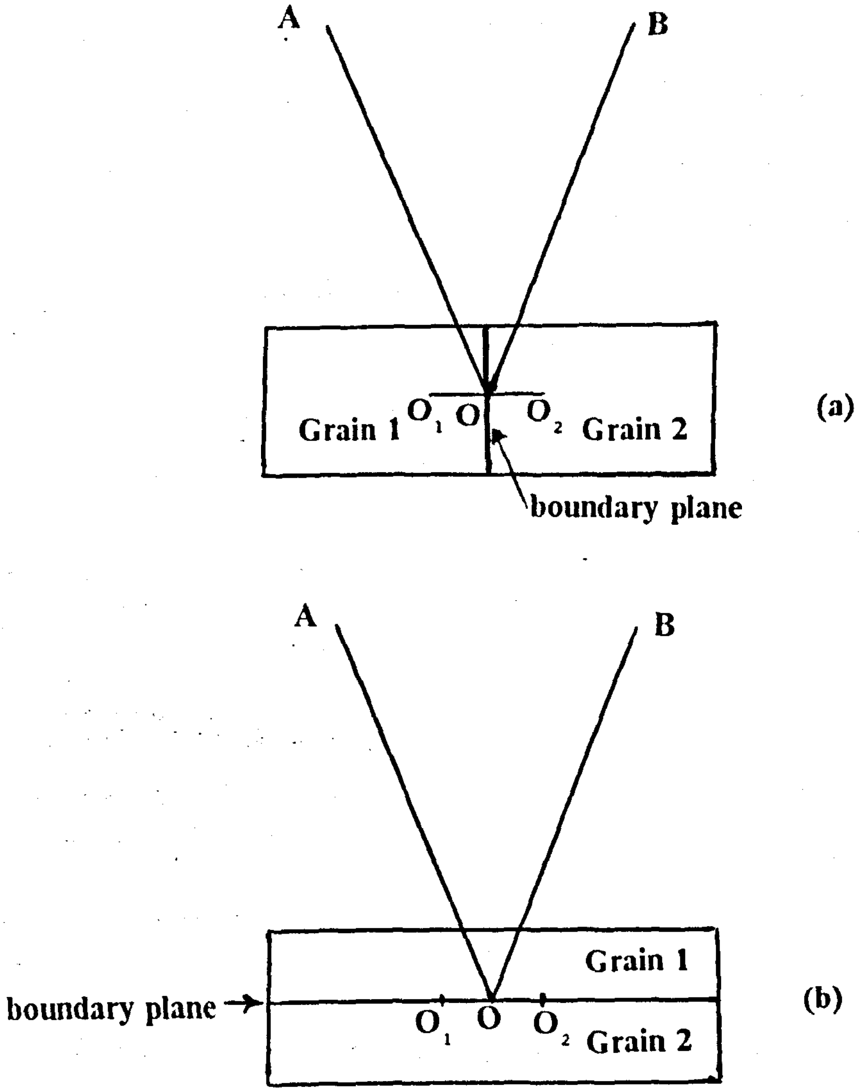

Fig. 6.1. A schematic diagram for an electron beam incident on: (a) an "edge-on" specimen, and (b) a "plan-view" specimen.

consideration in the present context. Each point on the focal spot can be regarded as the point focus of a cone incoherently related to the cone corresponding to any other point. Only cones focused on points very close to interface irradiate both crystals. The cones focused on points between O and O_1 irradiate crystal 1 predominantly, and those between O and O_2 irradiate crystal 2 predominantly. From the discussion above we would expect the CBED patterns obtained with relatively large spot sizes ($\geq$ 1μm) from such "edge-on" bicrystals to correspond to the superimposition of the patterns taken from the adjacent crystals separately, i.e. addition of the intensities of the two patterns. We shall refer to such patterns as exhibiting "complex symmetry", because this symmetry corresponds to the point symmetry of the dichromatic complex (see chapter 2) viewed along the appropriate direction. We note, therefore, that such patterns may be regarded as exhibiting antisymmetry, for example when an anti-mirror is present which relates a white disc, e.g. g_λ, to a black disc, g_μ. As spot size diminishes, the contributions to the final pattern from cones which irradiate both crystals, i.e. those focused at points close to the boundary, increases compared to cones which irradiate only one of the crystals. Under these circumstances complex symmetry is no longer expected. Thus, for very small spot sizes ($\approx$ 1nm), i.e. where virtually all incident cones irradiate both crystals, lower symmetry patterns are expected. We would also anticipate this result if the convergence angle is increased. Hence we expect that LACBED patterns may show lower symmetry than the complex symmetry exhibited by CBED patterns obtained using the same spot size.

We now consider the case of "plan-view" specimens. As depicted in Fig.6.1(b), when the focal spot is taken to be close to the boundary plane, it is seen that cones focused at each point between O_1 and O_2, i.e. all cones, will irradiate both crystals. Thus, in this case, we would expect the CBED pattern to exhibit the symmetry of the bicrystal, and not that of the dichromatic complex as in the above case.

The second cause of discrepancy between observed and anticipated CBED symmetry, as mentioned in the introduction to section 6.3, arises due to symmetry breaking as a consequence of specimen preparation. In the case of "edge-on" bicrystals, provided the specimen surfaces are flat and perpendicular to the interfacial plane, no bicrystal symmetry will be broken. However, this is not the case for "plan-view" specimens. The ideal "plan-view" bicrystal specimen, which has smooth surfaces and where the boundary plane is situated exactly centrally, is depicted in Fig.6.2(a). Such a specimen would exhibit, for example, an anti-mirror and/or an anti-diad parallel to the boundary plane if these were present in the bicrystal group. On the other hand these antisymmetry elements would be broken if the boundary plane were not central and/or because of specimen surface roughness.

In summary, from the discussion above it can be seen that, taking these further aspects into account, we anticipate that CBED patterns obtained from "plan-view" specimens should exhibit bicrystal symmetry, but those taken from "edge-on" specimens should exhibit primarily complex symmetry for the spot sizes used in the present work. Moreover, if any symmetry is broken by virtue of specimen preparation, we would expect only to see "the residue" of bicrystal or complex symmetries in the "plan-view" and "edge-on" cases, respectively. Consequently, in the discussion of the observations of CBED and LACBED patterns observed from individual interfaces to be presented in the following sections, we begin by considering the complex and bicrystal

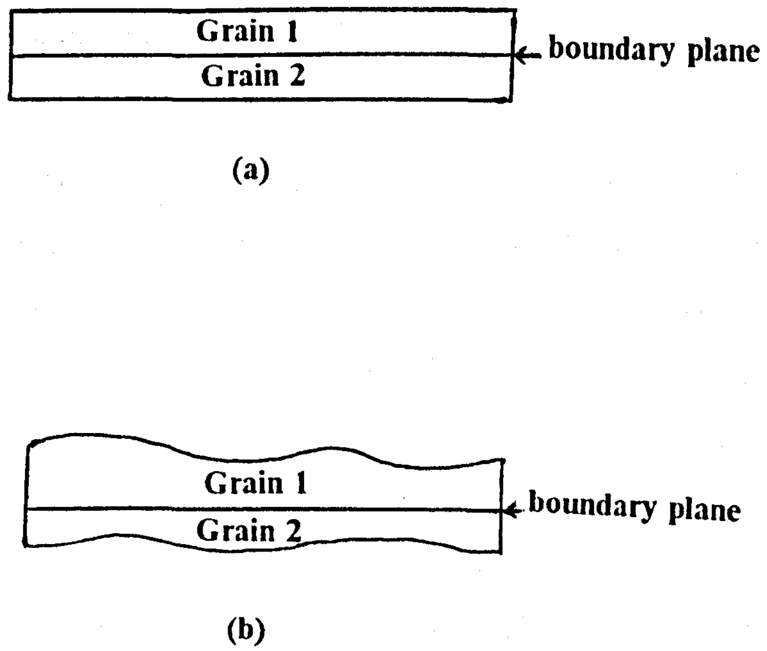

Fig. 6.2. A schematic diagram for a "plan-view" bicrystal specimen: (a) an ideal bicrystal specimen where the position of the boundary plane is exactly at the centre of the specimen and the specimen surfaces are smooth, and (b) a real bicrystal specimen where the boundary plane is not exactly at the centre of the specimen and the specimen surfaces are rough.

symmetries. The reader can then appreciate that the observed symmetries are in fact the residues of the complex and bicrystal symmetries as discussed above. For the reader's convenience we have also included the single crystal patterns obtained from the adjacent crystals (see chapter 5), which facilitate the visualisation of the complex symmetry.

6.4. INTERPRETATION OF SAD PATTERNS.

SAD patterns taken from bicrystal specimens can exhibit three types of distinct reflections, i.e. crystal, double diffraction and grain boundary reflections, and we begin this section by explaining how these various reflections can be identified. Firstly we outline the process for indexing crystal reflections, recalling that the concepts of the reciprocal lattice and structure factors were introduced in chapter 3. In the present work we are studying germanium crystals which have fcc lattices in direct space, and hence have bcc reciprocal lattices (see Fig.3.5). The unit vectors of the non-primitive fcc unit cell are e_1 = [100], e_2 = [010] and e_3 = [001] and hence the non-primitive reciprocal unit cell vectors are e_1^* = 100, e_2^* = 010 and e_3^* = 001. However, it is also necessary to consider the reflections systematically absent according to Eq.(3.5). These correspond to the set due to the fcc direct lattice, i.e. only reflections with h, k and l unmixed are present, and , in addition, absences due to the double atom basis, i.e. reflections where $h + k + l = 4(n + 1/2)$, where h, k and l are even and n is an integer, are absent. To be consistent with general practice, we shall refer to the reciprocal vector corresponding to reflection by a particular set of planes (hkl) in a diffraction pattern as $g = he_1^* + ke_2^* + le_3^*$. In the case of a bicrystal specimen, where the direct space unit cells of the white and black crystals are related by the transformation P (see chapter 2), the white and black reciprocal unit cells will also be related by this transformation. Thus, the indices of white and black crystal reflections can be identified in a given SAD pattern by determining the appropriate section of the white and black reciprocal lattices. We remind the reader that, as explained in chapter 3, some crystal reflections which are kinematically forbidden according to Eq.(3.5) may exhibit non zero intensities due to multiple scattering *(Tu et al. 1978)*.

Double diffraction is the process where a beam g_λ excited in the white crystal by the incident beam, is subsequently incident on the black crystal thereby exciting a beam g_μ (or vice versa). Such double diffraction is especially likely in "plan-view" specimens, but much less likely in "edge-on" specimens when the incident beam is parallel to the interface. It can be seen that the indices of double diffraction beams are given by $g_\lambda - Pg_\mu$ (using the white reciprocal lattice frame). This set of reciprocal vectors, designated $g_{\lambda\mu}$ (or $g_{\mu\lambda}$), is readily obtained for each of the systems studied in this work. For example, in the case of $\Sigma = 3$, the set $g_{\lambda\mu}$ corresponds to a hexagonal lattice with primitive reciprocal vectors $\frac{2}{3}\frac{\bar{2}}{3}\frac{4}{3}$, $\frac{2}{3}\frac{4}{3}\frac{\bar{2}}{3}$ and $\frac{1}{3}\frac{\bar{1}}{3}\frac{\bar{1}}{3}$. Hence, in order to establish whether a reflection observed in a given SAD pattern is due to double diffraction, it is necessary to obtain the appropriate section of this double diffraction lattice, i.e. that perpendicular to the beam direction. In addition, it should be kept in mind that if a reflection $g_{\lambda\mu}$ does lie in this section, its intensity will only be significant if the component reflections, g_λ and g_μ, are strongly excited. This enables one to investigate whether a particular reflection is actually due to double diffraction, as opposed to some other cause, by tilting the specimen in such a way that g_λ and g_μ are not strongly excited. If the intensity of the reflection in question does not diminish as a result of tilting, it is probably not due to double diffraction. It must be kept in mind also that, if the Ewald reflection sphere construction is used to identify excited reflections, the beam incident on the lower crystal is g_λ and hence the corresponding orientation of the Ewald sphere must be chosen.

The third type of reflection, and from the present point of view the most interesting type, is that due to interfacial relaxation. Such relaxation may include a displacement field extending from the boundary into the adjacent crystals, reconstruction of the bonds at the interface leading to new periodicities, and also possibly segregation of impurities to the interface. If the periodicity of an interface is defined in direct space by the primitive vectors s_1^i and s_2^i, diffracted beams g_1^i and g_2^i, or any combination, can arise. These may or may not be coincident with crystal or double diffraction reflections. The intensity of interfacial reflections, g^i, can be obtained using the kinematic structure factor equation (Eq.(3.2)) if the displacement field and segregation effects are known. These reflections are expected to be elongated in the direction perpendicular to the interface. We therefore expect that such streaks, or relrods, may be observed in SAD patterns from "edge-on" specimens, and other works have estimated grain boundary thickness from the length of such relrods *(Carter et al. 1980)*. We also note that bicrystal symmetries can be investigated from systematic absences in arrays of interfacial reflections, as has been described by *Bacmann et al. (1985)*.

One final point which it is appropriate to mention here, for the sake of completeness, concerns kinematically forbidden reflections (Eq.3.5(a), (b), (c) and (d)). For such reflections the structure factor, F_{hkl}

(Eq.(3.2)), will be zero for a perfect crystal column parallel to the incident beam and which contains an integral number of unit cells. However, F_{hkl} can be non-zero for crystal columns containing non-integral numbers of unit cells *(Cherns 1974)*. Thus, forbidden reflections can actually be present in SAD patterns, and, in the present context, it is important to consider this possibility.

6.5. OBSERVATION OF $\Sigma = 3(1\bar{1}\bar{1})_\lambda$ BOUNDARY.

We begin this section by considering briefly the current state of theoretical and experimental knowledge concerning the structure of the $\Sigma = 3(1\bar{1}\bar{1})_\lambda$ interface in germanium. Subsequently we compare this knowledge to the results obtained by electron diffraction experiments in the present work.

6.5.1. PREVIOUS EXPERIMENTAL OBSERVATIONS AND THEORETICAL MODELS OF $\Sigma = 3(1\bar{1}\bar{1})_\lambda$ BOUNDARY.

There is a general consensus that the structure of this interface is well understood. Recent theoretical studies, e.g. *Paxton (1987)*, suggest that the structure illustrated in Fig.6.3 is stable, and has low energy (calculated energy $\approx$ 29 erg/cm^2). This figure shows a projection along $[110]_\lambda$ direction. The vector normal to the boundary plane is $[1\bar{1}\bar{1}]_\lambda$ and points vertically up the page. The crosses and triangles represent atoms at heights 0 and $1/4[110]_\lambda$. The interfacial periodicity of this structure is $s_1 = 1/2[110]_\lambda$ and $s_2 = 1/2[\bar{1}1\bar{2}]_\lambda$. The twin interface consists of a single layer of six-membered rings or "T" units without dangling bond. The bond lengths between the atom pairs 1-1', 1-2 and 4-5 are shortened

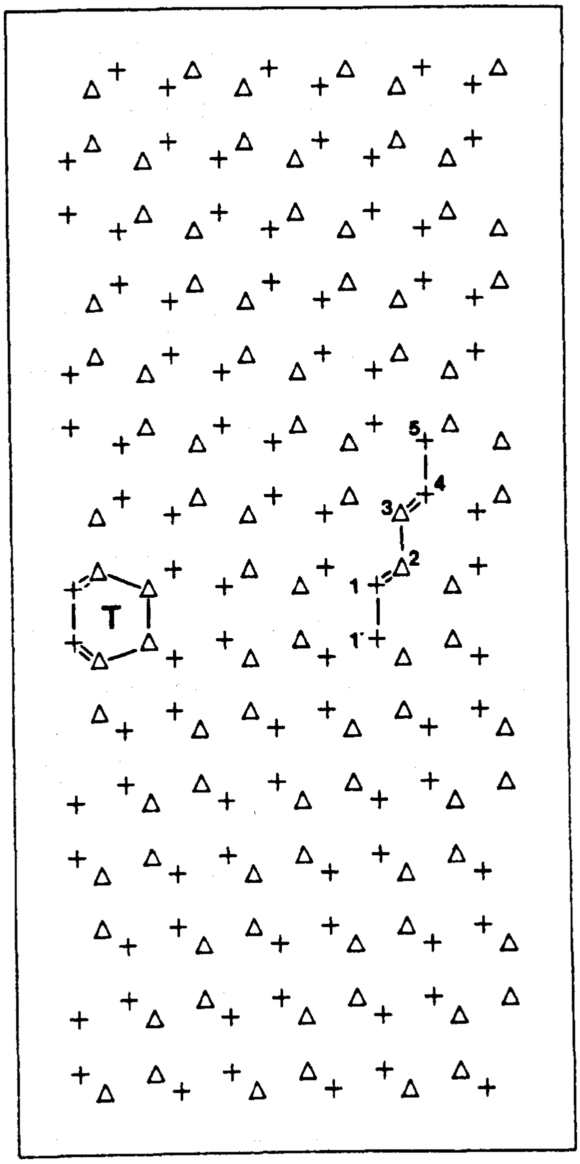

Atom Numbers	Δℓ(%)
1',1	-0.092
1,2	-0.071
2,3	0.022
3,4	0.023
4,5	-0.004

Fig. 6.3. $(1\bar{1}\bar{1})$ twin interface: atomic structure and changes in bond lengths(Δl), (reproduced from Paxton 1987).

while those between the atom pairs 2-3 and 3-4 are stretched. In the positions where the bond length decreases the bond energy increases and vice versa. The structure exhibits the point symmetry m'2'm, i.e. the identity, a mirror $m(110)_\lambda$, an anti-mirror $m'(1\bar{1}\bar{1})_\lambda$, and an anti-diad $2'[\bar{1}1\bar{2}]_\lambda$

Experimental evidence collected by various researchers is in agreement with this model. For example the HREM work of *D'Anterroches and Bourret (1984),* and α-fringes work of *Vlachavas and Pond (1980)* on $\Sigma=3(111)$ coherent twins in silicon proved that there is no relative displacement at the boundary plane (111). The CBED work by *Schapink (1986)* on gold bicrystals determined the point group of a "plan-view" bicrystal as 6'/m'm'm which indicates that the rigid body translation at a (111) boundary in gold is zero. Often $\Sigma=3(111)$ coherent twin observed in dissociation of other interfaces, but not observed to dissociate itself, implying that it is a particular stable boundary.

6.5.2. SAD PATTERNS.

The selected area electron diffraction patterns, which have been taken from $\Sigma=3(1\bar{1}\bar{1})_\lambda$ "edge-on", viewed along $[110]_\lambda$, and "plan-view" bicrystal specimens, are shown in Fig.5.6(c) and 5.8(d) respectively. The crystal reflections have been identified and indexed in the figures and a trace of the boundary plane $(1\bar{1}\bar{1})_\lambda$ is indicated, in the case of the "edge-on" specimen in Fig.5.6(c). We now consider the possibility of double diffraction and grain boundary reflections in this "edge-on" case. The primitive double diffraction vectors, $g_{\lambda\mu}$, in this section of the reciprocal lattice are $\frac{1}{3}\frac{\bar{1}}{3}\frac{\bar{1}}{3}$ and $\frac{2}{3}\frac{\bar{2}}{3}\frac{4}{3}$. No reflections were observed in these positions which is as expected for "edge-on" specimens. Similarly, no grain boundary reflections were detectable for these "edge-on" specimens. Since the interfacial periodicity corresponds to periodicity in both crystals, grain boundary reflections are expected to be coincident with crystal reflections in the present case. No additional grain boundary reflections were detectable in this work.

The SAD pattern from a "plan-view" specimen is shown in Fig.5.8(d). The white and black crystal reflections are all coincident in the zero layer for this $1\bar{1}\bar{1}$ section of the reciprocal lattice for example 202_λ is coincident with 220_μ. The primitive double diffraction reflections in this zero layer are $\frac{2}{3}\frac{\bar{2}}{3}\frac{4}{3}$ and $\frac{2}{3}\frac{4}{3}\frac{\bar{2}}{3}$, and clear evidence for such reflections is seen in Fig.5.8(d). These double diffraction reflections are weak because they involve component reflections from HOLZ which are only weakly excited. No evidence of grain boundary reflections was obtained.

6.5.3. CBED PATTERNS FROM "EDGE-ON" SPECIMENS.

We begin this section by writing the expected point symmetry for both the $\Sigma = 3$ dichromatic complex and $\Sigma=3(1\bar{1}\bar{1})_\lambda$ bicrystal, looking along $[110]_\lambda$ direction. The point symmetry for $\Sigma=3(1\bar{1}\bar{1})_\lambda$ dichromatic complex and bicrystal are

$$G(c) = mm'm'$$

$$= \{1, m(110), 2[110], \bar{1}, m'(\bar{1}1\bar{2}), m'(1\bar{1}\bar{1}), 2'[\bar{1}1\bar{2}], 2'[1\bar{1}\bar{1}]\}$$

and

$$G(b) = 2'mm' = \{1, m(110), 2'[\bar{1}1\bar{2}], m'(1\bar{1}\bar{1})\},$$

respectively.

The CBED patterns in Fig.5.7(c), has been taken from a $\Sigma=3(1\bar{1}\bar{1})_\lambda$ "edge-on" specimen where the electron beam was parallel to the surface normal $[110]_\lambda$. The observed elements of symmetry (BF and whole pattern) exhibited by this pattern are:

(1) an anti-mirror parallel to the boundary plane, $m'(1\bar{1}\bar{1})_\lambda$,

(2) an anti-mirror perpendicular to the boundary plane, $m'(\bar{1}1\bar{2})_\lambda$, and

(3) a diad perpendicular to the pattern plane, $2[110]_\lambda$.

Thus, the observed symmetry is 2m'm', i.e. $\{1, 2[110]_\lambda, m'(1\bar{1}\bar{1})_\lambda, m'(\bar{1}1\bar{2})_\lambda\}$. We note that $m(110)_\lambda$ has not been detected, and we assumed that this is due to specimen preparation as discussed in section 6.3. From a comparison between the observed symmetry and the expected bicrystal and complex point symmetry one can recognise that the observed symmetry is not equivalent to the bicrystal point symmetry but it is a residue of the complex symmetry, following some symmetry breaking due to specimen preparation.

6.5.4. CBED PATTERNS FROM "PLAN-VIEW" SPECIMENS.

The point symmetry of a $\Sigma = 3$ dichromatic complex and a $\Sigma=3(1\bar{1}\bar{1})_\lambda$ bicrystal, looking along $[1\bar{1}\bar{1}]_\lambda$ direction are

G(c) = $6'/m'mm'$ (see Tables 2.4(a) and 2.5(a) for the 24 symmetry and anti-symmetry elements of this point group)

and

$$G(b) = \bar{6}'m2' = \{1, 3^{+}, 3^{-}, m(110), m(101), m(01\bar{1}), \bar{6}^{+\prime}, \bar{6}^{-\prime}, m'(1\bar{1}\bar{1}), 2'[211], 2'[\bar{1}1\bar{2}], 2'[12\bar{1}]\},$$

respectively.

The CBED pattern in Fig.5.8(e), has been taken from a $\Sigma=3(1\bar{1}\bar{1})_\lambda$ "plan-view" bicrystal specimen where the electron beam was parallel to the specimen surface normal $[1\bar{1}\bar{1}]_\lambda$. The observed elements of symmetry (BF and whole pattern) exhibited by this pattern are:

(1) triad along $[1\bar{1}\bar{1}]_\lambda$ direction, 3^+, 3^-,
(2) $m(110)_\lambda$,
(3) $m(101)_\lambda$ and
(4) $m(0\bar{1}1)_\lambda$.

Thus, the observed symmetry is

$$3m = \{1, 3^+, 3^-, m(110), m(101), m(01\bar{1})\}.$$

In this case we note that the observed symmetry is a residue of the bicrystal point symmetry, assuming that the anti-mirror $m'(1\bar{1}\bar{1})_\lambda$ has been broken by specimen preparation.

6.5.5. LACBED PATTERNS FROM "EDGE-ON" AND "PLAN-VIEW" SPECIMENS.

The point symmetries of the $\Sigma=3$ dichromatic complex and $\Sigma=3(1\bar{1}\bar{1})_\lambda$ bicrystal are mentioned above.

The LACBED pattern in Fig.5.8(c), has been taken from a $\Sigma = 3(1\bar{1}\bar{1})_\lambda$ "edge-on" specimen where the electron beam was parallel to the surface normal $[110]_\lambda$. This pattern exhibits an anti-mirror symmetry parallel to the boundary plane, $m'(1\bar{1}\bar{1})_\lambda$. We note that, comparing by the CBED pattern taken from the same boundary and using the same spot size, the anti-mirror $m'(\bar{1}1\bar{2})_{\lambda}$ has been broken due to possibly the larger convergent angle which has been used for obtaining the LACBED patterns as discussed above.

The LACBED pattern in Fig.5.8(f), has been taken from a $\Sigma = 3(1\bar{1}\bar{1})_{\lambda}$ "plan-view" specimen where the electron beam was parallel to the specimen surface normal $[\,1\bar{1}\bar{1}\,]_{\lambda}$. It exhibits 3m symmetry , i.e., the same as CBED pattern, as was expected all the components cones irradiated both crystals.

6.5.6. SUMMARY OF OBSERVATIONS.

In summary the evidence collected in the present work using the SAD technique is consistent with other works, and supports the model of the $\Sigma=3(\,1\bar{1}\bar{1}\,)_{\lambda}$ coherent twin described by *Paxton (1987).* In particular, our observations imply the presence of a negligible interfacial displacement field, and that no reconstruction has occurred which modifies the interfacial periodicity.

Regarding the symmetry of the interfacial structure as studied using CBED and LACBED, we conclude that the present observations are also consistent with the model, Fig.6.3, which exhibits the symmetry $p\bar{6}m2'$. However, it must be remembered that the results from the "edge-on" specimens, i.e. showing the residue of the complex symmetry, does not provide information about the interfacial structure. In addition, although the bicrystal spacegroup can be determined from "plan-view" specimens in principle, only the residual group p3m has been detected here due to symmetry breaking in specimen preparation.

6.6. PREVIOUS EXPERIMENTAL OBSERVATIONS AND THEORETICAL MODELS OF $\Sigma = 3(\bar{1}1\bar{2})_\lambda$ BOUNDARY.

The structure of $\Sigma = 3(\bar{1}1\bar{2})_\lambda$ grain boundaries in covalent semiconductors, e.g. silicon and germanium, has been the subject of many experimental and theoretical studies. In particular a combination of electron diffraction, high resolution electron microscopy, and the α-fringe method has been applied to determine the atomic structure of this boundary. The electron diffraction study of *Bourret et al. (1985b)* for the boundary in germanium showed that this boundary exhibits the spacegoup c1m1. The centred unit cell has the periodicity $s_1 = [110]_\lambda$ and $s_2 = [2\bar{2}\bar{2}]_\lambda$, i.e. double the periodicity of the unrelaxed bicrystal (Fig.2.6(a)). High resolution electron microscopy, *Bourret et al. (1985a)*, directly confirmed the centred and doubled periodicity structure, or in short c(2x2). Hence, they concluded that this boundary is reconstructed along $[110]_\lambda$ such that successive reconstructed rows of atoms are shifted by $\frac{1}{2}[110]_\lambda$ forming a centred pattern. Also, a rigid body translation along $[1\bar{1}\bar{1}]_\lambda$ was measured using the α-fringe method, *Vlachavas and Pond (1980)*, in silicon and was confirmed directly by the high resolution observations mentioned above. This boundary has been observed to be sometimes stepped and facetted *(Bourret et al. 1985a)*. Also, dissociation of this boundary into Σ3(111) plus Σ9(221) has been observed *(Bourret et al. 1985b)*.

Several atomic models of the $\Sigma = 3(\bar{1}1\bar{2})_\lambda$ boundary have been proposed; but none of them are compatible with the c(2x2) structure observed above except that proposed recently by *Papon et al.(1985)* and which is shown in Fig.6.4. This figure has been reproduced from the

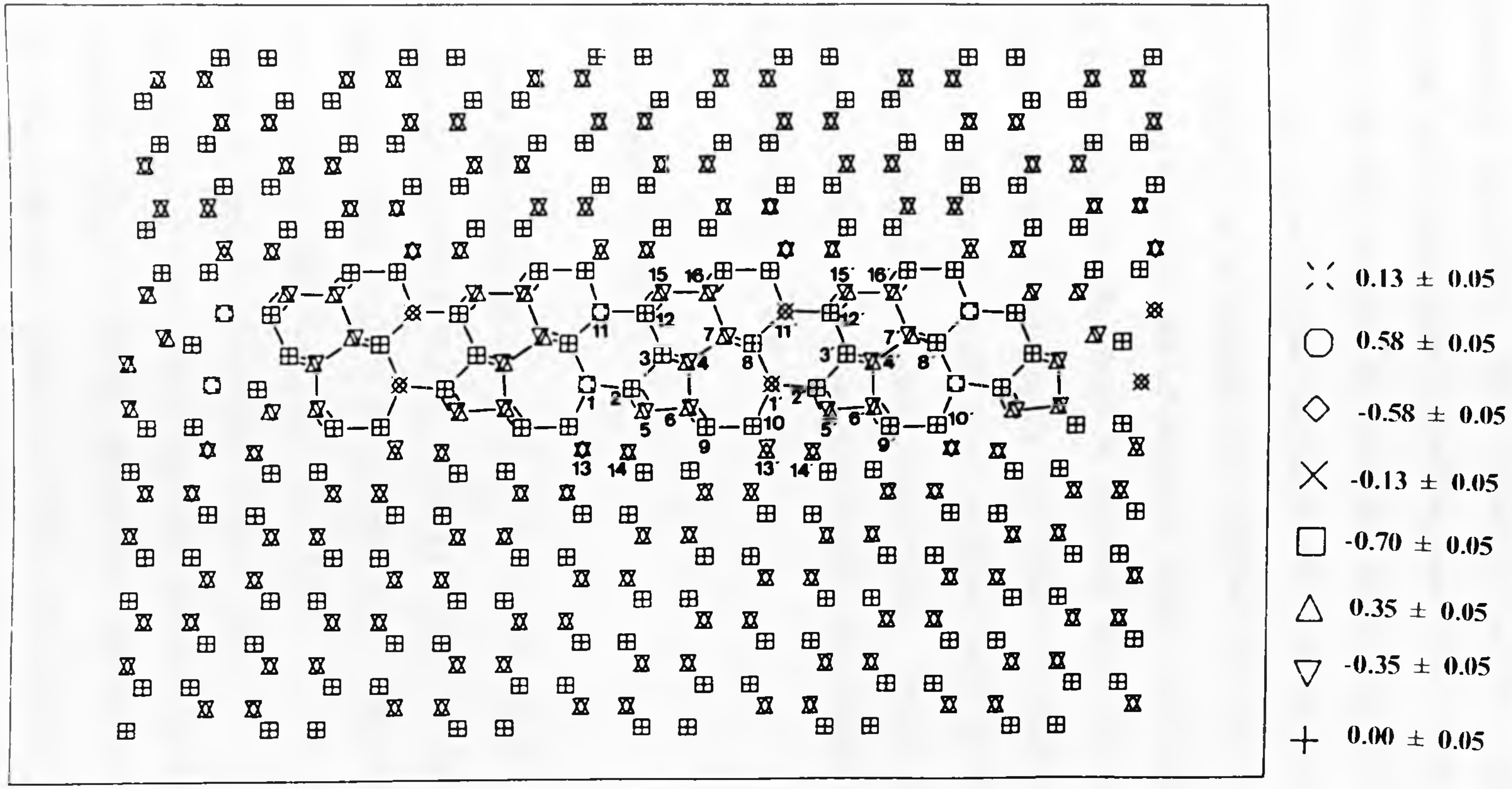

Fig. 6.4. $[1\bar{1}\bar{1}]60°(\bar{1}1\bar{2})$ grain boundary c(2x2):

Atomic structure (reproduced from Paxten 1987).

work of *Paxton (1987)*, who investigated its structure and energy using computer simulation. This structure can be regarded as a sequence of two structural units comprising one five- and one seven-membered ring per half period. No dangling bonds are present in the model at all. The structure has the interfacial periodicity $s_1 = [110]_\lambda$ and $s_2 = [2\bar{2}\bar{2}]_\lambda$. It is centred and exhibits the mirror symmetry, $m(110)_\lambda$, and therefore has the spacegroup c1m1. The calculated energy of the grain boundary structure in Fig.6.4 was 339 erg/cm². One notable feature of this boundary is the nature of reconstruction along $[110]_\lambda$, i.e the bonding between pairs of atoms such as numbers 1, 1', 11, 11' in the figure and the ones above them. These bonds also exhibit the maximum bond stretching that occurs, and hence the highest bond energies obtained in the study.

6.6.1. SAD PATTERNS.

The SAD pattern which has been taken from a $\Sigma = 3(\bar{1}1\bar{2})_\lambda$ "edge-on" bicrystal specimen viewed along $[1\bar{1}\bar{1}]_\lambda$ is shown in Fig.5.15(d). The white and black crystal reflections, e.g. 220_λ and 202_μ, are coincident in the zero layer for this $1\bar{1}\bar{1}$ section of the reciprocal lattice. The primitive double diffraction vectors, $g_{\lambda\mu}$, are $\frac{2}{3}\frac{\bar{2}}{3}\frac{4}{3}{}_\lambda$ and 110_λ, and reflections of the former type are present in Fig.5.15(d). The origin of these observed double diffraction reflections is not clear; reflections of this type were seen in $[1\bar{1}\bar{1}]_\lambda$ SAD patterns from single crystals, and were presumably caused by multiple scattering *(Tu et al. 1978)*, or due to non-integral number of unit cells *(Cherns 1974)*. Another possibility is that these reflections did arise by genuine double diffraction as a consequence of the presence of interfacial facets which would mean that the interface was not entirely parallel to the incident electron beam. The anticipated grain boundary reflections, g^i, are of the type $\frac{1}{2}\frac{1}{2}0_{\lambda}$ with all the odd orders systematically absent due to centring, but these were not detected.

The SAD pattern which has been taken from a $\Sigma = 3(\bar{1}1\bar{2})_{\lambda}$ "edge-on" bicrystal specimen viewed along $[110]_{\lambda}$ is shown in Fig.5.10(c). The white and black crystal reflections are indexed and we note that reflections of the type $1\bar{1}\bar{1}_{\lambda}$, $2\bar{2}4_{\lambda}$ are coincident in the zero layer for this 110 section of the reciprocal lattice. The primitive double diffraction vectors, $g_{\lambda\mu}$, are $\frac{2}{3}\frac{\bar{2}}{3}\frac{4}{3}\lambda$ and $\frac{1}{3}\frac{\bar{1}}{3}\frac{\bar{1}}{3}$, but no double diffraction reflections were observed. The expected grain boundary reflections, g^i, are of the type $\frac{1}{6}\frac{\bar{1}}{6}\frac{\bar{1}}{6}\lambda$, where odd orders are systematically absent due to centring, but none were detected. The possible reason for not observing these will be considered later.

The SAD pattern which has been taken from a $\Sigma = 3(\bar{1}1\bar{2})_{\lambda}$ "plan-view" bicrystal specimen viewed along $[\bar{1}1\bar{2}]_{\lambda}$ is shown in Fig.5.14(d). The white and black crystal reflections are coincident in the zero layer for this $\bar{1}1\bar{2}$ section of the reciprocal lattice depicted in Fig.6.5(d). The primitive double diffraction vectors, $g_{\lambda\mu}$, are $\frac{1}{3}\frac{\bar{1}}{3}\frac{\bar{1}}{3}\lambda$ and 110_{λ}, and reflections, e.g. $\frac{1}{3}\frac{\bar{1}}{3}\frac{\bar{1}}{3}\lambda$, $\frac{2}{3}\frac{\bar{2}}{3}\frac{\bar{2}}{3}\lambda$ and 110_{λ}, were observed. As described before, the expected grain boundary reflections are based on the centred cell with primitive reciprocal indices $\frac{1}{3}\frac{\bar{1}}{3}\frac{\bar{1}}{3}\lambda$ and 110_{λ}. Thus, the centre reflections have the form $\frac{4}{6}\frac{2}{6}\frac{\bar{1}}{6}\lambda$, and reflections of this type can be seen in Fig.5.14(d). The crystal, double diffraction and anticipated interfacial reflections are indicated schematically in Fig.6.5(a), (b) and (c), respectively. We note that although a subset of the double diffraction and grain boundary reflections

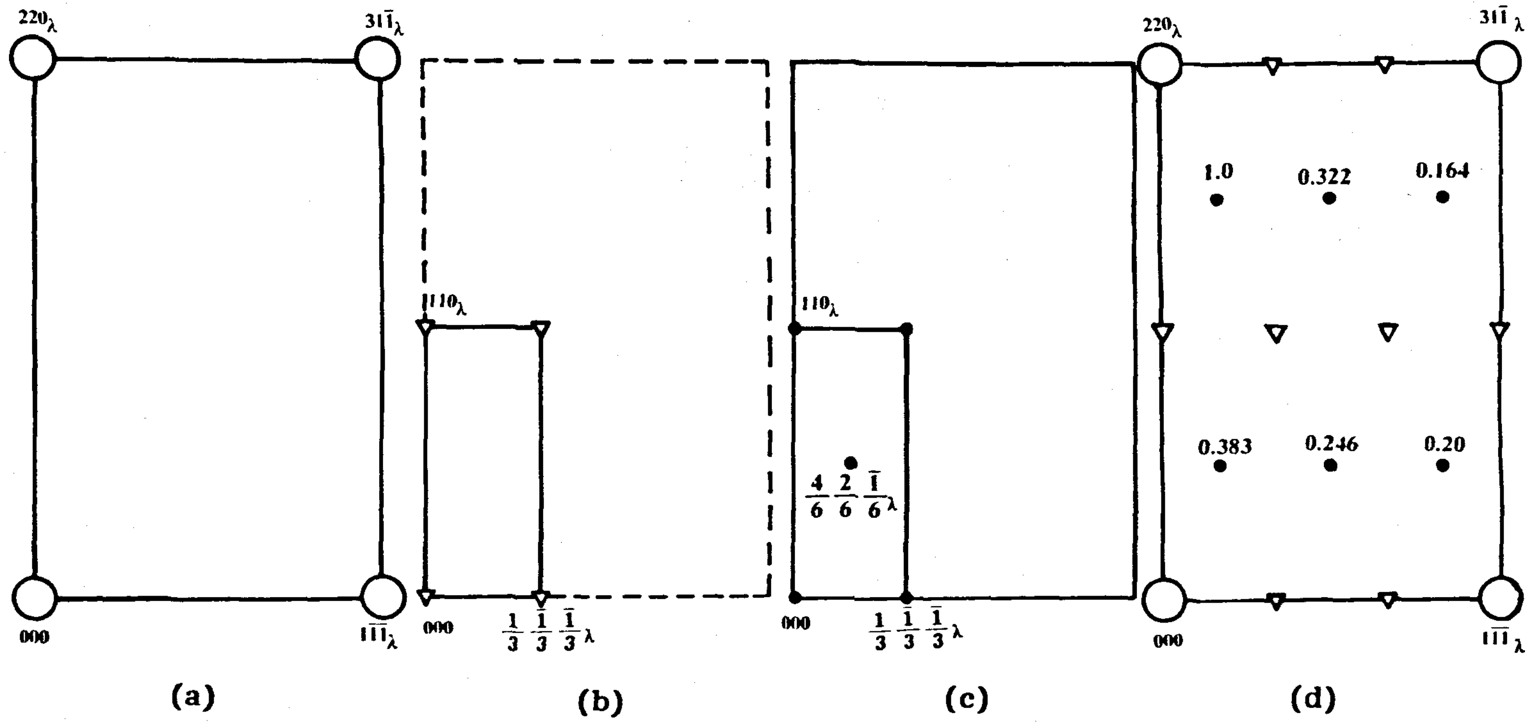

Fig. 6.5. A schematic illustration of (a) crystal reflections, (b) double diffraction reflections (c) grain boundary reflections and (d) calculated intensities of some grain boundary reflections for a $\Sigma = 3(\bar{1}1\bar{2})_\lambda$ "plan-view" specimen.

are coincident, the reflections corresponding to the grain boundary centring positions cannot arise due to double diffraction. In addition, scattering effects due to specimen thicknesses which are not equivalent to integral numbers of unit cells *(Cherns 1974)*, would also not lead to beams coincident with the centring grain boundary boundary reflections. Hence, for purposes of comparison between experimental observations and the model structure, it is advisable to concentrate our attention on the centring reflections.

In order to compare the observed intensities of the grain boundary reflections (Fig.5.14(d)) with the calculated ones, a structure factor calculation programme has been invoked. The calculations have been carried out for both the unrelaxed (Fig.2.6(a)) and the relaxed (2x2) Ge bicrystal (Fig.6.4) making use of the structure factor equation (Eq.(3.2)). For the relaxed bicrystal the atomic coordinates were obtained from *Sutton (1987)* and are tabulated in Table 6.1. The intensity of a reflection can be calculated using Eq.(3.3). In the case of the unrelaxed bicrystal, this equation leads to the result that the crystal reflections have strong intensities while all the anticipated grain boundary reflections have zero calculated intensities. On the other hand, in the case of the relaxed bicrystal the calculated intensities of the grain boundary reflections have intensities greatly less than those of crystal reflections, but are greater than zero. The calculated intensity of centring grain boundary reflections, relative to that of the strongest grain boundary reflection, $\frac{10}{6}\frac{8}{6}\frac{\bar{1}}{6}\lambda$, are written above each corresponding reflection in Fig.6.5(d). We have confined our attention to the intensities of only the centring reflections since no contribution to these can arise by double diffraction. Comparison between the cal-

Table 6.1. Coordinates for Bourret's (112) c(2X2) grain boundary, computed for Si by tight binding. The coordinates are given as x,y,z for each of the 8 atoms in the layer unit cell. x is parallel to [$1\bar{1}\bar{1}$], y is parallel to [$1\bar{1}2$] (the grain boundary normal), and z is parallel to the tilt axis [110]. Unit of length is the lattice parameter.

```
-1.732068598403, -3.062065246827, -0.3535589417173
-0.4330355164686, -3.061898632577, -0.3535260208838
1.1796445525096E-5, -3.06246429425, -0.3535586617023
1.299025657971, -3.061430872554, -0.3535375050751
-1.732099929733, -3.062170428015, 0.3535518587461
-0.432995624316, -3.061709875575, 0.3535790199655
6.422246378262E-5, -3.062288532092, 0.3535379294487
1.298999395254, -3.061631558703, 0.3536028447568
-1.010350243023, -2.857665588731, -0.7071142858703
-0.5773554637866, -2.85756736189, -0.7070024299263
0.7217640183136, -2.857393857383, -0.707179744627
1.154719518898, -2.857177758717, -0.7071652682046
-1.010390986101, -2.85766207622, -3.4822325514379E-5
-0.5774002402793, -2.857573028211, -6.0196862453951E-5
0.7217842954818, -2.857423289173, 3.2546419539134E-5
1.154749101089, -2.857213030619, 1.2634474240667E-4
-1.154634960214, -2.653315385626, -0.3535321776614
0.1444250337564, -2.654495876781, -0.3535797199716
0.5774059479523, -2.653406602182, -0.3535657507305
1.876394212298, -2.653997652178, -0.3535088080639
-1.154729567216, -2.653604409454, 0.3535552211736
0.1444478519932, -2.654233300504, 0.3534863785487
0.5775020779076, -2.653068137309, 0.3535256043181
1.876346929699, -2.654187089211, 0.3535630602877
-1.732108496842, -2.450348022852, -0.7071432737582
-0.4330884975671, -2.449219095405, -0.7069869561608
3.4241827902306E-5, -2.450698574454, -0.7070360559353
1.298939496638, -2.448767087617, -0.707313315997
-1.732064758431, -2.450277898805, 1.0530091705532E-4
-0.4331087790879, -2.449225749893, -1.9679210722437E-4
-1.9554292247813E-5, -2.450683794891, -1.6619558133574E-4
1.298935037275, -2.448770135486, 1.3083449989895E-4
-1.010304013654, -2.244889930526, -0.3535058680136
-0.5773754784178, -2.244224744966, -0.3536038674838
0.7217624167378, -2.244866469947, -0.3536306225849
1.154559912438, -2.244694929387, -0.3535811689789
-1.010328658175, -2.245156498536, 0.35358688904
-0.5774850960909, -2.245161169787, 0.3535249698425
0.7218783444684, -2.244338094199, 0.353478226018
1.154734296796, -2.243665371221, 0.3535003639141
-1.154493302275, -2.040652226895, -0.7072221428193
0.1444973694576, -2.043038733094, -0.7069800011165
0.5776372902314, -2.040223497842, -0.7070436183387
1.876485049516, -2.042788991065, -0.7071866682271
-1.154484740703, -2.040569010844, 2.009573975924E-4
0.1444356861392, -2.042978893076, -2.8918840140803E-4
0.5775816870434, -2.040241790698, -3.4541042671428E-4
1.876544140728, -2.042632765563, 2.5373530027546E-4
-1.73232831241, -1.840009556587, -0.3534693155653
-0.4332623901936, -1.835188145137, -0.3537326204758
-3.8957321538682E-5, -1.839287714183, -0.353698731474
1.298693437838, -1.836313078983, -0.3536288749714
-1.732030696824, -1.838891158554, 0.3536464900291
-0.4332910882362, -1.836841360114, 0.3534891933396
-2.5414919475948E-4, -1.840540830864, 0.3534561918013
1.29883008106, -1.83467356048, 0.3533665535143
-1.010157915767, -1.631715582751, -0.7073925706851
-0.5774056593551, -1.630684735036, -0.7082358694241
0.7219391355602, -1.631212163354, -0.7069487614033
1.15470942607, -1.630228079166, -0.7062373698093
-1.010101579521, -1.631673424302, 4.2227028003857E-4
-0.5773259534041, -1.630760240858, 8.7173742852488E-4
0.7218760114519, -1.631187186462, -5.7778530394137E-4
1.154598433949, -1.630168322609, -1.1384759926608E-3
-1.154813609139, -1.428327527864, -0.3534782815843
0.1445685239091, -1.43254697645, -0.3538157793645
0.5779667301781, -1.425758778423, -0.3537849563627
1.876517218534, -1.433961264357, -0.3534968004179
-1.154019901521, -1.426258186979, 0.3536049217742
0.1444635724778, -1.434326633963, 0.3533573680136
0.5772187310546, -1.427890332657, 0.3533413312674
1.876638352669, -1.432250131485, 0.353647273925
-1.731846117684, -1.230996225362, -0.7061609072174
-0.4334766363351, -1.221249898947, -0.7093618881615
2.4851143114138E-4, -1.231453543964, -0.7082635886732
1.298570524831, -1.220749101999, -0.7051407920507
-1.731788138815, -1.231024567728, -7.9717021698275E-4
-0.4333791913116, -1.221308134301, 1.6119861677285E-3
2.690540187827E-4, -1.231401266978, 6.3676980997505E-4
1.298616955348, -1.220764422102, -1.9590439579944E-3
-1.010290192093, -1.01909597735, -0.3532650272376
-0.5791005147856, -1.021341519111, -0.3538288325508
0.7220651775855, -1.014586187748, -0.3536320986004
```

```
1.15362019805, -1.007620453702, -0.3534834552418
-1.009797377014, -1.015279372804, 0.3536126985864
-0.5782720140821, -1.008150000756, 0.3532488007388
0.7216731942066, -1.018535913306, 0.3534025013531
1.15290899936, -1.020926016617, 0.3534885310285
-1.151270562688, -0.8110017187723, -0.7058780585828
0.1452047383663, -0.8274335848191, -0.7083712040041
0.5808294706084, -0.8101747278191, -0.7081351978858
1.877131339533, -0.8270974315119, -0.705910285827
-1.151191770029, -0.8106548556158, -9.8699360120199E-4
0.1450825548441, -0.827283477285, 6.0288405188151E-4
0.5806416481008, -0.8102332712521, 1.0382799747575E-3
1.877208229963, -0.8270668668316, -6.1462648993451E-4
-1.738383741159, -0.6280694124661, -0.3531380814577
-0.4360022133145, -0.6156700838442, -0.3539462462353
-2.4834119914885E-3, -0.6349527376906, -0.3539906903098
1.297949980169, -0.5907358040843, -0.3534611596428
-1.734610877331, -0.6346733001119, 0.35384568531
-0.4339618045505, -0.5912351412654, 0.3532024474681
-6.2627010127512E-3, -0.6283700182545, 0.3531245607909
1.295941255073, -0.6153269807298, 0.3535179775208
-1.003607688147, -0.3960514471158, -0.7031662178274
-0.5693895641714, -0.3854857634277, -0.6956098220251
0.7283897487938, -0.3951142550004, -0.7112863097281
1.162576498967, -0.3850569626597, -0.7190675364778
-1.003439966765, -0.3956919031312, -3.9290255536795E-3
-0.5692898040129, -0.3854374189007, -1.220991584535E-2
0.7282388176384, -0.3951357235569, 3.807290165401E-3
1.162550855133, -0.3849331413142, 1.1911864964514E-2
-1.17110839678, -0.2038083901953, -0.3536010889282
0.1583555292723, -0.245112284515, -0.3541034345141
0.5802828631099, -0.2071882638049, -0.3538614750171
1.86220011536, -0.2315962478202, -0.3531604171098
-1.151541737998, -0.2078174391034, 0.3536909778649
0.1298619513058, -0.2315824117687, 0.3531575349751
0.5605757402245, -0.2032151856638, 0.3533603094095
1.890418423373, -0.2450043773397, 0.354115376964
-1.709748561456, -2.5163912568972E-2, -0.7202145104629
-0.3977540577202, 1.4119763297628E-2, -0.5817048093386
2.2319216457656E-2, -2.5419576681585E-2, -0.6917569171643
1.334322818707, 1.4475303770821E-2, -0.8127927803819
-1.709466830065, -2.5622948290405E-2, 1.4203554406667E-2
-0.3977013678989, 1.4175344925681E-2, -0.1263666011505
2.2342190494302E-2, -2.5508320232008E-2, -1.4404782011737E-2
1.334484569821, 1.4404212975512E-2, 0.126132796591
-1.188762766535, 0.2275831526228, -0.3534810847916
0.310007197767, 0.2987761423886, -0.7026818778054
0.5630724724171, 0.2267330272001, -0.3538932469771
2.042490943572, 0.2985936719351, -0.7115683717363
-1.16864874749, 0.2262080718476, 0.353755599604
0.3099976766296, 0.2987332076392, -5.2691316904646E-3
0.5424205606922, 0.2283170950032, 0.3532196300658
2.042650662649, 0.2982450380763, 4.9448576096777E-3
-0.8417963996013, 0.4759123125281, -0.3539019449609
-0.5773175491638, 0.4042312798266, -0.688209087305
0.9248365442291, 0.4708860326181, -0.3533333850031
1.15438830763, 0.4047277638902, -0.72621046825
-0.8070413676749, 0.4706240321021, 0.353388628966
-0.5773189935338, 0.4043559321739, -1.9416352907637E-2
0.8893939599136, 0.4763824387064, 0.3517790171942
1.154409176351, 0.4045055618258, 1.9688024061302E-2
-1.584932798309, 0.6932570771744, -0.718026979452
-0.2772475445088, 0.7083235508783, -0.5814013526044
0.1470480350088, 0.6933708228981, -0.6954598599358
1.455006415549, 0.7083461747042, -0.8129356566633
-1.584383313615, 0.6930003881762, 1.2075815756488E-2
-0.2772291127477, 0.7082697310803, -0.1263030879122
0.1469403410117, 0.6933243142642, -1.1867296484002E-2
1.455181960187, 0.7081950578113, 0.126251507117
-1.001568798195, 0.8855614547475, -0.3539428201661
0.3179737694561, 0.8931144401415, -0.3535733478499
0.7548504513445, 0.8857776937412, -0.3533645084264
2.018906204489, 0.8904606145973, -0.3530811684118
-0.9770829548539, 0.8855951336342, 0.353571724258
0.2862926032679, 0.8904938568921, 0.353500210015
0.7298734819016, 0.8857423439856, 0.353698641841
2.050163061511, 0.8928100567838, 0.3540909168815
-0.8501515948149, 1.09548415737, -0.7037413743552
-0.418416783753, 1.100663794596, -0.6947377007912
0.8816889452733, 1.095404146176, -0.7106451854138
1.313509311119, 1.100506348645, -0.7194855856637
-0.8502180139742, 1.095292464573, -3.7177677766446E-3
-0.4185005675714, 1.100534042747, -1.2726365050354E-2
```

```
0.8818250251124, 1.095411436254, 3.8419985006052E-3
1.313740116086, 1.100481712645, 1.2919221691266E-2
-1.573788514882, 1.301382774173, -0.3530821627651
-0.2745881953441, 1.318551153039, -0.3536690026639
0.1629068466664, 1.303457837361, 0.353501813636
1.459177738783, 1.28998960842, -0.3531262670804
-1.569051870692, 1.303211715223, 0.3531907451928
-0.2730281548821, 1.290285411641, 0.3531338810022
0.1579813472077, 1.301463696484, 0.3515096158875
1.4575259633, 1.118525977704, 0.3538581414471
-0.9952723206615, 1.504402469713, -0.7065885185885
0.304058133166, 1.506348571922, -0.7071550219151
0.736637587189, 1.504406542051, -0.7075501849687
2.036245596217, 1.506352877646, -0.706814209473
-0.9952467851871, 1.504356927153, -4.398698031111E-4
0.304164107118, 1.506519411685, 1.301371102846E-4
0.7367288158617, 1.504391818942, 6.989297087971E-4
2.036281041399, 1.506354217615, 3.6081854964504E-4
-0.851292863505, 1.711006321552, -0.3515651721714
-0.4184283674739, 1.719681906991, -0.3515551578425
0.8812593984534, 1.707792005981, -0.351198002229
1.314486159688, 1.703884020808, -0.3531794690117
-0.85076280832, 1.708046654509, 0.3515613926026
-0.4176323130888, 1.704196456601, 0.3515592115434
0.8806720224511, 1.71119923119, 0.3536819529691
1.313658574958, 1.719630901787, 0.3517411869451
-1.572532491152, 1.914817780737, -0.7063697118488
-0.2736977774876, 1.915928411056, -0.7093676111336
0.1595006615526, 1.914814556719, -0.7076809119851
1.458330569164, 1.9158116612, -0.7066160472809
-1.572491148128, 1.914819796547, -1.2212145244817E-4
-0.2737321332099, 1.915896101476, 2.3206713908362E-3
0.159489709124, 1.914977772507, 7.2810182673808E-4
1.458197845718, 1.915729957975, -2.14779287961E-3
-0.9957488846015, 2.118973491171, -0.3533876382263
0.3018150099695, 2.118294169496, -0.3534895292023
0.7371531056486, 2.117292121971, -0.3534527895761
2.035827241581, 2.119491200644, -0.3533814748144
-0.9948646302668, 2.117540801064, 0.3515769389908
0.3036731150614, 2.119744318219, 0.3536709026138
0.7363015181963, 2.119041566119, 0.3536401952997
2.035924580646, 2.118381259411, 0.3537158110991
-0.8510416529058, 2.322680371589, -0.70728445044
-0.4180151510176, 2.321776941519, -0.7081899749985
0.8809528173753, 2.322621219502, -0.7066795128502
1.313997544154, 2.323622762613, -0.7057472261631
-0.8510446449996, 2.322791757782, 3.4191100860201E-4
-0.4180159881652, 2.32174504225, 1.2808552367719E-3
0.8809871955242, 2.322590061726, -2.3007936165222E-4
1.314042321227, 2.321557195921, -1.0741529670458E-3
-1.572634246138, 2.527574702542, -0.3534285187006
-0.2735848230912, 2.526770590019, -0.3534361531086
0.1595378385708, 2.526725021655, -0.3534606821559
1.458471567966, 2.528498519014, -0.3534111550261
-1.572477951228, 2.526730188247, 0.3536987841112
-0.2737247841128, 2.528702904618, 0.3536457559988
0.1592671349117, 2.52787577139, 0.3536581610169
1.458488922912, 2.526559230615, 0.3536858585798
-0.9953727218884, 2.731284870731, -0.7070726067388
0.3017124579086, 2.731621436362, -0.7068026133043
0.7367185243616, 2.731043777152, -0.7067620597511
2.015775024664, 2.731384896106, -0.7070866793421
-0.9953020121414, 2.731185633014, 2.5906231999787E-4
0.3017444220379, 2.731413365731, -1.0826684211131E-4
0.7367606068363, 2.731005845204, -1.5686183150499E-4
2.035829891186, 2.731276897907, 2.4311307541986E-4
-0.8509411597745, 2.935261815844, -0.3531838403552
0.4179207390186, 2.935309767722, -0.3531727616766
0.8810090152577, 2.935627919942, -0.3531513741855
1.314061975453, 2.936291114014, -0.3534456591351
-0.8510908030868, 2.935681925597, 0.3536856884547
-0.4181111258881, 2.936454728891, 0.3536163366949
0.8811040738894, 2.934850881843, 0.3536449401986
1.314162014987, 2.935097923201, 0.3536624105223
-1.572662258415, 3.139630851648, -0.7070520535685
-0.2736419080691, 3.139903631058, -0.7068489832501
0.1593946218748, 3.1396793243, -0.7068973431633
1.458419865218, 3.13981858472, -0.7071672882764
-1.572649082153, 3.139546026368, 2.4581830868677E-4
-0.273637445532, 3.139920128586, -1.1861867420095E-4
0.1594051273363, 3.139718510599, -6.3076229496641E-5
1.458411019002, 3.139786276108, 2.8801615998754E-4
```

culated and observed intensities indicates good agreement as summarised below:

(1) the reflection $\frac{10}{6}\frac{8}{6}\frac{\bar{1}}{6}\lambda$ has the highest, intensity, and that of $\frac{4}{6}\frac{2}{6}\frac{\bar{1}}{6}\lambda$ has the second highest,
(2) the reflection $\frac{14}{6}\frac{4}{6}\frac{\bar{5}}{6}\lambda$ has the lowest intensity and that of the $\frac{8}{6}\frac{\bar{2}}{6}\frac{\bar{5}}{6}\lambda$ has the second lowest intensity.

A comprehensive analysis of the SAD patterns, Fig.5.10(c), 5.15(d) and 5.14(d), has revealed that grain boundary reflections were clearly observed in the SAD pattern taken from "plan-view" bicrystal specimen but not observed in those taken from the "edge-on" ones. The possible reason behind this is that the intensity of grain boundary reflections in the "plan-view" case is considerably greater than that in the "edge-on" ones, so that one cannot detect these in the latter. To be more specific, the illuminated areas in both cases above are proportional to the size of the selected area aperture. In the "plan-view" case the amplitude of a grain boundary reflection, hkl, is proportional to the structure factor, F_{hkl}, times the number of interfacial 'unit cells' (i.e. the centred (2x2) cells), N_{pv}, present in the illuminated area, and hence the intensity, I_{pv}, is proportional to N^2_{pv}. On the other hand, in the case of "edge-on" bicrystal specimen the intensity of a grain boundary reflection from the same set of planes hkl, I_{eo}, is proportional to N^2_{eo}, where N_{eo} is the number of 'unit cells' in the illuminated area. Since the illuminated areas in both cases are the same, it follows from the geometry of the situation that, N_{pv} is much greater than N_{eo}. Consequently, I_{pv} is also relatively much greater than I_{eo}. For example, in the case of SAD patterns in Fig.5.10(c) and Fig.5.14(d), the size of the SAD aperture was 30μm in diameter, and, therefore, the number of unit cells N_{eo} and N_{pv} in this illuminated area can be estimated as follows. In the "edge-on" case, the area of boundary examined is approximately $30\mathrm{x}t\mu m^2$, where t is the specimen thickness which was of the order $0.1\mu m$. Therefore, since the area of an interfacial 2x2 unit cell is $(\sqrt{2}\mathrm{x}2\sqrt{3})a^2 = 4.9a^2\mu m^2$, $N_{eo} \approx 1912888.9$. In the "plane-view" case, the area illuminated is equal to 30&S2$\pi\mu m^2$, which means that $N_{pv} = 1.8\mathrm{x}10^9$. Hence, the ratio of intensities for the same reflection observed in the "plane-view" and "edge-on" cases is

$$I_{pv} : I_{eo} = N^2_{pv} : N^2_{eo} = 888264.39 : 1$$

i.e. the intensity of the grain boundary reflection in the "plane-view" case is much greater than in the "edge-on" case, and hence these reflections are more likely to be observed in the former case.

6.6.2. CBED PATTERNS.

The $[110]_\lambda$ surface normal "edge-on" bicrystal and dichromatic complex would exhibit the following expected point symmetry

$$G(b) = m'2'm = \{1, m(110)_\lambda, m'(\bar{1}1\bar{2})_\lambda, 2'[1\bar{1}\bar{1}]_\lambda\}, \text{ and}$$

$$G(c) = mm'm'$$

$$= \{1, m(110), 2[110], \bar{1}, m'(\bar{1}1\bar{2}), m'(1\bar{1}\bar{1}), 2'[\bar{1}1\bar{2}], 2'[1\bar{1}\bar{1}]\}$$

The observed CBED pattern, Fig.5.10(f) which was taken from an area containing the grain boundary, exhibits the following elements of symmetry (BF and whole pattern):

(1) an anti-mirror, $m'(1\bar{1}\bar{1})_\lambda$,

(2) an anti-mirror, $m'(\bar{1}1\bar{2})_\lambda$and

(3) a diad, $2[110]_\lambda$.

The observed symmetry is

$$2m'm' = \{1, 2[110]_\lambda, m'(1\bar{1}\bar{1})_\lambda, m'(\bar{1}1\bar{2})_\lambda\}$$

This is consistent with the residue of the complex point symmetry, assuming the mirror $m(110)_\lambda$ has been broken due to specimen preparation.

Similarly, the $[\,1\bar{1}\bar{1}\,]_\lambda$ surface normal "edge-on" bicrystal and dichromatic complex would exhibit the following point symmetry:

$$G(b) = \bar{6}'2'm = \{1, 3^+, 3^-, m(110), m(101), m(01\bar{1}), m'(\bar{1}1\bar{2}), \bar{6}^{+\prime}, \bar{6}^{-\prime}, 2'[211], 2'[\,1\bar{1}\bar{1}\,], 2'[\,12\bar{1}\,]\}, \text{ and}$$

$G(c) = 6'/mm'm'$ (see Tables 2.4(a) and 2.5(a) for the 24 symmetry and anti-symmetry elements of this point group)

The observed CBED pattern, Fig.5.15(c) which was taken from an area containing the grain boundary, exhibits the following elements of symmetry (BF and whole pattern):

(1) triad along $[\,1\bar{1}\bar{1}\,]_\lambda$ direction, 3^+, 3^-,
(2) $m(110)_\lambda$,
(3) $m(101)_\lambda$ and
(4) $m(0\bar{1}1)_\lambda$

Thus, the observed point symmetry is

$$3m = \{1, 3^+, 3^-, m(110), m(101), m(01\bar{1})\}.$$

This is consistent with the residue of the complex point symmetry, assuming that the anti-mirror $m'(1\bar{1}\bar{1})_\lambda$ has been broken by specimen preparation.

Finally, the point symmetry exhibited by $[\bar{1}1\bar{2}]_\lambda$ surface normal "plan-view" bicrystal and dichromatic complex are

$$G(b) = m2'm' = \{1, m(110), 2'[1\bar{1}\bar{1}], m'(\bar{1}1\bar{2})\},$$

and

$$G(c) = mm'm'$$
$$= \{1, m(110), 2[110], \bar{1}, m'(\bar{1}1\bar{2}), m'(1\bar{1}\bar{1}), 2'[\bar{1}1\bar{2}], 2'[1\bar{1}\bar{1}]\},$$

respectively.

The CBED patterns in Fig.5.14(e), have been taken from a $\Sigma = 3(\bar{1}1\bar{2})_\lambda$ "plan-view" specimen where the electron beam was parallel to the specimen surface normal $[\bar{1}1\bar{2}]_\lambda$. The observed element of symmetry (BF and whole pattern) exhibited by this pattern is:

(1) a mirror $m(110)_\lambda$,

hence, the observed point symmetry is $m = \{1, m(110)_\lambda\}$, which is equivalent to the residue of the bicrystal point symmetry, assuming that the anti-symmetry elements $m'(\bar{1}1\bar{2})_\lambda$ and $2'[\bar{1}1\bar{2}]$ are broken either due to specimen preparation (section 6.3), or due to a relative displacement parallel to $[1\bar{1}\bar{1}]$.

6.6.3. SUMMARY OF OBSERVATIONS.

In summary the evidence collected in the present work using the SAD technique is consistent with other recent works, and supports the c(2x2) model of the $\Sigma=3(\bar{1}1\bar{2})_\lambda$ grain boundary studied by *Paxton (1987)*. In particular our observations imply the presence of an interfacial displacement field, and that the boundary is reconstructed such that the interfacial periodicity is doubled. Good agreement has been found between the relative values of observed and calculated intensities.

Regarding the symmetry of the interfacial structure as studied using CBED, we conclude that the present observations are also consistent with the model, Fig.6.4, which exhibits the symmetry c1m1. However, it must be remembered that the result from the "edge-on" specimens, i.e. showing the residue of the complex symmetry, does not provide information about the interfacial structure. On the other hand, the bicrystal spacegroup was determined from a "plan-view" specimen and the symmetry observed is consistent with that of the proposed model, i.e. c1m1.

6.6.4. OBSERVATION OF DISSOCIATION IN $\Sigma=3(\bar{1}1\bar{2})_\lambda$ "EDGE-ON" SPECIMEN.

The $\Sigma=3(\bar{1}1\bar{2})_\lambda$ interface appears to be unstable with respect to dissociation (Fig.5.12(a)). The solution of the SAD pattern (Fig.5.12(b), which is taken from the dissociated boundary shows that the $\Sigma=3(\bar{1}1\bar{2})_\lambda$ interface has dissociated, as depicted schematically in Fig.6.6, according to the following reaction:

$$\Sigma=3(\bar{1}1\bar{2})_\lambda \rightarrow \Sigma=3(1\bar{1}1)_\lambda + \Sigma=3(\bar{1}12)_\lambda + \Sigma=9(\bar{2}\bar{1}2)_\mu + \Sigma=9(1\bar{4}\bar{1})_\mu$$

We note that all the interfaces following dissociation are symmetric; the $\Sigma=9(\bar{2}\bar{1}2)_\mu$ interface has been studied in some detail both experimentally *(see for example Papon et al.1982)* and theoretically *(Krivanek et al.1977)*, and is thought to have low energy. On the other hand, the $\Sigma=9(1\bar{4}\bar{1})_\mu$ interface, indicated by the dotted line in Fig.6.6, has not been observed frequently.

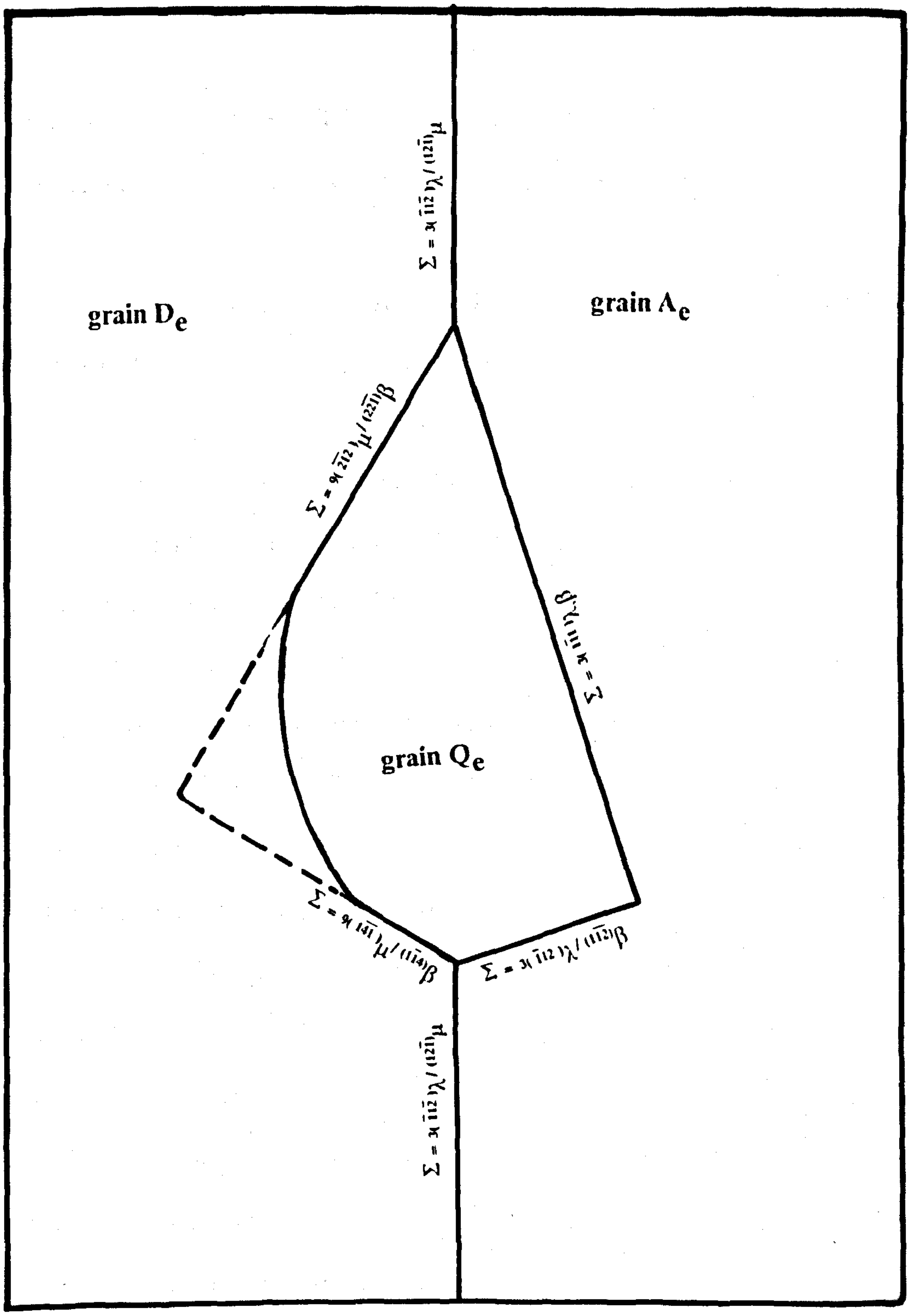

Fig. 6.6. A schematic of the dissociated $\Sigma = 3(\bar{1}1\bar{2})_\lambda$ boundary in Fig.5.12(a).

6.7. PREVIOUS EXPERIMENTAL OBSERVATIONS AND THEORETICAL MODELS OF $\Sigma=27(5\bar{5}\bar{2})_\lambda$ BOUNDARY.

A small number of experimental and theoretical works concerned with the structure of the $\Sigma=27(5\bar{5}\bar{2})_\lambda$ interface in silicon and germanium have been published. Selected area electron diffraction and high resolution electron microscopy techniques have been used in the experimental investigations. The electron diffraction investigations of *(Bourret et al. 1985b)* for the interface in germanium showed SAD patterns containing a large number of diffraction spots of low intensity. High resolution electron microscopy images for interfaces in polycrystalline silicon, *(Cunningham et al. (1982) and Vaudin et al. (1983))* and in a germanium bicrystal *(Bourret et al. 1985b),* looking down $[110]_\lambda$ show a periodicity of a magnitude 2.83nm along $[\bar{1}1\bar{5}]_\lambda$, i.e. the same as that of the unrelaxed bicrystal in Fig.2.6(c). This interface was also observed, using HREM and TEM techniques, to be facetted and dissociated. *Bourret et al. (1985a) and Vaudin et al. (1983)* observed successive facets along {110} and {111} planes with a width successively close to 3a and <211>a, where a is the lattice parameter. For this particular misorientation a {110} facet in one crystal faces a {111} facet in the other, and these are arranged alternatively along the boundary. The interface was also observed *(Cunningham et al. 1982)* to be dissociated into $\Sigma=3\{111\}/\{111\}$, $\Sigma=3\{115\}/\{111\}$ and $\Sigma=9\{122\}/\{122\}$ interfaces in <110> surface normal polycrystalline silicon specimens. Also, *Garg et al. (1988)* observed the dissociation in polycrystalline silicon, using optical and TEM microscopy techniques, into $\Sigma=3\{115\}/\{111\}$ and $\Sigma=9\{122\}/\{122\}$ boundaries.

Two atomic models for the structure of $\Sigma=27(\ 5\bar{5}\bar{2}\ )_\lambda$ interface, proposed by *Vaudin et al. (1983)*, are shown in Fig.6.7(a) and (b). The first consists of ABAC structural unit combinations and the second consists of AAD combinations as illustrated in the figures. The dotted lines in Fig.6.7(a) indicate {111} facets in one crystal and { $11\bar{1}$ } in the other. Good agreement exists between the HREM image for the facetted $\Sigma=27(\ 5\bar{5}\bar{2}\ )_\lambda$ boundary and the model shown in Fig.6.7(a), suggesting that the model gives a nearly correct representation of the HREM image. As far as we are aware, the energy of this interface has not been investigated by computer simulation.

6.7.1. DISSOCIATION OF THE $\Sigma=27(\ 5\bar{5}\bar{2}\ )_\lambda$ BOUNDARY.

In the cases of the boundaries considered previously, the discussion of dissociation was considered after that of SAD and CBED investigations, but in the present case dissociation was observed to be such a prominent feature that it is discussed first.

At low magnification, $M \leq 10x$ Fig.5.1(a) and (b), the grain boundary area between grain pairs B_c-C_c and B_e-C_e, apparently, consisted of a smooth interface. At high magnification, M=60,000x Fig.5.16, the major observed portion of the grain boundary showed a rather complicated appearance as is illustrated schematically in Fig.5.24. In some other areas, quite large grains were observed to be enclosed between the grain pair B_c-C_c, for example grain E_c which is confined by the triangular border "hlk" and the grain F_c which has a very complicated irregular shape. The CBED patterns taken from the microscopic grains E_c and F_c, Fig.5.19 and 5.20, showed them to have the direction

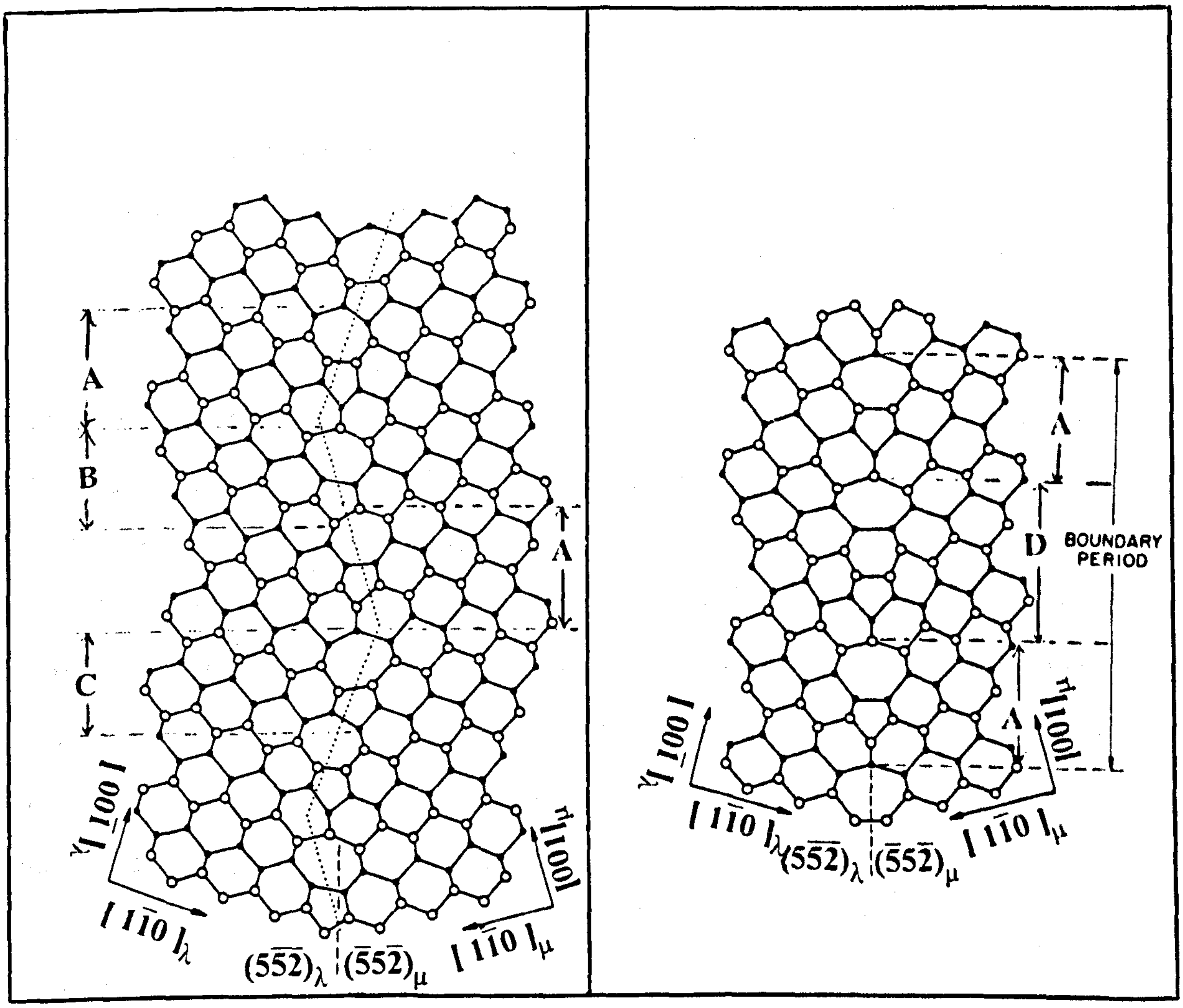

(a) (b)

Fig. 6.7. Proposed structures for $\Sigma = 27(5\bar{5}\bar{2})_\lambda$ boundary

(a) ABAC structure (the dotted lines indicates $(111)_\lambda$ and $(11\bar{1})_\lambda$ facets, and

(b) AAD structure (reproduced from Vaudin et al. 1983).

$[110]_\lambda$ parallel to the electron beam in common with the grains B_c and C_c. The pairs of grains B_c-E_c and C_c-E_c were found to be rotated about this direction by 71.0° ± 0.5°. Hence, the $\Sigma=27(\ 5\bar{5}\bar{2}\ )_\lambda$ interface at point "h" dissociated into a configuration of $\Sigma = 3(\ \bar{1}11\ )_\lambda$ and $\Sigma = 9(\ \bar{2}21\ )_\lambda$ symmetric tilt boundaries.

6.7.2. SAD PATTERNS FROM ″EDGE-ON″ AND ″PLAN-VIEW″ SPECIMENS.

In the case of $\Sigma = 27(\ 5\bar{5}\bar{2}\ )_\lambda$ "edge-on" bicrystal specimen, the $[110]_\lambda$ SAD pattern taken from the grain boundary region is shown in Fig.5.17. The area investigated was chosen carefully so as not to include regions where the interface had dissociated. However, the boundary was rarely found to be strictly planar, and hence was probably facetted on a microscopic scale. Crystal reflections $\bar{1}1\bar{5}_\lambda$ and $1\bar{1}\bar{5}_\mu$ are *coincident* in the zero layer for this 110 section of the reciprocal lattice. Some double diffraction reflections are present in Fig.5.17(c) and this was presumably due to facetting. The anticipated first order grain boundary reflection, g^i, is $\frac{\bar{1}}{27}\frac{1}{27}\frac{\bar{5}}{27}\lambda$. No evidence for this reflection was obtained, and the reason for this, as mentioned before in section 6.6.1 for a similar case, is presumably that the intensity of the grain boundary reflections is too small to be observed.

In the case of the "plan-view" bicrystal specimen, the $[\ 5\bar{5}\bar{2}\ ]_\lambda$ SAD pattern is shown in Fig.5.28. In the zero layer of the $5\bar{5}\bar{2}$ section of the reciprocal lattice all crystal reflections are coincident, for example white crystal reflections 220_λ, $\bar{1}1\bar{5}_\lambda$ and $13\bar{5}_\lambda$ are coincident with the black crystal reflections 220_μ, $1\bar{1}\bar{5}_\mu$ and $31\bar{5}_\mu$, respectively, as depicted in Fig.6.8. Crystal reflections from higher order Laue zones are observed in Fig.5.28, and crystal reflections from the first order Laue zones are also indexed in the figure, e.g. (519_λ, $3\bar{1}9_\lambda$, $1\bar{3}9_\lambda$, $\bar{1}\bar{5}9_\lambda$) and ($\bar{6}\bar{4}4_\mu$, $\bar{4}\bar{2}4_\mu$, $\bar{2}04_\mu$, 024_μ).

Double diffraction reflections, $g_{\lambda\mu}$ can be identified by considering the white and black reciprocal lattices and bearing in mind that these display the same symmetry as the dichromatic pattern, which includes $m(110)_\lambda$, $m'(5\bar{5}\bar{2})_\lambda$ and $m'(\bar{1}1\bar{5})_\lambda$. Thus, for example, the zero layers are coincident, and the $+n^{th}$ white layer is a mirror image of the $-n^{th}$ layer of the black reciprocal lattice. Therefore, reflections such as $g_{\lambda\mu} = \frac{2}{3}\frac{\bar{2}}{3}\frac{5}{3}\,\lambda$ arise by scattering by the planes corresponding to firstly $g_\lambda = 3\bar{1}9$ and subsequently $g_\mu = \frac{\overline{463}}{729}\frac{1929}{729}\frac{6824}{729}$.

The expected grain boundary reflections, g^I, are of the types $\frac{\bar{1}}{27}\frac{1}{27}\frac{\bar{5}}{27}\,\lambda$ and 110_λ. Reflections of the first type are observed in Fig.5.28 as satellites of crystal and double diffraction spots, as indicated in Fig.6.8. We note that grain boundary reflections of this type are to be expected from a facetted interface such as that shown in Fig.6.7(a). However, we note that such reflections could also arise due to the specimen thickness not comprising integral numbers of unit cells, and it was not possible to distinguish between these two possibilities in the present work.

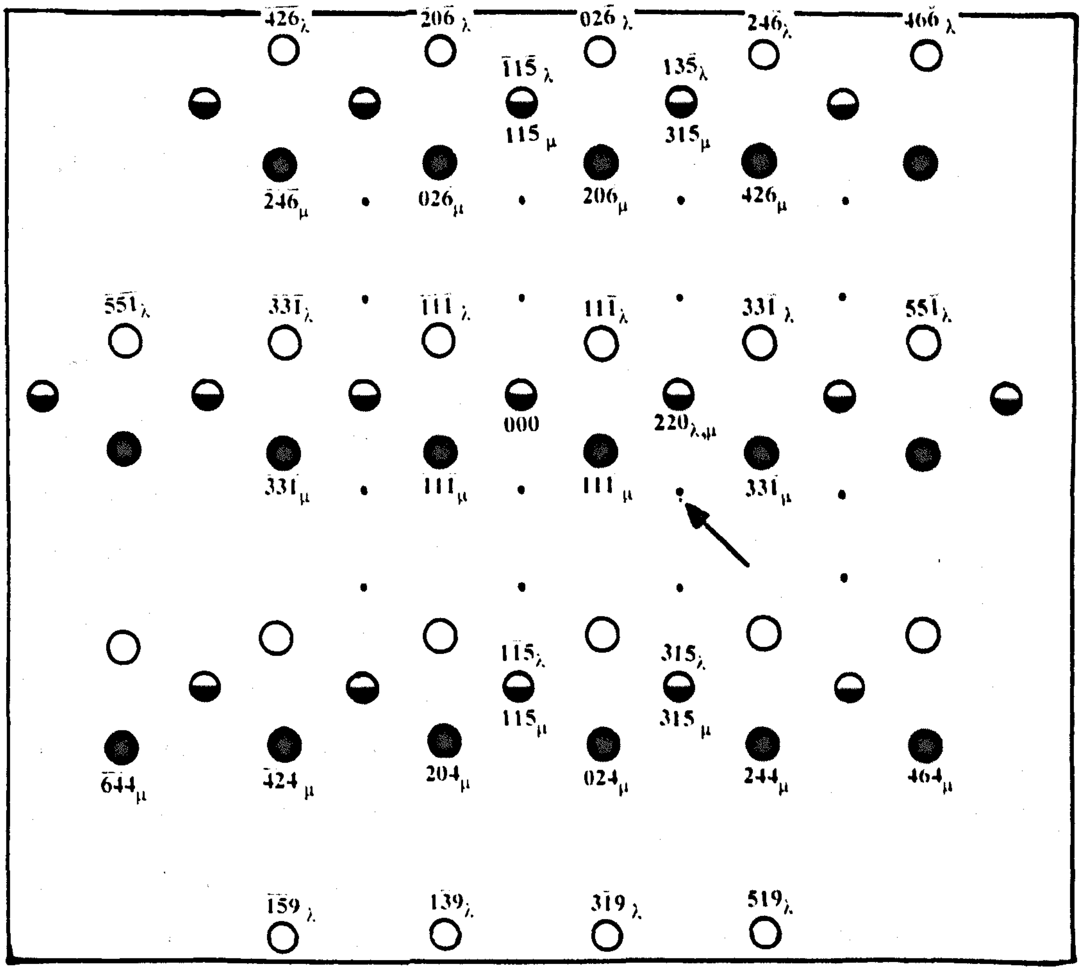

Fig. 6.8. A schematic representation of the SAD pattern in Fig.5.28, one example of a satellite spot associated with the doubly diffracted reflection is indicated by the arrow.

6.7.3. CBED PATTERNS FROM "EDGE-ON" AND "PLAN-VIEW" SPECIMENS.

The point symmetry for $\Sigma = 27(\ 5\bar{5}\bar{2}\ )_\lambda$ bicrystal and dichromatic complex (projected down [110[direction) are

$G(b) = 2'mm' = \{1, m(110)_\lambda, m'(\ 5\bar{5}\bar{2}\ )_\lambda, 2'[\ \bar{1}1\bar{5}\ ]_\lambda\}$, and

$G(c) = m'm'm$

$= \{1, m(110)_\lambda, 2[110], \bar{1}\ , m'(5\bar{5}\bar{2})_\lambda, m'(\bar{1}1\bar{5})_\lambda, 2'[\ \bar{1}1\bar{5}\ ], 2'[\ 5\bar{5}\bar{2}\ ]\}$,

respectively.

The observed symmetry elements of the $[110]_\lambda$ CBED pattern, which was taken from $\Sigma = 27(\ 5\bar{5}\bar{2}\ )_\lambda$ "edge-on" bicrystal specimen from the grain boundary, Fig.5.18(c), are:

(1) an antimirror parallel to the boundary plane, $m'(5\bar{5}\bar{2})_\lambda$,

(2) an antimirror perpendicular to the boundary plane, $m'(\bar{1}1\bar{5})_\lambda$, and

(3) a diad perpendicular to the plane of the pattern, $2[110]_\lambda$.

Thus, the observed symmetry is

$2m'm' = \{1, 2[110]_\lambda, m'(5\bar{5}\bar{2})_\lambda, m'(\bar{1}1\bar{5})_\lambda\}$.

Therefore, the observed symmetry is equivalent to a residue of the dichromatic complex point symmetry, assuming the mirror $m(110)_\lambda$ is broken due to specimen preparation and also due facetting and dissociation of $\Sigma = 27(\ 5\bar{5}\bar{2}\ )_\lambda$ interface in some places.

The point symmetry for $\Sigma = 27(\ 5\bar{5}\bar{2}\ )_\lambda$ bicrystal and dichromatic complex projected down the [$5\bar{5}\bar{2}$ [direction are

$G(b) = m2'm' = \{1, m(110)_\lambda, m'(\ 5\bar{5}\bar{2}\ )_\lambda, 2'[\ \bar{1}1\bar{5}\ ]_\lambda\}$

$G(c) = m'mm'$

$$= \{1, m(110)_\lambda, 2[110], \bar{1}, m'(5\bar{5}\bar{2})_\lambda, m'(\bar{1}1\bar{5})_\lambda, 2'[\bar{1}1\bar{5}], 2'[5\bar{5}\bar{2}]\}.$$

The observed symmetry of the $[5\bar{5}\bar{2}]_\lambda$ CBED pattern, which was taken from $\Sigma = 27(5\bar{5}\bar{2})_\lambda$ "plan-view" bicrystal specimen, Fig.5.29, exhibited only the identity element of symmetry. In the present case we believe that all symmetry in the bicrystal has been suppressed due to the combined effects of specimen preparation, facetting and dissociation of this interfacial structure.

6.7.4. SUMMARY OF OBSERVATIONS.

Our observations of facetting and dissociation of the $\Sigma = 27(5\bar{5}\bar{2})_\lambda$ interface are similar to other recent observations. Such observations indicate that, because facetting and dissociation are prominent features of the interface, this boundary probably has high interfacial energy. The SAD investigations presented here provide evidence that the periodicity of the interface is the same as that of the CSL. The absence of the expected symmetry in the CBED patterns taken from the "plan-view" bicrystal specimens is probably due to a combination of symmetry breaking by specimen preparation, and the instability of this grain boundary with its tendency to dissociate into more stable structures.

CHAPTER SEVEN

CONCLUSIONS AND SUGGESTIONS FOR FURTHER WORK

7.1. CONCLUSIONS REGARDING THEORETICAL CRYSTALLOGRAPHY.

(1) It has been shown that the 31 diffraction groups for single crystals, previously obtained by *Buxton et al. (1974)* using stereographic arguments, can be obtained in a straightforward manner using crystallographic theory. These groups have been derived here by starting with the 31 rosette groups and using the concept of antisymmetry to identify symmetry elements for which the reciprocity theorem must be invoked in CBED.

(2) A group theoretical method for obtaining the BF, projection diffraction and whole pattern symmetries corresponding to a given diffraction group has been presented.

(3) The results outlined above have been extended to obtain all possible diffraction groups for bicrystals. Procedures for determining the admissible diffraction groups for both "plan-view" and "edge-on" specimens have been discussed.

7.2. CONCLUSIONS REGARDING EXPERIMENTAL TECHNIQUES.

(1) "Edge-on" and "plan-view" germanium bicrystal specimens have been prepared successfully for investigations by transmission electron microscopy.

(2) SAD, CBED and LACBED techniques have been used to study bicrystal specimens. The SAD method was found to be particularly useful for studying interfacial reconstruction. Bicrystal symmetry was successfully investigated using CBED on "plan-view" specimens. On the other hand, CBED patterns obtained from "edge-on" specimens could not be interpreted directly in terms of bicrystal symmetry.

7.3. CONCLUSIONS REGARDING SPECIFIC INTERFACIAL STRUCTURES.

(1) $\Sigma = 3(\ 1\bar{1}\bar{1}\ )_{\lambda}$ boundary: the experimental observations are consistent with a bicrystal exhibiting symmetry $p\bar{6}'m2'$. Moreover, no evidence was found for interfacial reconstruction or a significant displacement field. This boundary is stable and showed no tendency to dissociate.

(2) $\Sigma = 3(\ \bar{1}1\bar{2}\ )_{\lambda}$ boundary: the experimental observations are consistent with a bicrystal exhibiting the symmetry c1m1. In particular, clear evidence of a c(2x2) reconstruction was obtained, and the intensities of interfacial reflections were found to be in good agreement with those calculated based on the model structure suggested by *Papon et al. (1985).* It was also observed that this interface is unstable with respect to dissociation into other $\Sigma = 3$ and $\Sigma = 9$ boundaries.

(3) $\Sigma = 27(\,5\overline{5}\overline{2}\,)_\lambda$ boundary: this boundary was observed to be highly unstable, exhibiting extensive dissociation and facetting. Due to this structural complexity, it was not possible to determine the bicrystal spacegroup using CBED. Some evidence was obtained using SAD indicating that the periodicity of the interface is the same as that of the $\Sigma = 27$ CSL.

7.4. SUGGESTIONS FOR FURTHER WORK.

In the course of this work it has become evident that two aspects of the experimental programme would benefit from further attention. These are, firstly, problems associated with the interpretation of CBED patterns from bicrystal specimens, and secondly, quantitative comparison between the calculated and measured intensities of diffracted beams.

Concerning CBED, three topics need to be considered. The first one follows from our observations that antisymmetry operators, such as m', and 2' in the interface of a "plan-view" specimen, were frequently broken, i.e. did not lead the anticipated symmetries being observed in CBED patterns. We have presumed that this has arisen due to surface roughness or the location of the interface not being coincident with the central plane of "plane-view" specimens. It would be valuable to carry out a systematic study by simulating the contrast expected from "plan-view" specimens where the interface location and surface smoothness and orientation were varied. The second topic concerns the symmetry observed in CBED patterns from "edge-on" specimens. As explained in the thesis, it is anticipated that the symmetry observed depends upon the spot size used, so called "complex symmetry" being observed for relatively large spot sizes as in the present work. It would therefore be interesting to investigate pattern symmetry using smaller spot sizes. Finally, as has been suggested by *Schapink et al. (1986)*, it would be valuable to investigate the symmetry of CBED patterns from "edge-on" bicrystal specimens using the double-rocking zone axis pattern (DRZAP) technique, and to vary the spot size in addition as outlined above.

With regard to quantitative measurement of diffracted intensities, it would be particularly valuable to carry out x-ray diffraction studies of "plan-view" bicrystal specimens using a synchrotron source. This would have the advantage of making the comparison between experimental measurements and theoretical calculations based on kinematical theory more justifiable. At the same time, use of a synchrotron source would overcome the experimental difficulties associated with the problem of weak x-ray diffraction by interfaces. This approach is currently being undertaken by *Sass et al. (1988)* in their work on gold bicrystals.

REFERENCES

Anderson, J. C. (1980), Thin Solid Films 37, 127.

Bacmann, J. J., A. M. Papon, M. Petit and G. Silvestre (1985), Phil. Mag., A51, No. 5, pp. 697-713.

Bourret, A., and J. J. Bacmann (1985a), Surface Sci., 162, pp. 495-509.

Bourret, A., and J. J. Bacmann (1985b), Proc. JIMIS-4, Supplement to Jpn. Inst. Metals, p. 125.

Bourret, A., and L. Billard and M. Petit (1985), Inst. Phys. Conf. Ser. No. 76: section 1, pp. 23-28.

Buxton, B.F.; Eades, J.A.; Steeds,J.W.; and Rackham,G.M. (1976), Phil. Trans. R. Soc. Lond., Series A281, 171-194.

Caron, R. P., and F. W. Schapink (1985), Ultramicroscopy, Vol. 17, pp. 383-386.

Carter, C.B.; Cosandey, F.; Hagege, S.; and Sass, S.L. (1980), Electron Microscopy, Vol.1, pp.234-235.

Cherns, D.(1974), Phil. Mag. 30, pp. 549-556.

Cherns, D., Kiely, C.J., and Eaglesham, D.J.(1986), Mat. Ress. Soc. Symp. Proc., 56, 145.

Chescoe, D., P. J. Goodhew (1984), The operation of the transmission electron microscope. Oxford Univ. Press.

Chu, T. L., S. S. Chu, K. Y. Yoo (1976), Proc. of the national workshop on low cost polycrystalline solar cells, May, Dallas, TX, p. 408.

Cullity, B. D.(1959), "Elements of x-Ray Diffraction", Addison-Wesley Pub. Co.

Cunningham, B., H. P. Strunk and D. G. Ast (1982), Scripta Met., Vol. 16, pp. 349-352.

D'Anterroches, C. and A. Bourret (1984), Phil. Mag. A49, pp. 783-807.

Eades, J. A. (1980), Ultramicroscopy, Vol. 5, pp. 71-74.

Edington, J. W. (1976), "Practical electron microscopy in materials science", Monograph 1, Macmillan. Vol. 5, pp. 71-74.

Fitzsimmons, M.R.; S. Sass (1988), Acta Metall. Vol.36, No.12, pp. 3103-3122.

Frank, F.C. (1965), Acta Cryst., 18, 862.

Garg, A., and W. A. T. Clark (1988), Mat. Res. Soc. Symp. Proc. Vol. 112, pp. 75-78.

Gjonnes, J.; and Moodie, A.F. (1965), Acta Cryst. 19, 65.

Goodhew, P. J. (1980), in "Grain Boundary Structure and Kinetics" (edited by R. W. Balluffi), p. 155. Am. Soc. Metals, Metals Park, Ohio.

Grimmer, H.; Bollmann, W.; and Warrington, D.H. (1974), Acta Cryst. A30, 197-207.

Hahn, T. (1984), "International Tables for Crystallography", D. Reidel Pub.Co.

Hirsch, P.B.; Howie, A.; Nicholson, R.B.; Pashley, D.W.; and Whelan, M.J. (1977), "Electron Microscopy of Thin Crystals", Butterworths, London.

Hornstra, J. (1959), Physica 25, 409.

Howie, A. (1978) "The theory of high energy electron diffraction, in diffraction and imaging techniques in material science", eds. S. Amelinckx et al.

Jones, P.M.; Rackham,G.M.; and Steeds, J.W. (1977), Proc. R. Soc. Lond., A354, 197-222.

Krivanek, O. L.; S. Isoda; and K. Kobayashi (1977), Phil. Mag., 36, 931.

Mahan, G. D., L. M. Levinson, and H. R. Phillips (1979), J. Appl. Phys. 50, 2799.

Papon, A. M.; M. Petit; G. Silvestr; J. J. Bacmann (1982), in "Grain Boundaries in Semiconductors", Vol. 5 edited by N. J. Leamy, G. E. Pike and C. H. Seager (Boston: Elsevier Science Publishing Co.), p. 27.

Papon, A. M. and M. Petit (1985), Scripta Met. 19, 391.

Paxton, A. T. (1987), "Atomic and electronic structure of grain boundaries in silicon", PhD thesis, Oxford Univ.

Paxton, A. T., and A. P. Sutton (1987), Submitted to Phys. Rev. Lett.

Pond, R.C. (1977) Proc. R. Soc. Lond., A357, 471-483.

Pond, R.C.; and Bollmann, W.(1979) Phil. Trans. Soc. Lond., A292, 449.

Pond, R.C.; and Vlachavas, D.S.(1983) Proc. Royal Soc. Lond., Series A386, 95-143.

Pumphrey, P. H. (1976), in "Grain Boundary Structure and Properties". (Eds. G. A. Chadwick and D. A. Smith) Academic Press London, p. 193.

Schapink F.W. (1986), Revue Phys. Appl. 21, 747-755.

Schapink F.W.; Forghany, S. K. E. and Caron, R.P. (1986), Phil. Mag. A53, No.5, 717-725.

Smallman R.E. (1985), "Modern physical metallurgy", 4th ed., Butterworths, London.

Spence, P.C.H.; and Carpenter, R.W. (1986), in "Principles of Analytical Electron Microscopy", (D.C.Joy; A.D.Romig; and J.I.Goldstein, ed.), Plenum Press, New York, pp. 301-352.

Steeds, J.W. (1979), "Introduction to Analytical Electron Microscopy" (J. J. Hren, J. I. Goldstein and D. C. Joy, ed.), Plenum Press, New York, p.387.

Sutton, A. P. (1984), Int. Met. Rev. 29, 377.

Sutton, A. P., (1987), Private communication.

Sutton, A. P., and R. W. Balluffi (1987), Acta Metall., Vol. 35, No. 9, pp. 2177-2201.

Sutton, A. P., and V. Vitek (1983), Phil. Trans. Roy. Soc. A309, 1.

Tanaka, M.; Saito, R.; Ueno, K.; and Harada, Y. (1980), J. Elect. Mic. 29, p.408.

Tu, K.N.; and Howie, A. (1978), Phil. Mag.B, Vol.37, No.1, 73-81.

Vaudin, M. D., B. Cunningham, and D. G. Ast (1983), Scripta Met., Vol. 17, pp. 191-198.

Vlachavas, D.S. and Pond, R.C. (1980) Inst. Phys. Conf. Ser. No. 52, pp. 195-196.

Werner, J. and H. Strunk (1982), J. Phys. c1-89.

Williams, D.B. (1984), "Practical Analytical Electron Microscopy in Materials Science", Philips Electronics Instruments, Inc. Electron Optics Publishing Group: New Jersey.

Wyckoff, R.W.G. (1963), "Crystal Structures", Vol. 1, second ed., Interscience Publisher, New York.

CHAPTER SEVEN

CONCLUSIONS AND SUGGESTIONS FOR FURTHER WORK

7.1. CONCLUSIONS REGARDING THEORETICAL CRYSTALLOGRAPHY.

(1) It has been shown that the 31 diffraction groups for single crystals, previously obtained by *Buxton et al. (1974)* using stereographic arguments, can be obtained in a straightforward manner using crystallographic theory. These groups have been derived here by starting with the 31 rosette groups and using the concept of antisymmetry to identify symmetry elements for which the reciprocity theorem must be invoked in CBED.

(2) A group theoretical method for obtaining the BF, projection diffraction and whole pattern symmetries corresponding to a given diffraction group has been presented.

(3) The results outlined above have been extended to obtain all possible diffraction groups for bicrystals. Procedures for determining the admissible diffraction groups for both "plan-view" and "edge-on" specimens have been discussed.

7.2. CONCLUSIONS REGARDING EXPERIMENTAL TECHNIQUES.

(1) "Edge-on" and "plan-view" germanium bicrystal specimens have been prepared successfully for investigations by transmission electron microscopy.

(2) SAD, CBED and LACBED techniques have been used to study bicrystal specimens. The SAD method was found to be particularly useful for studying interfacial reconstruction. Bicrystal symmetry was successfully investigated using CBED on "plan-view" specimens. On the other hand, CBED patterns obtained from "edge-on" specimens could not be interpreted directly in terms of bicrystal symmetry.

7.3. CONCLUSIONS REGARDING SPECIFIC INTERFACIAL STRUCTURES.

(1) $\Sigma = 3(1\bar{1}\bar{1})_\lambda$ boundary: the experimental observations are consistent with a bicrystal exhibiting symmetry $p\bar{6}'m2'$. Moreover, no evidence was found for interfacial reconstruction or a significant displacement field. This boundary is stable and showed no tendency to dissociate.

(2) $\Sigma = 3(\bar{1}1\bar{2})_\lambda$ boundary: the experimental observations are consistent with a bicrystal exhibiting the symmetry c1m1. In particular, clear evidence of a c(2x2) reconstruction was obtained, and the intensities of interfacial reflections were found to be in good agreement with those calculated based on the model structure suggested by *Papon et al. (1985)*. It was also observed that this interface is unstable with respect to dissociation into other $\Sigma = 3$ and $\Sigma = 9$ boundaries.

(3) $\Sigma = 27(\ 5\bar{5}\bar{2}\ )_\lambda$ boundary: this boundary was observed to be highly unstable, exhibiting extensive dissociation and facetting. Due to this structural complexity, it was not possible to determine the bicrystal spacegroup using CBED. Some evidence was obtained using SAD indicating that the periodicity of the interface is the same as that of the $\Sigma = 27$ CSL.

7.4. SUGGESTIONS FOR FURTHER WORK.

In the course of this work it has become evident that two aspects of the experimental programme would benefit from further attention. These are, firstly, problems associated with the interpretation of CBED patterns from bicrystal specimens, and secondly, quantitative comparison between the calculated and measured intensities of diffracted beams.

Concerning CBED, three topics need to be considered. The first one follows from our observations that antisymmetry operators, such as m', and 2' in the interface of a "plan-view" specimen, were frequently broken, i.e. did not lead the anticipated symmetries being observed in CBED patterns. We have presumed that this has arisen due to surface roughness or the location of the interface not being coincident with the central plane of "plane-view" specimens. It would be valuable to carry out a systematic study by simulating the contrast expected from "plan-view" specimens where the interface location and surface smoothness and orientation were varied. The second topic concerns the symmetry observed in CBED patterns from "edge-on" specimens. As explained in the thesis, it is anticipated that the symmetry observed depends upon the spot size used, so called "complex symmetry" being observed for relatively large spot sizes as in the present work. It would therefore be interesting to investigate pattern symmetry using smaller spot sizes. Finally, as has been suggested by *Schapink et al. (1986)*, it would be valuable to investigate the symmetry of CBED patterns from "edge-on" bicrystal specimens using the double-rocking zone axis pattern (DRZAP) technique, and to vary the spot size in addition as outlined above.

With regard to quantitative measurement of diffracted intensities, it would be particularly valuable to carry out x-ray diffraction studies of "plan-view" bicrystal specimens using a synchrotron source. This would have the advantage of making the comparison between experimental measurements and theoretical calculations based on kinematical theory more justifiable. At the same time, use of a synchrotron source would overcome the experimental difficulties associated with the problem of weak x-ray diffraction by interfaces. This approach is currently being undertaken by *Sass et al. (1988)* in their work on gold bicrystals.